Modelling the ~~Thermospheres~~ of the Giant Planets

Christopher Glyn Alun Smith

Submitted for the Degree of Doctor of Philosophy

Atmospheric Physics Laboratory
Department of Physics and Astronomy
University College, London

May 5, 2006

ProQuest LLC
789 East Eisenhower Parkway
P.O. Box 1346
Ann Arbor, MI 48106-1346

Abstract

At Jupiter and Saturn the thermosphere is the region of the neutral atmosphere that coexists with the ionosphere. It is thus the region of the atmosphere that is most strongly coupled to the magnetosphere, and is responsible via the ionosphere for the transfer of planetary angular momentum to the magnetosphere. Both planets also exhibit high thermospheric temperatures that are yet to be explained.

We study the coupled thermosphere-ionosphere-magnetosphere systems of Jupiter and Saturn using a thermospheric general circulation model and simple models of the ionosphere and magnetosphere. Our principle result is that meridional winds in the thermosphere are of critical importance to the interaction. Angular momentum extracted from the thermosphere by magnetospheric drag is found to be replaced largely by meridional advection, not, as commonly supposed, by vertical viscous transfer. These same meridional winds are also able to couple together regions of the magnetosphere that otherwise would not interact.

We find it very hard to reproduce the observed thermospheric temperatures with our model. Under a limited range of circumstances it is shown that redistribution of thermal energy from high- to low-latitudes by winds can explain the available observations. However, the inclusion of ion drag generates a circulation in the polar regions that acts as a heat pump and efficiently cools the thermosphere, significantly reducing the efficiency of the redistributive winds.

Acknowledgements

Unreserved thanks are due to my Mum for her love and support throughout my education.

I am also indebted to other family and friends who have, in their various ways, provided me with companionship and support during my PhD. Special thanks in this regard are due to Charlotte and Asa.

I would also like to acknowledge the help and support of everyone at the Atmospheric Physics Lab, in particular my supervisors Alan and Steve, whose approach has been an exemplary of light touch regulation. I am also grateful to various other members of the scientific community within and beyond UCL who have assisted or entertained me from time to time, in particular the members of the planetary magnetospheres group at Leicester University, whose research has inspired much of this study.

To put one brick upon another,
Add a third, and then a fourth,
Leaves no time to wonder whether
What you do has any worth.

But to sit with bricks around you
While the winds of heaven bawl
Weighing what you should or can do
Leaves no doubt of it at all.

Philip Larkin

Contents

List of Figures

List of Tables

Chapter 1

Introduction

This thesis is about the upper atmospheres — the thermospheres — of the giant planets Jupiter and Saturn. Our present knowledge of these planets is derived largely from the data collected by seven spacecraft (Table 1.1), although ground-based telescopic observations still play an important role. The Voyager 2 spacecraft also visited the 'ice giants', Uranus and Neptune. The forms of measurements performed by these missions are, by necessity, prejudiced towards those most easily carried out from a spacecraft. With the exception of the Galileo mission, which released a probe into the atmosphere of Jupiter (Seiff et al., 1997), the only in-situ measurements are of the planets' magnetospheres. Thus our knowledge of the upper atmospheres of these planets consists of a rather threadbare collection of remote sensing observations, propped up by a single set of direct atmospheric measurements from the Galileo probe.

This is a very different situation from that encountered at Earth. Our knowledge of the terrestrial atmosphere and space environment is rooted in a diverse range of in-situ and remote sensing measurements, made systematically over many decades, which provide a sound basis for studying the intricacies of the system. Our knowledge base is 'bottom up'. At the giant planets our knowledge is, conversely, 'top down': there is very little ground truth but a reasonably

Spacecraft	Jupiter	Saturn	Uranus	Neptune
Pioneer 10	1973	—	—	—
Pioneer 11	1974	1979	—	—
Voyager 1	1979	1980	—	—
Voyager 2	1979	1981	1986	1989
Ulysses	1992	—	—	—
Galileo	1995–2003	—	—	—
Cassini	2001	2004–?	—	—

Table 1.1: Flyby and tour dates for the seven missions to study the gas giants.

reliable body of 'space truth'.

Our ignorance of the gas giants' upper atmospheres is well illustrated by one of the principal problems that this study seeks to address. This is the so-called 'energy crisis' in the thermospheres of the gas giants, which are observed to be much hotter than predictions by simple models indicate. Ignorance of the origin of the thermal structure — possibly, alongside chemical composition, the most fundamental atmospheric quantity — underpins uncertainty in understanding every other aspect of the atmosphere.

In order to resolve the energy crisis, scientists have been forced to invoke various sources of energy to explain the observations. The energy sources that have been suggested as solutions to the energy crisis fall conveniently into two categories: energy from above, and energy from below. Measurements of the magnetosphere, which lies immediately above the upper atmosphere, are much more numerous than measurements of the lower atmosphere, lying immediately below it. Thus most of the research effort directed at upper atmospheric heating has focussed on how to transfer and thermalise energy from the magnetosphere. This is a promising and fertile area, and it is on this that we shall focus in what follows.

Studies of energy transfer from the lower atmosphere are often rather speculative due to the lack of observational evidence. There is considerable scope for research in this area, but an adequate treatment of the issues involved is beyond the scope of this work. For this reason we will almost entirely neglect the possibility of energy transfer from the lower atmosphere, concentrating instead on the contribution to the thermal balance made by magnetospheric sources alone.

A second issue that we will address in this study is the transfer of angular momentum from the rapidly rotating planets to their magnetospheres. The magnetospheres of Jupiter and Saturn are often described as 'rotation dominated': however it is often forgotten or ignored that this rotation is not a direct result of the magnetic field of the planet 'rotating' but is a consequence of angular momentum transfer from the planet via the thermosphere. We hope to shed some new light on this process.

1.1 Basic physics of the upper atmosphere

1.1.1 The neutral atmosphere

Hydrostatic equilibrium

To first order, the structure of the neutral component of a planetary atmosphere is dominated by a balance between gravitational and pressure forces. The pressure p at any altitude z is related to the weight of the gas above it:

$$p(z) = \int_z^\infty \rho g dz \tag{1.1}$$

where g is the acceleration due to gravity and ρ is the mass density of the gas. (Note that g varies slightly with altitude, but in this discussion we will assume it to be a constant.) Thus, locally, we have the relation:

$$\frac{dp}{dz} = -\rho g \tag{1.2}$$

This situation is termed 'hydrostatic equilibrium'. If we assume an ideal gas we have an equation of state for the gas that relates p and ρ:

$$p = \frac{\rho RT}{\mu} \tag{1.3}$$

Here $R = 8.31\text{JK}^{-1}\text{mol}^{-1}$ is the molar gas constant, μ is the mean molar mass in kg, and T is the temperature in degrees K. Combining this with Eq. 1.2 yields:

$$\frac{dp}{dz} = -\frac{p}{H} \tag{1.4}$$

where we have introduced the pressure scale height, H:

$$H = \frac{RT}{\mu g} \tag{1.5}$$

The meaning of the pressure scale height becomes apparent if we solve Eq. 1.4 to find p as a function of z:

$$p(z) = p_m \exp\left[-\frac{(z - z_m)}{H}\right] \tag{1.6}$$

where p_m is the pressure at some arbitrary reference altitude z_m. Thus pressure falls off exponentially with altitude. The (sensibly named) pressure scale height represents the scale length of this behaviour.

Eq. 1.6 has several important implications. Over a vertical distance of several H, the pressure will change by over an order of magnitude. This leads to vastly different behaviour — governed by different physics — in layers of the atmosphere separated by only a few H. Also, it indicates that lower layers of the atmosphere are very much denser than those above them. This means in general that coupling between atmospheric layers is prejudiced towards the denser lower layers driving the more tenuous higher layers. However, there are important exceptions to this rule of thumb. For example, some terrestrial studies have shown that changes in upper atmospheric chemistry driven by solar variability can have important consequences for the lower atmospheric chemistry and circulation (e.g Haigh, 1996).

We have referred to H as the pressure scale height because it describes the behaviour of the total atmospheric pressure with altitude. We may equally define a scale height H_i for each atmospheric constituent i, defined as:

$$H_i = \frac{RT}{\mu_i g} \tag{1.7}$$

where μ_i is the molecular mass of the constituent. In the absence of any mixing processes other than molecular diffusion, each gas will distribute itself vertically according to its own scale height.

Adiabatic Lapse Rate

The lapse rate refers to the vertical temperature gradient dT/dz. The adiabatic lapse rate $-\Gamma$ is a measure of the variation of temperature of a parcel of gas that expands or contracts adiabatically as it rises or falls in the atmosphere. It is given by

$$\Gamma = \frac{g}{c_p} \tag{1.8}$$

where c_p is the heat capacity per unit mass at constant pressure[1]. This equation follows by combining the ideal gas law (Eqn. 1.3), hydrostatic equilibrium (Eqn. 1.4) and the adiabatic relation $p^{(1-\gamma)}T^{\gamma} = \text{constant}$, where γ is the ratio of heat capacities $c_p/c_v = c_p/(c_p - R/\mu)$. This quantity $-\Gamma$ is, more specifically, the *dry* adiabatic lapse rate, since the presence of water (or some other vapour) complicates the situation. In the thermosphere such effects are negligible.

The adiabatic lapse rate determines the stability of an atmosphere to convective overturn. If the lapse rate is greater than $-\Gamma$ — which includes any positive lapse rate — then clearly a parcel of air that rises, and thus cools according to the adiabatic lapse rate, will find itself surrounded by warmer, and thus more rarefied air, and will sink back to its previous altitude. In this situation the atmosphere is stable to convective overturn.

The opposite situation occurs if the lapse rate is less than $-\Gamma$. In this case the rising parcel of air find itself surrounded by cooler and denser air and continues to rise. Thus a strongly negative lapse rate is unstable to convective overturn.

1.1.2 The ionised atmosphere

The particles that make up the ionised component of the atmosphere have their source in the ionisation of neutral particles. The ionised particles then return to the neutral atmosphere upon recombination.

The physics that governs the behaviour of these ionised gases is different to that which governs the neutral atmosphere: the ionised components are subject not only to gravitational forces and collisional effects, but also to the influence of electromagnetic forces.

Sources of ionisation

The principle global source of ionisation in planetary atmospheres is the absorption of solar radiation. In order for a photon to cause ionisation its energy must exceed the ionisation potential of the atom or molecule by which it is absorbed. For H_2, H and He, the dominant components of the gas giants' atmospheres, the ionisation potentials correspond to photons with wavelengths of 80.4, 50.4 and 91.2nm respectively (Strobel and Atreya, 1983). It is thus radiation in the extreme

[1]Note that the heat capacities per unit mass c_p and c_v are related to the molar heat capacities C_p and C_v by the relations $C_p = c_p\mu$ and $C_v = c_v\mu$, where μ is the mean molecular mass.

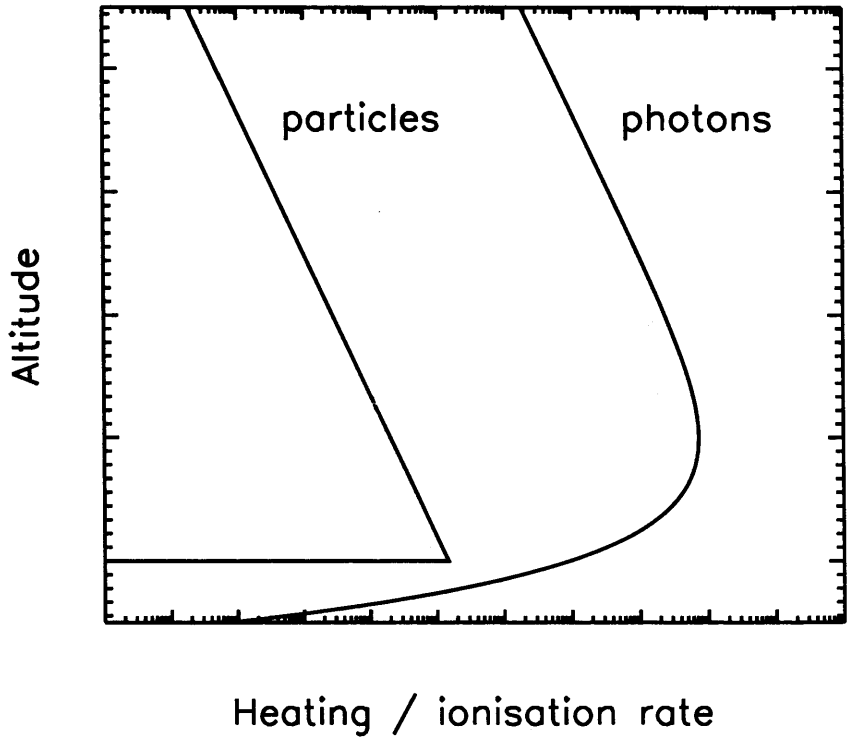

Figure 1.1: Idealised absorption profiles for radiation and particles.

ultra-violet (EUV) portion of the spectrum, shortwards of 91.2nm, that has the potential to generate significant ionisation.

A secondary source of ionisation, most important at high latitudes, is the precipitation of energetic charged particles, usually electrons and protons, from the magnetosphere and solar wind. If these particles have kinetic energy in excess of the ionisation potential of any neutral particles they impact, they may also cause significant ionisation.

In both these cases it is clear that at very high altitudes, where the neutral density is low, the neutral atmosphere will do little to attenuate the beam of photons/particles, and the ionisation rate will be approximately proportional to the neutral density. At very low altitudes, the beam will have been entirely attenuated by the neutral atmosphere, and the ionisation rate will fall to zero. Between these two regimes there must exist a peak. The altitude and distribution of this ionisation peak is important for the resulting structure of the ionosphere.

To understand the morphological differences between the ionisation peaks produced by photons and particle precipitation, we can distinguish two idealised cases. In the first, corresponding to photons, the beam is attenuated by discrete absorption events which reduce the flux by remov-

ing photons from the beam. In the second, corresponding to particles, the beam is attenuated by many collisions between the precipitating particles and neutral particles which gradually reduce the energy of the particles in the beam — but not the flux — until they are slowed to a halt, at which point the flux falls to zero.

In both cases the behaviour can be characterised in terms of a cross section σ: in the first case, this is a cross-section for absorption of a photon; in the second, it is a cross-section for a collision reaction that removes some threshold energy E_{th} from the kinetic energy of the precipitating particle. In our idealised example, the latter cross-section is independent of the energy of the precipitating particle; in reality this is not the case.

We write the flux of either photons or particles as F, initially F_0, and the energy of each photon or particle as E, initially E_0. We assume an isothermal atmosphere of uniform composition with scale height H and number density $n = n_0 \exp(-z/H)$ where n_0 is the number density at altitude $z = 0$. We then find, for a beam of monochromatic photons of energy E_0:

$$\begin{aligned} F &= F_0 \exp\left[-\sigma H n\right] \\ q &= E_0 \frac{dF}{dz} = \sigma n E_0 F_0 \exp\left[-\sigma H n\right] \end{aligned} \tag{1.9}$$

where q is the ionisation rate. This distribution is known as a *Chapman function*, and exhibits the behaviour described above in which the ionisation rate is proportional to n in the low density limit, and zero in the high density limit. It is easily shown that the peak ionisation occurs at $n = 1/(\sigma H)$.

A similar calculation for particles yields:

$$\begin{aligned} E &= E_0 - \sigma H n E_{th} \\ q &= F_0 \frac{dE}{dz} = \sigma n E_{th} F_0 \end{aligned} \tag{1.10}$$

where in this case $F = F_0$ everywhere. Clearly the energy cannot be negative, so the beam stops when E has fallen to zero at $n = E_0/(\sigma H E_{th})$. Since $q \propto n$, which increases monotonically with depth, this cut-off point is also the ionisation peak.

These two contrasting distributions of q are plotted in Fig. 1.1, in arbitrary units. Beneath each curve the region in which the rate is greater than 10% of the peak value is shaded. The important differences between the two forms of ionisation profiles are clear. The peak in photon absorption is wide and reasonably symmetric. In contrast, the peak in particle absorption is narrow and skewed towards lower altitudes.

This greater concentration of the ionisation peak due to particle precipitation can lead to an ionosphere with a considerably different structure in the auroral regions. In particular it can contribute towards the generation of significantly enhanced electron densities.

In practice, the profiles shown in Fig. 1.1 are a gross simplification. The atmosphere is penetrated by a whole spectrum of energies of both photons and particles. This smears out the profiles shown in the vertical direction. Cross-sections for the energy degradation of particles

and absorption of photons are also dependent on the energy of the particle and the composition of the neutral atmosphere, and thus vary along the particle's path, complicating the situation considerably.

Ionisation events can also lead to the liberation of further energetic particles, usually electrons, that cause further ionisation at lower altitudes. If these electrons are liberated by photoionisation they are known as *photoelectrons*; if they are liberated by collisions with precipitating particles they are known as *secondary electrons.*

Acceleration of precipitating particles

In order for precipitation of energetic particles to take place it is necessary for these particles, originating in the magnetosphere or solar wind, to be accelerated above their ambient thermal velocities. In the case of electron precipitation this takes place when the ionosphere draws currents from the magnetosphere such that the upwards field-aligned current density is too great to be carried by the ambient plasma alone. In this situation a field-aligned voltage must develop which accelerates electrons towards the planet. The resultant downwards flow of energetic electrons provides the necessary upwards current, and these electrons are then responsible for ionisation of the neutral atmosphere and the generation of auroral emissions. Note that auroral emissions may also be generated by the precipitation of hot particles directly from the magnetosphere.

Electrostatic forces

Any small separation of the positive and negative components of the ionised atmosphere results in a large electric field which prevents any further separation taking place. For example, supposing the ionosphere to have a uniform ion density n_i in the presence of an electron density $n_e = n_i$, we may calculate the vertical electric field produced if these two components are separated by a small vertical distance δ, $E = en_i\delta/\epsilon_0$. If we assume that $n_i \sim 10^{10}\mathrm{m}^{-3}$ then it is easily shown that E will produce an acceleration on a proton of the same order of magnitude as gravity if $\delta \sim 10^{-10}\mathrm{m}$. This acceleration will act to remove the charge separation. This scale is of the order of an atomic radius, and it is thus effectively impossible to separate the ions and electrons. The result is that the relation $n_i = n_e$ must always hold almost exactly. This situation is known as *quasi charge neutrality.*

Motion in a magnetic field

Both the Earth and the giant planets possess considerable global magnetic fields. Since the ionised component of the atmosphere possesses a non-zero temperature — i.e. the ionised gases undergo random thermal motions at the molecular level — the particles experience continual motion relative to the magnetic field. This makes them subject to the Lorentz force $\boldsymbol{F}$, which

for singly charged ions is given by:

$$\boldsymbol{F} = |e|\boldsymbol{v} \times \boldsymbol{B} \tag{1.11}$$

where e is the electronic charge, $\boldsymbol{v}$ is the velocity and $\boldsymbol{B}$ is the magnetic field. In the absence of collisions this causes the ions to gyrate about the magnetic field with gyrofrequency Ω:

$$\Omega = \frac{|e|B}{m} \tag{1.12}$$

where m is the particle mass. Note that Ω is independent of the velocity of the particle. The effect of this gyration about the field line is that, in the absence of other forces, the ions become 'tied' to the field lines. They are still able to move parallel to the field, since the Lorentz force does not act upon these motions. Electrons exhibit the same behaviour but with the sense of gyration reversed. We will discuss these motions in more detail in Chapter 2.

Ambipolar diffusion

The influence of gravitational and electrostatic forces combine to produce the effect known as ambipolar diffusion. The ions and electrons in the ionosphere are both encouraged by gravity to settle according to their scale heights (Eqn. 1.7), as described for the neutral atmosphere above. Since they are tied to the field lines by their gyratory motions, this settling process occurs along the magnetic field direction. At high latitudes this is in general a slightly non-vertical angle; at low latitudes the situation is much more complicated.

The ions are much heavier than the electrons, and this gravitational settling process thus tends to produce a situation in which the ions try to move downwards relative to the electrons. However, as this process begins, a small positive charge forms at the base of the ionosphere and a small negative charge at the top. As described above, the charge separation required to produce large electrostatic forces between the ions and electrons is tiny. The result is that the electrons are dragged downwards by the ions and the ions dragged upwards by the electrons, in order to preserve charge neutrality. The consequence is that the entire quasi-neutral plasma becomes distributed in the manner of a neutral gas whose molecular mass is given by the average molecular mass of the ions and electrons. The electrons are much lighter than the ions, so this average mass is, to a good approximation, half of the ion mass. Thus, for a plasma containing only one species of ion, the plasma scale height H_p is given by

$$H_p = \frac{2RT}{\mu_i g} \tag{1.13}$$

where in this case μ_i is the molar mass of the ion species i. For a more detailed discussion of this phenomena, the reader is referred to Ratcliffe (1972).

An important consequence of ambipolar diffusion is that, for example, H^+ becomes distributed with twice the scale height of H and four times the scale height of H_2. Thus, if ambipolar diffusion prevails, the ionospheric density may fall off much more slowly than the neutral

density, such that at very high altitudes the neutrals become unimportant relative to the ions and electrons.

It should be noted that ambipolar diffusion is only important when two conditions are fulfilled. Firstly, the neutral densities must be low enough that ions are not inhibited by collisions with neutrals as they move parallel to field lines. Secondly, the chemical lifetimes of the ionised gases must be long enough that they have time to distribute themselves in the manner described before being destroyed by recombination or charge exchange. It thus only dominates the ionospheric structure at high altitudes, where low neutral and plasma densities ensure that both of these conditions are satisfied simultaneously.

Ion chemistry

Due to the the condition of quasi charge neutrality, any ions present in the atmosphere must always exist in the presence of equal numbers of electrons. The ions and electrons will thus tend to recombine, depleting the ion density. If there is no continuous or periodic source of ionisation, then in time the ionised gases will all recombine.

In general molecular ions recombine more rapidly, because degrees of freedom afforded by their molecular structure allows energy and momentum to be conserved more easily during recombination reactions. Thus recombination may be accelerated by atomic ions charge exchanging with molecular neutrals to produce molecular ions. These species, when formed, may then be destroyed by recombination much more rapidly. We will give an example of such a sequence of reactions in Section 1.3.2.

1.1.3 The collisionless regime

At very high altitudes interactions with neutrals become almost entirely unimportant and the gas may be described reasonably accurately as a fully ionised quasi-neutral plasma. In this regime the gas is subject to both hydrodynamic and electromagnetic forces, but collisions can be considered negligible. The theory that describes these circumstances is known as magnetohydrodynamics (MHD). Since MHD is not a major focus of this work we will not enter into a detailed discussion, but it is useful to summarise some of the most important concepts.

Alfvèn's Theorem

Ohm's law may be expressed as:

$$\boldsymbol{j} = \sigma(\boldsymbol{E} + \boldsymbol{v} \times \boldsymbol{B}) \tag{1.14}$$

and in a highly conducting plasma the conductivity σ may be so large that to ensure equality the condition

$$\boldsymbol{E} + \boldsymbol{v} \times \boldsymbol{B} = 0 \tag{1.15}$$

must hold. In these circumstances *Alfvèn's theorem*, also known as the *frozen-in flux condition* may apply. This states that the total magnetic flux threading any surface element within the fluid must remain constant with time, independent of any motion or deformation of that surface.

The simple consequence of this is that the field lines appear to move with the flow of plasma. A series of regions of space linked together by a single magnetic field line — a *flux tube* — can then be treated as a coherently behaving entity. This concept is extremely useful in describing motions of plasma within the magnetosphere, since the magnetic field structures those motions and thus reduces the complexity of the problem.

Magnetic pressure and tension

The Lorentz force on the plasma is the vector product of the current density and the magnetic field (Kivelson and Russell, 1995)

$$\boldsymbol{j} \times \boldsymbol{B} = \frac{1}{\mu_0}\left(-\frac{1}{2}\nabla\left(B^2\right) + (\boldsymbol{B}\cdot\nabla)\boldsymbol{B}\right) \tag{1.16}$$

Note that the components of the first and second terms that are parallel to $\boldsymbol{B}$ cancel exactly, ensuring that this force acts perpendicular to $\boldsymbol{B}$, as implied by the cross product.

The first term is identical in form to a pressure gradient force, and for this reason is referred to as the *magnetic pressure*. This tells us that to compress a magnetised plasma requires energy, not only because of its thermal (collisional) pressure, but also because of the energy stored in the electromagnetic fields.

The second term is often referred to as *magnetic tension*. The operator $\boldsymbol{B}\cdot\nabla$ generates the spatial derivative of the $\boldsymbol{B}$-field in the field direction itself. The component of this perpendicular to $\boldsymbol{B}$ represents curvature of the field line, and the force therefore acts in the direction of this curvature. Thus the force acts to reduce the curvature of the $\boldsymbol{B}$-field. In this sense it behaves like an elastic stress acting on a solid body.

The above expression should strictly include a term due to the electric field acting on the charge density. However, provided that any motions of the plasma are non-relativistic then charge neutrality is an excellent approximation and this term can be safely neglected. This is the case in all situations considered in this thesis.

Breakdown of ideal MHD

Combining the concepts of frozen-in flux, magnetic pressure and magnetic tension, we can see that the plasma in the magnetosphere can be treated as a collection of elastic, compressible tubes of fluid defined by the magnetic field. This picture is useful, but is an approximation based on various assumptions, in particular that the plasma is almost perfectly conducting and that the scale lengths of any structure in the plasma are large.

The former assumption breaks down at the lower boundary of the magnetosphere, as it merges with the neutral atmosphere and ionosphere. Collisions with neutrals significantly modify the conductivity, which becomes finite and non-isotropic. In these circumstances ideal MHD is no longer suitable. We will discuss the physics of this region in greater detail in Chapter 2.

The latter assumption breaks down at boundaries between two very different plasma regimes. The frozen-in flux condition means that even if regions with very different plasma conditions are adjacent to each other, no plasma can mix across the boundary. If, for example, there is a large change in magnetic field strength or direction across the boundary — for example in the neutral sheet of the Earth's magnetotail — then there is a curl in the magnetic field strength, which, by Maxwell's equations, implies the existence of a current sheet.

At these current sheets the approximations of ideal MHD break down, and magnetic field lines are able to break and reconnect across the boundary through the action of small-scale diffusive effects. This process is known as *magnetic reconnection.* This leads to the connection by magnetic field lines of regions of plasma which, under ideal MHD, would be unable to mix. Thus it is magnetic reconnection that allows plasma from the solar wind to enter a planetary magnetosphere, and vice versa.

Reconnection between magnetic field lines originating in the Earth's core and those embedded in the solar wind leads to the classification of field lines as *closed* or *open.* Closed field lines begin and end at the Earth, whereas open field lines have undergone reconnection such that one end is rooted in the Earth's core, while the other is connected to the solar wind. The behaviour of plasma lying on these two sets of field lines is very different, and thus the location of the open-closed field line boundary is often found to be important.

1.2 Structure of the terrestrial atmosphere

We have now covered enough background theory to embark on a basic description of the terrestrial atmosphere, ionosphere and magnetosphere. This description will set the scene for our later discussion of the analagous structures at the gas giant planets.

The Earth, of course, is a solid body with a well-defined surface and a global intrinsic magnetic field. It is surrounded by a significant gaseous envelope — an atmosphere — composed of approximately 80% nitrogen and 20% oxygen. Hydrogen and helium — the dominant components of the gas giant's atmospheres — are trace gases in the lower regions of the terrestrial atmosphere, but due to their relatively small molecular masses they become important components in the topside ionosphere and magnetosphere.

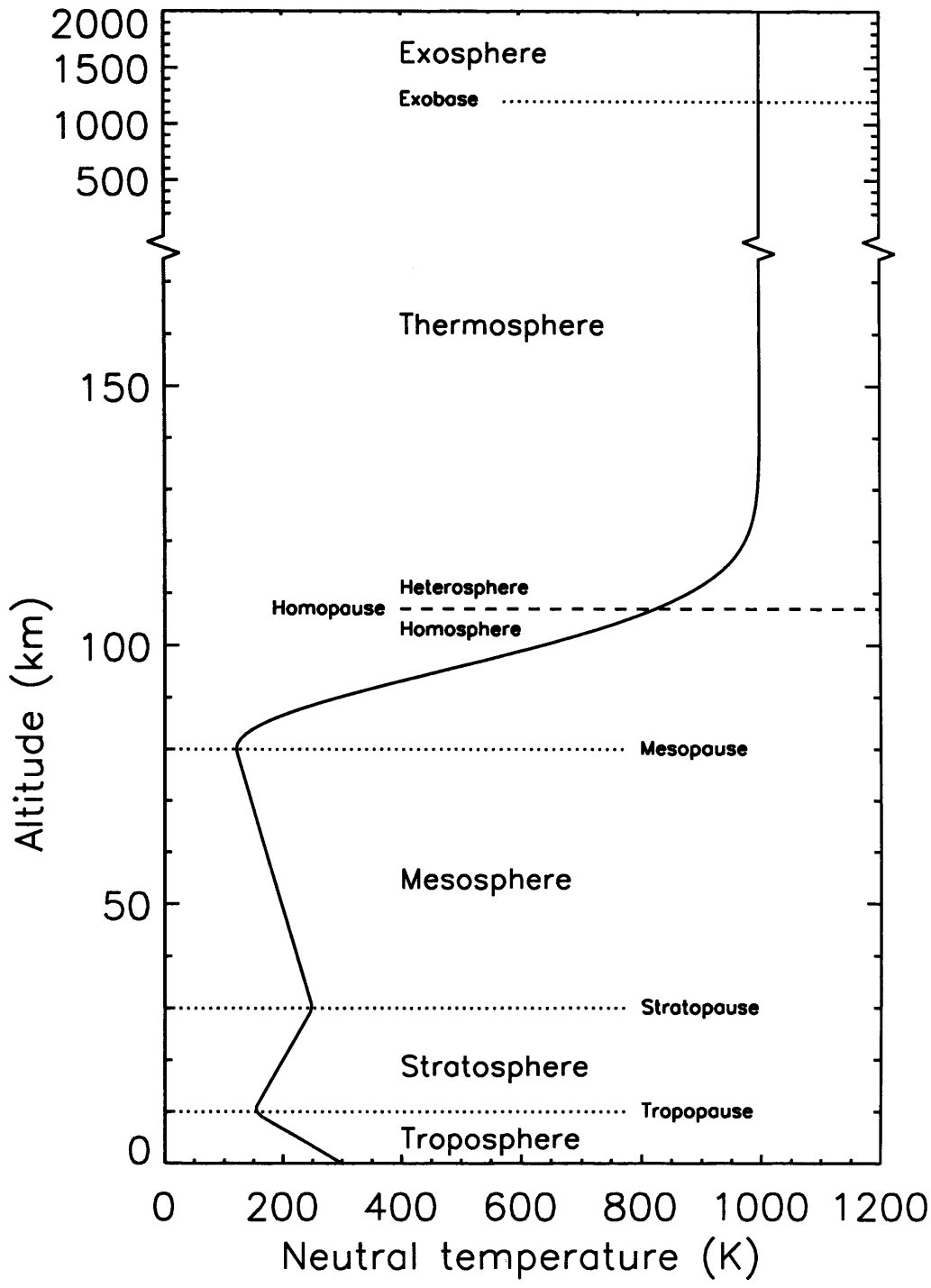

Figure 1.2: Schematic of the terrestrial neutral atmospheric structure.

1.2.1 The neutral atmosphere

The neutral atmosphere is traditionally divided into several well defined layers (Fig. 1.2). The lowest atmospheric layer is known as the *troposphere* ('turning' sphere). This region is dominated by sunlight heating the Earth's surface, which in turn heats the atmosphere. Heat is transferred upwards convectively, and since the gas compresses and expands adiabatically as it rises and falls, the tropospheric temperature gradient is well described by the adiabatic lapse rate $-\Gamma$.

At the *tropopause* the temperature reaches a minimum and then begins to rise with altitude in the *stratosphere* ('layered' sphere). The positive temperature gradient means that the stratosphere is stable to convective overturn. This temperature rise occurs because direct absorption of sunlight begins to become more important than energy transfer from the ground. On Earth the stratosphere is largely a consequence of the absorption of UV sunlight by atmospheric ozone.

The temperature peak produced by this absorption is known as the *stratopause*. Above this level temperatures begin to decrease again in the *mesosphere* ('middle' sphere). The energy balance in this region is a complex combination of radiative cooling (mainly by carbon dioxide) and heating by a mixture of exothermic chemical reactions, absorption of sunlight and breaking of gravity waves.

The mesosphere terminates at a second temperature minimum, the *mesopause*. Above this level is the *thermosphere* ('hot' sphere). This is the atmospheric region with which we will be principally concerned in this work. On Earth the thermosphere increases in temperature with altitude, reaching extremely high temperatures of the order of 1000-2000K. These high temperatures are largely a consequence of the efficient absorption of solar extreme ultraviolet (EUV) radiation, coupled with the low atmospheric densities and the absence of an efficient cooling mechanism. The thermosphere is also heated by processes associated with coupling between the Earth's atmosphere and the solar wind. These and related processes are a major focus of this work, and will be discussed in some detail in Chapter 2.

The main energy sink in the terrestrial thermosphere is downwards thermal conduction. Radiative cooling is relatively unimportant because there are few species present that radiate actively in the infrared. At Venus, in contrast, the thermosphere is much cooler due to the influence of radiative cooling by carbon dioxide, even though the planet is much closer to the Sun.

The definition of the upper boundary of the thermosphere is not well-defined. With altitude the atmospheric density decreases to such an extent that at some stage collisions between gas molecules become so rare that we may no longer treat the atmosphere hydrodynamically. At this altitude the particles follow essentially ballistic trajectories in the Earth's gravitational field. This region is known as the *exosphere* ('outer' sphere). The boundary between the thermosphere and exosphere is usually known as the *exobase*. A typical definition of the exobase is to define it as the point at which the pressure scale height is equal to the mean free path. It is supposed that

above this altitude the trajectories of the particles are more important to the structure than hydrostatic equilibrium. Accurately capturing the transition from hydrodynamic to ballistic behaviour presents, in principle, a problem for thermospheric modelling (Chapter 3).

We will mention one further important division of the neutral atmosphere, into the *homosphere* ('same' sphere) and *heterosphere* ('different' sphere). In the homosphere, which extends from the surface of the Earth upwards to the *homopause* (also known as the *turbopause*), the various component gases of which the atmosphere consists are evenly mixed together by bulk-flow turbulent motions. In the heterosphere, which lies above the homopause, molecular diffusion of individual component gases becomes more important to their distribution than bulk-flow turbulence. In this situation the component gases separate out according to their individual scale heights (Eqn. 1.7). Those gases with large molecular masses have small scale heights, and thus their densities fall off rapidly with altitude. These gases are thus found only in the homosphere or just above the homopause. Lighter gases, however, have the largest scale heights, and dominate the atmosphere at high altitudes. Atomic hydrogen is the lightest neutral gas, and is thus the dominant component of the *geocorona*, the cloud of neutral gas that surrounds the Earth beyond the thermosphere.

1.2.2 The ionosphere

Coexistent with the thermosphere-mesosphere region on Earth is the *ionosphere* (Ratcliffe, 1972). We can either define this as a spatially delimited region of the atmosphere (a common definition is that the ionosphere is the region in which electron densities are large enough to significantly effect the propagation of radio waves) or as an entity (in which case the ionosphere consists simply of all the charged particles existing at any one time in the Earth's atmosphere).

The main peak of electron density in the terrestrial ionosphere normally lies at altitudes greater than ~250km and is known as the F2 layer. The topside of the F2 layer is structured by ambipolar diffusion. At these altitudes the ionosphere is composed mostly of O^+, an atomic ion, which recombines slowly. In the absence of diffusion, the peak would occur much higher in the atmosphere.

The bottomside of the F2 layer is structured by chemistry, and in certain circumstances a small subsidiary peak (the F1 layer) forms close to the peak of electron production, below the main (F2) peak. There are two further subsidiary peaks at lower altitudes — the E layer at ~110km and the D layer at ~80km. Both of these layers are associated with peaks in electron production due to absorption of ionising radiation.

At mid and low latitudes the diffusion of ionospheric plasma along field lines above the electron density peak results in the ionospheric plasma filling the magnetic field lines at these latitudes. Thus the ionosphere effectively extends into space in the low latitude regions. This inner region of the planetary magnetic field that is filled with ionospheric plasma is known as

the *plasmasphere.*

1.2.3 The magnetosphere

Beyond the plasmasphere lies a region of more tenuous plasma which is best described using collision-free plasma physics. This is known as the *magnetosphere.* The Earth's magnetosphere is principally driven not by coupling to the upper atmospheric regions but by interaction with the solar wind. The prevailing paradigm for our understanding of the solar wind interaction is the *Dungey cycle.*

This process is illustrated in Figure 1.3. This shows a cut-away view of the magnetosphere through the noon-midnight meridian. Solar wind flux tubes (1') approach from the left, undergoing reconnection with closed flux tubes that lie just inside the magnetopause (1). This generates two newly opened flux tubes (2,2'). Each of these open flux tubes has one end anchored in the anti-sunward solar wind flow and the other in the Earth's ionosphere. Under the action of the solar wind flow, these flux tubes are dragged antisunward across the polar cap and into the *magnetotail* (3-5).

In the magnetotail, flux tubes from the northern and southern lobes are able to reconnect (6,6'). After this second reconnection event there is now a newly closed flux tube (7) and a newly reconnected solar wind flux tube (7'). The latter is ejected down tail with the solar wind flow, initially under the action of the magnetic tension force. The former moves back towards the planet and flows back to the noon side of the magnetosphere around either the dawn or dusk flank.

The lower diagram shows the convection pattern of plasma in the ionosphere that corresponds to this cycle. There is an anti-sunward flow of open flux tubes across the pole, and a sunward return flow of closed flux tubes to the dawn and dusk. The result is a double-cell plasma convection pattern that is approximately fixed in the Sun-Earth frame. The timescale for this cycle to complete itself is of the order of $\sim$6 hours. This is much shorter than the Earth's rotation period, indicating that planetary rotation probably does not play an important role in structuring the solar wind interaction.

The motions associated with the Dungey cycle are associated with electric fields which drive currents in the magnetosphere and ionosphere. These currents include upwards field-aligned currents just above the ionosphere which, as discussed above, lead to the precipitation of charged particles responsible for the aurora.

The above discussion provides only a brief sketch of the behaviour of the Earth's magnetosphere. The true behaviour is complicated considerably by the detailed structure of the thermosphere, ionosphere and solar wind, and there are many aspects of the system that are not yet well understood.

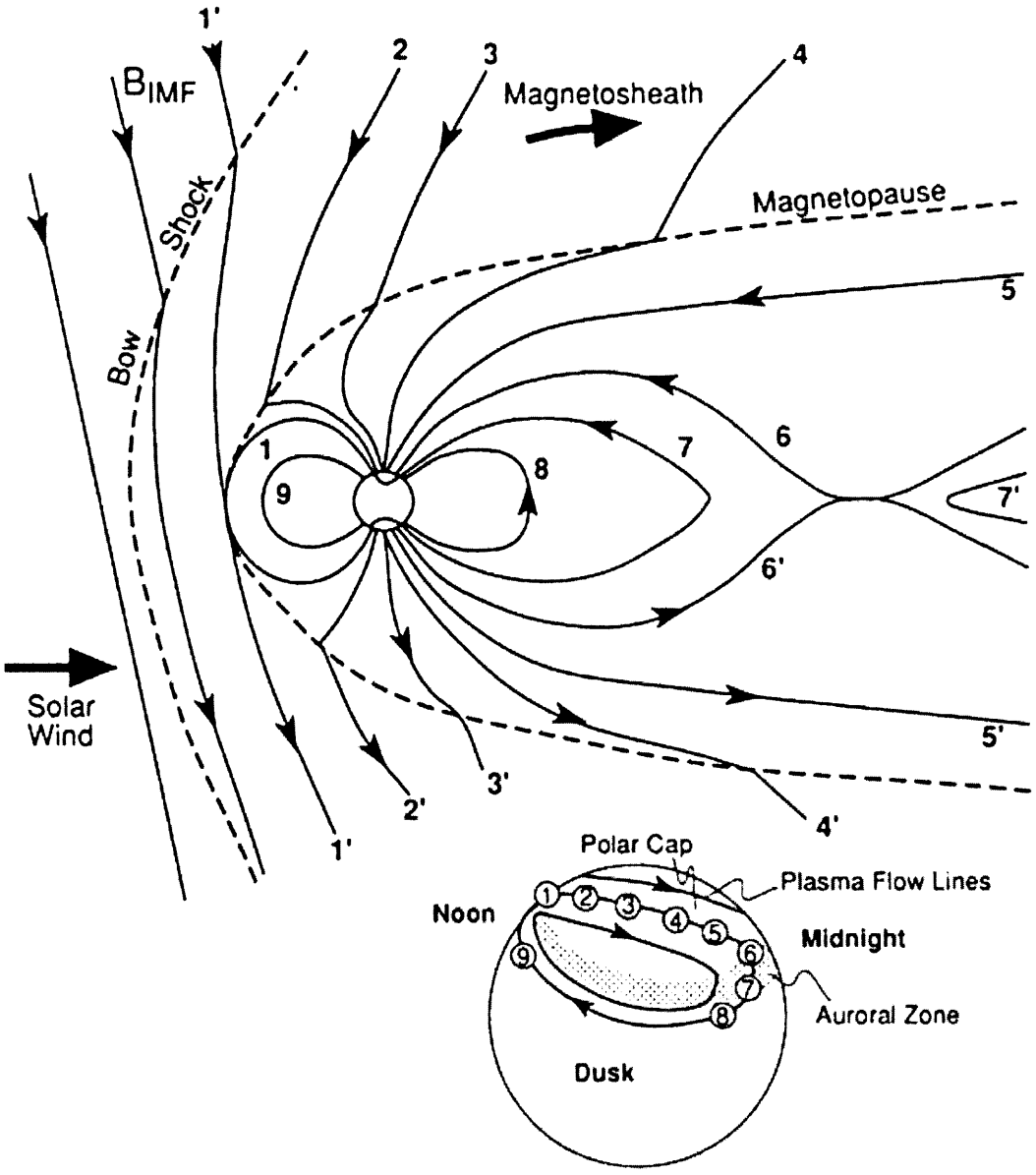

Figure 1.3: Schematic of the Earth's magnetosphere (from Kivelson and Russell, 1995).

	Earth	Jupiter	Saturn
Orbital semi-major axis (AU)	1.0	5.2	9.6
Mass (10^{24}kg)	5.974	1899	568.5
Equatorial radius at 1 bar (Mm)	6.38	71.49	60.27
Polar radius at 1 bar (Mm)	6.36	66.85	54.364
Oblateness	0.00693	0.144	0.229
Sidereal rotation frequency (10^{-4} rad/s)	0.7292	1.759*	1.6378†
Equatorial gravity (m/s^2)	9.80	24.78	10.44
Obliquity (°)	23.45	3.13	26.73
Polar B-field (10^{-4}T)	~0.6	~8.5	~0.6
Magnetic dipole tilt (°)	~11	~9	<0.1

Table 1.2: Parameters of Earth, Jupiter and Saturn. *System III; †determined from SKR emissions.

1.3 Structure of the Gas Giants' upper atmospheres

Jupiter and Saturn have many similarities. Both planets are composed mostly of molecular hydrogen and atomic helium in a ratio of roughly 9:1. There are significant traces of water, ammonia, and various hydrocarbons (Atreya et al., 2003). Both planets have a radius approximately 10 times that of the Earth and a sidereal angular velocity approximately twice as great. Jupiter, however, is approximately three times more massive than Saturn and has a correspondingly stronger gravitational field. Some of these fundamental parameters are listed in Table 1.2.

1.3.1 The neutral atmosphere

Temperature profiles for Jupiter and Saturn are shown in Figs. 1.4 and 1.5 respectively. The profile for Jupiter is derived from the Galileo probe (Seiff et al., 1998) and the profile for Saturn is from Moses et al. (2000), and was derived from a mixture of occultation data (Smith et al., 1983; Lindal et al., 1985; Hubbard et al., 1997). The zero altitude for both of these profiles is the 1 bar level.

We have a much firmer picture of Jupiter's atmosphere because of the data returned by the Galileo probe. Its structure is similar to that of the Earth, with the temperature gradients clearly indicating a troposphere and a thermosphere. The stratosphere and mesosphere are less clearly delineated, but the essential structure remains the same. The temperature structure at Saturn is also, in outline, similar to the Earth's.

The homopause altitudes are determined through analysis of stellar occultation experiments (Atreya et al., 1981; Atreya, 1982, see also Appendix A). At Jupiter this level lies at or just below the mesopause; at Saturn it lies a few scale heights above the mesopause. This altitude is

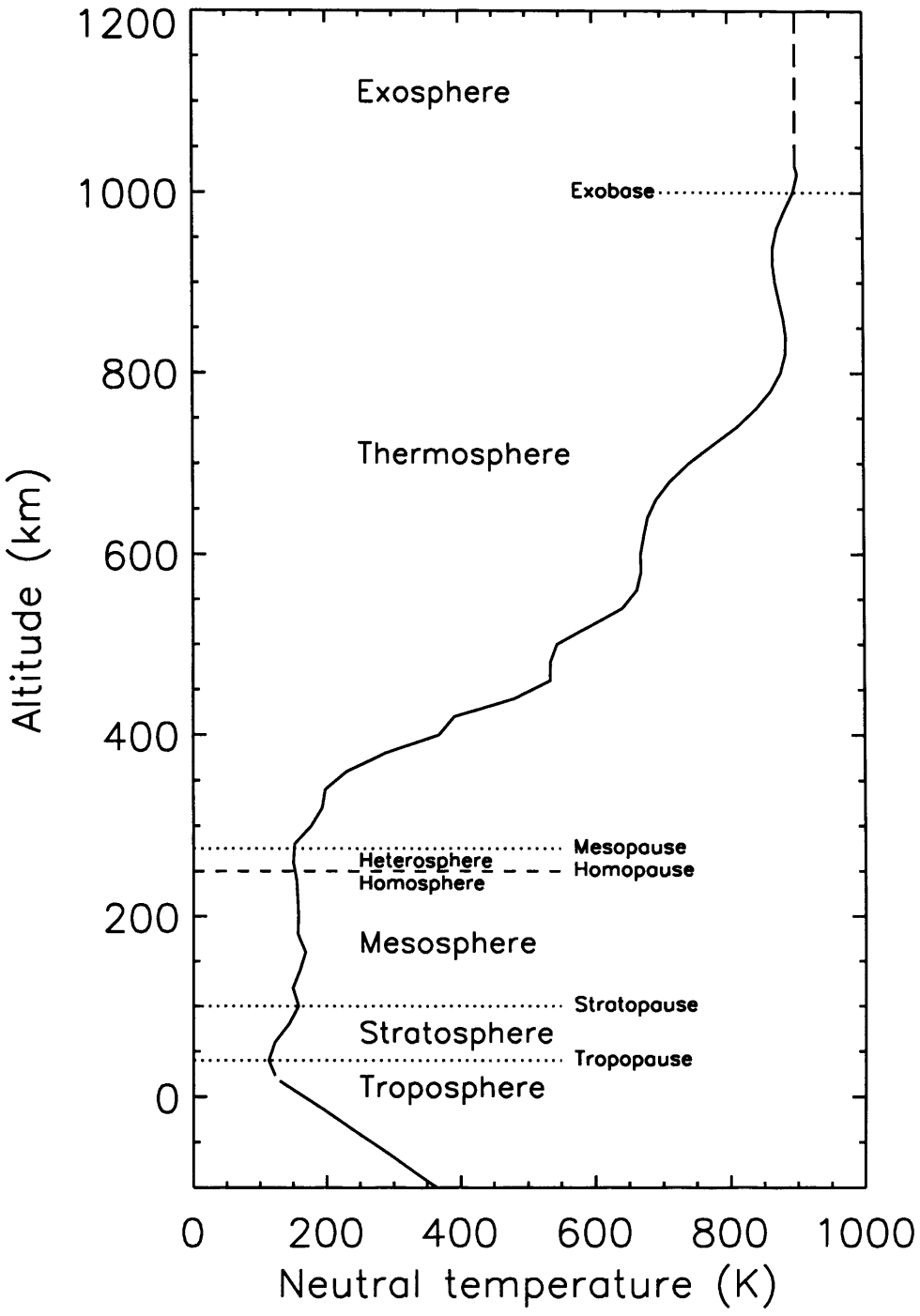

Figure 1.4: Schematic of Jupiter's neutral atmospheric structure. Temperature profile from Seiff et al. (1998). The short break in the temperature curve close to the tropopause is at the start of the probe descent phase. The dashed line above 1000km is an extrapolation. The altitude scale is referenced to the 1 bar level.

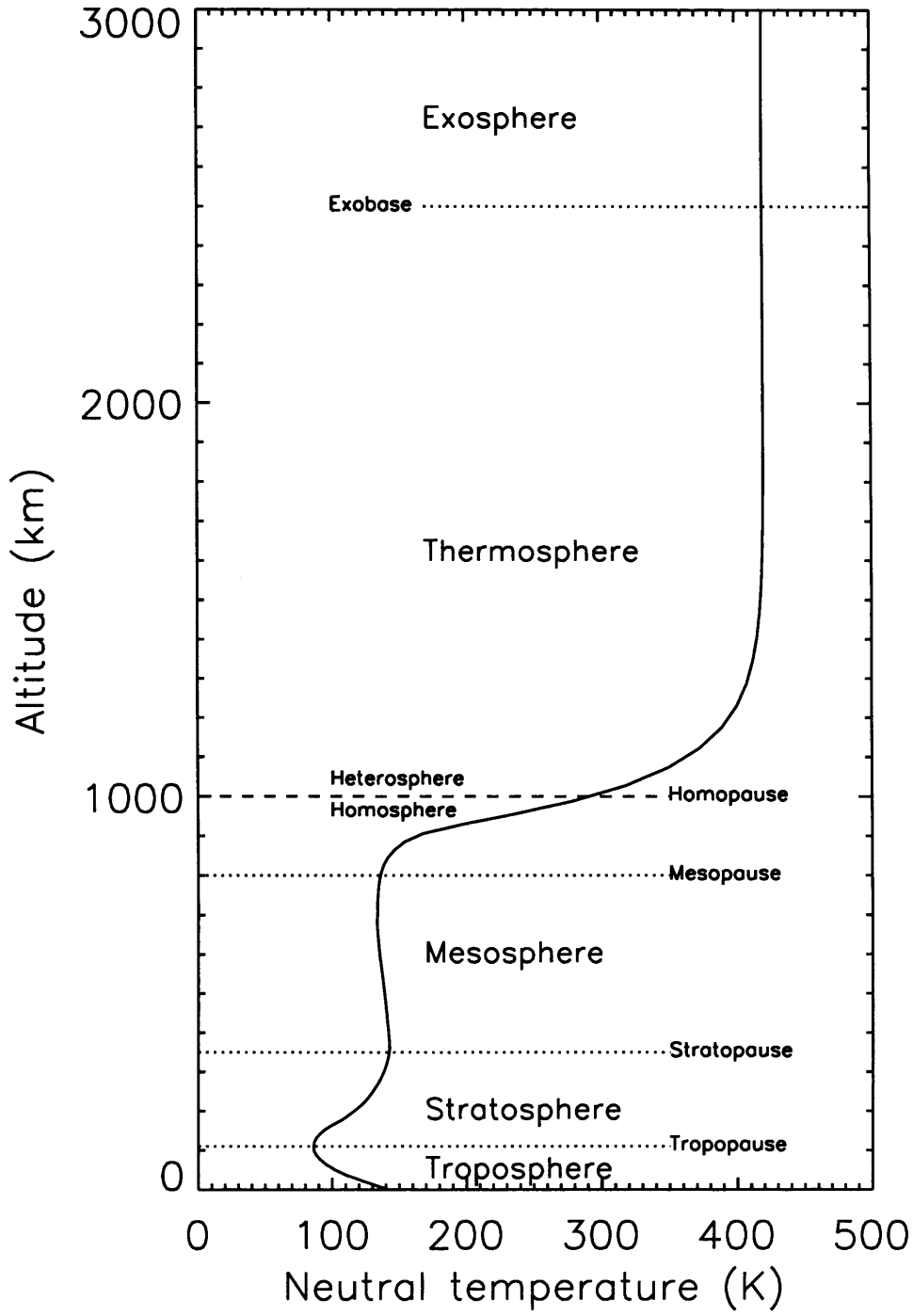

Figure 1.5: Schematic of Saturn's neutral atmospheric structure. Temperature profile from Moses et al. (2000). The altitude scale is referenced to the 1 bar level.

important for ionospheric modelling because above the homopause the densities of hydrocarbons, which are abundant in the homosphere, fall away much more quickly than the densities of hydrogen and helium. Thus in the heterosphere hydrocarbon chemistry is relatively unimportant.

Beyond this brief discussion we will deal very little with the behaviour of regions of the atmosphere below the mesopause, which we adopt as a lower boundary condition for most of our modelling. For this reason we will from henceforth use the term 'lower atmosphere' to refer to all layers below the mesopause.

Thermospheric temperatures

Our principle region of interest is the thermosphere. This coexists with the ionosphere which, for reasons to be discussed further below, exists largely above the homopause.

Looking at Jupiter's thermal structure (Fig. 1.4) it is clear that the thermosphere is almost as hot as Earth's — in the region of ~1000K. This is surprising, since the principle heat source for Earth's thermosphere is solar radiation, and Jupiter receives solar radiation with approximately 4% the intensity of that at Earth due to its greater orbital distance. Saturn (Fig. 1.5), which receives radiation with only 1% of the intensity of that at Earth, also has a moderately hot thermosphere at ~400K.

These temperatures are well in excess of those estimated theoretically under the assumption that solar EUV is the only energy source. Prior to 1971 no reliable measurements of thermospheric temperatures at either planet existed. Based on limited data, the mesopause temperature at Jupiter was estimated to lie in the range 95-140K with an exospheric temperature in the range 110-270K (Gross and Rasool, 1964; Shimizu, 1971, see also Section 2.4).

However, in 1971 the occultation of the double star Beta Scorpii by Jupiter was observed from Earth. Analysis of the light curve by Hubbard et al. (1972), Veverka et al. (1974) and Combes et al. (1975) provided experimental verification of the predicted mesopause temperature, but the Hubbard et al. study also tentatively suggested that the exosphere might be as hot as 300K, a value at the high end of the range of predictions. This was the first indication that the gas giants might possess unusually hot thermospheres.

The possible 300K temperature found by Hubbard et al. motivated Strobel and Smith (1973) to carry out a more detailed energy balance calculation for the Jovian thermosphere. This essentially confirmed the previous studies (Gross and Rasool, 1964; Shimizu, 1971), indicating an exospheric temperature of 160K. Strobel and Smith also extended their analysis to Saturn and predicted a very small temperature contrast of ~10K between the mesopause and exosphere.

As Jupiter was visited by successive spacecraft (Table 1.1) evidence accumulated that the upper atmosphere was much hotter even than the Hubbard et al. (1972) experiment had initially indicated. These results are summarised in Table 1.3. All of these temperatures — with the exception of the Galileo probe measurement — are determined via occultations. The neutral

Spacecraft	Topside plasma temperature	Neutral exospheric temperature
Pioneer 10	900±400K[a]	–
Pioneer 11	850±100K[b]	–
Voyager 1	1100-1300K[c]	1100±200K[f]
Voyager 2	1200-1600K[d]	–
Galileo	1500K[e]	900±200K[g]

Table 1.3: High altitude plasma and neutral temperatures in the thermosphere/ionosphere of Jupiter. The plasma temperatures are from radio occultation experiments spanning a range of latitudes, all lower than 80°. There is no obvious correlation between temperature and latitude. The Voyager 1 neutral temperature measurement is from a solar occultation close to the equator. The Galileo neutral temperature was determined from data collected by the atmospheric probe. [a]Fjeldbo et al. (1975); [b]Ashihara and Shimizu (1977); [c]Eshleman et al. (1979a), Atreya et al. (1979); [d]Eshleman et al. (1979b); [e]Hinson et al. (1997); [f]Atreya et al. (1981); [g]Seiff et al. (1998).

exospheric temperatures are measured by observing from the spacecraft the occultation of either the solar disk or a bright UV star by the planet. A review of these occultation measurements from the Pioneer and Voyager era is given by Smith and Hunten (1990).

The plasma temperature measurements are determined from electron density profiles from radio occultation events (see Section 1.3.2, Figs 1.6 and 1.7). These profiles yield the topside plasma scale height which, assuming that the plasma is mainly composed of H^+ and electrons in diffusive equilibrium, gives the temperature from Eqn. 1.13.

The interpretation of these measurements is difficult. Firstly, as is clear from Fig. 1.6, the data in the topside ionosphere is often noisy, and there may also be real structure in the topside which makes the definition of a single plasma scale height somewhat ambiguous. Secondly, it is not always clear that the assumption of diffusive equilibrium is appropriate. This is especially the case at low latitudes, where the terrestrial experience indicates that electrodynamics will generate complex structures that are not well represented by diffusive equilibrium (e.g Millward et al., 2001). Thirdly, the plasma temperature in the topside is generally not the same as the neutral temperature, since the ionised and neutral components of the atmosphere may not be in thermal equilibrium. The plasma is normally expected to be hotter than the neutrals, and thus the plasma temperature must be interpreted as an upper limit to the neutral temperature.

At Saturn, similar evidence for a hot thermosphere has gradually accrued (Table 1.4). All these temperatures are derived from occultations. The most mature analysis of the Voyager radio occultations (Lindal et al., 1985) does not discuss the topside plasma scale heights, so the values shown in the table are estimates by the present author using the Voyager 1 and 2 ingress profiles shown in Fig. 1.7 (the dot-dash and solid lines respectively). The lower Voyager 1 value of $\sim$ 300K refers to the region at around 3000km, and the higher value to the highest scale height that may

Spacecraft	Topside plasma temperature	Neutral exospheric temperature
Pioneer 11	1150K[a]	–
Voyager 1	300/1300K[b]	800K[c]
Voyager 2	600K[b]	400K[d]

Table 1.4: High altitude plasma and neutral temperatures in the thermosphere/ionosphere of Saturn. The Voyager 1 neutral temperature is from a stellar occultation and the Voyager 2 temperature is from a solar occultation.
[a]Kliore et al. (1980); [b]Determined by the present author from results of Lindal et al. (1985) (see Fig. 1.7).; [c]Festou and Atreya (1982); [d]Smith et al. (1983).

reasonably be deduced from the region above 4000km. The lower value seems improbable, since it is cooler than the observed neutral temperatures in this region. This indicates either that this region is not in diffusive equilibrium, or that the ionosphere is dominated by H_3^+ in this region, which would imply a plasma temperature closer to $\sim$ 1000K. The kink in the profile would then correspond to a transition from an H_3^+ dominated ionosphere to an H^+ dominated ionosphere at high altitudes.

The 800K Voyager 1 measurement of the neutral temperature also seems very different to the 400K Voyager 2 determination. However, the Voyager data has recently been reanalysed (Vervack et al., paper in preparation). This reanalysis suggests that the 800K measurement is incorrect, and proposes that the Voyager 1 and Voyager 2 data both point to an exospheric temperature in the region of 450K.

There have been numerous attempts to explain these temperature measurements in terms of energy transfer either from the magnetosphere or from the lower atmosphere. Transfer from the lower atmosphere has focused on the effects of breaking gravity or acoustic waves (French and Gierasch, 1974; Prasad, 1975; Atreya, 1986; Young et al., 1997; Matcheva and Strobel, 1999; Hickey et al., 2000; Müller-Wodarg et al., 2006), particle precipitation (Hunten and Dessler, 1977; Waite et al., 1983; Atreya, 1986; Achilleos et al., 1998; Grodent et al., 2001) and Joule heating (Heaps, 1976; Atreya, 1986; Cowley et al., 2004b; Müller-Wodarg et al., 2006). Many of these studies will be discussed in the chapters that follow; none of them are able to satisfactorily explain the high temperatures.

1.3.2 The ionosphere

The ionospheres of Jupiter and Saturn are dominated by ionised hydrogen and helium. At low altitudes hydrocarbon and metallic ions are also thought to play an important role (see e.g Kim and Fox, 1994; Moses and Bass, 2000). The atomic ions H^+, H_2^+ and He^+ form by direct ionisation of the corresponding neutral species. The relatively low proportion of neutral helium compared to molecular hydrogen means that He^+ is a minor component compared to

the hydrogen species. A third hydrogenic ion, the molecular species H_3^+, forms by a two stage process. Firstly, H_2^+ is generated, perhaps by photoionisation of H_2:

$$H_2 + h\nu \rightarrow H_2^+ + e^- \tag{1.17}$$

However, this H_2^+ reacts with H_2 on timescales of a few seconds to generate H_3^+:

$$H_2^+ + H_2 \rightarrow H_3^+ + H \tag{1.18}$$

This reaction is so efficient that almost all of the H_2^+ generated by ionisation is converted to H_3^+. Consequently H_3^+ is a major component of the ionosphere, whereas H_2^+ is of negligible importance.

The ionosphere thus consists largely of H^+ and H_3^+. The principle sink for these species at high altitudes is recombination reactions with ambient electrons

$$\begin{aligned} H^+ + e^- &\rightarrow H \\ H_3^+ + e^- &\rightarrow H + H_2 \\ &\rightarrow 3H \end{aligned} \tag{1.19}$$

Recombination of H_3^+ is much more rapid than recombination of H^+ because it decomposes into multiple particles. This means that it is much easier for both energy and momentum to be conserved in the reaction. H_3^+ thus persists only in the presence of a continuous source of ionisation, and is therefore found almost exclusively in the dayside ionosphere and the auroral zones, whereas H^+ persists in darkness, such that its distribution is relatively uniform in local time, a situation first anticipated by Rishbeth (1959).

At low altitudes, below the homopause, the situation is altered by the presence of multiple hydrocarbon species. These are able to charge exchange with the hydrogenic species, for example:

$$H^+ + CH_4 \rightarrow H + CH_4^+ \tag{1.20}$$

The hydrocarbon ions generated by such processes recombine much more rapidly than either H^+ or H_3^+. Thus, below the homopause, ionospheric densities are considerably lower. At these altitudes layers of hydrocarbon ions are often predicted (Kim and Fox, 1994; Moses and Bass, 2000), but the peak electron densities inferred for this region are much lower than those predicted above the homopause.

Radio occultations

The only available measurements of the Jovian and Kronian ionospheres are derived from remote sensing observations. Radio occultations performed by spacecraft have yielded numerous electron density profiles (see Figs. 1.6 and 1.7). A restriction of the radio occultation technique is that the

radio signal transmitted by the spacecraft must be received at Earth. This restricts occultations to regions close to the dawn and dusk limbs. Furthermore, most spacecraft occultations have been performed close to the equatorial plane. Thus the regions of the ionosphere sampled are rather limited.

Figure 1.6 shows a number of these profiles for Jupiter from the Galileo and Voyager missions. The morphology of these profiles is not well understood. In particular, the main ionospheric peak, normally observed in the range 1500-2000km, is not well-produced by models that include only photochemistry and ambipolar diffusion. These models tend to overpredict the maximum electron density and underpredict its altitude. It is also interesting that in two profiles (G0N and V2N) the peak ionosphere is denser and appears much lower in altitude, close to 750km, while the topside is considerably less dense. Peculiarly, none of the profiles shown exhibit intermediate behaviour, particularly in terms of the peak location. The statistics are not yet good enough to judge whether this represents two distinct modes of ionospheric structure, or is just an artefact of the particular measurement locations.

Given that most of the profiles exhibit a high altitude peak ionosphere, which conflicts with simple models, much research has sought a means of reducing the peak density and shifting it to higher altitudes. A possible chemical solution to this discrepancy is to find a process which increases ion recombination rates below the observed peak. One way to achieve this is the introduction of external material, such as water, into the system (Moses and Bass, 2000; Moore et al., 2004). These materials have a similar effect to the hydrocarbons discussed above, but at higher altitudes, thus depleting the densities of the peak ionosphere.

An alternative is to invoke excited electronic states of the H_2 molecule. For sufficiently excited vibrational levels charge exchange between H^+ and H_2 becomes energetically possible:

$$H^+ + H_2(v \geq 4) \rightarrow H + H_2^+ \tag{1.21}$$

and following this with Reaction 1.18 leads to the generation of H_3^+. This thus provides a mechanism for converting slowly recombining atomic ions into rapidly recombining molecular ions (Majeed et al., 1991; Majeed and McConnell, 1996). However, Huestis (2005) has recently cast doubt on the importance of this process, pointing out that there also exists a reaction between H^+ and H_2 that quenches the excited states of H_2, rendering the former reaction insignificant.

A second possible mechanism for shifting the electron density peak upwards and reducing its magnitude is the introduction of field-aligned plasma drifts driven by neutral winds, which may shift the peak in the electron density (see e.g. Moses and Bass, 2000). This process is part of the larger problem of calculating the internal electrodynamics of the ionosphere that is so important for the Earth's equatorial ionospheric structure. Given the near-equatorial location of so many of the radio occultation measurements, it seems unlikely that the morphology of the profiles will be fully explained until the complex coupled thermosphere-ionosphere system in this region is subjected to detailed modelling.

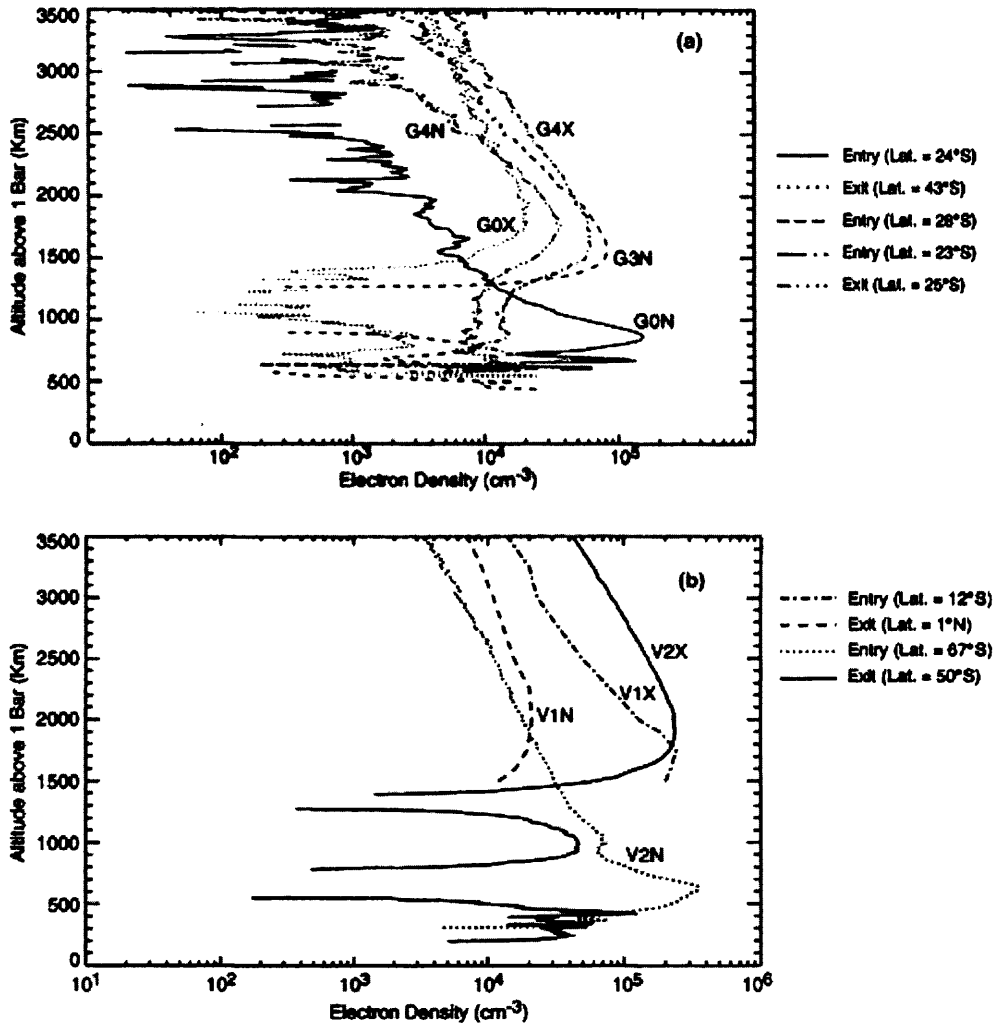

Figure 1.6: Observed electron density profiles in Jupiter's ionosphere. (a) Galileo radio occultations. (b) Voyager radio occultations. (from Majeed et al., 2004)

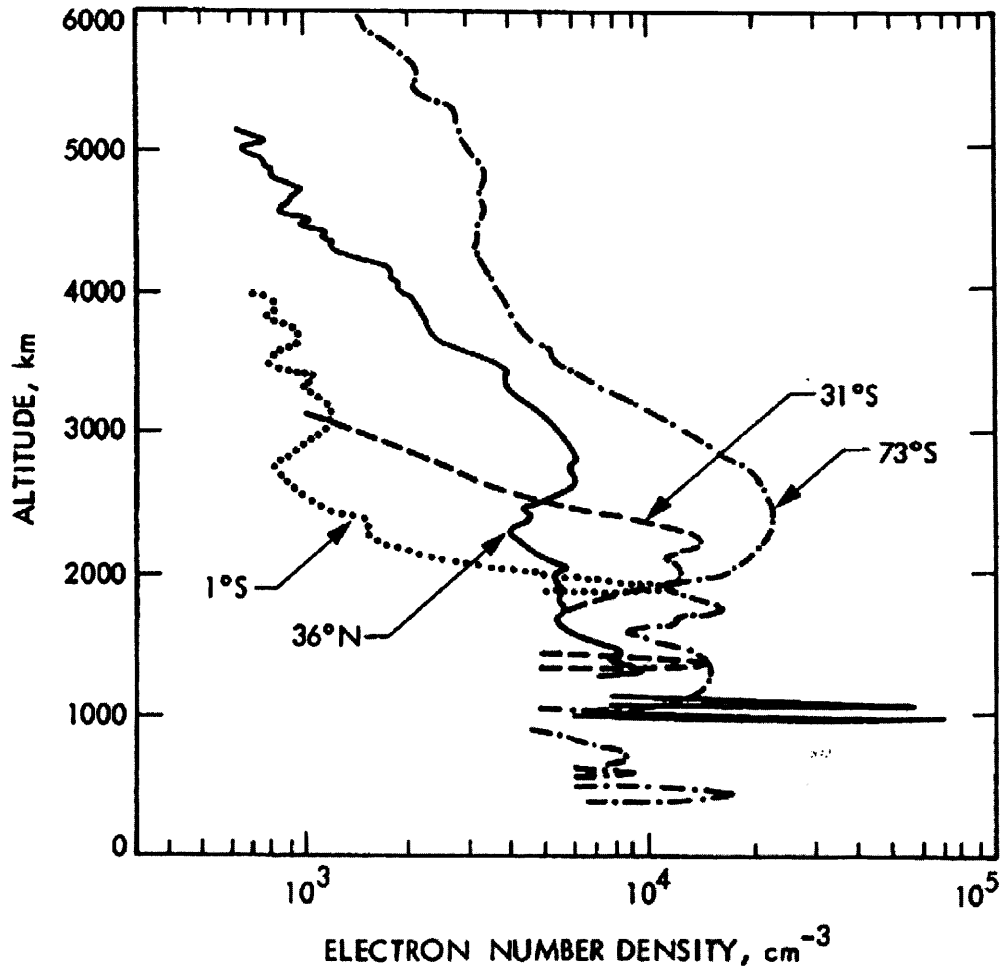

Figure 1.7: Observed electron density profiles in Saturn's ionosphere, form the Voyager 1 and 2 radio occultation experiments. Dot-dash line: Voyager 1 ingress (evening). Dotted line: Voyager 1 egress (morning). Solid line: Voyager 2 ingress (evening). Dashed line: Voyager 2 egress (morning). From Lindal et al. (1985).

Planet	Reference	Date	$T(H_3^+)$ (K)	$N(H_3^+)$ (m^{-2})
Jupiter	Lam et al., 1997	May 1993	700-1000	1.0×10^{16}
	Stallard et al., 2002	Sep 1998	900-1250	$0.5 - 1.0 \times 10^{16}$
Saturn	Melin, 2006	Sep 1999	380±70	1.9×10^{16}
	Melin, 2006	Feb 2004	420±70	7.3×10^{16}

Table 1.5: Summary of spectroscopic H_3^+ temperatures and columnn densities.

For comparison, Fig. 1.7 shows the Voyager radio occultation profiles for Saturn (Lindal et al., 1985). These present similar interpretative difficulties in terms of the location and density of the electron density peak. Particularly striking in these data are the sharp layers of electron density at an altitude of ~1000km. These have been discussed in terms of structuring of the ionosphere by shears in the vertical wind velocity (Chen, 1981), or as layers of long-lived metallic ions of meteoric origin (Moses and Bass, 2000).

H_3^+ measurements

Emission from H_3^+ was first detected in Jupiter's ionosphere by Drossart et al. (1989). Since then a number of studies have examined the morphology and intensity of the aurora through imaging in the infrared (e.g. Baron et al., 1991; Satoh and Connerney, 1999), and have also studied low latitude emission (Miller et al., 1997; Stallard et al., 1999). Of most relevance for this study, however, are spectroscopic studies of the H_3^+ emission in the auroral regions of Jupiter (Lam et al., 1997; Stallard et al., 2002) and Saturn (Melin, 2006), summarised in Table 1.5. These measurements have the advantage of providing more global coverage than the occultation experiments, and better coverage at high latitudes, but are only able to provide column densities of the H_3^+ ion — no information on the likely vertical distribution of ionisation is available.

It is interesting that these spectroscopic temperatures accord very well with the spacecraft observations summarised in Tables 1.3 and 1.4. It is also interesting that the column densities of H_3^+ at Jupiter and Saturn are very similar, both lying in the range $10^{16} - 10^{17} m^{-2}$. These measurements act as important constraints on the ionospheric conductivity and thermospheric temperature, issues which will be discussed further subsequently.

Jovian auroral model

Alongside these H_3^+ observations there have been numerous UV studies of the polar aurorae at Jupiter (e.g. Grodent et al., 2003; Gustin et al., 2004) and Saturn (e.g Trauger et al., 1998; Gérard et al., 2004; Clarke et al., 2005). A model of the auroral precipitation and associated UV emissions at Jupiter has been developed by Grodent et al. (2001). This model predicts column H_3^+ densities in the auroral regions of $1.8 \times 10^{17} m^{-2}$. This is considerably higher than

the observations described in Table 1.5. However Melin et al. (2005) has shown that, taking into account effects due to non-local thermodynamic equilibrium, the Grodent et al. (2001) column densities may be overestimated by a factor of ~3. Scaling the densities down by this factor brings them into line with the measurements of Lam et al. (1997) and Stallard et al. (2002).

Excepting these problems, the Grodent et al. (2001) precipitation model represents the best available model of the vertical distribution of ionisation in the auroral regions of Jupiter, and we will use their H_3^+ density profiles extensively in the modelling studies that follow.

1.3.3 The magnetosphere

The Jovian and Kronian magnetospheres are governed by the same basic physics as the terrestrial magnetosphere, but are structured by additional processes not present at the Earth. Indeed, the outer regions of both magnetospheres are believed to be controlled by a Dungey cycle type interaction with the solar wind. However, whereas at Earth the only source of plasma other than the solar wind is the ionosphere, at Jupiter and Saturn plasma is also injected directly into the magnetosphere from moons and rings. This internal injection of plasma leads to behaviour that is not observed at Earth.

Internal sources of plasma

At Jupiter the dominant source of internal plasma is volcanism on the moon Io, which orbits Jupiter every ~40 hours at approximately $6R_J$. Clouds of sodium and oxygen ejected from Io form a vast torus of neutral gas close to the equatorial plane. Some of this neutral gas subsequently becomes ionised and is then under the influence of the planet's magnetic field.

Newly ionised plasma must of course be moving at or close to the Keplerian orbital velocity of Io. However, upon ionisation it immediately becomes connected magnetically to the much more rapidly rotating — and partially ionised — upper atmosphere of Jupiter. We have already discussed the notion that magnetic field lines may be treated as conveying stresses in a similar manner to an elastic solid. Thus the newly created plasma in the Io torus immediately feels a torque exerted on it by the upper atmosphere — a torque that is mediated by the magnetic field — which accelerates it towards corotation with the planet's upper atmosphere. Of course, the upper atmosphere feels an equal and opposite anti-corotational torque. In steady state it is supposed that the upper atmosphere is viscously and convectively coupled to the deep atmosphere of Jupiter, and that this coupling supplies sufficient angular momentum to balance the anti-corotational torque from the plasma disk.

In the Io torus, this ionospheric torque is adequate to enforce almost perfect corotation of the plasma. However, the plasma is known to diffuse radially outwards, driven by centrifugal 'interchange instabilities' (e.g Siscoe and Summers, 1981). This outwards diffusion leads to the formation of a plasma disk in the equatorial plane of the magnetosphere (Fig. 1.8). With

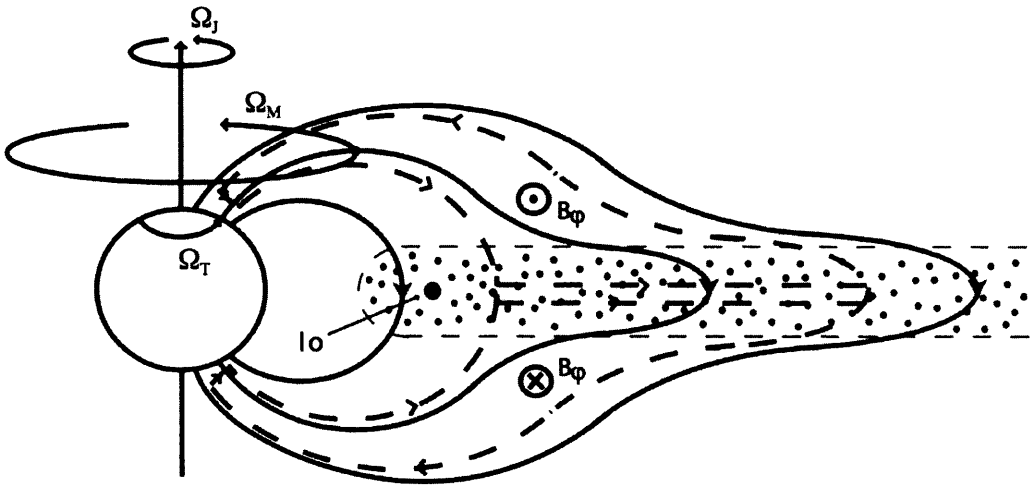

Figure 1.8: Schematic diagram of Jupiter's inner and middle magnetosphere (adapted from Cowley and Bunce, 2001).

increasing radial distance the total angular momentum flux per unit area of the plasma disk required to enforce perfect corotation remains constant, but the area of the ionosphere to which unit area of the plasma disk maps decreases, since it maps closer to the pole. At large enough distances the ionosphere is thus unable to supply sufficient torque to enforce corotation.

This system of angular momentum transfer can, equivalently, be viewed in terms of current systems associated with the stresses and torques conveyed by the magnetic field (Fig. 1.8). In the ionosphere, equatorward currents exert an anti-corotational torque; in the plasma disk, radial currents exert a corotational torque (this system is treated in more detail in Chapter 2). Field-aligned currents couple the two regions. The magnetic fields generated by the currents result in an azimuthal component of magnetic field which causes the field lines to 'bend' as if under stress. The upwards field-aligned currents in the ionosphere resulting from this system are believed to be responsible for the main auroral oval at Jupiter (Cowley and Bunce, 2001; Hill, 2001; Southwood and Kivelson, 2001).

A further perspective on the interaction is to view the system in terms of frictional interactions (Fig. 1.9). In this mechanical analogue for the system (Pontius, 1997), the inertia of plasma injected from Io acts as a brake on the rotation of the plasma disk; the plasma disk in turn acts as a brake on the rotation of the ionosphere; and the ionosphere acts as a brake on the rotation of the planet. In this idealised system Io acts as an infinite source of inertia and Jupiter as an infinite source of angular momentum. In the process each component of the system is also heated by the frictional interaction.

An essentially idential process is believed to occur at Saturn (Fig. 1.10). The principle

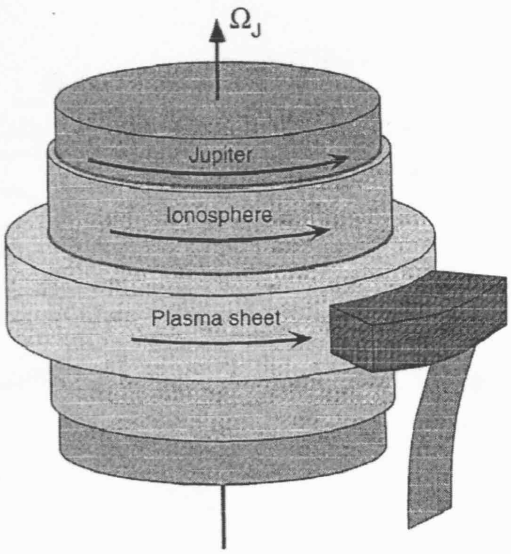

Figure 1.9: Mechanical analogue for the magnetosphere-atmosphere interaction at Jupiter (from Pontius (1997)).

difference is that the mass-loading at Saturn is not dominated by volcanism on a single moon, but consists of material originating from the various rings and icy moons. This complicates the interaction with the ionosphere and the outwards diffusive transport of plasma, a problem treated recently by Saur et al. (2004).

In the case of both planets we initially expect the rotational velocities of the planet (Ω_P), the upper atmosphere (Ω_T), the magnetosphere (Ω_M) and the Keplerian neutral gas cloud (Ω_K) to satisfy:

$$\Omega_K < \Omega_M < \Omega_T < \Omega_P \tag{1.22}$$

We will see, however, that this inequality does not hold universally, since meridional motions in the atmosphere or radial motions in the magnetosphere may cause components to rotate either more quickly or more slowly due to angular momentum conservation.

Vasyliūnas cycle

Ultimately the internally supplied plasma diffuses out to large enough radial distances that it is not stably confined by the planetary magnetic field. The magnetic field becomes distended outwards under the centrifugal action of the rotating plasma (Fig. 1.11). If the field is sufficiently distended, reconnection may occur between the northern and southern lobes of the distorted dipole such that plasma blobs or *plasmoids* become separated from the magnetosphere. This process is expected to occur preferentially in the pre-midnight sector as mass-loaded flux-tubes rotate into the tail and become distended anti-sunward as they move away from the region on

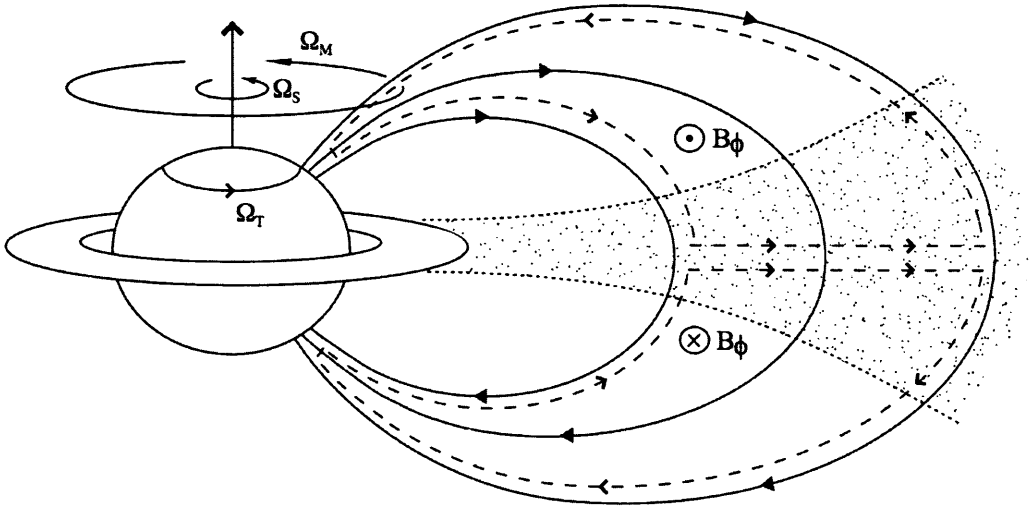

Figure 1.10: Schematic diagram of Saturn's magnetosphere (adapted from Cowley and Bunce, 2003).

the dayside of the planet that is confined by the pressure of the solar wind. This process of plasmoid break-off is believed to be the principle loss mechanism of internally produced plasma from the system (Vasyliunas, 1983).

Possible evidence for this outflow process was presented by Woch et al. (1998), who observed modulations with a period of 2-3 days in the Jovian magnetotail. One interpretation of this period is that it represents the intrinsic timescale for the cycle of mass loading and subsequent plasmoid loss (Fig. 1.11).

Dungey cycle

The Dungey cycle solar-wind interaction described in Section 1.2.3 is also expected to occur at Jupiter (Cowley et al., 2003) and Saturn (Cowley et al., 2004a). By analogy with Earth one would initially expect the Dungey cycle to take the form of a two-cell convection pattern, with anti-sunward flow of open field lines across the polar cap and return flow on both the dawn and dusk flanks. However, at both Jupiter and Saturn the Dungey cycle is believed to form a single convection cell, with antisunward flow across the dawn side of the polar cap and return flow along the dawn flank of the magnetosphere.

Two processes influence this behaviour. Firstly, the rapid planetary rotation means that newly closed flux tubes in the magnetotail are subject to a significant corotational torque by virtue of their coupling to the upper atmosphere. This torque naturally encourages the closed flux tubes to return to the dayside in the direction of the planetary rotation, i.e. around the

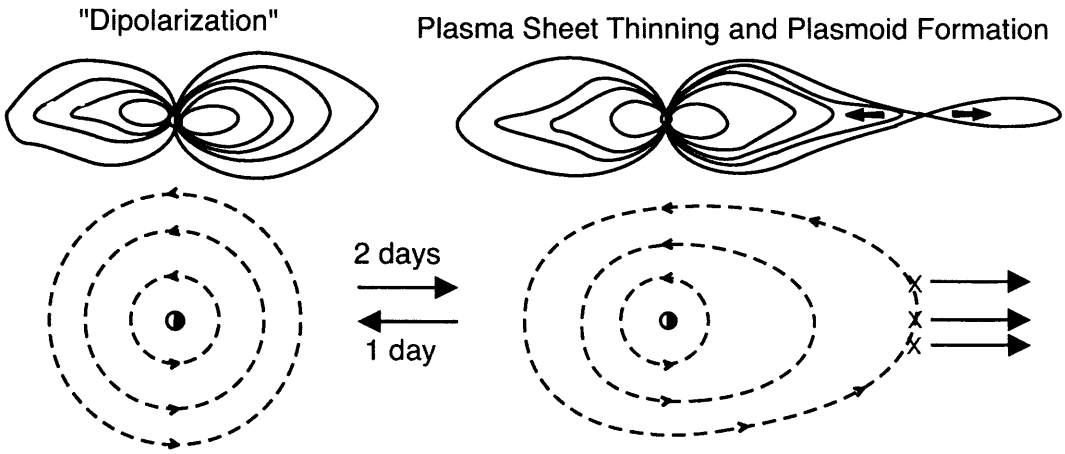

Figure 1.11: Schematic of plasmoid pinch-off in the Jovian magnetosphere. From Woch et al. (1998).

dawn flank. Secondly, the dusk flank is believed to be occupied by the Vasyliūnas cycle outflow discussed above. This forces the Dungey cycle to occur largely towards the dawn side of the magnetosphere.

Ionospheric plasma flows

From the perspective of the upper atmosphere these complex magnetospheric flows manifest themselves as flows of plasma in the polar ionosphere. The expected flows for Jupiter and Saturn are sketched in Figs. 1.12 and 1.13 respectively.

In Fig. 1.12 the innermost, shaded region represents the region of open field lines associated with the Dungey cycle flow. As discussed above, this flow is thought to be confined to the dawn flank of the magnetosphere and is correspondingly confined to the dawn side of the polar cap. The return flow of closed field lines associated with the Dungey cycle occurs in a narrow region, equatorwards of the shaded region, on the dawn side.

At Earth, the timescale for circulation of the Dungey cycle convection cells is ~6 hours. At Jupiter it is estimated to be 5-10 days (Cowley et al., 2003). This corresponds to 10-20 rotations of Jupiter. The consequence of this is that the antisunwards Dungey cycle flow is almost zero compared to the rotational flows observed elsewhere in the ionosphere.

On the dusk side the flow is believed to be dominated by the Vasyliūnas cycle. Flux tubes that have experienced plasma pinch-off in the tail (at the Vasyliūnas cycle 'X-line' shown in Fig. 1.12) must then rotate back towards the dayside on the dawn flank, and this flow is thought to occur just equatorwards of the Dungey cycle return flow.

Finally, the region equatorwards of the Dungey and Vasyliūnas cycle flows is occupied with sub-corotational flow related to the mass-loaded inner and middle magnetospheres. This is

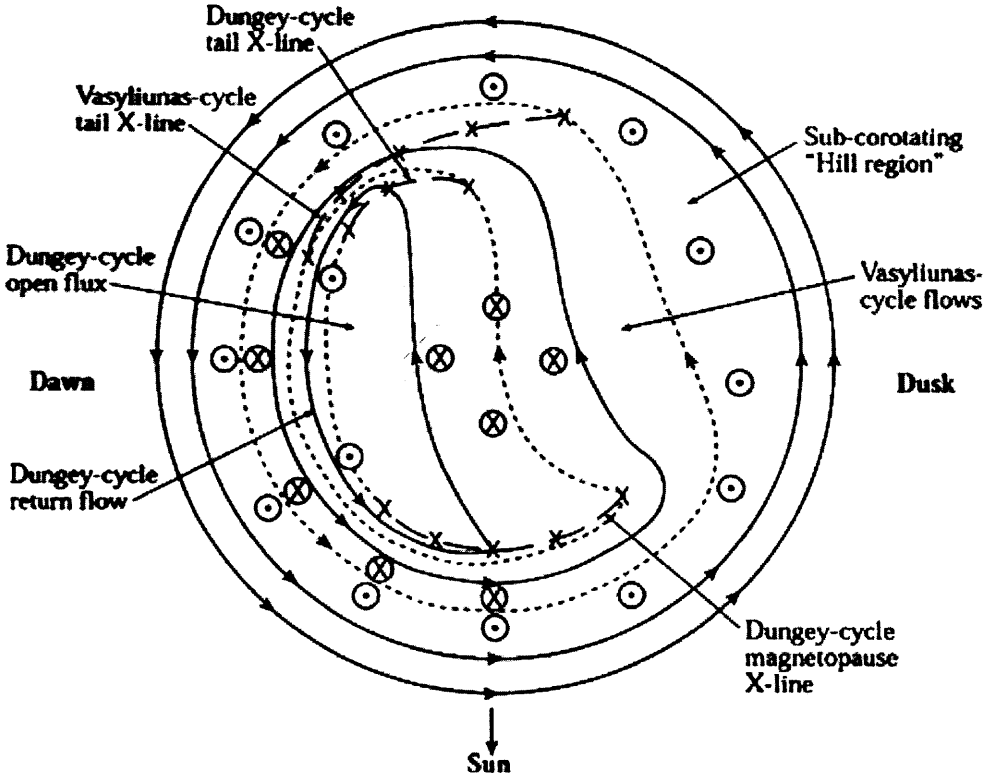

Figure 1.12: Sketch of plasma flows in the Jovian polar ionosphere (from Cowley et al., 2003). The shaded region corresponds to the 'dark polar region' believed to correspond to open field lines. Solid lines represent streamlines and dashed lines show boundaries between different flow regions.

referred to as the 'Hill region' after Hill (1979).

Direct ionospheric evidence for this system of plasma flows is provided by the H_3^+ Doppler measurements of Stallard et al. (2003). They observe a 'dark polar region' on the dawn side of the polar cap in which the plasma flows are almost stagnant with respect to the planetary rotation. This is clearly consistent with an almost 'stagnant' antisunwards Dungey cycle flow in this region. In contrast the region surrounding the dark polar region rotates with a substantial fraction of the planetary angular velocity. This is believed to correspond to the Vasyliūnas cycle outflow on the dusk flank and the Dungey and Vasyliūnas cycle return flows on the dawn flank (Cowley et al., 2003).

Cowley et al. (2004a) envisage a similar situation at Saturn, largely by analogy with the situation at Jupiter (Fig. 1.13). Again the outer regions of the polar ionosphere correspond to the 'Hill region' of sub-corotating internally supplied plasma. Within this region lies the Vasyliūnas cycle outflow on the dusk flank and return flow on the dawn flank. A Dungey cycle

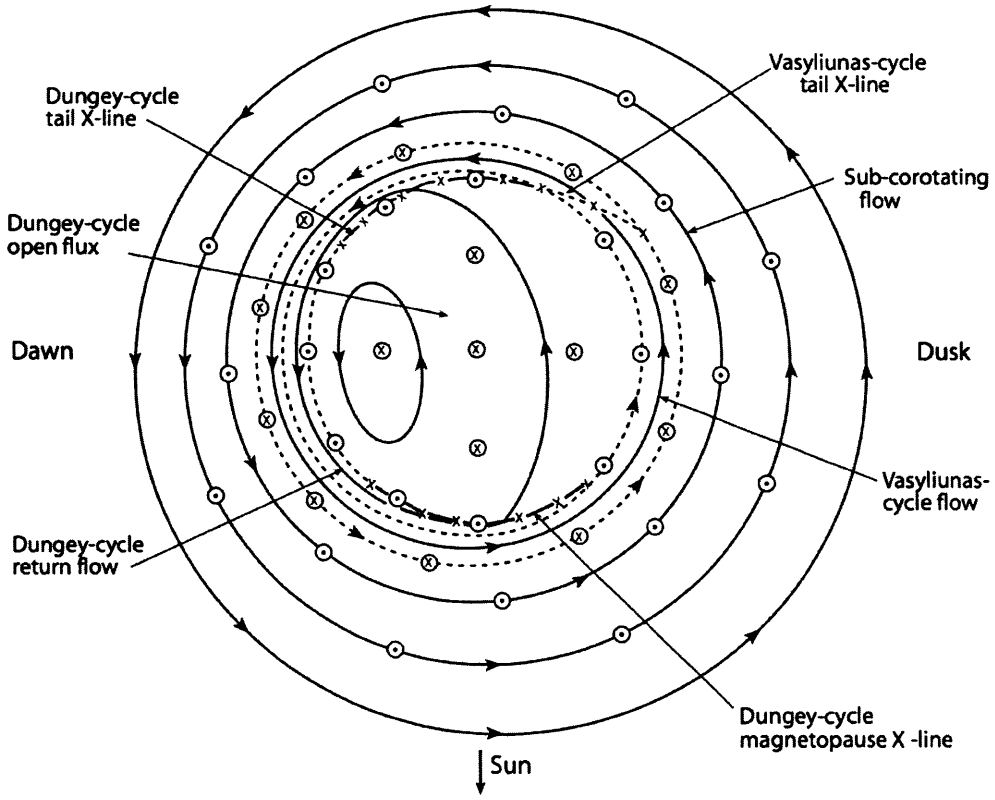

Figure 1.13: Sketch of plasma flows in the Kronian polar ionosphere (from Cowley et al., 2004a). Solid lines represent streamlines and dashed lines show boundaries between different flow regions.

convection cell occupies the polar cap and the dawn flank. An important difference at Saturn is that planetary rotation is believed to be more important in the open field line region. This is indicated by the Doppler observations of Stallard et al. (2004) which show that the polar ionosphere rotates at approximately one third of the planetary rotation velocity. This behaviour may be interpreted in terms of the theory of Isbell et al. (1984) which is discussed further in subsequent chapters and summarised in Appendix B. The possible implications of the planetary rotation for the structure of the magnetotail have recently been discussed by Milan et al. (2005).

Generation of auroral emission

One important application of these models of the ionospheric plasma flows is to provide some insight into the possible generation of auroral emissions. Such emissions at Earth normally correspond to regions of intense upwards field-aligned currents in the ionosphere. If the current densities are too large to be carried by the ambient thermal plasma then field-aligned voltages develop which accelerate electrons downwards. These electrons excite the neutral atmosphere, which radiates, generating aurora.

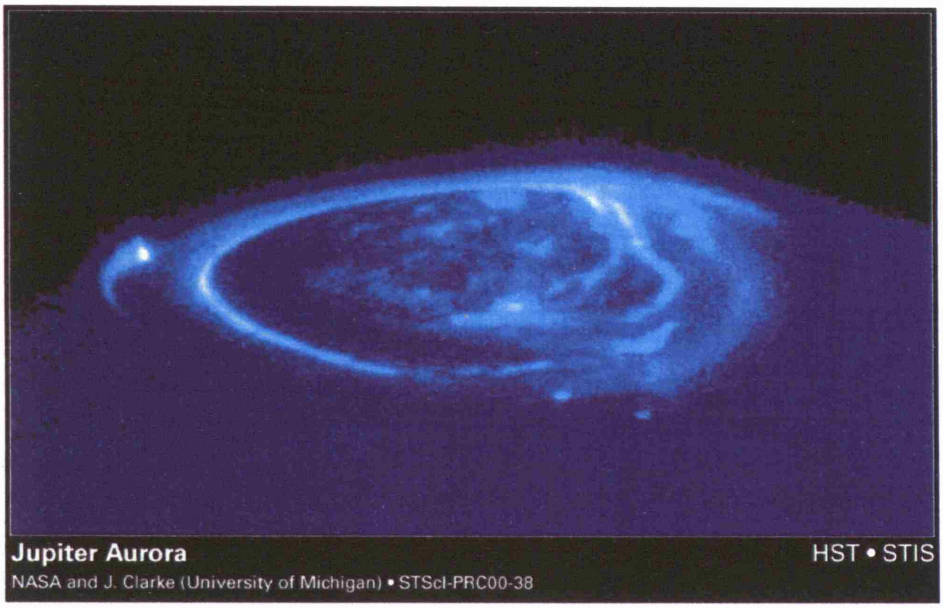

Figure 1.14: Hubble Space Telescope image of the Jovian UV northern polar aurora (John Clarke, NASA/ESA).

A Hubble Space Telescope Imaging Spectrograph (HST/STIS) UV image of the Jovian northern polar auroral emissions is shown in Fig. 1.14. Dawn is on the left and dusk on the right. This image contains many complex features which we will not attempt to treat in detail here (see e.g Grodent et al., 2003, for a more detailed discussion). On the far left the discrete 'spot' is associated directly with the location of the moon Io. The so-called 'main oval' is visible as the continuous, intense arc on the left of the picture and a more diffuse continuous arc on the right. The location of the main oval appears to be stable on long timescales. Within the main oval are various complex and variable auroral emissions, loosely divided into 'dark' and 'bright' regions on the left and right respectively.

Fig. 1.15 shows a sequence of UV images of Saturn from the same instrument, acquired in January 2004. The auroral emissions at Saturn are more difficult to observe, since they are fainter than the Jovian emissions and the greater orbital distance of Saturn dilutes the observed intensity of the emissions by a further factor of $\sim$4. However, these images still show considerable structure. A persistent 'main oval' of emission is observed between colatitudes of 15° and 20°. Although this 'main oval' is persistent, it varies considerably in brightness and co-latitude, sometimes breaking into 'blobs' (e.g. image c), forming spiral structures about the pole (image k) or sometimes generating a more concentrated 'filled in' emission closer to the pole (image j). These variations have been interpreted in terms of solar-wind control of the aurora

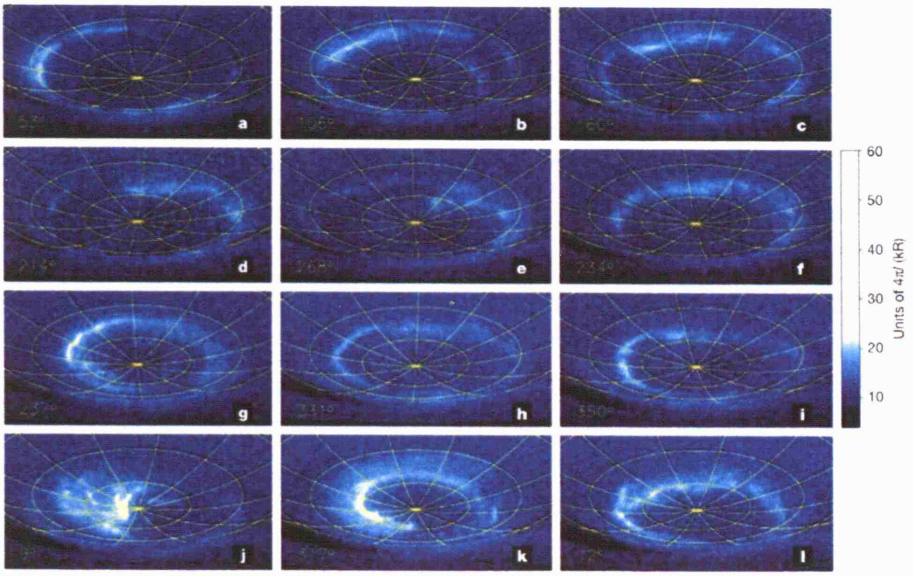

Figure 1.15: Hubble Space Telescope images of the Kronian UV southern polar aurora (Clarke et al., 2005).

(Grodent et al., 2005; Cowley et al., 2005; Badman et al., 2005).

The theoretical representations of the polar ionospheric flows shown in Figs. 1.12 and 1.13 can be related to these observed emissions. In the rotation dominated flows observed at Jupiter and Saturn, the currents flowing horizontally in the polar ionosphere are generally thought to be equatorwards Pedersen currents driven by the rotational plasma flow. Upwards currents that may generate aurora occur when the intensity of these currents decreases in the direction of the equator. Such a decrease corresponds to an increase in the rotational flow velocity (see Chapter 2 for further details).

The Jupiter model of Fig. 1.12 predicts that this will occur primarily at two locations: at the boundary between the stagnant dark polar region and the faster Dungey cycle return flow on the dawn side; and throughout the Hill region. The Hill region flows are believed to account for the main oval emissions (Hill, 2001; Cowley and Bunce, 2001; Southwood and Kivelson, 2001): this explains the stability of the main oval, since mass outflow from the Io torus is thought to be a reasonably steady process. Cowley et al. (2005) predict that some auroral emissions may be generated at the boundary between open field lines and the Dungey cycle return flow, but that this emission will be much less bright than that observed in the main oval.

At Saturn upward currents are related to the equivalent flow boundaries, but the situation in terms of the generation of auroral emission is reversed. Cowley and Bunce (2003) have argued

that the currents generated by the Hill region flow may lead to some auroral emission, but that this will be of lower intensity and at lower latitude than the observed main oval. Cowley et al. (2004a) thus suggest that the open-closed field line boundary corresponds to the main oval at Saturn.

1.4 Aim of this study

In this introductory chapter we have summarised our current basic understanding of the coupled atmosphere-magnetosphere system at the giant planets Jupiter and Saturn. We have emphasised three areas of research common to both planets: the unexplained high thermospheric temperatures, the complex ionospheric structures, and the large scale magnetospheric flows that generate plasma motions and auroral emissions in the upper atmosphere.

These three subjects are all intertwined and vastly complex, and it is not possible for us to study them all simultaneously with a maximal degree of sophistication. Our approach in analysing their interactions will therefore be to simplify many of the processes involved in order to gain physical insight in specific areas. Our area of greatest interest is that of thermospheric dynamics and how this may influence the thermospheric temperature structure and the magnetospheric flows.

We thus employ simple models of the ionosphere and magnetosphere that are not physically exact but afford useful insight. We will reduce the behaviour of the almost inertia-less ionosphere to its role as a coupling parameter between the respective inertias of the thermosphere and magnetosphere. By developing a simple model of this coupling process we hope to peer through the cloud of ionospheric complexity that might otherwise obscure our insight.

We use simple models of the magnetospheres (Cowley et al., 2004b; Cowley et al., 2005) that describe a series of axisymmetric nested layers rotating at different angular velocities. These models were developed specifically to calculate parameters of auroral current sheets. However, they are particularly useful in our context. From the thermospheric perspective they reduce the magnetosphere to a giant fluid flywheel that is a source and sink of energy and angular momentum. By treating the magnetosphere in this simple manner we are able to gain some preliminary insights into how its dynamics may be structured by the thermosphere.

Finally, the most complex component of our study is a numerical general circulation model of the thermosphere that calculates temperature and wind fields self-consistently. It is this model that allows us to assess the possible influence of the magnetosphere on the thermal structure of the upper atmosphere, and vice versa.

In Chapter 2 we describe our adopted magnetosphere models; develop the theory of the coupling between these models and the plasma flows and currents in the ionosphere; describe our adopted ionosphere models; and provide some initial considerations concerning the influence

of magnetospheric energy and momentum sources on the thermosphere. In Chapter 3 we lay out the details of our thermosphere model and its coupling to the ionosphere and magnetosphere.

In Chapter 4 we then present the results of some simple experiments in heating the thermosphere model in the auroral regions. This provides the backdrop to the more sophisticated experiments in Chapters 5 and 6 in which we present the output of our coupled models of the thermosphere, ionosphere and magnetosphere. Finally, in Chapter 7, we conclude.

Chapter 2

Background theory

In this Chapter we discuss some of the more detailed background theory necessary for the studies that follow. Firstly, we follow on from the preceding discussion to describe our adopted models of the Jovian and Kronian magnetospheres in more detail. We then work back downwards towards the thermosphere, first considering the influence of the magnetosphere on the charged particles in the upper atmosphere, and finally the effect of the resulting energy and momentum inputs on the thermosphere.

2.1 Models of the magnetosphere

The simple models of the Jovian and Kronian magnetospheres that we employ in this study all make the assumption that the planetary magnetic field is symmetric about the planetary rotation axis (axisymmetric). In the case of Saturn this seems to be an excellent approximation, as current determinations of the magnetic field indicate the dipole and rotation axes to be aligned to within less than $\sim 1°$ (Davis and Smith, 1990; Giampieri and Dougherty, 2004). In the case of Jupiter it is a less accurate approximation: some of the potential magnetospheric consequences of a non-aligned, non-centred dipole field have been discussed by Pontius (1997). However, many successful physical models of the Jovian magnetosphere make this assumption, following the lead of Hill (1979), including the magnetosphere model that we adopt (Nichols and Cowley, 2004).

We further assume axisymmetry for all other aspects of the system. This does not follow from the assumption of an axisymmetric magnetic field. If the Earth's dipole was aligned with its rotation axis, the plasma flow structures related to the Dungey cycle would remain highly asymmetric about the rotation axis. However, we have already discussed the notion that the plasma flows in the Jovian and Kronian magnetospheres are dominated by effects related to planetary rotation. While this is particularly the case in the regions of the magnetosphere that are dominated by mass loading, the outer regions that are coupled to the solar wind are still thought to be structured significantly by the planetary rotation. Recent studies for Jupiter

(Nichols and Cowley, 2004; Cowley et al., 2005) and Saturn (Cowley et al., 2004b) have thus used an axisymmetric approximation for first-order studies of the solar wind coupling. It seems reasonable to adopt such simple models for this first detailed look at the thermospheric aspect of magnetosphere-atmosphere coupling.

Since the magnetosphere models assume that the magnetic field is axisymmetric, we can describe the behaviour of the magnetosphere in terms of the rotation velocities of axisymmetric shells of magnetic field lines. Each shell then intersects the ionosphere at some colatitude θ and axial distance $\rho_i = R\sin\theta$ and the equatorial plane at some axial distance ρ_e, independent of longitude (ϕ). The mapping between these two key points is achieved by the introduction of a 'flux function' F defined by:

$$\boldsymbol{B} = (1/\rho)\nabla F \times \boldsymbol{e}_\phi \tag{2.1}$$

where $\boldsymbol{e}_\phi$ is the unit vector in the ϕ (east longitude) direction. Since the quantity ∇F is always perpendicular to surfaces of constant F, any field line will always lie within such a surface. Taken together with the assumption of axisymmetry this means that any value of F defines a surface of revolution about the planetary axis that represents a shell of field lines.

Even without performing detailed calculations of the field geometry in the region between the ionosphere and equatorial plane it is then possible to map field lines along these shells — provided the flux function in the ionosphere F_i and in the equatorial plane F_e are well defined — by setting $F_e = F_i$. The values of ionospheric and equatorial flux functions adopted for this study are summarised in Appendix C.

We then associate an angular velocity $\Omega_M(\theta)$ with each shell of flux tubes[1]. At the foot of each flux tube we also associate an angular velocity $\Omega_T(\theta)$ with the rotation velocity of the thermosphere. This is a 'height-integrated' rotation velocity, which will be described in greater detail below.

Assuming for now, though, that the conducting region of the thermosphere-ionosphere is a thin sheet with a uniform rotational velocity at each co-latitude, the appropriate electric field in the ionosphere is the electric field in the rest-frame of the neutrals (see Section 2.2):

$$E^*_\theta = \rho_i(\Omega_T - \Omega_M)B_i \tag{2.2}$$

where we have assumed that the ionospheric magnetic field B_i is vertical. This implies an equatorward-directed Pedersen current J_θ (the theory of which will be described in more detail later):

$$J_\theta = \Sigma_P E^*_\theta = \Sigma_P \rho_i(\Omega_T - \Omega_M)B_i \tag{2.3}$$

where Σ_P is the height-integrated Pedersen conductivity of the ionosphere, to be discussed shortly. As shown in Figs. 1.8 and 1.10, to ensure continuity this current, which flows in both the

[1]The original papers that describe these models (Nichols and Cowley, 2004; Cowley et al., 2004b) use slightly different notation to that used here. The symbol ω is used for the quantity we call Ω_M; Ω^*_J or Ω^*_S is used for the quantity Ω_T, depending on the planet in question; i_θ and i_ρ are used instead of J_θ and J_ρ.

northern and southern hemispheres, must close in the magnetosphere via field-aligned currents and a radial current J_ρ which flows in the equatorial plane of the magnetosphere.

Rotational torque

Assuming that the magnetosphere sub-rotates with respect to the thermosphere, the ionospheric current J_θ exerts an anticorotational (clockwise viewed from above the north pole) $\boldsymbol{j} \times \boldsymbol{B}$ torque on the ionosphere, to be discussed further below. Integrating this in azimuth, we can obtain the total torque δG_i acting on a small colatitude range $\delta\theta$ in the ionosphere:

$$\delta G_i = 2\pi\rho_i^2 \Sigma_P B_i^2 (\Omega_T - \Omega_M)\delta\theta \tag{2.4}$$

An equal and opposite corotational torque acts on the plasma in the equatorial magnetosphere in the small range $\delta\rho$ to which the range $\delta\theta$ maps.

In the Saturn model (Cowley et al., 2004b), and in part of our adopted Jupiter model (Cowley et al., 2005), these torques in the equatorial magnetosphere are not explicitly calculated, since the rotation velocities are specified empirically without the use of a physical model of the magnetosphere. It is thus implicitly assumed that the torques in the magnetosphere due to the coupling currents are balanced by torques associated with mass loading or with the solar wind interaction. In the inner region of our adopted Jupiter model (Nichols and Cowley, 2004), the torque is explicitly calculated and assumed to be balanced by the inertia of plasma diffusing outwards from the Io torus, as first proposed by Hill (1979). If the total rate of mass outflow is given by $\dot{M}$ then this balance of torques reduces to the so-called 'Hill-Pontius' equation (Nichols and Cowley, 2004):

$$\frac{1}{\rho_e}\frac{d}{d\rho_e}\left(\rho_e^2 \Omega_M\right) = \frac{8\pi\Sigma_P F_e |B_{ze}|}{\dot{M}}\left(\Omega_T - \Omega_M\right) \tag{2.5}$$

where we have rewritten the equation using our slightly altered nomenclature.

Field-aligned currents

Any divergence of the Pedersen current J_θ flowing in the ionosphere must be balanced by field-aligned currents $j_{\parallel i}$, which we define as positive upwards:

$$j_{\parallel i} = -\frac{1}{\rho_i}\frac{d}{d\theta}(J_\theta \sin\theta) \tag{2.6}$$

In the Saturn case, Cowley et al. (2004b) used this equation to calculate the likelihood of field-aligned currents associated with different regions of the magnetosphere being responsible for the generation of UV aurora. In the Jupiter case, this equation is used to explicitly calculate the field-aligned current in the ionosphere (Nichols and Cowley, 2004):

$$j_{\parallel i} = \frac{4B_J}{\rho_e |B_{ze}|}\frac{d}{d\rho_e}\left[\Sigma_P F_e \left(\Omega_T - \Omega_M\right)\right] \tag{2.7}$$

where, again, the equation has been re-expressed in our notation.

Saturn model

We now move on to the details of our adopted model of Saturn's magnetosphere (Cowley et al., 2004b). As we have already mentioned, this model does not explicitly include the influence of torques in the magnetosphere. Instead the model ascribes a fixed angular velocity Ω_M to each shell of flux tubes. This angular velocity is defined, as a function of the flux function F, by the equation:

$$\begin{aligned} \Omega_M(F) &= \Omega_A \\ &+ (\Omega_B - \Omega_A)T_{AB}(F) \\ &+ (\Omega_C - \Omega_B)T_{BC}(F) \\ &+ (\Omega_D - \Omega_C)T_{CD}(F) \end{aligned} \tag{2.8}$$

where the parameters Ω_X represent the nominal rotation velocities of different regions of the magnetosphere which we label A, B, C and D, and the functions $T_{XY}(F)$ represent smooth transitions between these regions, and are given by:

$$\begin{aligned} T_{AB}(F) &= \frac{1}{2}\left(1 + \tanh\frac{F - F_{AB}}{\Delta F_{AB}}\right) \\ & \qquad F_{AB} = 1526\text{nTR}_\text{S}^2 \qquad \Delta F_{AB} = 50.0\text{nTR}_\text{s}^2 \\ T_{BC}(F) &= \frac{1}{1 + (F_{BC}/F)^{n_{BC}}} \\ & \qquad F_{BC} = 2200\text{nTR}_\text{S}^2 \qquad n_{BC} = 50.0 \\ T_{CD}(F) &= \frac{1}{1 + (F_{CD}/F)^{n_{CD}}} \\ & \qquad F_{CD} = 3600\text{nTR}_\text{S}^2 \qquad n_{CD} = 8.0 \end{aligned} \tag{2.9}$$

The resulting profile of angular velocity against flux function is plotted as the solid line in Fig. 2.1. The model is also shown in Fig. 2.2 mapped into the upper atmosphere, as a function of co-latitude. Note that we have written this plasma velocity model in a different, and hopefully clearer, form to that originally provided by Cowley et al. (2004b), but it is otherwise identical.

This angular velocity model is supported principally by two sets of data, both of which are summarised in Fig. 2.1. Firstly, the angular velocity corresponding to the open field region — which, for brevity, we label region A — is informed by the H_3^+ observations of Stallard et al. (2004). From three observing runs on the night of February 6, 2003, they inferred polar cap angular velocities of $0.2\Omega_S$, $0.44\Omega_S$ and $0.4\Omega_S$, where $\Omega_S \simeq 1.64 \times 10^{-4}\text{rad s}^{-1}$ is the standard rotation rate of Saturn. These velocities are shown by the horizontal dashed lines in Fig. 2.1. The average of these is $\sim 0.35\Omega_S$.

This sub-corotational behaviour was predicted by Isbell et al. (1984) in terms of an interaction between the solar wind and the rotation of the planet. Field lines open to the solar wind have one end 'anchored' in the downstream solar wind flow, and the other end subject to rotational torques in the polar ionosphere. The result is a twisting of the field lines in the magnetotail lobes.

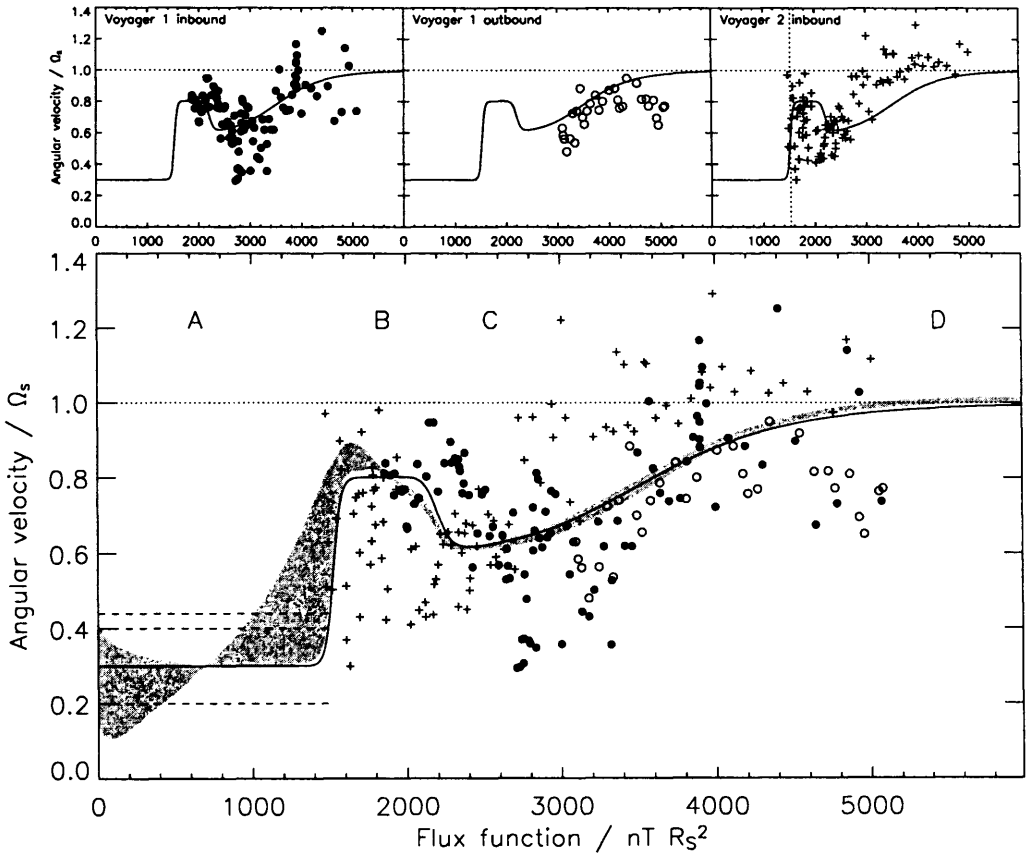

Figure 2.1: Data used to constrain Saturn plasma velocity model. The Cowley et al. (2004b) plasma velocity model is shown by the solid line, plotted against flux function. Data points from the Voyager 1 inbound and outbound passes and the Voyager 2 inbound pass are shown by filled circles, open circles, and crosses respectively (Richardson, 1986). These data are also shown individually in the top panels. The horizontal dashed lines on the left hand side of the main plot represent the three polar cap rotation velocities determined by Stallard et al. (2004). The light shaded region represents the 'outer magnetosphere' region of the plasma flow model, which we call region B. The dark shaded region shows the range explored by our modified model in the runs described in Chapter 5. The Voyager data was supplied by the NASA Planetary Data System.

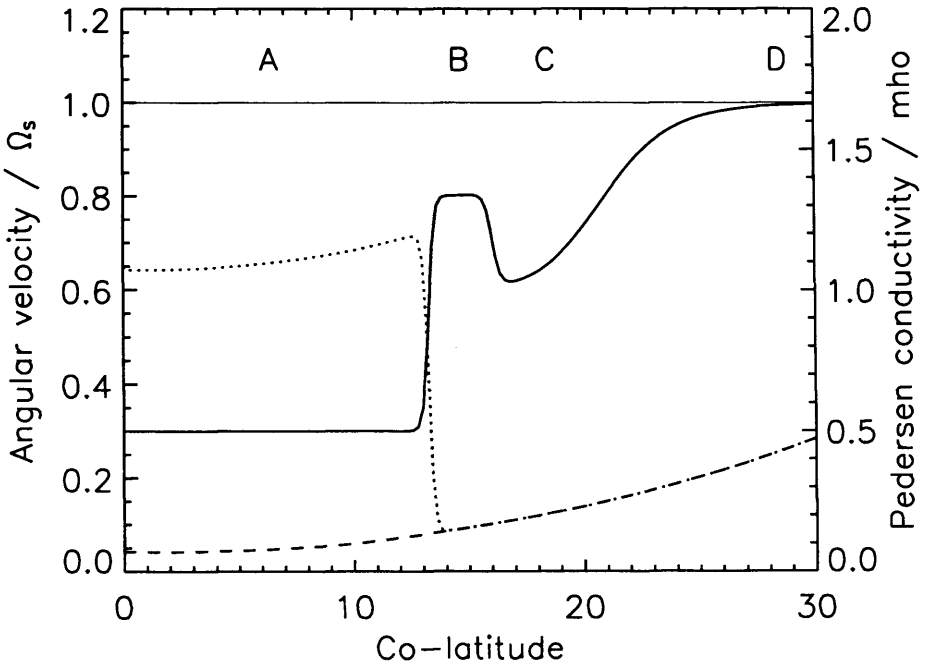

Figure 2.2: Plasma velocity model of Cowley et al. (2004b), mapped into the polar ionosphere (solid line). The dashed line indicates the solar-produced height-integrated conductivity model; the dotted line polar conductivity enhanced by ~0.5mho. The shaded area denotes region B.

Using a simplified geometry to describe this twisting motion Isbell et al. (1984) calculated the expected sub-corotational velocity of the plasma in the polar ionosphere, relative to the neutral rotation velocity in the same region (see Appendix B for a summary of the calculation). This theory yields a value of $\Omega_A \simeq 0.33\Omega_S$ if the effective Pedersen conductivity of the ionosphere (to be discussed shortly) is 1 mho. This value is consistent with the average value of $\sim 0.35\Omega_S$ observed by Stallard et al. (2004). For this reason Cowley et al. (2004b) set the rotation velocity in this region to a round value of $\sim 0.3\Omega_S$, consistent with both observations and theory.

It is worth noting that more recent observations (T. Stallard, private communication, 2005) indicate that $\sim 0.45\Omega_S$ may be closer to the average value, and that there is considerable extra structure beyond a simple constant rotational velocity. However, for the purposes of this study, we retain the lower value to facilitate direct comparison with the results of Cowley et al. (2004b).

The remainder of the model is constrained by plasma flow data collected by the two Voyager spacecraft (Richardson, 1986). This data is shown in Fig. 2.1 by the filled circles (Voyager 1 inbound) open circles (Voyager 1 outbound) and crosses (Voyager 2 inbound). Voyager 2 outbound data is not available. Each of these data sets exhibits slightly different behaviour, but

some common features may be discerned.

The Voyager 1 inbound data (filled circles) is approximately corotational for values of F above 4000nTR$_S^2$. Moving to smaller values of F (moving outwards in the magnetosphere and polewards in the ionosphere) the rotation velocity drops substantially. This is normally interpreted as sub-corotation of the magnetosphere associated with outwards radial mass transport, as discussed in Chapter 1. Some authors have interpreted the very low rotation velocities close to 3000nTR$_S^2$ as signatures of mass-loading specifically associated with the moons Dione and Rhea (most recently Saur et al., 2004; Cowley et al., 2004b). In this study we neglect any effects due to these signatures, for simplicity. At 2500nTR$_S^2$, the plasma velocity rises again. Cowley et al. (2004b) interpret this as the signature of the Dungey and Vasyliūnas cycles in the outer regions of the magnetosphere. Flux tubes involved in these cycles are periodically emptied by mass loss during reconnection events in the magnetotail, such that this region may be accelerated towards corotation by the ionosphere relatively easily.

This essential behaviour defines the three remaining regions of the plasma velocity model. We label the corotating inner magnetosphere as region D, setting its angular velocity $\Omega_D = \Omega_S$. We label the mass-loaded, sub-corotating middle magnetosphere region C, and define its rotation velocity with the parameter $\Omega_C = 0.6\Omega_S$. Regions C and D can also be thought of as a single region dominated by the same physics, with the parameters Ω_C and Ω_D representing the minimum and maximum rotation velocities respectively. Finally, the outer magnetosphere, exhibiting slightly faster flow, is labelled region B and we set the parameter $\Omega_B = 0.8\Omega_S$. This is intended to represent the combined effects of the Vasyliūnas cycle outflow on the dusk flank and the Dungey cycle and Vasyliūnas cycle return flows on the dawn flank.

The Voyager 1 outbound data, which is only available in the range 3000-5000nTR$_S^2$, broadly supports the model velocities in regions C and D. The Voyager 2 data is more complex, exhibiting apparently persistent super-corotational velocities at around 4000nTR$_S^2$, and then a sharp dip to a minimum at ~2500nTR$_S^2$. The velocities then rise again in a similar manner to the Voyager 1 data, but become considerably more scattered. Our plasma velocity model does not presently attempt to represent either the super-corotation in regions C and D or the scattered behaviour in region B.

Initially we employ this flow model as a fixed boundary condition to our thermosphere. However, our initial runs expose various inconsistencies that arise when the magnetosphere model is fixed in this way. The modifications that are necessary to restore consistency are described in Chapter 5.

Jupiter model

Our model of the plasma flows in Jupiter's magnetosphere is a combination of the simple model of the whole magnetosphere presented by Cowley et al. (2005) and the more sophisticated model

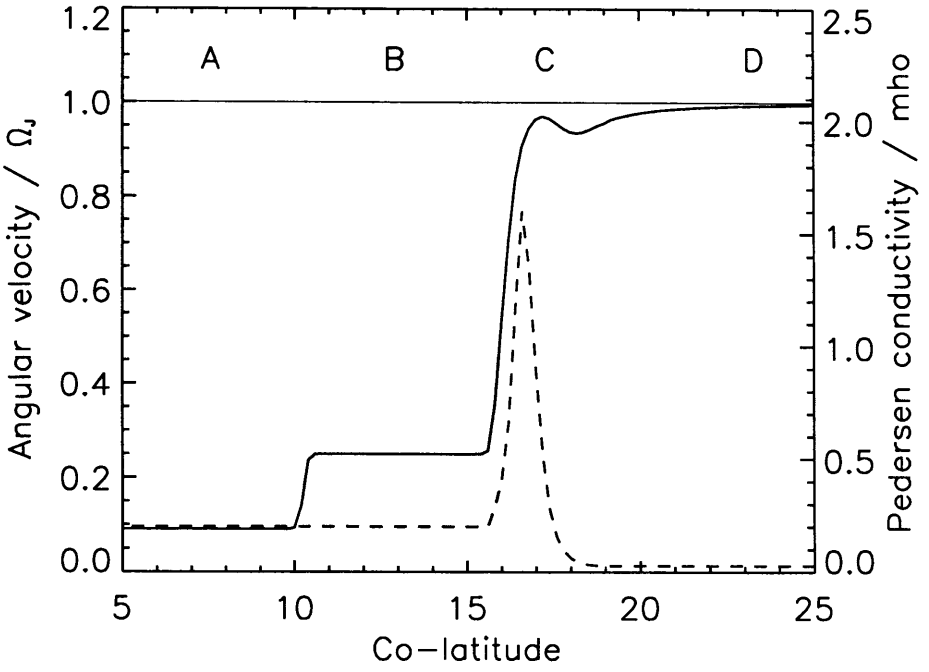

Figure 2.3: Plasma velocity model for Jupiter, based on Nichols and Cowley (2004) and Cowley et al. (2005), mapped into the polar ionosphere (solid line). The dashed line represents the height-integrated conductivity profile for a typical run. Note that equatorwards of ~16° colatitude (regions C and D) the plasma velocity and conductivity values are functions of the neutral rotation velocity (see text). The shaded area denotes region B.

of the middle magnetosphere of Nichols and Cowley (2004). The model may again be split, conceptually, into the four regions A-D described above in the context of the Saturn model. For regions A and B we use Cowley et al. (2005) and for regions C and D we use Nichols and Cowley (2004) (Fig. 2.3).

The flow in regions A and B is given by:

$$\Omega_M(\theta) = \omega_A + \frac{1}{2}\left[1 + \tanh\left(\frac{\theta - \theta_{AB}}{\Delta\theta_{AB}}\right)\right](\omega_B - \omega_A) \tag{2.10}$$

Region A is again supposed to represent the region of 'open' field lines associated with the tailward flow of the Dungey cycle. The colatitudinal extent of this region, which extends from the pole to $\theta_{AB} = 10.25°$, was determined by Cowley et al. (2005) through consideration of the amount of 'open' flux expected in the system. A rotation velocity of $\omega_A = 0.091\Omega_J$ is chosen. This gives a rotation velocity close to zero, which is consistent with the Isbell theory if the effective conductivity is 0.2mho (we will discuss our adopted conductivities in more detail below). This 'stagnant' behaviour is also consistent with the IR Doppler observations of Stallard

et al. (2003). Region B is again analagous to that described for Saturn, representing the Dungey cycle return flow and Vasyliūnas cycle. We use a value of $\omega_B = 0.25\Omega_J$, which, in the formulation of Cowley et al. (2005), represents 'expanded' conditions in which the magnetosphere is not overly compressed by the dynamic pressure of the solar wind.

For regions C and D we use the formulation of Nichols and Cowley (2004). Their model solves for the rotation velocity of the middle magnetosphere plasma sheet (Eqn. 2.5), taking into account the observation that particle precipitation in the ionosphere associated with upwards field-aligned currents (Eqn. 2.7) will tend to enhance the Pedersen conductivity. In order to solve for this situation self-consistently, a third equation is required, relating the field-aligned current to the ionospheric Pedersen conductivity:

$$\Sigma_P(\theta) = \Sigma_P\left(j_{\|i}(\theta)\right) \tag{2.11}$$

The form of this function will be described in Section 2.4.

Briefly, the three coupled equations (Eqns 2.5, 2.7 and 2.11) are solved by a shooting method, integrating inwards from a boundary condition at the outer edge of the magnetosphere. Our boundary condition is that the radial current at $100R_J$ should be equal to 100MA. This is the same boundary condition adopted by Nichols and Cowley to represent 'realistic' conditions. In all other respects our approach to the problem is essentially identical to that of Nichols and Cowley, except that they integrated the equations using the *Mathematica* package (J.D. Nichols, private communication, 2005) whereas we perform the integration using a FORTRAN subroutine directly coupled to our thermospheric model (Chapter 3).

2.2 Ion-neutral coupling

The transfer of angular momentum between the upper atmosphere and magnetosphere is only possible because ions in the upper atmosphere are controlled by a combination of electromagnetic forces (the magnetosphere) and collisions with neutrals (the thermosphere). To properly understand this transfer process we must discuss some of the details of these interactions.

2.2.1 Motion in the absence of collisions

Initially we consider the motion of an ion of charge e and mass m_i moving in free space, in some general inertial frame $\mathcal{S}$, at a velocity[2] $\mathbf{v}_i$ under the influence of an electric field $\boldsymbol{E}$ and a magnetic field $\boldsymbol{B}$. First we consider its equation of motion parallel to magnetic field lines:

$$m_i\dot{\mathbf{v}}_{i\|} = e\boldsymbol{E}_{\|} \tag{2.12}$$

[2]Note that we write the velocity of an individual ion $\mathbf{v}_i$ to distinguish it from the bulk plasma velocity $\boldsymbol{v}$ which will be used much more extensively in this work.

which is such that parallel electric fields simply accelerate ions along field lines. In this thesis we deal mostly with quasi-neutral plasmas in which such field-aligned accelerations act to rapidly remove field-aligned electric fields. Thus our electric fields are almost exclusively perpendicular to the magnetic field. For this reason we will henceforth assume that there are no electric fields or particle motions parallel to the field lines, so that we deal with an essentially two-dimensional situation[3].

The perpendicular component of the equation of motion contains an extra component proportional to $\mathbf{v}_i \times \boldsymbol{B}$:

$$m_i \dot{\mathbf{v}}_i = e(\boldsymbol{E} + \mathbf{v}_i \times \boldsymbol{B}) \tag{2.13}$$

We may simplify this by defining a quantity which we call, for reasons which will become clear, the 'plasma drift velocity' $\boldsymbol{v}$:

$$\boldsymbol{v} = \frac{\boldsymbol{E} \times \boldsymbol{B}}{|B|^2} \tag{2.14}$$

such that $\boldsymbol{E}$ is now given by:

$$\boldsymbol{E} = -\boldsymbol{v} \times \boldsymbol{B} \tag{2.15}$$

If we transform into the frame $\mathcal{S}'$ of this velocity the equation of motion becomes:

$$m_i \dot{\mathbf{v}}_i' = e\mathbf{v}_i' \times \boldsymbol{B} \tag{2.16}$$

where $\mathbf{v}_i' = \mathbf{v}_i - \boldsymbol{v}$ is the ion velocity in $\mathcal{S}'$. If we define a unit vector $\hat{\boldsymbol{b}} = \boldsymbol{B}/|B|$ and make use of the gyrofrequency Ω_i (Eqn 1.12) we may simplify this further:

$$\dot{\mathbf{v}}_i' = \Omega_i \mathbf{v}_i' \times \hat{\boldsymbol{b}} \tag{2.17}$$

This reduced equation of motion simply represents circular motion perpendicular to the magnetic field direction, with angular frequency Ω_i. Thus the mean motion of the ion is the velocity $\boldsymbol{v}$, combined with circular motion at the gyrofrequency about the magnetic field direction.

The electrons that co-exist with the ions in our quasi-neutral plasma must behave identically, but with circular motion in the opposite direction:

$$\dot{\mathbf{v}}_e' = -|\Omega_e| \mathbf{v}_e' \times \hat{\boldsymbol{b}} \tag{2.18}$$

Thus the mean relative motion of ions and electrons is zero, and in this situation no currents flow.

Note that the electric field is removed entirely from our equations simply by changing frames, and, equivalently, that the mean drift motion is determined solely by the electric field. This means that the electric field is a frame dependent quantity that expresses the drift velocity of the ions in that frame, defined by Eqn. 2.15.

[3]This means that we can write, for example, $\boldsymbol{E}$ instead of $\boldsymbol{E}_\perp$, which makes the equations that follow considerably more readable!

2.2.2 Effect of ion-neutral collisions

To include the effect of collisions between ions and neutrals we assume that the interaction can be parameterised using a 'collision frequency for momentum transfer' ν_{in} such that Eq. 2.17 acquires an extra term:

$$\dot{\mathbf{v}}_i' = \Omega_i \mathbf{v}_i' \times \hat{\boldsymbol{b}} + \nu_{in}(\boldsymbol{u}' - \mathbf{v}_i') \tag{2.19}$$

where $\boldsymbol{u}' = \boldsymbol{u} - \boldsymbol{v}$ is the bulk neutral velocity in the frame $\mathcal{S}'$ and $\boldsymbol{u}$ is the bulk neutral velocity in the general frame $\mathcal{S}$. Thus an extra drag term is added to the equation of motion of the ions, proportional to the velocity difference between the velocity of the individual ion and the bulk velocity of the neutrals[4].

We are interested in the steady state motion of the ions given this equation of motion. To find this we set $\dot{\mathbf{v}}_i = 0$ to find that:

$$\mathbf{v}_i' \times \hat{\boldsymbol{b}} = -r_i(\boldsymbol{u}' - \mathbf{v}_i') \tag{2.20}$$

where we have now defined the important ratio r_i:

$$r_i = \nu_{in}/\Omega_i \tag{2.21}$$

Now, noting that $\mathbf{v}_i' = -(\mathbf{v}_i' \times \hat{\boldsymbol{b}}) \times \hat{\boldsymbol{b}}$ we have:

$$\begin{aligned} \mathbf{v}_i' &= r_i(\boldsymbol{u}' - \mathbf{v}_i') \times \hat{\boldsymbol{b}} \\ &= r_i(\boldsymbol{u}' \times \hat{\boldsymbol{b}} - \mathbf{v}_i' \times \hat{\boldsymbol{b}}) \\ &= r_i(\boldsymbol{u}' \times \hat{\boldsymbol{b}} + r_i(\boldsymbol{u}' - \mathbf{v}_i')) \end{aligned} \tag{2.22}$$

where the last step follows from Eqn. 2.20. If we rearrange this equation for $\mathbf{v}_i'$ we find:

$$\mathbf{v}_i' = \frac{1}{r_i + r_i^{-1}} \boldsymbol{u}' \times \hat{\boldsymbol{b}} + \frac{r_i}{r_i + r_i^{-1}} \boldsymbol{u}' \tag{2.23}$$

To understand the physical significance of this equation we need to examine the meaning of the two velocities it relates. The velocity $\mathbf{v}_i'$ is the mean velocity of the ions in the frame in which the electric field is zero. If we assume that the collisions between electrons and neutrals are negligible, then the mean motion of the electrons must still be zero, as expressed by Eqn. 2.18. Thus $\mathbf{v}_i'$ is now the relative velocity of the ions and electrons, and a current $\boldsymbol{j}$ flows:

$$\boldsymbol{j} = e n_i \mathbf{v}_i' \tag{2.24}$$

However, the velocity $\boldsymbol{u}'$ is, by definition, the neutral velocity in the frame in which the electric field is zero. Thus the plasma drift velocity in the frame of the neutral wind must be $-\boldsymbol{u}'$ and it follows from Eqn. 2.15 that the electric field in the frame of the neutral wind $\boldsymbol{E}^*$ is

$$\boldsymbol{E}^* = \boldsymbol{u}' \times \hat{\boldsymbol{b}}|B| = (\boldsymbol{u} - \boldsymbol{v}) \times \boldsymbol{B} \tag{2.25}$$

[4]This parameterisation makes the assumption that the effect of neutral collisions is to exert a continual drag force on the ions; in reality the drag force is exerted by discrete collisions. For a treatment that takes into account discrete collisions (and comes to the same answer) see Ratcliffe (1972).

We may now rewrite Eqn. 2.23 as:

$$\boldsymbol{j} = \frac{en_i}{|B|}\frac{1}{r_i + r_i^{-1}}\boldsymbol{E}^* - \frac{en_i}{|B|}\frac{r_i}{r_i + r_i^{-1}}\boldsymbol{E}^* \times \hat{\boldsymbol{b}} \tag{2.26}$$

Thus we find that the ion-neutral collisions cause a current to flow whose magnitude is proportional to $\boldsymbol{E}^*$, the electric field in the rest frame of the neutrals.

This current consists of two components. The first term on the RHS of Eqn. 2.26 is known as the Pedersen current, and flows parallel to $\boldsymbol{E}^*$. This results from the neutral collisions liberating the ions from repeated gyration about the magnetic field, thus freeing them to move in the direction of the electric field. The second term on the RHS is the Hall current, flowing parallel to the relative velocity between ions and neutrals. This results simply from the neutrals retarding the drift motion of the ions through collisions.

We may simplify the expression for $\boldsymbol{j}$ by introducing the Pedersen and Hall conductivities σ_{Pi} and σ_{Hi} due to a particular ion i:

$$\sigma_{Pi} = \frac{en_i}{|B|}\frac{1}{r_i + r_i^{-1}} = \frac{en_i}{|B|}f(r_i) \tag{2.27}$$

$$\sigma_{Hi} = \frac{en_i}{|B|}\frac{r_i}{r_i + r_i^{-1}} = r_i\sigma_{Pi} \tag{2.28}$$

where the interesting function $f(r_i)$ is defined as

$$f(r_i) = \frac{1}{r_i + r_i^{-1}} \tag{2.29}$$

We may usefully refer to $f(r_i)$ as the 'potential Pedersen conductivity', in that it describes, in a dimensionless way, the magnitude of Pedersen conductivity that it is possible to generate at a particular altitude for a fixed ion density. Similarly the function $r_i f(r_i)$ represents the potential Hall conductivity.

The limits of these functions give us insight into the distribution of Pedersen and Hall conductivity at different altitudes in the atmosphere. At very high altitudes we expect $r_i \to 0$, since the ion-neutral collisions will go towards zero. At very low altitudes we expect $r_i \to \infty$ as the ion-neutral collisions become very frequent. In both these limits $f(r_i) \to 0$. Thus we expect there to be an intermediate layer in which it maximises. It is easily shown that this occurs at the altitude where $r_i = 1$, such that $f(1) = 0.5$.

The potential Hall conductivity $r_i f(r_i)$ behaves differently. In the very high altitude limit it is zero — this makes sense since the low frequency of collisions prevent the neutral flow from imposing itself on the ions. At very low frequency $r_i f(r_i) \to 1$ so that at very low altitude the collisions are so frequent that the neutral flow is exactly imposed on the ions. This again makes sense.

Note that the expressions given are for the conductivities due to a single ion species, and assume that electron-neutral collisions are negligible. If there is more than one ion we may find the total conductivity by summing over i, for example $\sigma_P = \Sigma_i \sigma_{Pi}$.

The introduction of the Pedersen and Hall conductivities allows us to write the perpendicular current $\boldsymbol{j}$ in the concise form:

$$\boldsymbol{j} = \boldsymbol{\sigma}.\boldsymbol{E}^* \tag{2.30}$$

where we have defined a tensor conductivity $\boldsymbol{\sigma}_P$:

$$\boldsymbol{\sigma} = \begin{pmatrix} \sigma_P & -\sigma_H \\ \sigma_H & \sigma_P \end{pmatrix} \tag{2.31}$$

2.2.3 Energy and momentum inputs

Ion drag

The acceleration balance on a single ion undergoing the motion described above is given by Eqn. 2.19. The RHS of this equation contains a term due to electromagnetic forces and a term due to collisions. We have described the situation in which these two terms balance exactly. We can think of this balance as a continual input of momentum by the electromagnetic forces which is repeatedly extracted by collisions with neutrals. This constitutes a net force on the neutrals whose magnitude must be given by either of the two equal terms. However, it clearly must have the same sign as the first, electromagnetic term, since it is this that acts as the source of the momentum. We must further multiply this term by the ion mass (to obtain a force rather than an acceleration) and by the ion density (to obtain the total force per unit volume), such that the electromagnetic 'ion drag' force f_D on the neutrals is:

$$f_D = en_i|B|\mathbf{v}_i' \times \hat{\boldsymbol{b}} = \boldsymbol{j} \times \boldsymbol{B} \tag{2.32}$$

where the last equality follows from Eqn. 2.24.

Ion drag energy and Joule heating

Of course any input of momentum into the atmosphere must be accompanied by an input of kinetic energy — this is the 'work done by ion drag'. For brevity we refer to this K.E. input as 'ion drag energy'. Since the momentum input is mediated by collisional processes, we would also expect some thermalisation of energy as a by-product of the interaction. This thermal energy input is known as Joule heating since, as we shall see, it has the same mathematical form as resistive heating due to an electrical current.

The ion drag energy is frame-dependent because the K.E. of the gas depends on the frame. Thus we calculate the energy inputs in the general frame $\mathcal{S}$. The only work done by the magnetosphere is done by the electric field, since the magnetic field acts perpendicular to the velocity.

Thus the total work done is[5]:

$$\begin{aligned} q_{tot} &= n_i e \mathbf{v}_i \cdot \boldsymbol{E} \\ &= n_i e (\mathbf{v}_i' - \boldsymbol{v}) \cdot (-\boldsymbol{v} \times \boldsymbol{B}) \\ &= n_i e \mathbf{v}_i' \cdot (-\boldsymbol{v} \times \boldsymbol{B}) \\ &= \boldsymbol{j} \cdot (-\boldsymbol{v} \times \boldsymbol{B}) \\ &= \boldsymbol{j} \cdot (\boldsymbol{E}^* - \boldsymbol{u} \times \boldsymbol{B}) \\ &= \boldsymbol{j} \cdot \boldsymbol{E}^* + \boldsymbol{u} \cdot (\boldsymbol{j} \times \boldsymbol{B}) \end{aligned} \tag{2.33}$$

where we have used, respectively, the identities $\mathbf{v}_i' = \mathbf{v}_i - \boldsymbol{v}$ and Eqn. 2.15; $\boldsymbol{v} \cdot (\boldsymbol{v} \times \boldsymbol{B}) = 0$; Eqn. 2.24; Eqn. 2.25; and $\boldsymbol{j} \cdot (\boldsymbol{u} \times \boldsymbol{B}) = -\boldsymbol{u} \cdot (\boldsymbol{j} \times \boldsymbol{B})$. The result is that the total energy input from the magnetosphere is divided into two components. We may identify the first component as the Joule heating q_J:

$$q_J = \boldsymbol{j} \cdot \boldsymbol{E}^* \tag{2.34}$$

The current $\boldsymbol{j}$ is frame-independent since it depends only on the *relative* velocities of ions and electrons. The electric field in the frame of the neutrals $\boldsymbol{E}^*$ is also frame-independent, by definition, since it represents the electric field in a specific frame. Thus the Joule heating is also frame-independent, which is a required property of a thermal energy source.

As noted above, the Joule heating has the same mathematical form as resistive heating due to an electric current. Vasyliūnas and Song (2005) have argued that this is nothing more than a formal mathematical coincidence, and that the 'Joule heating' is in reality more similar to a frictional heating effect between the ions and neutrals. While interesting, this perspective does not in practice have any effect on our calculations.

The second component of the energy input is the ion drag energy q_D:

$$q_D = \boldsymbol{u} \cdot (\boldsymbol{j} \times \boldsymbol{B}) \tag{2.35}$$

and we can identify this as the work done by the $\boldsymbol{j} \times \boldsymbol{B}$ force on the neutral winds in the frame $\mathcal{S}$. While this clearly *is* frame-dependent, this is what we expect and require.

Electric field variability

In order to represent these magnetospheric energy inputs it is necessary to use a model of the magnetospheric plasma flows such as those discussed in Section 2.1. The models that we use — and all other available models for the giant planets — represent flows that are both spatially smooth and time-averaged. The electric fields and current systems implied by these models inherit these qualities.

[5] A note on the symbols used to represent energy inputs: whenever we refer to per unit volume energy changes these will be represented by a roman q, while per unit mass energy changes will be represented by an italic q. These quantities are of course related by $q = \rho q$, where ρ is the mass density.

However, it has been shown for Earth that electric fields due to magnetospheric plasma flows may fluctuate on timescales of less than a minute (Codrescu et al., 2000; Aruliah et al., 2005). The magnitude of these fluctuations may be comparable to, or greater than, the magnitude of the flow itself.

We can understand the effect of such fluctuations intuitively if we consider that they add an alternating current (AC) component to the smooth direct current (DC) flows envisaged in the magnetosphere models. It is a well understood fact that an AC current causes resistive heating even if the mean current is zero because the resistive heating goes as the square of the current, which is positive definite. Similarly, the effect of adding AC fluctuations to the DC magnetosphere models is to increase the Joule heating, as first discussed in detail by Codrescu et al. (1995), in the terrestrial context.

The spatial and temporal frequencies of such fluctuations will clearly also be important. If the fluctuations are large scale and slowly varying, then the influence of ion drag on the neutral winds will tend to reduce the component of $\boldsymbol{E}^*$ due to fluctuations by reducing the differential velocity $\boldsymbol{u} - \boldsymbol{v}$. Thus the increase in Joule heating will not be as great as it would be if the neutral winds were fixed. However, if the fluctuations are small scale or very rapid, the neutral atmosphere will be unable to respond, and the increase in heating will be unaffected. Thus the scale of the fluctuations is crucial to their influence on the energy and momentum balance of the thermosphere.

Suppose that we write the fluctuating plasma drift velocity $\boldsymbol{v}_f$ as the sum of a constant mean value $\boldsymbol{v}$ and a fluctuating component $\boldsymbol{f}(t)$, then the fluctuating rest frame field becomes:

$$\boldsymbol{E}_f^* = \boldsymbol{E}^* - \boldsymbol{f}(t) \times \boldsymbol{B} \tag{2.36}$$

By definition we have $\overline{\boldsymbol{f}} = \boldsymbol{0}$, where the line denotes an average over a suitably long period of time. We can also make the initial assumption that the fluctuations are well characterised by a parameter s, defined by $s^2 = \overline{\boldsymbol{f} \cdot \boldsymbol{f}}/(\boldsymbol{v} \cdot \boldsymbol{v})$, which is the r.m.s. fluctuation of the plasma velocity normalised to the mean of the plasma velocity in our general frame $\mathcal{S}$.

Having made these assumptions, it is easily shown that the time-averaged ion drag energy and momentum inputs are unchanged from the case without fluctuations, whereas the time-averaged Joule heating becomes:

$$\overline{q_{Jf}} = q_J + \sigma_P B^2 |\boldsymbol{v}|^2 s^2 \tag{2.37}$$

Thus we can extend our description to include heating from the fluctuating component of the plasma flows using the single parameter s. It is worth emphasising that the only assumption this parameterisation makes about the form of the fluctuations, other than the definition of s, is that they behave in such a way as not to directly alter the neutral wind velocity $\boldsymbol{u}$.

2.2.4 Application to Jupiter and Saturn

We now apply the general expressions above to the simple axisymmetric situations described in Section 2.1. The principle characteristics of these models is that the plasma drift $\boldsymbol{v}$ is approximately westwards and the magnetic field $\boldsymbol{B}$ approximately vertical. For simplicity, we assume that these approximations hold exactly in our region of interest. The latter assumption is discussed in Appendix C.

We deal with a region of the atmosphere in which electron-neutral collisions are negligible. This means that we can treat the magnetic field lines as almost perfectly conducting, and thus equipotential. Thus the plasma drift velocity $\boldsymbol{v}$ does not vary with altitude within our region of interest, and always represents the drift velocity of the electrons. The neutral velocity $\boldsymbol{u}$, however, is a function of altitude[6].

We take our general frame S to be the frame corotating with the planet. This is the frame of our thermospheric model (see Chapter 3). The only motional effects introduced by the rotating frame are centrifugal and Coriolis forces. We assume that the magnetic field is vertical, and since the vertical is defined as the direction of the combined gravitational and centrifugal forces, this means that the centrifugal force has no effect on the $\boldsymbol{B}$-field perpendicular motion of the ions. The Coriolis force has a similar effect to the magnetic field in that it causes the ions to gyrate. However, since Ω_J, $\Omega_S \ll \Omega_i$ this effect is negligible.

We use a right handed-coordinate system in which the x- or θ-direction is south, the y- or ϕ-direction east, and the z-direction vertical, i.e. aligned with $\boldsymbol{B}$. This is consistent with the coordinate system used in the thermospheric model (Chapter 3). We may then, at any altitude, write the neutral wind $\boldsymbol{u}$ as an eastwards component u_ϕ and a southwards component u_θ. The eastwards plasma drift velocity is v_ϕ and the southwards plasma drift velocity v_θ is, according to our assumptions, zero. Assuming that we are in the northern hemisphere, such that the magnetic field is positive upwards, the rest frame electric fields E^*_θ and E^*_ϕ are, from Eqn. 2.25:

$$E^*_\theta = -(v_\phi - u_\phi)B = (1 - k_\phi)E_\theta \tag{2.38}$$

$$E^*_\phi = u_\theta B = k_\theta E_\theta \tag{2.39}$$

where $E_\theta = -v_\phi B$, the field due to the plasma velocity only, and:

$$k_\theta = u_\theta / v_\phi \tag{2.40}$$

$$k_\phi = u_\phi / v_\phi \tag{2.41}$$

[6]Note that in the following almost all physical variables that are written in lower case represent quantities that depend on altitude z. The plasma velocity $\boldsymbol{v}$ is the principal exception to this. Almost all variables written in upper case are height-integrated analogues of their corresponding lower case variables. The principal exceptions to this are the electric and magnetic fields, of which $\boldsymbol{E}$ and $\boldsymbol{B}$ are constant with altitude and $\boldsymbol{E}^*$ varies with altitude.

i.e. the neutral velocities normalised to the zonal plasma drift velocity. Normalising the velocities in this way greatly simplifies the equations that follow. Note that if the plasma velocity v_ϕ is negative, i.e. westwards, then positive values of k_ϕ and k_θ represent westwards and polewards neutral winds respectively.

Ion drag

We can now employ Eqn. 2.30 to calculate the $\boldsymbol{B}$-field perpendicular current density $\boldsymbol{j}$:

$$\boldsymbol{j} = \boldsymbol{\sigma}.\boldsymbol{E}^* = \sigma_P E_\theta \begin{pmatrix} (1-k_\phi) - rk_\theta \\ k_\theta + r(1-k_\phi) \end{pmatrix} \tag{2.42}$$

where we have written $r = \sigma_H/\sigma_P$. If there is only one ion species i present, $r = r_i$. This in turns yields the $\boldsymbol{j} \times \boldsymbol{B}$ force that acts on the neutrals:

$$\boldsymbol{j} \times \boldsymbol{B} = \sigma_P B E_\theta \begin{pmatrix} k_\theta + r(1-k_\phi) \\ -(1-k_\phi) + rk_\theta \end{pmatrix} \tag{2.43}$$

This represents zonal and meridional forces on the neutrals due to both the Pedersen and Hall currents driven by both zonal and meridional electric fields. Inclusion of the meridional winds coupled to the Hall conductivity shows that there is a small component of *zonal* drag associated with meridional winds. This means that even if the zonal neutral and plasma velocities are equal ($k_\phi = 1$) there is still a drag force between the thermosphere and the plasma, provided the meridional wind is non-zero. Thus the neutral velocity that the plasma in the magnetosphere 'feels' via the atmospheric conductivity should, properly, be a linear combination of the zonal and meridional neutral velocities, which we call k:

$$k = k_\phi + rk_\theta \tag{2.44}$$

The zonal component of the $\boldsymbol{j} \times \boldsymbol{B}$ force can then be rewritten:

$$[\boldsymbol{j} \times \boldsymbol{B}]_\phi = -\sigma_P B E_\theta (1-k) \tag{2.45}$$

so that when $k = 1$ the coupling force does indeed fall to zero. When height-integrated (see below), this k is equivalent to the 'slippage' described in previous studies. Clearly this includes a small, previously ignored component due to meridional winds.

We may consider two limiting cases. Firstly, the situation that applies to the majority of the thermosphere-ionosphere, in which the Pedersen conductivity is much greater than the Hall conductivity, i.e. $r \ll 1$, such that $k \sim k_\phi$:

$$[\boldsymbol{j} \times \boldsymbol{B}]_\phi \simeq -\sigma_P B E_\theta (1-k_\phi) \tag{2.46}$$

which represents a simple westwards drag on the neutrals caused by the westwards drifting plasma. This approximation, in which the Hall conductivity and meridional winds are neglected, is the simple situation adopted by previous studies (e.g Huang and Hill, 1989; Cowley

et al., 2004b; Millward et al., 2005). The opposite case is that encountered when $r \gg 1$. This corresponds to altitudes below the thermosphere where collisions are frequent enough to fully couple the ions and neutrals:

$$[\boldsymbol{j} \times \boldsymbol{B}]_\phi \simeq \sigma_H B E_\theta k_\theta = -n_i e u_\theta B \tag{2.47}$$

Thus in this situation the meridional current is driven directly by ion-neutral collisions, as the neutral winds entirely control the ion motion. An equatorwards wind in this situation will have the effect of spinning up the magnetosphere. Radio occultations have often revealed low altitude layers of electron density that exist in exactly this regime: whether meridional winds coupled to these layers structure the magnetosphere is an interesting question, but, since these regions at present lie below the lower boundary of our thermospheric model (see Chapter 3), it is a question we will defer for future consideration.

The meridional component of the $\boldsymbol{j} \times \boldsymbol{B}$ force is associated with zonal current flow. Because our model is axisymmetric, this component of current flow is not divergent and therefore does not contribute to the field aligned magnetosphere-ionosphere coupling currents. A further consequence of axisymmetry is that any meridional acceleration of the neutrals by the $\boldsymbol{j} \times \boldsymbol{B}$ force automatically conserves momentum, and thus these currents can have no role in transferring momentum between the atmosphere and magnetosphere. However, if we introduced asymmetries into our modelling these terms could become important.

Joule heating and ion drag energy

Using Eqns. 2.34 and 2.35 we can now calculate the Joule heating rate q_J and the ion drag energy q_D. If we write the Joule heating in the absence of neutral winds as $q_0 = \sigma_P E_\theta^2$ then we may calculate the total normalised energy inputs. We further split the ion drag energy into components $q_{D\theta}$ and $q_{D\phi}$ that represents kinetic energy associated with θ and ϕ components of the winds:

$$\begin{aligned} q_J/q_0 &= k_\theta^2 + (1-k_\phi)^2 \\ q_{D\theta}/q_0 &= -k_\theta^2 + r k_\theta k_\phi - r k_\theta \\ q_{D\phi}/q_0 &= -(1-k_\phi)^2 - r k_\theta k_\phi + (1-k_\phi) \end{aligned} \tag{2.48}$$

The Joule heating q_J is seen to consist of two components: one each due to the relative westwards and equatorwards motions of plasma and neutrals k_θ and $1-k_\phi$ respectively. It can be seen that the first terms of $q_{D\theta}$ and $q_{D\phi}$ together balance the total Joule heating term. Indeed, the Joule heating can be seen to be proportional to the bulk K.E. of the neutrals in the rest frame of the plasma; it is thus has the appearance of thermalisation of this K.E. through collisions between the ions and neutrals.

The second terms of $q_{D\theta}$ and $q_{D\phi}$ represent a drag perpendicular to the neutral flow due to

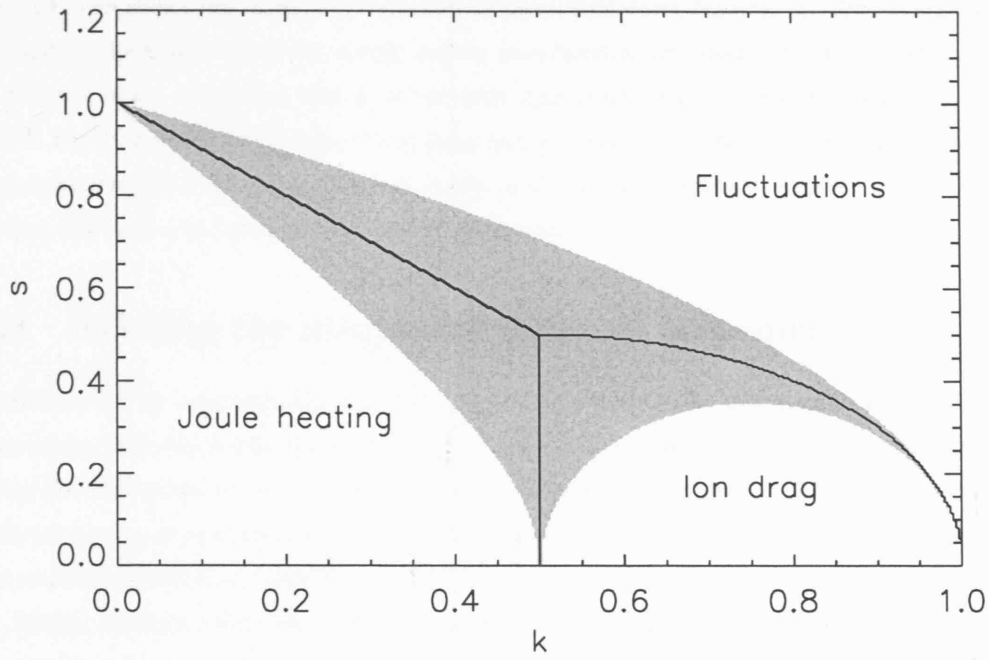

Figure 2.4: Relative importance of energy sources as a function of k and s. The marked areas represent regions of parameter space in which each energy source is the most important. In the unshaded regions the marked energy source accounts for greater than 50% of the total energy input.

the component of the $\boldsymbol{j} \times \boldsymbol{B}$ force related to the Hall current. This causes no net energy input, but acts to change the direction of the neutral flow.

Since the sum of all these terms cancel, the final terms of $q_{D\theta}$ and $q_{D\phi}$ thus represent the actual net magnetospheric energy input q_{tot}:

$$q_{tot}/q_0 = (1 - k_\phi) - rk_\theta = 1 - k \tag{2.49}$$

Thus, even though the details of Joule heating and ion drag depend on non-linear functions of k_θ and k_ϕ, the *total* energy input depends only on $1-k$, which represents the difference between the plasma velocity and effective neutral velocity. In total, the energy input behaves like a frictional interaction between the plasma and neutrals: when $k = 1$ the energy input falls to zero, since there is no 'friction'.

Electric field variability

If we adopt the parameterisation of electric field variability using a single parameter s, we can write (from Eqn. 2.37):

$$\overline{q_{Jf}/q_0} = k_\theta^2 + (1 - k_\phi)^2 + s^2 \tag{2.50}$$

Fig. 2.4 then shows the relative contribution of mean-field Joule heating, ion drag energy, and fluctuation Joule heating to the energy inputs, as a function of k and s, in the approximation in which $k \sim k_\phi$. It is clear that q_J is the most important energy source if s and k are both small. Ion drag is only important if k is large and s is small. In general different points in the atmosphere will correspond to different points in this parameter space, because both k and s presumably vary with altitude, latitude and longitude.

2.3 Relating the magnetosphere and atmosphere

In Section 2.1 we described models of the rotational velocity in the magnetosphere Ω_M and its interaction with the thermosphere-ionosphere in terms of a height-integrated Pedersen conductivity Σ_P. In Section 2.2 we then described, independently, the influence of an eastwards plasma drift velocity v_ϕ on the thermosphere in terms of local conductivities σ_P and σ_H. We now discuss the relationship between these two perspectives.

Firstly, we must relate the rotation velocity Ω_M of each shell of flux tubes to the eastwards ionospheric plasma velocity v_ϕ:

$$v_\phi = -\rho_i(\Omega_P - \Omega_M) \tag{2.51}$$

where ρ_i is the perpendicular off-axis distance. Using the assumptions discussed in Section 2.2 this equation fully describes the projection of the magnetosphere's behaviour into the upper atmosphere.

From a magnetospheric perspective the relationship is more complicated. Most studies of the magnetosphere assume that the conducting region of the upper atmosphere is a thin sheet with uniform properties (e.g Cowley and Bunce, 2003). This assumption can be viewed as a parameterisation of the complexities of the coupled thermosphere and ionosphere. It is possible to recover this parameterisation from our complicated picture by appropriately height-integrating various atmospheric quantities.

If we consider the system as an electrical circuit, we can view each small vertical layer of the atmosphere as a resistor (the tensor conductivity $\boldsymbol{\sigma}$) wired in series with a voltage source (the neutral wind $\boldsymbol{u}(z)$). These layers are then wired together in parallel with the magnetosphere, which is considered to act as a resistiveless voltage source (the plasma velocity v_θ).

We then find that the height-integrated current $\boldsymbol{J}$ flowing in the ionosphere is just the integral sum[7] of the current in each layer. We are primarily concerned with the equatorwards current J_θ since, in our axisymmetric model, it is this component of the current that is divergent and closes in the magnetosphere:

$$J_\theta = \int j_\theta dz$$

[7]Unless otherwise stated, all integrals over dz implicitly cover the entire vertical extent of the conducting region of the ionosphere.

$$= \left(\int \sigma_P(1-k)dz\right) E_\theta$$
$$= \Sigma_P(1-K)E_\theta \tag{2.52}$$

where we have defined the height-integrated Pedersen conductivity

$$\Sigma_P = \int \sigma_P dz \tag{2.53}$$

and a height-integrated analogue of the local parameter k:

$$K = \frac{\int \sigma_P k dz}{\Sigma_P} \tag{2.54}$$

The equation for the current (Eqn. 2.52) is that used by previous authors to describe the magnetosphere-ionosphere interaction. The thermosphere-ionosphere is now a 'sheet' with total conductivity Σ_P (in units of mho). The electric field E_θ is reduced from the pure magnetospheric field by the factor of $1-K$, which encapsulates the effect of the neutral wind on the electric field. K has often been described as 'slippage' of the neutral atmosphere in response to the magnetospheric drag.

The thermosphere-ionosphere thus becomes represented locally by two numbers Σ_P and K. Since both are rather uncertain, they are often combined to form an 'effective conductivity':

$$\Sigma_P^* = (1-K)\Sigma_P \tag{2.55}$$

which will be discussed further in Section 2.4. The origin of this parameterisation is the study by Huang and Hill (1989) in the Jovian context, which found that K should be independent of the plasma velocity for a given conductivity profile. Assuming the true conductivity Σ_P to be approximately constant, this finding is used to justify an approximately constant effective conductivity Σ_P^*. In Chapters 5 and 6 we will show that Huang and Hill (1989) neglected important physics, and that the parameterisation thus breaks down severely under various circumstances.

Comparing the expression given in Eqn. 2.52 for J_θ to that in Eqn. 2.3, and making use of Eqn. 2.51 and the relation $E_\theta = -v_\phi B$, we can see that:

$$K = \frac{\Omega_S - \Omega_T}{\Omega_S - \Omega_M} \tag{2.56}$$

which is the conventional definition of the parameter K (e.g. Cowley et al., 2004b). Notice that this implicitly defines the 'height-integrated' neutral rotation velocity Ω_T as a function of K. As such the neutral rotation velocity Ω_T is, like K, a weighted combination of zonal and meridional winds. This makes sense if we think of Ω_T not as an actual angular velocity but as a useful parameter that describes the rotational friction between the thermosphere and magnetosphere.

We may also write the height-integrated total energy input Q_{tot}:

$$Q_{tot} = (1-K)Q_0 \tag{2.57}$$

where $Q_0 = \Sigma_P E_\theta^2$. In this context the total energy input again behaves like a simple frictional dissipation, proportional to the 'velocity difference' between plasma and neutrals. We can also write this in terms of the separate components of K, height-integrated:

$$Q_{tot} = [(1 - K_\phi) - RK_\theta]\, Q_0 \tag{2.58}$$

where $R = \Sigma_H/\Sigma_P$ and

$$\begin{aligned} \Sigma_P K_\phi &= \int \sigma_P k_\phi dz \\ \Sigma_H K_\theta &= \int \sigma_H k_\theta dz \\ \Sigma_H &= \int \sigma_H dz \end{aligned} \tag{2.59}$$

This shows that the separation into components of neutral wind parallel and perpendicular to the plasma drift velocity, and the different couplings to the Pedersen and Hall conductivities that they generate, can be extended to the height-integrated case.

However, calculating the Joule heating it is clear that:

$$Q_J = E_\theta^2 \int \sigma_P((1 - k_\phi)^2 + k_\theta^2)dz \neq Q_0(1 - K)^2 \tag{2.60}$$

due to the non-linear dependence of the Joule heating on the neutral wind parameters. Magnetospheric studies (e.g Cowley et al., 2004b) have in the past used the height-integrated 'slippage' factor K to calculate the Joule-heating. This is incorrect, since the Joule heating depends on the vertical distribution of k_θ and k_ϕ. The fallacy that leads to this error is the implicit assumption that the conducting layer is a thin sheet with a single rotation velocity at each latitude. We will discuss this further in Section 2.5.3.

2.4 Ionospheric conductivity

2.4.1 Determining the conductivity

There are a number of sometimes conflicting determinations of the actual value of the height-integrated Pedersen conductivity (Table 2.4.1). The most obvious method for determining this quantity is to directly integrate Eqn. 2.53. The ion-neutral collision frequencies necessary for this calculation are conventionally taken to be (Banks and Kockarts, 1973):

$$\nu_{in} = 2.6 \times 10^{-15} n_n \sqrt{\frac{\alpha_0}{\mu_{in}}} \tag{2.61}$$

where α_0 is the polarisability of the neutral gas (in units of $10^{-30}\mathrm{m}^3$), given as 0.82, 0.667 and 0.21 for H_2, H and He respectively, n_n is the number density of the neutral species in m^{-3}, and μ_{in} is the reduced mass of the neutral and ionised species in atomic mass units. This parameterisation of the collision frequencies is not the only one available. For example, Achilleos

Planet	Location	Σ_P / mho	Reference	Comments
Jupiter	Equatorial	0.2	Atreya (1986)	Model
	Mid-latitudes	0.4-0.5	Hinson et al. (1998)	Occultation data
	Sub-auroral	0.0275*	Hill (1980)	M'sphere model + data
	Auroral	10.0	Atreya (1986)	Model
		~ 0.5	Grodent et al. (2001)	Model
		< 8.0	Millward et al. (2002)	Model
		< 2.5	Nichols and Cowley (2004)	Model
		< 1.0	this work	see text
		< 0.2*	this work	Isbell theory/IR data
Saturn	Equatorial	5.0	Atreya (1986)	Model
		0.3	Cheng and Waite (1988)	Occultation data
		5.0	Moore et al. (2004)	Model
	Sub-auroral	17.0	Cheng and Waite (1988)	Occultation data
		< 2*	Bunce et al. (2003)	Magnetometer data
		0.2	Moore et al. (2004)	Model
	Auroral	60.0	Atreya (1986)	Model
		1*	Cowley et al. (2004b)	Isbell theory/IR data
		< 100.0	this work	see text

Table 2.1: Determinations of height-integrated ionospheric Pedersen conductivity (mho) at Jupiter and Saturn (see text). * indicates a determination of the 'effective' conductivity.

et al. (1998) use ion-neutral collision frequencies from Geiss and Bürgi (1986). This study finds slightly different values from those quoted by Banks and Kockarts (1973). The discrepancy between these different sources is not serious — less than a factor of two — but it should be noted that while these parameters are reliable to well within an order of magnitude, they are not yet perfect.

Early applications of this method, summarised by Atreya (1986), were based on modelling of the electron density profiles observed in the Pioneer-Voyager era. Since models generally over-predict the electron density, Atreya (1986) points out that the values he quotes are probably a little high. For Jupiter, Hinson et al. (1998) finds values of 0.4 and 0.5 mho at 66°S and 51°S respectively from the Voyager 2 radio occultations and the Galileo probe atmospheric structure (Fig 1.4; Seiff et al., 1998). These values are in general agreement with those quoted by Atreya (1986).

For Saturn, though, explicit calculations from electron density profiles (Cheng and Waite, 1988) found conductivities an order of magnitude smaller than those indicated by modelling. Recently, Moore et al. (2004) have published results from a new Kronian ionosphere model,

which at present includes ionisation due to solar EUV absorption only[8]. At low latitudes their results are consistent with the older modelling studies cited by Atreya (1986). At sub-auroral latitudes they find conductivities two orders of magnitude smaller than those calculated by Cheng and Waite (1988). This may be a model-dependent effect, or may indicate that at sub-auroral latitudes there is some form of particle precipitation that enhances the ionospheric densities.

At Jupiter, auroral conductivities have been explicitly predicted using numerical models of ionisation by precipitating electrons. The one-dimensional model of Grodent et al. (2001) predicts height-integrated conductivities of ~0.5mho. The JIM ionosphere model (Achilleos et al., 1998) has been used by Millward et al. (2002) to predict conductivities for a range of auroral conditions, peaking at ~8mho. Nichols and Cowley (2004) used this data to generate a model of conductivity as a function of field-aligned current in the magnetosphere, peaking at a value of ~2.5mho.

The JIM values are higher than the Grodent et al. (2001) and Nichols and Cowley (2004) values because JIM models the auroral precipitation using a monochromatic beam of electrons. Thus the conductivity peaks when the peak ionisation altitude of these electrons lies precisely in the layer where the potential Pedersen conductivity maximises. The Grodent et al. (2001) model uses a polychromatic electron beam, such that its ionisation is more evenly spread through the upper atmosphere; the Nichols and Cowley (2004) study performs an intelligent average over the parameter space explored by Millward et al. (2002), and it is this that produces lower peak conductivities. Bearing this in mind, the calculated Jovian auroral conductivities of Grodent et al. and Millward et al. are reasonably consistent.

Estimates of the height-integrated conductivity have also been made by examining the signatures of magnetosphere-ionosphere coupling currents in the magnetosphere itself. For Jupiter, Hill (1980) fitted his simple (1979) model to Voyager 1 data, yielding a best fit that depends on Σ_P^* and $\dot{M}$. Given the present best estimate that $\dot{M} = 1000\text{kgs}^{-1}$, this yields a Σ_P^* of 0.0275mho. For Saturn, Bunce et al. (2003) showed that at sub-auroral latitudes ($\sim 70°$ colatitude) field-line bending possibly associated with magnetosphere-ionosphere coupling currents was consistent with $\Sigma_P^* < 2$mho.

Another estimate of the effective conductivity can be extracted from the twisting of tail field lines predicted by Isbell et al. (1984), described in Appendix B. Eqn. B.7 relates the polar cap angular velocity Ω_A to the effective Pedersen conductivity Σ_P^*. The observed value of Ω_A for Saturn is ~ 0.3 of corotation, and for Jupiter approximately zero. This leads to predicted values of $\Sigma_P^* \sim 1$mho for Saturn (Cowley et al., 2004b) and $\Sigma_P^* < 0.2$mho for Jupiter.

The structure of Eqn. 2.27 also allows us to place upper limits on the integrated conductivity in terms of the column density of an ion. Clearly the maximum possible conductivity will occur

[8]Due to an error in the published calculations, the actual values quoted in this paper are an order of magnitude too high. Corrected values are given in Table 2.4.1 (Luke Moore, private communication, 2005)

if *all* of the column density occurs at the peak of the potential Pedersen conductivity, at which point $f(r_i) = 0.5$. This situation is of course effectively impossible, but it provides the useful limit:

$$\Sigma_{Pi} \leq \frac{N_i e}{2|B|} \tag{2.62}$$

where Σ_{Pi} is the height-integrated Pedersen conductivity due to an ion i, and N_i is the column density of that ion. This allows us to put constraints on the maximum possible conductivity due to H_3^+ in the polar regions, for which column densities are available (see Table 1.5). These upper limits for Jupiter and Saturn, using polar B-field strengths of 8×10^{-4}T and 6×10^{-5}T, are 1mho and 100mho respectively. Note that there may be additional conductivity due to H^+, which may increase this upper limit. However, since the H^+ potential conductivity peaks about one scale height below the H_3^+ potential conductivity, there would either need to be much more H^+ than H_3^+ or a very fortuitous arrangement of ionisation for the conductivity to be much greater than this limit.

For Jupiter the upper limit is slightly below the peak values calculated from JIM. This is because the peak column densities reported by Millward et al. (2002) are slightly larger than those reported by Lam et al. (1997) and Stallard et al. (2002). For Saturn the limit is much larger than the empirical determinations of conductivity from Bunce et al. (2003) and Cowley et al. (2004b). This indicates either that the H_3^+ is inefficiently distributed relative to the potential conductivity, or that the value of K in the polar regions of Saturn is very large — of the order of 0.9 or greater.

2.4.2 Conductivity models

It is clear from the preceding discussion that there is very little convergence between different determinations of the conductivity. The only determinations that are reasonably consistent with each other are the calculated auroral values for Jupiter: however this is might be considered unsurprising given that the model calculations are all based upon similar assumptions.

For this reason it is not necessarily particularly constructive for us to employ full ionospheric calculations in our calculations of coupling between the magnetosphere and the atmosphere. Such an approach is at first sight alluring, but it is clear that our understanding of the ionosphere is insufficient to render such calculations reliable. Indeed, to properly couple an ionosphere model to a two- or three-dimensional thermosphere model (such as will shortly be described in Chapter 3) normally requires considerable simplification of the physics to maintain manageable model runtimes. Even the most sophisticated one-dimensional ionosphere models are unable to fully account for the observations, so it seems unlikely that a simplified version would fare any better.

Our conclusion is that detailed ionosphere modelling is a distraction from our main objective, which is to understand the thermospheric dynamics. Our approach is therefore to use the output

from one particular ionosphere model, calculate the conductivity, and then fix it. Thus we neglect feedback to the conductivity from any changes in the dynamics and thermal structure of the thermosphere. Not only does this approach considerably improve the runtime of our numerical model over fully coupled models such as JIM, it also gives us confidence that the results of the model represent processes of purely thermospheric origin.

In the following we describe appropriate fixed conductivity models for Jupiter and Saturn in terms of the conductivities σ_P and σ_H expressed as a function of pressure. We will describe in Chapter 3 how these quantities are applied to our thermosphere model.

Jupiter

For Jupiter our model of the ionospheric conductivity is inextricably related to our model of the magnetosphere. In Section 2.1 we described the specification of the magnetospheric rotation velocity in regions C and D through the simultaneous solution of Eqns. 2.5, 2.7 and 2.11. In solving these equations we generate a latitudinal profile of height-integrated conductivity Σ_P as a function of the field-aligned current $j_{\parallel i}$, as described by Eqn. 2.11. We now expand on the precise form of this function:

$$\Sigma_P(j_{\parallel i}) = \Sigma_{P0} + \Sigma_{Pj}(j_{\parallel i}) \tag{2.63}$$

where the two components are, respectively, a 'background' conductivity due to solar-produced conductivity, and an auroral enhancement that depends on $j_{\parallel i}$.

The auroral enhancement is described using the same function as Nichols and Cowley (2004), in order to maximise our consistency with their model:

$$\begin{aligned} \Sigma_{Pj}(j_{\parallel i}) &= 0.16 j_{\parallel i} + \left\{ 2.45 \left[\frac{(j_{\parallel i}/0.075)^2}{1 + (j_{\parallel i}/0.075)^2} \right] \right. \\ &\times \left. \frac{1}{\left[1 + \exp(-(j_{\parallel i} - 0.22)/0.12)\right]} \right\} \end{aligned} \tag{2.64}$$

where Σ_P is in mho and $j_{\parallel i}$ is in $\mu\mathrm{Am}^{-2}$. This function is plotted in Fig. 2.5. Note that we use this function to specify the true conductivity, and explicitly calculate any neutral winds that may reduce the 'effective conductivity'. Nichols and Cowley assume $K = 0.5$ such that their $\Sigma_P^* = 0.5\Sigma_P$; this curve is plotted as a dashed line on Fig. 2.5.

For the background conductivity, Nichols and Cowley use a value of $\Sigma_{P0}^* = 0.0275$mho, consistent with the results of Hill (1980) mentioned above. For consistency with Nichols and Cowley we also adopt this value. However, we specify the true conductivity Σ_{P0}. Since we do not know in advance the factor of $(1 - K)$ required to convert between these two quantities, we assume that in the inner region of the magnetosphere to which this background conductivity applies $K \sim 0$ and set the background conductivity $\Sigma_{P0} = 0.0275$. We will see in Chapter 6 that this is not necessarily a good assumption.

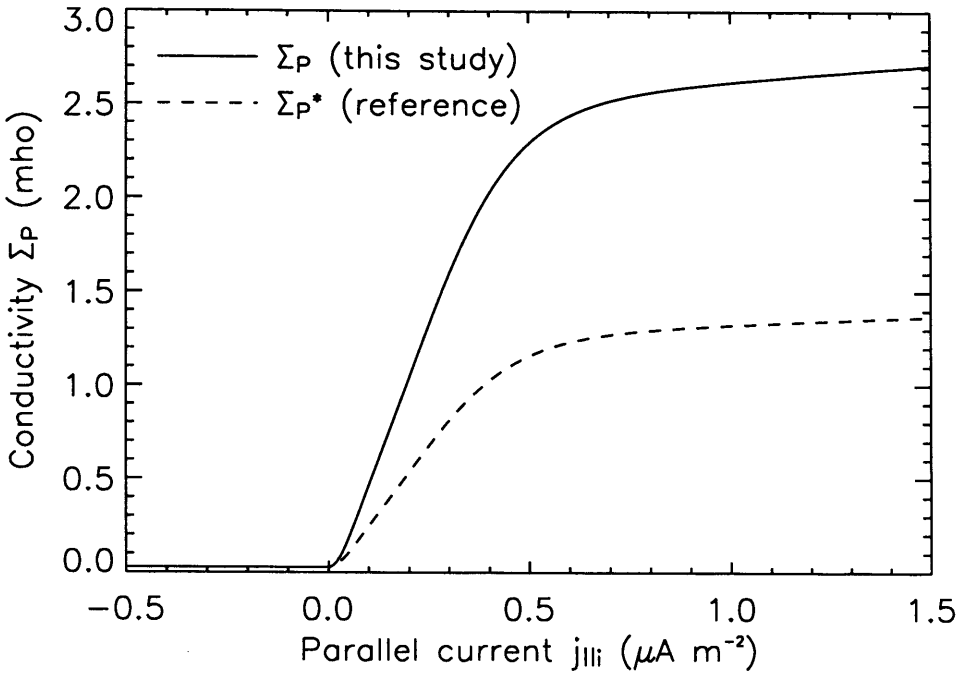

Figure 2.5: Relation between ionospheric parallel current and height-integrated conductivity. Solid line: true conductivity model used in this study; dashed line: effective conductivity model used by Nichols and Cowley (2004) for $\dot{M} = 1000$. Note that for negative values of the parallel current both models take a constant value of 0.0275 mho.

For regions A and B we expect the conductivity to be enhanced over the background level, since diffuse UV and IR emission is observed in these regions, indicating some level of particle precipitation. The observed emission is rather complex (e.g. Stallard et al., 2003), but for simplicity we assume a constant conductivity across this region. We follow Cowley et al. (2005) in setting the conductivity here to $\Sigma_P = 0.2$mho (although, again, we note that they specified $\Sigma_P^* = 0.2$mho). Note that at the boundary between regions A and B we expect a sheet of upwards field-aligned current, which, according to Eqn. 2.64 may enhance the conductivity (Cowley et al., 2005). For simplicity we neglect any such enhancement at this boundary; our major focus is understanding the influence of the neutral atmosphere on region C.

In addition to a model of the height-integrated conductivity as a function of latitude we also require its vertical distribution in order to couple the magnetosphere model to the thermospheric model described in Chapter 3. For this purpose we use the H_3^+ density profiles from the 'diffuse' auroral model of Grodent et al. (2001). Using the background neutral atmosphere from this model we calculate the quantities σ_P and σ_H as a function of pressure. We then scale these

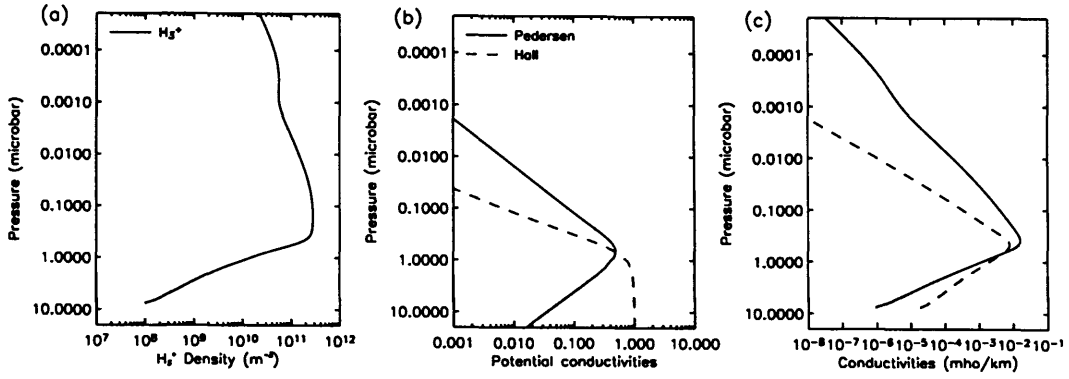

Figure 2.6: Parameters of the Jovian auroral conductivity model. The H_3^+ densities are taken directly from the 'diffuse' profiles of Grodent et al. (2001). Conductivities are calculated assuming a magnetic field strength of $2B_J$, where $B_J = 426400$nT. a) H_3^+ density from Grodent et al. (2001). b) Potential conductivities (solid line, Pedersen; dashed line, Hall). c) Conductivities (same line formats). The grey shaded area shows altitudes lying below the lower boundary of our Jovian thermosphere model.

profiles at each latitude to obtain the required value of Σ_P.

The parameters of this conductivity model are illustrated in Fig. 2.6. This shows the generation of the conductivity in terms of the ion density profile and the potential conductivity functions. We can see that the peak in the Pedersen conductivity is associated with both the peak of the ion density and the peak in the potential conductivity. The Pedersen and Hall conductivities are approximately equal at this altitude: above the peak Pedersen dominates; below it Hall dominates. However, because the ionisation cuts off very sharply on the bottomside, the total Hall conductivity is much smaller than the Pedersen.

Note that the H_3^+ densities shown in Fig. 2.6 are taken directly, unscaled, from the 'diffuse' profiles of Grodent et al. (2001). The potential conductivities have been calculated assuming a magnetic field strength of $2B_J$, where $B_J = 426400$nT. This is the field strength used throughout the Jovian model (see Appendix C). Thus the morphology of the conductivity profiles as a function of pressure is identical throughout the model to those shown here. It is only the absolute magnitude of the profile that is varied with latitude to provide the required values of Σ_P.

One difficulty of our approach is that at low latitudes our 'background' conductivity, which is supposed to represent conductivity due to solar-produced ionisation at mid latitudes, has the same profile as the enhanced conductivity in the auroral zones. This, of course, is incorrect. However, if our background conductivity was of a different vertical form to the enhanced conductivity, then both the magnitude and the form of the conductivity profile would vary with $j_{\|i}$.

If the form of the conductivity profile varied with $j_{\|i}$, then the integration of Eqn. 2.54 with which we calculate the height-integrated thermospheric velocity K would also depend on $j_{\|i}$. Consequently the integrated thermospheric velocity K would become a function of the parallel current. While one might envisage this producing some interesting effects, it seems an unnecessary complication for this initial study. Hence we tolerate some inaccuracy in the mid-latitude conductivity profile for the sake of simplicity.

Saturn

For Saturn we do not have the same restriction on the form of the conductivity profile, since our conductivity model is independent of the magnetosphere model. Thus we may use a full model of solar-produced conductivity.

To this end we use results from the ionosphere model of Moore et al. (2004). For this study, the model has been run specially in an equinox configuration, at solar maximum, using the neutral atmosphere of Moses et al. (2000) as a fixed global background (Luke Moore, private communication, 2005). The resultant ion densities are then used to calculate the conductivities σ_P and σ_H, using the Moses et al. (2000) neutral atmosphere, in the same manner as described above for Jupiter. Again, the procedure with which we apply these conductivities to a variable thermosphere is described in Chapter 3.

The resulting conductivity profiles for 70° latitude are plotted in Fig. 2.7. The densities of H^+ and H_3^+ are both approximately constant, close to $10^9 m^{-3}$, in the topside of the potential Pedersen conductivity between 10 and 0.1nbar. Below 10nbar they drop off rapidly due to charge exchange with hydrocarbons. This drop begins at almost exactly the altitude of the peak potential Pedersen conductivities. The consequence of this is that the Pedersen conductivity peaks strongly at this altitude, with a very flat bottomside and a slower drop off above the peak. In contrast, the potential Hall is only significant at very low altitudes where the ion densities are low, so the Hall conductivity is several times smaller than the Pedersen everywhere. It is possible that the sharp ionospheric layers observed at low altitudes by radio occultations (Fig. 1.7) may contribute significant Hall conductivity, but for the purposes of this study we neglect this component of the ionosphere, which is not well understood.

We also require a model of aurorally generated conductivity at Saturn. This may be associated either with the bright main oval or with the substantial H_3^+ emission observed across the entire region polewards of the main auroral oval (Stallard et al., 2004; Melin, 2006). At present there is no detailed precipitation model for the generation of H_3^+, and thus conductivity, in either of these regions. We are most interested in the conductivity across the whole of the polar cap, since this covers a greater area and is thus likely to have a greater influence on thermospheric dynamics.

The best possibility for calculating the possible ionisation due to such precipitation is to

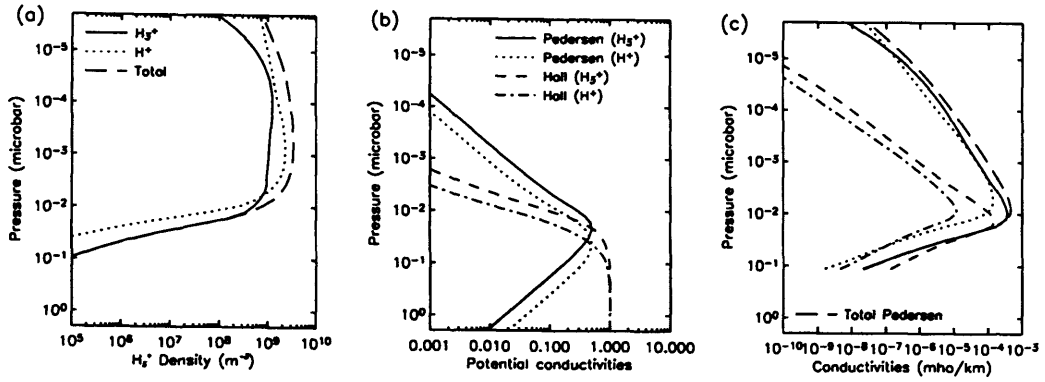

Figure 2.7: Parameters of the Kronian solar-produced conductivity model at 70° latitude. (a) Density profiles of H_3^+ (solid line), H^+ (dotted line) and total ion density (long dashed line) . (b) Potential conductivities: for line formats see legend. (c) Conductivities: line formats are the same as plot (b); the total Pedersen conductivity is also shown (long dashed line). The grey shaded area in each plot lies below the lower boundary of our Kronian thermosphere model.

scale the Jovian model of Grodent et al. (2001) to Kronian conditions. This model represents 'hard' precipitation that is energetic enough to penetrate below the homopause and generate substantial UV emissions. Little UV emission is observed inside the polar cap, such that any precipitation that does generate H_3^+ in this region must be 'soft' precipitation that does not penetrate substantially below the homopause. However, the H_3^+ densities in the Grodent et al. model are only substantial above the homopause, and are thus principally generated by the softer component of the incident electron energy spectrum. Thus it seems not unreasonable to use this model as a first approximation to a soft precipitation source at Saturn, even though a Saturn-specific model would be preferable.

Given that the bottomside of the Grodent et al. H_3^+ density profile is structured by the onset of hydrocarbon chemistry at the homopause, our scaling procedure from Jupiter to Saturn involves shifting the H_3^+ densities in pressure such that the form of the vertical profile is similar relative to the homopause at the two planets. We choose to judge this shift by eye such that the flat bottomside of the auroral H_3^+ is located at a similar pressure to that of the solar produced H_3^+ (Fig. 2.7). Specifically, we shift the H_3^+ to pressures at Saturn a factor of 30 smaller than those at Jupiter. Small variations about this chosen pressure shift do not significantly affect our results.

The resultant profiles of H_3^+, σ_P and σ_H are shown in Fig. 2.8 for a magnetic field strength of 60,000nT. The peak of the Pedersen conductivity lies at a slightly lower altitude than the peak in the solar produced conductivity. This is partly because the cut off below the ionisation peak is sharper in the auroral model; and partly because the H^+ peak in the solar produced conductivity

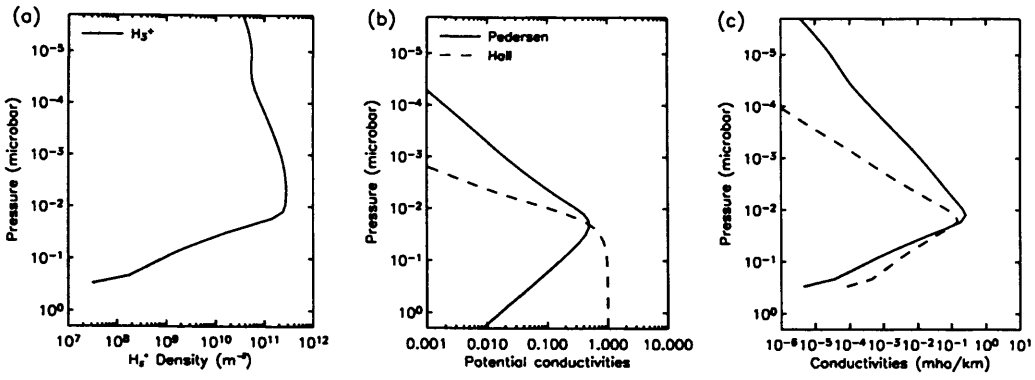

Figure 2.8: Parameters of the Kronian auroral conductivity model. a) H_3^+ density, derived from the Jovian model of Grodent et al. (2001). b) Potential conductivities (solid line, Pedersen; dashed line, Hall). c) Conductivities (same line formats). The grey shaded area shows altitudes lying below the lower boundary of our Kronian thermosphere model.

model, which lies slightly above the H_3^+ peak, shifts the peak conductivity to a slightly higher altitude. Note that when this conductivity model is applied to our thermospheric model, the exact profile of conductivity varies with the local magnetic field strength (see Chapter 3 for further details).

2.4.3 Limits of our approach

The derivation given above make several important assumptions. In particular, we neglect all collisions involving electrons. In the real atmosphere, electrons may collide with both neutrals and ions. Song et al. (2001) have calculated expressions for the Pedersen and Hall conductivities of the thermosphere-ionosphere taking into account all such interactions. However, their expressions reduce to our simple formulae (Eqns. 2.27 and 2.28) if the conditions

$$\begin{aligned} m_e\nu_{en}/m_i\nu_{in} &\ll 1 \\ \nu_{en}\nu_{in}/\Omega_i\Omega_e &\ll 1 \\ \nu_{ei}\nu_{in}/\Omega_i\Omega_e &\ll 1 \end{aligned} \tag{2.65}$$

are all satisfied.

In Fig. 2.9 we show the three quantities on the LHS of these conditions for the Jupiter and Saturn auroral models (see Figs. 2.6 and 2.8) by the solid, dashed and dot-dash lines respectively. For the electron-neutral collision frequencies we use (Geiss and Bürgi, 1986):

$$\nu_{en} = 2.6 \times 10^{-16} T^{0.62} n_n \tag{2.66}$$

for the electron-ion collision frequencies we use (Banks and Kockarts, 1973)

$$\nu_{ei} = 5.4 \times 10^{-5} T^{-1.5} n_i \tag{2.67}$$

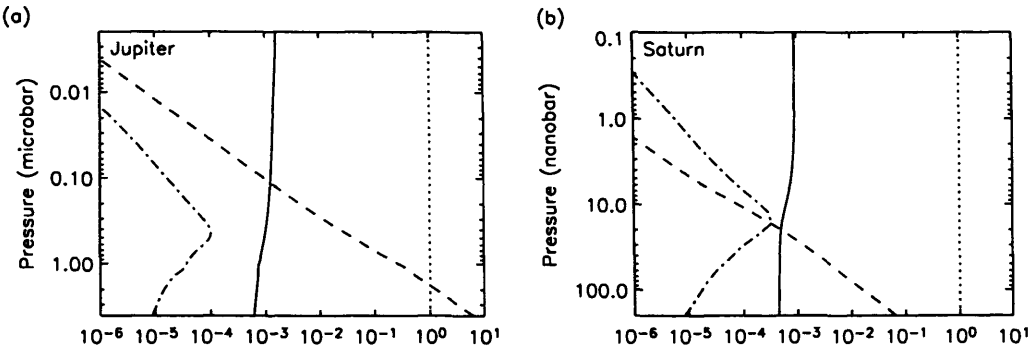

Figure 2.9: Conditions for neglecting electron collisions. (a) Jupiter. (b) Saturn. Electron collisions may be safely neglected (Song et al., 2001) provided that the quantities $m_e\nu_{en}/m_i\nu_{in}$ (solid line), $\nu_{en}\nu_{in}/\Omega_i\Omega_e$ (dashed line) and $\nu_{ei}\nu_{in}/\Omega_i\Omega_e$ (dot-dash line) are all $\ll 1$ (dotted line). The shaded regions lie below the lower boundaries of our thermosphere models.

and for the ion-neutral collision frequencies we use Eqn. 2.61. The H_3^+ densities have been scaled so that for Jupiter $\Sigma_P = 3$mho and for Saturn $\Sigma_P = 16$mho. These are the maximum values of Σ_P employed in the studies that follow, so the implied electron-ion collision frequencies are upper limits for all of the situations we consider.

The figure clearly shows that all three conditions are robust throughout the Jupiter and Saturn models, excepting the second condition, which is not satisifed at very low altitudes in our Jupiter model. However, this is not a problem if the electron densities at these altitudes are small, since any conductivity will be correspondingly unimportant. It is clear from Fig. 2.6 that this is the case.

It is also worth pointing out that any derivation involving 'collision frequencies' makes the assumption that they represent a valid parameterisation of the momentum transfer between different species. This assumption is essentially that the rate of momentum transfer between two species is linearly related to their relative velocities (as expressed in Eqn. 2.19). This, of course, is not necessarily the case. However, a detailed discussion is beyond the scope of the present work.

Finally, we note that even if the motion of ions is exactly described using the collision frequency parameterisation, it is still necessary for the collision frequencies to be known for these descriptions to have any useful purpose. The expressions for the collision frequencies that we have used in the discussion above are theoretical expressions that are in general use. As such we expect them to be correct to well within an order of magnitude, although errors of a few tens of percent would not be surprising. Given the many other pervasive uncertainties in our modelling, this does not seem a subject worth agonising over any longer.

2.5 Diffusion processes

We have already hinted in Chapter 1 at the importance of diffusion processes in the upper atmosphere. These processes may be associated with random motions on a molecular level or with small scale turbulence — eddies — in the bulk flow.

2.5.1 Molecular and eddy diffusion

Turbulent processes are parameterised using the eddy diffusion coefficient K_τ (units m^2/s). There is some ambiguity in the definition of K_τ, since it is intended to describe all 'small scale' processes that result in vertical mixing: the meaning of the term 'small scale' may vary depending upon the context. In a one-dimensional model that contains no vertical mixing by large scale wind systems, K_τ must parameterise *all* vertical mixing motions; in a more complex two- or three-dimensional model that incorporates large scale atmospheric motions self-consistently, K_τ must parameterise all motions that are too small for the model to resolve. This is a problematic area which we will not attempt to address in this study.

The eddy diffusion coefficient determines the altitude of the homopause — the boundary between the homosphere, below, in which eddy processes are dominant, and the heterosphere, above, in which molecular processes are dominant. The homopause is thus often defined as the point at which eddy diffusion and molecular diffusion are of equal magnitude. The problem with this definition is that this equality occurs at slightly different altitudes for different diffusive processes.

In the Jovian and Kronian context the term homopause is thus most often employed as shorthand for the *methane* homopause. We can define this as the altitude at which the eddy diffusion coefficient K_τ is equal to the diffusion coefficient for methane through molecular hydrogen. This serves as a useful operational definition, even though the precise meaning of K_τ remains rather unclear.

2.5.2 Thermal conduction

Molecular thermal conduction

The expression for the upwards heat flux F_m due to molecular diffusion is relatively simple

$$F_m = -\kappa_m \frac{\partial T}{\partial z} \tag{2.68}$$

where κ_m is the molecular conductivity, which may be expressed in the form

$$\kappa_m = \lambda T^s \tag{2.69}$$

where the parameters s and λ depend on the composition of the gas. The adopted values of these coefficients are discussed in Appendix A.

Eddy thermal conduction

The upwards heat flux F_τ due to bulk-flow turbulence (often referred to as the 'eddy conduction') is more complex (Brunt, 1929):

$$F_\tau = -\kappa_\tau \left(\frac{\partial T}{\partial z} + \Gamma \right) \tag{2.70}$$

where the eddy thermal conductivity is defined by:

$$\kappa_\tau = \rho c_p K_\tau \tag{2.71}$$

where ρ, c_p and K_τ are the mass density, specific heat capacity at constant pressure, and eddy coefficient respectively. Γ is the magnitude of the adiabatic lapse rate (Eqn. 1.8).

The factor of Γ in Eqn. 2.70 is introduced because the turbulent eddies that transport heat expand and contract adiabatically during their vertical motion. An eddy moving downwards will heat adiabatically, and an eddy moving upwards will cool. Thus, even if the temperature gradient is zero, there is a net transport of heat downwards.

Priestley and Swinbank (1947) give a critical discussion of Eqn. 2.70 in which they point out several problems with the simple theory from which it is derived. Firstly, they propose that there should be an additional term (which they call the 'buoyancy term') which stems from the observation that warm eddies are more likely to rise and cool eddies to sink than vice versa. This has the effect of adding a small upward heat flux, but is difficult to quantify.

Secondly, they point out that by itself Eqn. 2.70 is inconsistent with the Second Law of Thermodynamics, since if $-\Gamma < \partial T/\partial z < 0$ it allows heat to flow downwards from cold to hot. However, this apparent violation of basic physics is resolved if we include the energy input that drives the turbulent eddies. This energy input may be some dynamical process such as wind shears or breaking gravity waves. Ultimately this energy must be dissipated as heat, and Hunten (1974) argued that this dissipation will approximately balance the divergence of the heat flux F_τ, and it may thus be a good approximation to neglect the eddy conduction entirely. Prasad (1975) later suggested that this dissipation might even be greater than the divergence of F_τ, and that this might then explain the high temperatures of the Jovian thermosphere.

It is also interesting that in Hunten's subsequent paper on the energy balance of the Jovian thermosphere (Hunten and Dessler, 1977), he did not include the eddy flux in his calculations. Although he does not reference his 1974 paper on the subject, it is tempting to suspect that he had these considerations in mind when he chose to neglect the eddy flux. Indeed, this seems a sensible approach — we are faced with a process that has both a heating and a cooling effect, both of which are extremely difficult to quantify. We will thus adopt a compromise position in our modelling, whereby, when eddy conduction is included in our calculations, we include the term proportional to the temperature gradient but neglect the term in Γ. This ensures that our calculations do not violate the second law of thermodynamics, while encapsulating the likely enhancement of conductivity by eddy processes.

Alongside the foregoing discussion of eddy conduction it seems appropriate to discuss the possible contribution of breaking gravity waves[9] to the thermospheric energy balance. Without going into too much detail, the essential concept is that atmospheric gravity waves may propagate upwards into the thermosphere. In order to conserve energy, their amplitude must increase as the density decreases with altitude. Ultimately the atmosphere cannot sustain the necessary amplitudes and the waves break, dumping energy and momentum.

There has been much discussion of the contribution of this process to the energy balance of the Jovian thermosphere ever since wave-like structures were noticed in the Galileo probe temperature profile (Fig. 1.4; Seiff et al., 1998). It has since been debated (Young et al., 1997; Matcheva and Strobel, 1999; Hickey et al., 2000) whether dissipation of these waves might heat the thermosphere. Young et al. (1997) initially argued that they might provide the necessary energy; Matcheva and Strobel (1999) claimed that Young et al.'s calculations were incorrect, and that the energy was insufficient; Hickey et al. (2000) suggested that the waves might even *cool* the thermosphere.

The relation between this debate and the issue of eddy conduction is not immediately clear, except for the parallel uncertainty in whether the process provides net heating or cooling. However, since the eddies that cause the conduction are themselves, presumably, driven to some extent by breaking gravity waves, we can see that the two problems may in fact be the same side of the same coin. Indeed, neither question is likely to be satisfactorily resolved until there are more numerous measurements available of the small scale structure of the upper atmosphere.

Beyond these brief comments we will not enter into any further discussion of gravity waves, a detailed treatment of which is beyond the scope of this thesis.

Energy balance

We now illustrate some of the above discussion with some simple estimates of the temperature structure predicted by a balance between a heat source and thermal conduction. Initially, we follow a calculation first carried out by Hunten and Dessler (1977) in the Jovian context, but which, more recently, has been applied to the other giant planets by Yelle and Miller (2004)[10].

Firstly we assume that thermal energy is deposited in the thermosphere in a thin layer at pressure p_1, and transported downwards via thermal conduction to a pressure p_m, representing the mesopause, from where it is radiated away efficiently. It is then shown, combining Eqns. 1.2, 2.68 and 2.69 and integrating with respect to pressure p and temperature T, that the temperature profile in the range $p_1 < p < p_m$ is given in terms of the mesopause temperature T_m by:

$$T^s = T_m^s + \frac{skF}{\lambda\mu g} \ln\left(p_m/p\right) \tag{2.72}$$

[9] Also referred to variously as 'buoyancy waves' and 'inertia-gravity' waves.

[10] Yelle and Miller (2004) quote Eqn. 2.72 incorrectly; the form given here corrects their error.

At pressures $p < p_1$ the the temperature is constant with height. This equation provides some interesting insights into the generation of thermal structure. Note that no absolute pressure appears in the equation: only the pressure contrast between the absorption and radiation layers. Furthermore, since the logarithm of the pressure contrast is required, the dependence on this parameter is relatively weak. These two observations imply that even though the pressures of the absorption and radiation layers at Saturn and Jupiter are likely to differ considerably, this will not have a major influence on the thermal structure (provided thermal conduction dominates). Indeed, even though the column mass of Jupiter's thermosphere is much greater than that at Saturn, this difference in itself does not require a greater flux to generate a particular temperature structure, since a particular flux will require a similar temperature gradient regardless of the heat capacity of the atmosphere. Nevertheless, the time constant for thermal equilibriation will presumably be longer at Jupiter due to the greater mass of gas that must be heated to generate the required temperatures.

Of much greater importance to the thermal structure are the flux F and the gravity g. Increasing the flux unsurprisingly increases the temperatures. Increasing gravity has the opposite effect. This can be understood in terms of the smaller scale heights that prevail in a stronger gravity field, such that the atmosphere occupies a smaller vertical extent, making a diffusive process such as thermal conduction more efficient.

The distribution of temperature with height predicted by Eqn. 2.72 is shown by the solid line in Fig. 2.10 for parameters $T_m = 140\text{K}$, $\mu = 2\text{amu}$, $g = 10\text{ms}^{-2}$, $F = 1 \times 10^{-2}\text{mWm}^{-2}$, and values of λ and s appropriate for H_2 (see Appendix A). These parameters are round values of those appropriate for Saturn, the value of F being consistent with the total absorbed solar flux estimated by Yelle and Miller (2004). It can be seen that in the region where F is non-zero, between the absorption and radiation layers, the temperature gradient is approximately constant. The exospheric temperature of $\sim$170K is far below the observed value of $\sim$400K or greater. It is this discrepancy between the predicted and observed values that consitutes the 'energy crisis'. This clearly must be resolved either by invoking increased inputs of energy or reduced thermal conductivities. There seems no obvious process that might reduce the thermal conductivity: thus the focus is on supplementing the solar energy inputs.

Also shown in Fig. 2.10, for comparison, are profiles generated by numerically solving for the same parameters, but with the inclusion of eddy conduction. We show profiles for eddy coefficients of $K_\tau = 10^{3-5}\text{m}^2\text{s}^{-1}$. The dotted lines indicate the effect of including only the first term in the eddy conduction — i.e. the term proportional to the temperature gradient. Unsurprisingly, the effect of this is simply to decrease the temperature gradient, since with an enhanced conductivity, the gradient required to pass an equal flux is smaller. This effect is most prominent at the lowest altitudes, where the enhancement due to eddy conductivity is most important. At higher altitudes, just below the absorption layer, the gradient of the curve for the

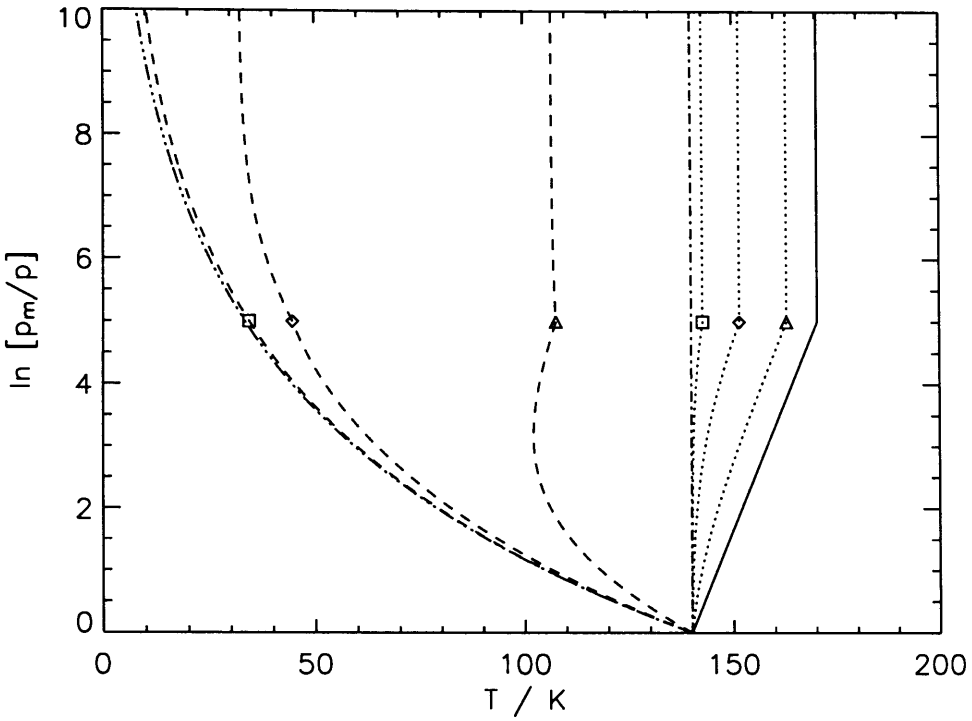

Figure 2.10: Temperature profiles predicted by simple energy balance considerations. Solid line: molecular conduction only. Dotted lines: molecular conduction and first eddy conduction term ($\kappa_\tau[\partial T/\partial z]$). Dashed lines: molecular conduction and both eddy conduction terms ($\kappa_\tau[\partial T/\partial z + \Gamma]$). Dot-dash line: $T = T_m$. Triple dot-dash line: $\partial T/\partial z = -\Gamma$. Triangle: $K_\tau = 10^3 \mathrm{m}^2\mathrm{s}^{-1}$. Diamond: $K_\tau = 10^4 \mathrm{m}^2\mathrm{s}^{-1}$. Square: $K_\tau = 10^5 \mathrm{m}^2\mathrm{s}^{-1}$.

lowest eddy coefficient (marked with the triangle) is almost identical to that for the molecular conductivity curve (solid line), indicating that molecular conduction dominates at this altitude.

The dashed lines show the effect of including the term in Γ which, we argued above, should be neglected in the majority of our modelling. The effect at low altitudes is to generate a temperature profile that decreases with altitude. This is a consequence of the downwards heat flux implied by the Γ term even in the absence of an appropriate temperature gradient. In order to balance this downwards heat flux, an inverted temperature profile must form so that a conventional upwards eddy flux along the temperature gradient may balance it out. The difference between these two large eddy fluxes is the absorbed flux F. This behaviour persists into the exosphere above the absorption layer, where temperature continues to drop with altitude. There is a kink at the absorption layer itself, representing the discontinuity in the flux required here.

The triple-dot-dash line on the left shows the limiting case in which the eddy conduction fluxes dominate. In this limit the temperature gradient must be equal to $-\Gamma$ to ensure thermal balance. The curve with the highest eddy coefficient is clearly almost in this limiting regime, and the absorbed flux has little influence on the temperature profile. This represents a situation in which the dominant thermospheric energy source is eddy mixing from lower regions of the atmosphere. It is possible that this term in the eddy conduction is important, but without including the dissipation of eddies that must occur for the term to be thermodynamically consistent, the behaviour shown is physically absurd. It is for this reason that we neglect this term from henceforth.

2.5.3 Viscosity

Viscosity results from the same molecular and eddy diffusion processes as thermal conduction. It describes the diffusive transport of bulk flow momentum and kinetic energy. It is described by a coefficient $\eta = \eta_m + \eta_\tau$, where η_m is due to molecular diffusion and η_τ due to eddies.

Molecular viscosity

The molecular viscosity takes a similar form to the molecular thermal conductivity:

$$\eta_m = \mu T^\beta \tag{2.73}$$

where μ and β depend on the composition of the gas. The adopted values of these coefficients are discussed in Appendix A.

Eddy viscosity

The eddy viscosity is given by:

$$\eta_\tau = \mathrm{Pr}\,\rho \mathrm{K}_\tau \tag{2.74}$$

where Pr is the turbulent Prandtl number, ρ is the mass density, and K_τ is the eddy coefficient.

The Prandtl number is an empirical parameter that describes the relative magnitudes of the heat and momentum fluxes due to eddies. Detailed simulations for the Earth's upper atmosphere (see e.g. Gavrilov and Yudin, 1992; Akmaev, 2001, and references therein) suggest a Prandtl number of between 2 and 3. For consistency with the JIM model (Achilleos et al., 1998) we choose $\mathrm{Pr} = 2$.

Viscous acceleration

The viscous stress τ acting on a plane in a fluid can be considered to represent either a force per unit area acting on the plane or a flux of momentum through the plane. If we consider a one-dimensional situation in which the velocity u is in a direction x and varies only in a perpendicular

direction z then the viscous stress acting in the x-direction on a plane perpendicular to z is

$$\tau = \eta \frac{\partial u}{\partial z} \tag{2.75}$$

If the velocity gradient does not vary in z then this stress will not result in a net acceleration, because an equal and opposite stress will be exerted on the opposite side of the plane. To find the actual viscous force we require the vertical derivative of this stress. We can understand this by considering a small layer of gas lying between altitudes z and $z + \delta z$. The difference between the viscous stresses acting on the lower and upper boundaries of this layer is:

$$\delta\tau = \frac{\partial \tau}{\partial z}\delta z \tag{2.76}$$

and this quantity is the net force per unit area that acts on the layer of gas. To find the viscous force per unit volume f_η in the x-direction, due to gradients in z, we simply divide by δz and take the limit to find:

$$f_\eta = \frac{\partial \tau}{\partial z} = \frac{\partial}{\partial z}\left(\eta \frac{\partial u}{\partial z}\right) \tag{2.77}$$

Transfer of momentum

In the conventional picture of magnetosphere-atmosphere coupling (Huang and Hill, 1989; Pontius, 1995), the angular momentum extracted from the thermosphere by ion drag is continually replaced by upwards viscous transfer from the lower atmosphere.

If we neglect meridional winds, we can express this transfer as a simple balance between the $\boldsymbol{j} \times \boldsymbol{B}$ force (Eqn. 2.32) and the viscous force (Eqn. 2.77):

$$\sigma_P B^2 (v_\phi - u_\phi) + \frac{\partial}{\partial z}\left(\eta \frac{\partial u_\phi}{\partial z}\right) = 0 \tag{2.78}$$

and it is clear that the behaviour is linear in the plasma velocity v_ϕ, such that we can express this force balance in terms of k_ϕ, which in the absence of meridional winds is equal to k:

$$\sigma_P B^2 (1 - k) + \frac{\partial}{\partial z}\left(\eta \frac{\partial k}{\partial z}\right) = 0 \tag{2.79}$$

Solving this equation given a distribution of σ_P and η with altitude provides a profile of k which may be integrated to provide the height-integrated slippage factor K (Eqn. 2.54).

Even without solving this equation it is clear that for a given atmospheric structure K should be independent of the plasma velocity v_ϕ. This is the origin of the description of slippage by Eqn. 2.56, in which K is a 'spring constant' that describes the neutral atmosphere's linear response to the plasma. One obvious deficiency with this theoretical framework is that the atmospheric structure will quite clearly vary across the planet, such that even if the slippage could be described accurately by such a simple 'Hooke's Law' approach, K would be different at different locations. Indeed, calculating K via this formulation for different latitudes using our solar produced conductivity model for Saturn gives values of ~ 0.8 at 45° colatitude and ~ 0.5

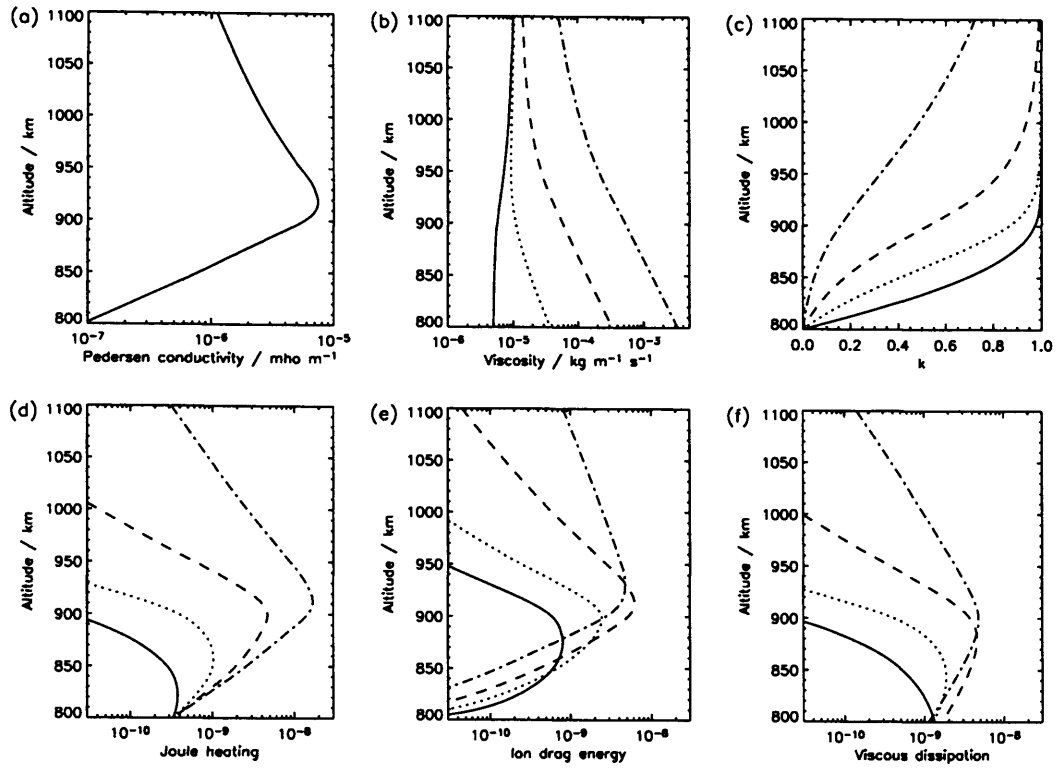

Figure 2.11: Transfer and dissipation of momentum and energy by viscosity. (a) Pedersen conductivity. (b) Viscosity, including molecular and eddy contributions. Dotted line: $K_\tau = 10^3 \mathrm{m}^2\mathrm{s}^{-1}$, dashed line: $K_\tau = 10^4 \mathrm{m}^2\mathrm{s}^{-1}$, dot-dash line: $K_\tau = 10^5 \mathrm{m}^2\mathrm{s}^{-1}$, solid line: eddy viscosity set to zero. (c) k parameter. We consider only zonal winds, so $k = k_\phi$. (d) Joule heating. (e) Ion drag energy. (f) Thermal energy input due to viscous dissipation of kinetic energy. The absolute values of the quantities in plots (d), (e) and (f) are dependent upon the plasma velocity v_ϕ, which, in the examples shown, is set to 1000 m s^{-1}.

polewards of 15° colatitude. One might expect further variations if the conductivity is enhanced in the auroral zones.

In Fig. 2.11a-c we show parameters for some solutions of Eqn. 2.79 using the Kronian auroral conductivity model outlined above. The conductivity has been scaled to generate a value of $\Sigma_P = 1\mathrm{mho}$. We show solutions for $K_\tau = 10^3 \mathrm{m}^2\mathrm{s}^{-1}$, (dotted lines), $K_\tau = 10^4 \mathrm{m}^2\mathrm{s}^{-1}$ (dashed lines), and $K_\tau = 10^5 \mathrm{m}^2\mathrm{s}^{-1}$ (dot-dash lines). The solid line shows the limiting case in which eddy viscosity is set to zero: in this case the only viscosity is due to molecular diffusion.

From Fig. 2.11b we may discern the relative importance of eddy and molecular viscosity at different altitudes. The molecular viscosity is negligible at low altitudes, but at higher altitudes is of the same order of magnitude as our standard eddy viscosity. Upon enhancing the eddy

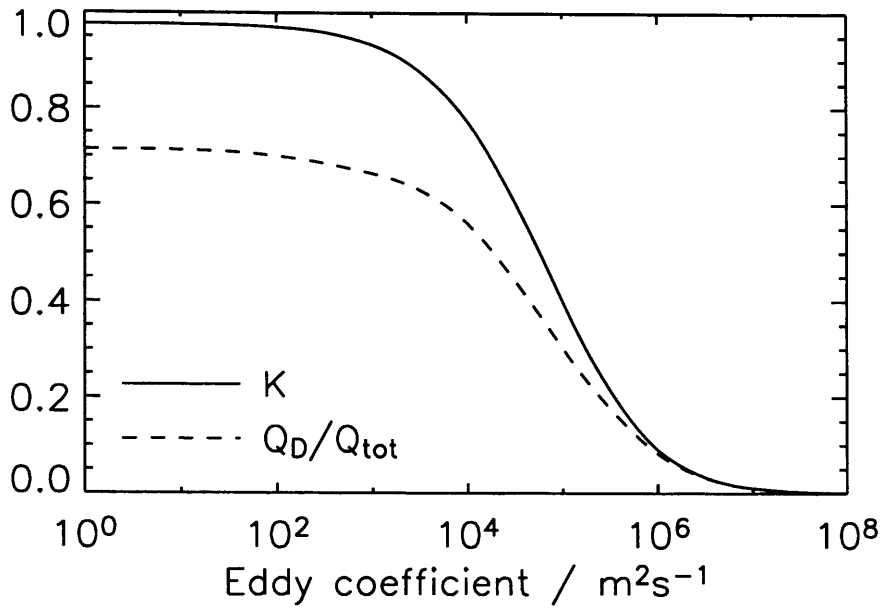

Figure 2.12: K as a function of eddy viscosity (solid line). The dashed line shows the quantity Q_D/Q_{tot}, which is equal to K in the 'thin sheet' approximation.

coefficient though, eddy viscosity becomes the dominant contribution throughout the conducting layer.

The 'slippage' profile of the thermosphere is shown in Fig. 2.11c. This is similar to Figs. 3 in Huang and Hill (1989) and Pontius (1995), and exhibits similar behaviour. In the low viscosity limit $k \sim 1$ throughout most of the conducting region. Below this region of almost total 'slippage' k decreases almost linearly to the lower boundary of the model. The enhanced runs, in contrast, are able to sustain lower k values. This is because the higher viscosity is able to transport the necessary angular momentum with a reduced vertical velocity gradient.

The solid line in Fig. 2.12 (the dashed line will be discussed later) shows the value of the height-integrated K-parameter as a function of the eddy viscosity. Again, this is equivalent to Figs. 4 in Huang and Hill (1989) and Pontius (1995), except that they plot the parameter $1 - K$, and we do not employ a log scale for the y axis. This shows, in correspondence with previous studies, that for a high eddy viscosity we move into a regime where the 'slippage' tends towards zero. At low eddy viscosity we observe a slightly different behaviour, since we include molecular viscosity: K saturates at a maximum value of ~ 0.98. Although it is interesting that eddy viscosity is not strictly necessary to maintain partial corotation of the conducting layer, this limit is in practice never likely to occur, since the eddy coefficients required to reach it are

much lower than those observed.

Joule heating and ion drag

Given these calculated profiles of k we may go on to also calculate the vertical distribution of Joule heating and ion drag energy using Eqns. 2.48. These distributions are shown, for $v_\phi = 1000\text{m s}^{-1}$, in Figs. 2.11d and 2.11e respectively. Looking first at the Joule heating, we can see that in the low viscosity limit it is confined to regions below the conductivity peak. This is a natural consequence of its dependence upon the factor $(1-k)^2$, which becomes very small when k approaches unity. Increasing the viscosity correspondingly decreases k and the Joule heating both increases and moves to higher altitudes as a result of this behaviour.

The ion drag exhibits a similar structure, but peaks at a higher altitude than the Joule heating. In the highest viscosity example shown, the peak ion drag energy has begun to drop with increasing viscosity. This is because the ion drag depends on the factor $k(1-k)$ which goes to zero as k goes to either zero or unity. Thus, as the eddy viscosity begins to reduce k below 0.5 over a substantial proportion of the thermosphere, the ion drag begins to becomes less important.

Using this simple model, we are also able to test the accuracy of calculating the height-integrated Joule heating (Q_J) and ion drag (Q_D) using the height-integrated slippage parameter K (see e.g. Eqn. 2.60). In the approximation in which the thermosphere-ionosphere is treated as a thin sheet, the Joule heating goes as $(1-K)^2$ and the ion drag as $K(1-K)$. The total energy input Q_{tot} always goes as $(1-K)$: thus the proportion of the total energy input consisting of ion drag is proportional to K in the thin sheet approximation.

The solid line in Fig. 2.12 that we have already described thus represents this proportion. The dashed line represents the *actual* proportion of the energy input consisting of ion drag, as calculated from the profiles in Fig. 2.11. This demonstrates that in the high viscosity limit, both the thin sheet and full models correctly calculate that the energy input will consist almost entirely of Joule heating. However, in the low viscosity limit we tend towards a situation in which the thin sheet approximation predicts almost zero Joule heating ($\sim 2\%$), whereas the full model predicts a relatively very high proportion of Joule heating ($\sim 30\%$).

This is because the thin sheet model supposes that when $K \sim 1$ we also have $k \sim 1$ across the whole conducting region, and in this regime the ion drag will always dominate over the Joule heating. However, in the full model, k takes a variety of values across the conducting region either side of K and the influence of the smaller values of k, for which ion drag is less dominant, increases the Joule heating.

This observation means that while magnetospheric studies may make statements about the *total* energy input in terms of the height-integrated parameter K, they are unable to infer directly the division of this energy input into Joule heating and ion drag energy.

Viscous heating

The viscous force described above has the effect of redistributing both momentum and kinetic energy. While momentum must always be conserved by this process, and this acts as an inviolable constraint, the kinetic energy does not have to be conserved, because some of it may be converted into thermal energy to ensure overall conservation of energy. Thus, in general, viscosity has the effect of both redistributing kinetic energy and converting some of it into thermal energy.

We can gain some understanding of this conversion process by calculating the work done by viscosity in two different ways. Considering again the one-dimensional situation described above, we may consider the simple work done by the viscous force to accelerate the gas in the x-direction q_η:

$$q_\eta(\text{K.E.}) = u\frac{\partial \tau}{\partial z} \tag{2.80}$$

This represents the change in the kinetic energy. However, it tells us only about the local energy change. It does not tell us anything about whether the viscous redistribution of momentum conserves energy in a global sense.

To determine the total energy change, we calculate the work done on the layer between z and $z + \delta z$. This is the difference between the work done on the upper boundary

$$\left(u + \delta z\frac{\partial u}{\partial z}\right)\left(\tau + \delta z\frac{\partial \tau}{\partial z}\right) \tag{2.81}$$

and the work done on the lower boundary $u\tau$, which, to highest order, and dividing by δz, is clearly

$$q_\eta(\text{total}) = u\frac{\partial \tau}{\partial z} + \tau\frac{\partial u}{\partial z} = \frac{\partial (u\tau)}{\partial z} \tag{2.82}$$

This is the total energy change due to viscosity. Compared to the kinetic energy change alone (Eqn. 2.80) it contains the extra term

$$q_\eta(\text{dissipation}) = \tau\frac{\partial u}{\partial z} = \eta\left(\frac{\partial u}{\partial z}\right)^2 \tag{2.83}$$

representing the viscous heating. Note that it is positive definite, as we expect from a frictional heating term.

Dissipation of ion drag

The usefulness of these considerations lies in calculating the heating due to the dissipation of ion drag energy. The viscous heating calculated using the 'slippage' profiles described above is shown in Fig. 2.11f. Since the only input of kinetic energy into this simple model is the ion drag energy, all of the viscous heating must represent dissipation of this energy.

The profiles of viscous dissipation shown here all peak considerably below the peak in the ion drag energy, and slightly below the peak in the Joule heating. This is consistent with the kinetic energy being 'conducted' downwards by viscosity, while simultaneously undergoing

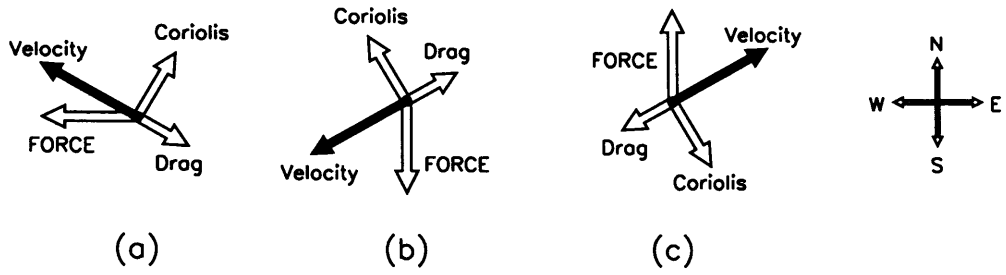

Figure 2.13: Three possible force balances in the thermosphere.

dissipation. The dissipation is seen to be a necessary consequence of the velocity structure, since the momentum which is flowing down under the action of viscosity must 'shed' kinetic energy in order to enter the low velocity region at the base of the model. In order for the momentum to pass through the zero velocity lower boundary condition it must shed all of its associated kinetic energy, and thus all of the ion drag energy is dissipated as heat in the regime shown.

The consequence of this dissipation occurring at altitudes below both the Joule heating input layer and the ion drag energy input layer is that its influence on temperatures will be considerably reduced compared to the Joule heating and to a situation in which it might be dissipated at altitudes coincident with or above the ion drag energy input layer. Thus it seems unlikely, given these considerations, that the ion drag energy by itself makes an important contribution to the thermal energy balance — certainly it seems extremely unlikely that it is the solution to the 'energy crisis', as suggested by Miller et al. (2000) and Smith et al. (2005). However, we will see in Chapter 5 that the dissipation of ion drag may be a more complicated and important process than these simple considerations suggest.

2.6 Importance of Coriolis force

While the above discussion of balance between injection of momentum from the magnetosphere and extraction of momentum by viscous drag is useful, it omits the influence of the planetary rotation on the thermosphere's dynamical response. It is useful to briefly outline this behaviour as an aid to discussion in Chapters 4, 5 and 6.

Planetary rotation leads to two 'fictitious' inertial forces in the atmosphere. The centrifugal force represents the tendency of the atmosphere to move away from the rotation axis. This can be represented simply as a reduction in the acceleration due to gravity. The Coriolis force represents the tendency of wind systems to rotate in the opposite sense to the planetary rotation (see Chapter 3 and Appendix D).

In the terrestrial lower atmosphere, where viscosity is negligible, the Coriolis force tends to combine with pressure gradients such that wind systems flow almost along isobars (lines of constant pressure). In the upper atmosphere, viscous drag becomes important, and can be almost as important as Coriolis in the force balance.

Three examples of such force balances are shown in Fig. 2.13. Fig. 2.13a shows the effect of a westwards pointing force in the northern hemisphere (this might correspond to ion drag associated with sub-corotation in the magnetosphere). The effect of Coriolis combined with drag is to produce not only a westwards velocity but also a polewards flow.

Figs. 2.13b and c show the effect of north-south aligned forces in the northern hemisphere. The southwards pointing force might, for example, be an equatorwards pressure gradient generated by Joule heating in the polar regions. This also results in a westwards flow, but in this case the meridional component is towards the equator. The northwards pointing force might correspond to a polewards pressure gradient driven by solar heating in the equatorial regions. The flow that results is expected to be eastwards — i.e. super-corotational. We will see in Chapters 5 and 6 that this behaviour has some interesting consequences.

Chapter 3

The Model

We now describe our thermospheric model, which forms the core of this study. The model is derived from a model of the terrestrial thermosphere developed over 20 years ago (Fuller-Rowell, 1981). This model has evolved considerably in the interim, principally through coupling to models of the terrestrial ionosphere (CTIM; Fuller-Rowell et al., 1996) and the terrestrial ionosphere-plasmasphere (CTIP; Millward et al., 1996).

The first application of the model to gas giants was by Achilleos et al. (1998) who converted both the thermospheric and ionospheric components of the CTIM model (Fuller-Rowell et al., 1996) to Jupiter to generate the Jovian ionosphere model (JIM). A number of studies have since been carried out using JIM, including investigations of the response of the neutral atmosphere to magnetospheric drag and particle precipitation (Achilleos et al., 2001; Millward et al., 2002, 2005), and a study of the aeronomy of giant exoplanets (Williams, 2004). A major problem with JIM is its complexity, which restricts its practical runtime to a few Jupiter rotations. It has thus not been run to full thermal equilibrium, and probably not to full dynamical equilibrium, although Millward et al. (2005) showed that at the conductivity peak dynamical equilibrium was reached in approximately one hour.

The thermospheric component of CTIM/CTIP was later modified independently by Müller-Wodarg et al. (2000) to generate a model of Titan's thermosphere. This Titan model has been further developed by Moffat (2005) to simulate the thermosphere of Mars, and by Müller-Wodarg et al. (2006) to simulate the thermosphere of Saturn. This newly developed Saturn model is also easily converted to model the other gas giants, and it is this model that we use throughout this study.

3.1 Model structure

The model calculates the time-evolution of the thermosphere by solving the equations of energy, momentum and continuity on a three-dimensional grid. The numerical integration is achieved

with a forward Euler time-stepping scheme. This is a relatively simple method, but has been used successfully in the terrestrial version of the model for many years. Improvements to the terrestrial model incorporating more sophisticated and accurate time-stepping schemes are currently in progress, and these should ultimately be included in the gas giant models.

Horizontally, the grid consists of points equally spaced in colatitude (x), measured from the north pole, and west longitude (y). This (x,y) coordinate system is thus exactly equivalent to the spherical polar coordinates (θ,ϕ). Vertically, the grid points are located at fixed pressures (p), rather than at fixed altitudes (z). Since we calculate the values of physical quantities at fixed points in our coordinate system, the model is referred to as Eulerian, as opposed to a Lagrangian system in which the calculated quantities would explicitly move with the flow of gas.

For both Jupiter and Saturn, the lower boundary condition of the model is a surface of fixed pressure at fixed altitude, with a constant temperature and zero neutral wind velocity. This boundary condition is intended to correspond to the mesopause. At the mesopause temperatures are expected to be regulated by hydrocarbon radiative cooling, such that a constant temperature is a good approximation. It is also expected that the large eddy viscosity in this region will ensure relatively low wind speeds.

For Jupiter we choose a lower boundary pressure of 0.2Pa, consistent with the JIM model (Achilleos et al., 1998). We fix the temperature here to be 260K, which is the temperature at 0.2Pa in the Grodent et al. (2001) diffuse auroral precipitation model. We choose this value because we are mostly concerned with the dynamics and structure of the polar cap: the Grodent et al. model is the best available one-dimensional model of the thermal structure of this region.

For Saturn we follow Müller-Wodarg et al. (2006), choosing lower boundary pressures and temperatures of 0.01Pa and 143K respectively. These values are consistent with the position of the mesopause in the model of Moses et al. (2000). We note that recent observations reported by Gustin et al. (2005) have suggested that temperatures at 0.02Pa in the auroral zones may be closer to $\sim$ 400K, signficantly higher than those in the Moses et al. model, which was derived from low latitude observations. However, it is not yet clear whether these new temperatures are relevant in regions outside the rather narrow auroral zones. For this reason we retain the cool lower boundary condition of 143K globally.

For both planets the sensitivity of the behaviour to the lower boundary temperature is relatively small, global temperatures scaling roughly linearly with variation of the order of several tens of Kelvin about the values quoted.

3.2 Pressure coordinates

The system of pressure coordinates already mentioned is adopted because of the dominance of hydrostatic equilibrium in the atmosphere. We make the assumption that deviations from

hydrostatic equilibrium — in other words strong vertical winds — do not occur, and we may treat vertical winds as small perturbations from equilibrium. This assumption is termed quasi hydrostatic equilibrium.

In the model the vertical resolution is specified in terms of pressure scale heights. Thus, if the pressure at the base of the model — the mesopause — is given by p_m, and we label surfaces of constant pressure n = 1, 2, 3 .... etc., we specify the pressure $p(n)$ of each level using the following formula:

$$p(n) = p_m \exp\left(-\gamma(n-1)\right) \tag{3.1}$$

where γ is a dimensionless number that represents the spacing between pressure levels in units of local pressure scale height. The altitude of the lowest level is then kept fixed (in the terrestrial and Martian models this altitude is varied to include the influence of tides on the thermosphere) and the altitude of each level explicitly calculated by integrating Eqn. 1.2 with respect to pressure.

The introduction of pressure coordinates presents a further problem, in that the altitude of a pressure level is generally a function of latitude and longitude, since different thermal structures prevail in different regions of the thermosphere. We thus make the assumption that the pressure levels are only very slightly tilted with respect to the horizontal, such that the pressure coordinate system (x, y, p) can be considered approximately orthogonal.

We will now summarise some of the basic results that are necessary for the use of pressure coordinates (Fuller-Rowell, 1981). Some of these results are treated in more detail in Appendix E. We first introduce the gravitational potential Φ defined as:

$$d\Phi = g dz \tag{3.2}$$

and it is easily shown that the equation of hydrostatic equilibrium (Eqn. 1.2) can be rewritten:

$$\frac{d\Phi}{dp} = -\frac{1}{\rho} \tag{3.3}$$

It can then be shown that the partial derivative $(\partial a/\partial x)_z$ of some scalar a with respect to x keeping z fixed may be expressed as:

$$\left.\frac{\partial a}{\partial x}\right|_z = \left.\frac{\partial a}{\partial x}\right|_p + \rho \left.\frac{\partial a}{\partial p}\frac{\partial \Phi}{\partial x}\right|_p \tag{3.4}$$

Physically, the left hand side of this equation is the horizontal spatial derivative of a. The right hand side represents splitting this derivative into two components: the first a component moving along the slightly tilted surface of constant pressure; the second a vertical component to compensate for the change in altitude. Similar expressions may be derived for partial derivatives with respect to y and t. These relations lead to two different definitions of the horizontal component of the Laplacian: ∇_z, the Laplacian calculated along surfaces of fixed altitude, and ∇_p, the Laplacian calculated along surfaces of fixed pressure (see Appendix E for further details).

These results can then be used to transform between the absolute vertical wind in the fixed altitude frame $u_z = dz/dt$ and the vertical wind relative to the pressure surface w, which we define as:

$$w = \frac{dp}{dt} \tag{3.5}$$

The required relationship, derived in Appendix E, is:

$$u_z = \left.\frac{\partial z}{\partial t}\right|_p + \boldsymbol{u} \cdot \boldsymbol{\nabla}_p z - \frac{w}{\rho g} \tag{3.6}$$

The first term represents the vertical wind due to vertical motion of the pressure level relative to a point fixed in space. The second term represents the vertical component of the winds that blow, at constant pressure, along the slightly tilted pressure surfaces. The third term represents winds that blow vertically *relative* to the fixed pressure surfaces.

3.3 The continuity equation

The continuity equation is the simplest of the equations that govern the behaviour of the atmosphere, since it is not necessary for us to include any sources or sinks of mass in our formulation. In a coordinate system fixed in space it is given by:

$$\frac{\partial \rho}{\partial t} + \boldsymbol{\nabla} \cdot (\rho \boldsymbol{u}) = 0 \tag{3.7}$$

This expresses the notion that in the absence of sources and sinks of mass the local density change must be caused entirely by divergence or convergence of the local mass flux. One great advantage of pressure coordinates is that this equation becomes much simplified (a full derivation may be found in Appendix E):

$$\boldsymbol{\nabla}_p \cdot \boldsymbol{u} + \frac{\partial w}{\partial p} = 0 \tag{3.8}$$

This now expresses the very simple notion that the horizontal divergence of the winds $\boldsymbol{u}$ that blow along the levels of constant pressure (the isobaric winds) must be balanced by a divergence of the vertical wind w that blows relative to the pressure levels. The partial derivative $\partial\rho/\partial t$ has been eliminated entirely. This is because, in a constant gravity field, the column mass between two pressure levels is fixed. Using pressure coordinates automatically takes this into account.

Note that if the gravity g varies with altitude z then this formulation does not apply exactly. In a constant gravity field, an expansion or contraction of a fixed column mass of gas will not change the weight of that gas, and thus will not change the pressure at the base of the column. Thus a pressure level is equivalently defined by the column mass of the gas that lies above it. This is why the column mass between two pressure levels is fixed.

However, in a gravity field that falls off with altitude, the expansion of a fixed column mass of gas will push some of that mass into regions of lower gravity. This reduces the total weight of the gas, and thus the pressure at the base of the column will fall. This effect is not currently taken

into account in the model: although it is small, it may be important in some circumstances. Thus, to maximise the self-consistency of our model, we will assume that gravity is constant throughout our region of interest. Given that the thickness of the thermosphere is typically a few 1000km or less, compared to planetary radii of several times 10,000km, it is clear that the errors introduced by this assumption are only of the order of 10% or less.

The continuity equation also provides us with our method of calculating the vertical wind w. As described below, the momentum equation only contains horizontal terms in x and y. We do not explicitly calculate vertical forces, since hydrostatic equilibrium is assumed to be prevalent. Thus we have no explicit method of calculating w. However, Eqn. 3.8 relates the vertical derivative of w to the divergence of the horizontal winds. Thus, given the horizontal winds $\boldsymbol{u}$ and a boundary condition for w we may integrate this equation to obtain w globally. This boundary condition is that $w = 0$ at the upper level of the model. Since w represents the wind that blows vertically *relative* to the fixed pressure surfaces, this boundary condition is equivalent to the assumption that there is no outflow of mass from the top of the model. This means that there *is* outflow and inflow through the base of the model, in order to preserve continuity.

In reality, there is likely to be a small outflow of escaping gas from the top of the thermosphere. Some gas molecules at high altitude will acquire a random thermal velocity greater than the escape velocity and exit the atmosphere ballistically (Banks and Kockarts, 1973). The escape velocity is approximately 35km/s at Saturn and 50km/s at Jupiter, compared to a characteristic thermal velocity of about 5km/s for atomic hydrogen at 1000K. Clearly the escape velocities are considerably greater than the characteristic thermal velocities that are likely to be prevalent in the thermosphere, and without entering into detailed discussion of escape processes it seems likely that outflow of this type is negligible.

Our assumption of zero escape will certainly have a small effect on the vertical winds in the upper regions of the model. However, any such effects will not propagate significantly to the low altitude regions, since the mass density is orders of magnitude larger in these regions. A small vertical mass flux at the top of the model, associated with a strong vertical wind, translates into an identical mass flux at the bottom of the model associated with an almost negligible vertical wind. For the same reason, it is generally the case that even though the integration that yields w at an altitude covers the entire region above the level in question, it is only the behaviour in the few scale heights above a particular pressure level that contributes significantly to the vertical wind w at that point.

3.4 The horizontal momentum equation

The horizontal momentum equation is Newton's second law applied to a gas

$$\frac{d\boldsymbol{u}}{dt} = \frac{1}{\rho}\boldsymbol{f} = \boldsymbol{a} \tag{3.9}$$

where $\boldsymbol{u}$ is the horizontal vector velocity, ρ is the mass density, and $\boldsymbol{f}$ and $\boldsymbol{a}$ are the force per unit volume and force per unit mass respectively. However, we must express $\boldsymbol{u}$ in terms of its component unit vectors which are a function of the coordinates:

$$\boldsymbol{a} = \frac{d\boldsymbol{u}}{dt} = \frac{d(u_i \boldsymbol{e}_i)}{dt} = \frac{du_i}{dt}\boldsymbol{e}_i + u_i \frac{d\boldsymbol{e}_i}{dt} \tag{3.10}$$

where u_i are the scalar components of $\boldsymbol{u}$ and $\boldsymbol{e}_i$ are the corresponding unit vectors. Note that we are implicitly summing over i. This must be further complicated by writing the total derivatives d/dt as a combination of partial derivatives — the so called 'advective' derivative:

$$\frac{d}{dt} = \frac{\partial}{\partial t} + u_k \frac{\partial}{\partial x_k} \tag{3.11}$$

where here we are implicitly summing over k. Substituting Eq. 3.11 into Eq. 3.10:

$$\boldsymbol{a} = \left[\frac{\partial u_i}{\partial t} + u_k \frac{\partial u_i}{\partial x_k}\right]\boldsymbol{e}_i + u_i \left[\frac{\partial \boldsymbol{e}_i}{\partial t} + u_k \frac{\partial \boldsymbol{e}_i}{\partial x_k}\right] \tag{3.12}$$

which, noting that $\partial \boldsymbol{e}_i/\partial t = 0$ (because the unit vectors of the coordinate system have no inherent time variation), reduces to, with some rearrangement:

$$\frac{\partial u_i}{\partial t}\boldsymbol{e}_i = \boldsymbol{a} - u_k \frac{\partial u_i}{\partial x_k}\boldsymbol{e}_i - u_i u_k \frac{\partial \boldsymbol{e}_i}{\partial x_k} \tag{3.13}$$

The LHS is the vector sum of the partial derivatives of each component of the velocity with respect to time. This is the quantity that the model needs in order to calculate the change in vector velocity at a point *fixed in space*. The first term on the RHS represents the actual forces acting on the gas. The second term represents advection of the velocity, and the third term advection of the coordinate system. These terms represent the notion that gas arriving at a point 'brings with it' a memory of its velocity at its previous position. The first of these terms is the part of this difference due to variations in the actual velocity with position; the second is due to variations in the orientation of the coordinate system.

We now treat each of these three components in turn.

3.4.1 Forces acting on the gas

The horizontal forces we consider are pressure gradients, horizontal and vertical viscosity, and ion drag:

$$\boldsymbol{a} = \boldsymbol{a}_P + \boldsymbol{a}_\eta + \boldsymbol{a}_D \tag{3.14}$$

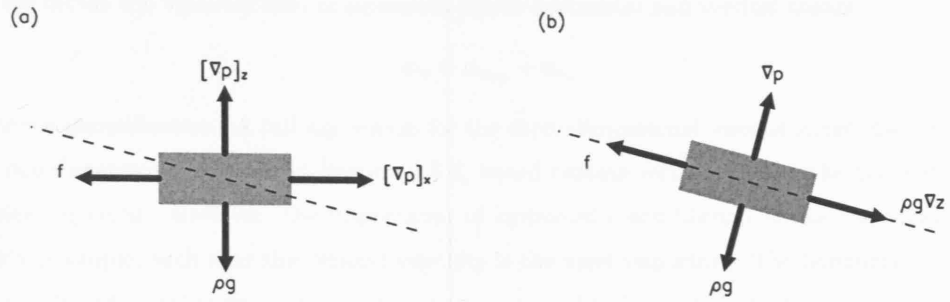

Figure 3.1: Schematic of forces acting on a tilted pressure level. The dashed line represents a pressure level (surface of constant pressure).

Pressure gradient a_P

The acceleration due to the horizontal pressure gradient is

$$\boldsymbol{a}_P = -\frac{1}{\rho}\nabla_z p \tag{3.15}$$

This is defined with respect to the fixed altitude coordinate system. We must re-express it in our fixed pressure coordinate system. To convert between coordinate systems we use Eqn. E.10 (derived in Appendix E):

$$\nabla_z p = \nabla_p p + \rho\frac{\partial p}{\partial p}\nabla_p\Phi = \rho\nabla_p\Phi = \rho g\nabla_p z \tag{3.16}$$

and we see that in this coordinate system the pressure gradient reduces to the gradient of the gravitational potential along the fixed pressure surface. Thus, while we refer to this force as a pressure gradient, it could equivalently be considered to be the component of the gravitational acceleration that acts along the slightly tilted pressure surfaces.

These two possible interpretations are illustrated schematically in Fig. 3.1. Hydrostatic equilibrium does not hold exactly, due to the presence of non-hydrostatic forces f. We can either balance out the vertical components of pressure and gravity such that f is balanced by the horizontal component of the pressure gradient; or we can balance the total pressure gradient with the parallel component of gravity, such that f is balanced by the component of gravity that points along the constant pressure surface. Of course, this approximation only works if the small angle approximation is valid, in which case the angle of tilt is given, in radians, by $\nabla_p z$.

Viscosity a_η

We have already described in Section 2.5.3 the equations for viscous transfer and dissipation of energy and momentum. In order to apply these equations to the model we need to transform them into the pressure coordinate system detailed above.

We divide the viscosity into components due to horizontal and vertical shears

$$\boldsymbol{a}_\eta = \boldsymbol{a}_{\eta_{xy}} + \boldsymbol{a}_{\eta_z} \tag{3.17}$$

This is a simplification. A full expression for the three-dimensional viscous stress, distinct from the one-dimensional analysis in Section 2.5.3, would contain terms coupling the horizontal and vertical motions. However, the importance of hydrostatic equilibrium makes the atmosphere highly isotropic, such that the vertical viscosity is the most important. The horizontal viscosity is a small additional term, and cross-terms are expected to be unimportant.

Because the viscosity is a diffusive process, its effectiveness depends strongly on the mean free path, and thus on the pressure. However, it also follows that along a fixed pressure level it does not vary strongly with position, and thus can be considered approximately constant, at least locally. Thus we can approximate the horizontal viscosity as a simple diffusion equation:

$$\boldsymbol{a}_{\eta_{xy}} = \frac{\eta}{\rho}\nabla_p^2 \boldsymbol{u} \tag{3.18}$$

The vertical viscous force is slightly more complex because the viscosity varies strongly with altitude. However, we need only take Eqn. 2.77 and convert to pressure coordinates, using Eqn. E.5 to transform the partial derivatives:

$$\begin{aligned} \boldsymbol{a}_{\eta_z} &= \frac{1}{\rho}\frac{\partial}{\partial z}\left(\eta\frac{\partial \boldsymbol{u}}{\partial z}\right) \\ &= \frac{1}{\rho}\left(-\rho g\frac{\partial}{\partial p}\right)\left(\eta\left(-\rho g\frac{\partial \boldsymbol{u}}{\partial p}\right)\right) \\ &= g^2\frac{\partial}{\partial p}\left(\eta\rho\frac{\partial \boldsymbol{u}}{\partial p}\right) \end{aligned} \tag{3.19}$$

and this is the expression used in the model.

Ion drag $\boldsymbol{a}_D$

The force $\boldsymbol{j} \times \boldsymbol{B}$ exerted by ion-neutral collisions is calculated according to the formulation laid out in Chapter 2. The force per unit mass $\boldsymbol{a}_D$ is, of course

$$\boldsymbol{a}_D = \frac{1}{\rho}\boldsymbol{j} \times \boldsymbol{B} \tag{3.20}$$

This term is only included in the experiments described in Chapters 5 and 6.

3.4.2 Advection

The second term in Eqn 3.13 is the so-called advection term. In the pressure coordinate frame (x,y,p), the advective part of the total derivative is expressed

$$u_k\frac{\partial}{\partial x_k} = \boldsymbol{u}\cdot\nabla_p + w\frac{\partial}{\partial p} \tag{3.21}$$

such that the relevant term in the momentum equation is written

$$-u_k\frac{\partial u_i}{\partial x_k}\boldsymbol{e}_i = -\boldsymbol{e}_\theta(\boldsymbol{u}\cdot\nabla_p u_\theta + w\frac{\partial u_\theta}{\partial p}) - \boldsymbol{e}_\phi(\boldsymbol{u}\cdot\nabla_p u_\phi + w\frac{\partial u_\phi}{\partial p}) \tag{3.22}$$

The first part of each of these two terms represents advection of momentum by horizontal winds blowing along the fixed pressure surfaces; the second part of each term represents vertical advection by the winds that blow across the fixed pressure surfaces.

3.4.3 Fictitious forces

The final terms in the momentum equation are so-called fictitious or inertial forces which arise in an accelerating frame or non-Cartesian coordinate system. These terms are derived and discussed in detail for a rotating spherical polar coordinate system in Appendix D. Here we quote them verbatim:

$$-u_i u_k \frac{\partial \boldsymbol{e}_i}{\partial x_k} = \boldsymbol{a}_C + \boldsymbol{a}_\Omega \tag{3.23}$$

where $\boldsymbol{a}_C = a_{C_\theta}\boldsymbol{e}_\theta + a_{C_\phi}\boldsymbol{e}_\phi$ is the curvature term:

$$\begin{aligned} a_{C_\theta} &= \frac{u_\phi^2 \cot\theta}{r} - \frac{u_r u_\theta}{r} \\ a_{C_\phi} &= -\frac{u_\phi u_\theta \cot\theta}{r} - \frac{u_\phi u_r}{r} \end{aligned} \tag{3.24}$$

and $\boldsymbol{a}_\Omega = a_{\Omega_\theta}\boldsymbol{e}_\theta + a_{\Omega_\phi}\boldsymbol{e}_\phi$ is the Coriolis term, given by the horizontal components of $-2\boldsymbol{\Omega} \times \boldsymbol{u}$:

$$\begin{aligned} a_{\Omega_\theta} &= -2\Omega u_\phi \cos\theta \\ a_{\Omega_\phi} &= 2\Omega u_\theta \cos\theta \end{aligned} \tag{3.25}$$

Since these 'forces' are simply adjustments for the non-Cartesian coordinate system and non-inertial frame in which we perform our calculations they do no work and corresponding terms do not appear in the energy equation.

3.5 The energy equation

There are three components of the energy that we consider. Gravitational potential energy per unit mass Φ, defined by Eqn. 3.2, the bulk flow kinetic energy per unit mass $t = \frac{1}{2}v^2$, and the internal energy per unit mass $u = c_p T$. For brevity we write the sum of the kinetic and internal energies as $\epsilon = u + t$.

The internal energy (u) and gravitational potential energy (Φ) are related because both depend on the thermal structure of the atmosphere. Heating the atmosphere not only increases the internal energy, but also has the effect of expanding the atmosphere, thus increasing Φ. We need to check that our formulation takes into account both of these effects simultaneously. We consider a unit mass of gas lying at a pressure p. Heating or cooling this gas with a heat input or output dq will not affect the pressure, because as discussed above it is fixed by the weight of the column of gas that lies above. However, it will change the volume by dV and the temperature by dT. Conceptually, we may thus split the heating into two stages, a heat input dq_T which causes

the volume to change by dV at fixed T, and a heat input dq_V which causes the temperature to change by dT at fixed V. Then the following relations hold:

$$\begin{aligned} dq &= dq_T + dq_V \\ dq_V &= c_V dT \\ dq_T &= pdV = \frac{RdT}{\mu} \end{aligned} \tag{3.26}$$

where the last equality follows from the ideal gas law (Eqn. 1.3), noting that for a unit mass of gas $\rho = 1/V$. Combining these we find that:

$$dq = (c_V + R/\mu)dT = c_p dT \tag{3.27}$$

This is why we use the heat capacity at fixed pressure c_p to calculate the internal energy: it automatically incorporates the energy required to increase the gravitational potential of the gas at higher altitudes as the atmosphere expands.

We may now express conservation of energy as follows:

$$\frac{d\epsilon}{dt} + \frac{d\Phi}{dt} = q_g + q \tag{3.28}$$

which states that the total time rate of change of the energy is equal to work done by gravity q_g, and other energy sources and sinks q to be considered below. Since gravity acts vertically we have:

$$q_g = u_z g = g\frac{dz}{dt} = \frac{d\Phi}{dt} \tag{3.29}$$

Thus the term q_g perfectly balances the derivative of Φ on the left hand side of the energy equation. Incorporating the advective derivative (Eqn. 3.11) we find that the partial derivative of ϵ reduces to:

$$\frac{\partial \epsilon}{\partial t} = q - u_k \frac{\partial \epsilon}{\partial x_k} \tag{3.30}$$

This is the 'energy equation'. We now examine the two components in turn.

3.5.1 Sources and sinks of energy

We split q into the following components:

$$q = q_p + q_D + q_\eta + q_\kappa + q_J + q_\nu + q_m \tag{3.31}$$

The terms on the RHS are the changes in the energy due to work done by pressure gradients (q_p) and ion drag (q_D), redistribution and dissipation of kinetic energy by viscosity (q_η), and thermal energy changes due to thermal conduction (q_κ), Joule heating (q_J), absorption and emission of radiation (q_ν) and any other processes (q_m).

Work done by pressure gradients q_p

Now, in our pressure coordinate system as illustrated schematically in Fig. 3.1a, we have both vertical and horizontal pressure gradients — the horizontal pressure gradient being a small perturbation to the assumption of hydrostatic equilibrium. The work done by pressure gradients thus consists of two components

$$q_p = q_{p_z} + q_{p_{xy}} \tag{3.32}$$

The only work done by the vertical pressure gradient must be on the component of the vertical winds that represents motion of gas *relative* to the fixed pressure surfaces. This is the component $-w/(\rho g)$. The work done in the vertical direction is hence:

$$q_{p_z} = -\frac{w}{\rho g}\frac{1}{\rho}\frac{dp}{dz} = \frac{w}{\rho} \tag{3.33}$$

Clearly a positive value of w, corresponding to subsidence, leads to heating of the gas, whereas a negative value, corresponding to upwelling, leads to cooling of the gas. Intuitively this behaviour corresponds to adiabatic heating and cooling of the gas as it is undergoes compression and rarefaction in its vertical motion, and it can be shown that this term does indeed have the characteristics of an adiabatic temperature change.

The work done by the horizontal winds on the horizontal pressure gradient (Eqn. 3.16) is then given simply by either of the two equivalent forms:

$$q_{p_{xy}} = -\boldsymbol{u} \cdot \frac{1}{\rho}\boldsymbol{\nabla}_z p = -\boldsymbol{u} \cdot g\boldsymbol{\nabla}_p z \tag{3.34}$$

The first form corresponds to work done against the horizontal pressure gradient, as illustrated in Fig. 3.1a. The second form is work done by the horizontal wind blowing along the tilted pressure surface against the component of gravity projected along this direction, as shown in Fig. 3.1b. In the small angle approximation these two perspectives are equivalent.

Work done by ion drag q_D

We must also include work done by ion drag, which is simply the scalar product of $\boldsymbol{u}$ with the $\boldsymbol{j} \times \boldsymbol{B}$ force:

$$q_D = \boldsymbol{u} \cdot \frac{1}{\rho}\boldsymbol{j} \times \boldsymbol{B} \tag{3.35}$$

A detailed treatment of ion drag has already been given in Chapter 2. This component is only included in the experiments described in Chapters 5 and 6.

Viscosity q_η

Viscosity causes changes in both the thermal and kinetic energy of the gas. Since the changes in both of these components are calculated simultaneously in the energy equation, we need only

transform the total energy change term (Eqn. 2.82) to pressure coordinates using Eqn E.5, and divide by ρ, to obtain the required form for the model:

$$q_\eta = g^2 \frac{\partial}{\partial p}\left(\eta \rho \boldsymbol{u} \cdot \frac{\partial \boldsymbol{u}}{\partial p}\right) \tag{3.36}$$

Thermal conductivity q_κ

The heating term due to the thermal conductivity is simply the divergence of the thermal conductive flux described in Section 2.4. We may employ the same arguments that we used to justify decoupling of the horizontal and vertical viscous momentum terms, so

$$q_\kappa = q_{\kappa_{xy}} + q_{\kappa_z} \tag{3.37}$$

We then have a horizontal term:

$$q_{\kappa_{xy}} = \frac{\kappa}{\rho} \nabla_p^2 T \tag{3.38}$$

and a vertical term:

$$q_{\kappa_z} = g^2 \frac{\partial}{\partial p}\left(\kappa \rho \frac{\partial T}{\partial p}\right) + \left[g^2 \frac{\partial}{\partial p}\left(\frac{\kappa_\tau}{c_p}\right)\right] \tag{3.39}$$

The term in square brackets is the second eddy conduction term, which we omit, as discussed in Section 2.4, but which we write here for completeness.

Joule heating q_J

The Joule heating has already been discussed in Chapter 2, and is given by:

$$q_J = \frac{1}{\rho} \boldsymbol{j} \cdot \boldsymbol{E}^* \tag{3.40}$$

where $\boldsymbol{j}$ is the current and $\boldsymbol{E}^*$ is the rest-frame electric field. This component is only included in the experiments described in Chapters 5 and 6.

Radiation q_ν

Absorption of solar radiation is included as a source of thermal energy. This is a relatively minor energy source in all of our experiments, so we will not discuss its form in detail: see Moore et al. (2004) and Müller-Wodarg et al. (2006) for details of the adopted solar spectrum and radiation absorption calculations.

Radiative cooling is neglected. The most important contributor to this energy sink is infrared radiation emitted by the H_3^+ molecular ion. At Saturn, H_3^+ radiative cooling is believed to be of some significance in the auroral regions: for example, using the highest temperature (420K) and highest column density ($7.3 \times 10^{16} \mathrm{m}^{-2}$) of Melin (2006) together with his formulation of total H_3^+ radiative output, we find an upper limit to the total column H_3^+ cooling rate of $0.1 \mathrm{mWm}^{-2}$. This is enough to compete with other thermal energy terms: for example a conductivity of 1mho, a plasma velocity of 250m $\mathrm{s}^{-1}$and a K-parameter of 0.5 corresponds to energy input in the form

of Joule heating and ion drag at a similar rate. At lower temperatures and column densities H_3^+ becomes a much less effective coolant. It is probably only in the extreme circumstances outlined above that it makes an important contribution at Saturn: it thus seems reasonable to suppose that radiative cooling may affect the immediate energy balance of the polar regions, but not global thermal structure and dynamics. As such we expect in general that the neglect of radiative cooling may lead to slight overestimates of temperatures in the auroral zones, but otherwise have little effect on our results.

At Jupiter the situation is much more complicated, because H_3^+ cooling is believed to be important globally. However, to correctly calculate H_3^+ emission we would require a full ionosphere model, which we have specifically chosen not to implement in order to self-consistently couple the thermosphere model to the magnetosphere model of Nichols and Cowley (2004). We will discuss in Chapter 7 whether the inclusion of H_3^+ radiative cooling might significantly alter our results.

Other energy sources q_m

Another contributor to q is the arbitrary imposed heating source q_m used for the experiments in Chapter 4. The form of this heat source is discussed in Section 4.2.

3.5.2 Advection

Advection terms enter the energy equation for precisely the same reasons as outlined above in the context of the momentum equation. We may thus follow closely the arguments presented in Section 3.4 to show that the advection term can be written:

$$-u_k \frac{\partial \epsilon}{\partial x_k} = -\boldsymbol{u} \cdot \boldsymbol{\nabla}_p \epsilon - w \frac{\partial \epsilon}{\partial p} \tag{3.41}$$

representing horizontal and vertical advection of ϵ respectively.

3.6 Imposing energy and momentum inputs

The remainder of this thesis consists of a series of experiments in forcing the thermosphere model with inputs of energy and momentum. In Chapter 4 we examine the influence of an imposed source of thermal energy in the polar regions of Saturn; in Chapters 5 and 6 we apply Joule heating and ion drag to the model using the models of the magnetosphere and ionosphere described in Chapter 2. In order to carry out these simple experiments we require a clear and self-consistent method with which to impose the various energy and momentum inputs involved.

3.6.1 Pure heating experiments

Experiments in which polar heating distributions are imposed upon a gas giant general circulation model have been performed by previous authors (Bougher et al., 2005; Müller-Wodarg et al., 2006). However, neither of these studies clearly described their method. The issue is not trivial, because there are various potential methods of imposing such a heating input. This is because heating an atmosphere changes many of its physical properties. If, for example, we fix the absolute altitude of a heating input, in kilometres, above some fixed level, the atmosphere will expand on being heated such that the fixed altitude lies deeper in the atmosphere in terms of the column mass of gas that lies above it. Thus a feedback effect is introduced whereby the heating input causes itself to move deeper into the atmosphere, where the heat capacity of the gas is higher.

We may alternatively move to a scenario in which the heating input is fixed as a function of pressure. This seems more logical, since, as discussed in Section 3.3, the column mass of gas above a given pressure is always approximately fixed. Heating due to radiation or particles is likely to be roughly fixed as a function of column mass, since this determines the ability of the radiation or particles to penetrate the atmosphere. However, in this case we must be careful not to fix the heating input per unit volume, q_v, since heating the atmosphere will cause its volume to increase, and thus increase the heating!

The most logical quantity to fix is thus the heating input per unit mass, q_m. The mass of gas in the atmosphere is very nearly independent of temperature: thus the total energy input will always remain independent of temperature if q_m is fixed. Furthermore, since heat capacity is proportional to mass for a given composition, q_m represents the thermal energy input per unit heat capacity; in other words it represents the ability of the thermal energy input to increase the temperature. In Section 4.2 we describe an arbitrary energy input that is defined in this way.

3.6.2 Joule heating and ion drag

The imposition of Joule heating and ion drag presents a similar problem, except that these inputs vary with the behaviour of the neutral winds.

It is tempting to fix the ionospheric densities, and then recalculate the conductivity and thus the Joule heating and ion drag, at each timestep. In this case the conductivity would change with the thermal structure of the thermosphere, since the neutral number densities and thus the collision frequencies would change with the temperature. This is of course what must actually happen in reality. However, with this approach we lose control of the distribution of the conductivity and energy and momentum inputs and of their height-integrated values. In our context it is considerably more helpful to fix the conductivity itself. This situation is physically extremely unlikely, but it gives us a measure of control over the magnetosphere-atmosphere coupling processes that allows us to compare different situations more cleanly.

Following the discussion above, we fix the conductivity such that, in the absence of neutral winds, the energy and momentum inputs *per unit mass* from Joule heating and ion drag are fixed everywhere in the model. This, of course, is the same as fixing the thermal energy inputs per unit of heat capacity and fixing the kinetic energy and momentum inputs per unit of inertia. Now, the energy and momentum inputs from Joule heating and ion drag *per unit volume* are all directly proportional to the conductivities σ_P and σ_H (e.g. Eqns. 2.43 and 2.48). Thus, to fix the *per unit mass* inputs we must fix the quantities $s_P = \sigma_P/\rho$ and $s_H = \sigma_H/\rho$, where ρ is the mass density. We will refer to these quantities s_P and s_H as 'conductivities per unit mass'.

Fixing s_P and s_H has the important advantage that Σ_P and Σ_H are also fixed, since, for example:

$$\Sigma_P = \int \sigma_P dz = \frac{1}{g} \int s_P dp \tag{3.42}$$

so that by fixing the conductivities per unit mass we fix not only the distribution of the conductivity throughout the thermosphere, but also its height-integrated value, which is the value 'seen' by the magnetosphere.

In Section 2.4 we discussed conductivity models for Jupiter and Saturn in terms of profiles of σ_P and σ_H calculated, as a function of pressure, upon fixed background neutral atmospheres from Grodent et al. (2001) and Moses et al. (2000) respectively. To calculate s_P and s_H from these profiles we simply use the mass densities in these fixed background atmospheres, and apply the values so derived to our thermosphere model.

3.7 Limits of our approach

The principal difficulty with our approach is that at high altitudes the accuracy of the fluid approach begins to break down as ballistic behaviour becomes more important. A useful reference height for the onset of this breakdown is the altitude at which the mean free path equals the pressure scale height.

If we assume that the mean free path $l \sim 1/(An)$ where A is the molecular area and n the number density, then the ratio of l to the scale height is:

$$\frac{l}{H} \sim \frac{\mu g}{Ap} \tag{3.43}$$

assuming that $A \sim 10^{-20}\mathrm{m}^2$, $g \sim 10\mathrm{m/s}^2$ (appropriate for Saturn) and $\mu = 2$ amu we find that this ratio is equal to unity at ~0.03nbar. This lies approximately 8 scale heights above the base of our Saturn model, which lies at 100nbar. Our model extends to ~10-11 scale heights above the 100nbar level, so that the top 2-3 scale heights lie in the ballistic regime. A similar calculation for Jupiter shows that the top 1-2 scale heights lie in the ballistic regime.

Our results at these altitudes should thus be treated with caution. However it can be argued that the ballistic behaviour is at least partially captured by the very high molecular viscosities

and thermal conductivities in these regions. These result in wind and temperature profiles that are almost constant at the highest altitudes. This is similar to the behaviour expected if mean free paths are very long.

Also we note that at lower altitudes — in particular in the regions of high Pedersen conductivity that are most pertinent to coupling with the magnetosphere — the fluid approach is perfectly valid, and we expect to model this region with reasonable accuracy.

Chapter 4

Heating experiments

4.1 Introduction

As a prelude to the detailed studies of magnetospheric energy inputs that follow in Chapters 5 and 6, we now pursue an initial investigation of the influence of a general source of thermal energy in the polar regions of a gas giant. We will use Saturn as our model planet, and then briefly compare its behaviour with that of Jupiter towards the end of the chapter.

A preliminary study along these lines has already been carried out by Müller-Wodarg et al. (2006). They employed the model described in Chapter 3 to investigate the thermal energy inputs required to explain the observed temperatures. They were able to reproduce the occultation measurement of ~400K at 30° N (Smith et al., 1983) by imposing either an arbitrary, globally distributed 'wave heating' rate of ~14TW or a combination of a polar heat source of ~10TW of Joule heating (consistent with Cowley et al., 2004b) with an arbitrary 'wave heating' rate of ~6TW. This chapter builds on this work by examining a full parameter space of simple, plausible polar heating distributions.

4.2 Distribution of polar heating

4.2.1 Vertical distribution of energy

The vertical distribution of our chosen heating source (Fig. 4.1) resembles a Chapman profile (Eqn. 1.9). Specifically, we specify the heating rate per unit mass q_m as a function of the pressure p:

$$q_m = q_{m\infty} \exp\left(-\frac{p}{p_0}\right) \tag{4.1}$$

Here $q_{m\infty}$ is the asymptotic value of the heating rate in the upper thermosphere. We fix q_m, so that, as discussed in Section 3.6, the heating is not dependent on the thermal structure of the atmosphere. This means, however, that the heating rate per unit volume q_v is dependent

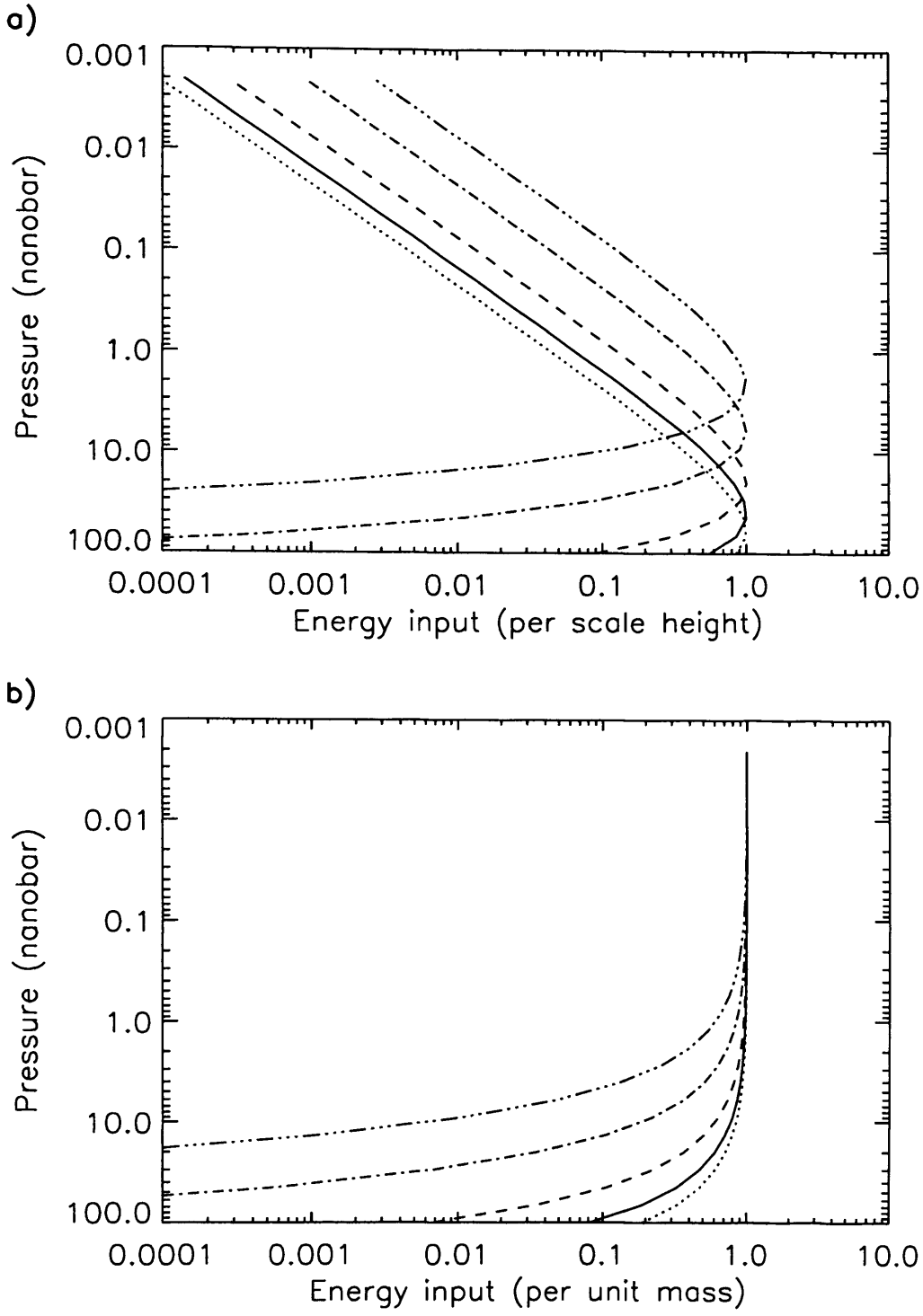

Figure 4.1: Vertical distribution of polar heating. (a) Normalised heating rates per scale height q_h/q_{h0} as a function of pressure. The distributions peak at the following pressures (see Section 4.5): dotted line: 60nbar, solid line: 40nbar, dashed line: 20nbar, dot-dash line: 6nbar triple dot-dash line: 2nbar (b) Normalised heating rates per unit mass $q_m/q_{m\infty}$.

on the thermal structure. However, we can usefully specify the heating rate per unit area per unit pressure scale height q_h—which is equivalent to q_v within a constant scaling factor if the atmosphere is isothermal—by multiplying q_m by the mass density per unit area per unit pressure scale height p/g:

$$q_h = q_{h0} \frac{p}{p_0} \exp\left(1 - \frac{p}{p_0}\right) \tag{4.2}$$

where $q_{h0} = q_{m\infty}(p_0/g)e^{-1}$ and g is the acceleration due to gravity. The peak heating rate is then q_{h0} at a pressure of p_0.

We have quoted both of these formulae because it is useful to understand the behaviour of both q_h and q_m. The rate q_h represents more accurately the location of the heating inputs: most of the heating enters the atmosphere at the peak of q_h. However, q_m is more representative of the atmospheric response to the heating, because it indicates the energy input relative to the local heat capacity of the atmosphere.

As discussed in Chapter 1, the physical origin of the Chapman profile is the description of atmospheric heating and ionisation rates resulting from monochromatic irradiation. However, in this context we employ the Chapman profile purely as a simple distribution which contains the main features we expect a polar heat source to exhibit. In particular, a sharp cut-off below the peak energy input at p_0 and an exponentially decaying tail on the topside. The Chapman profile is a very specific case in that q_m tends asymptotically to a constant value with altitude. The consequences of deviations from this simple behaviour are discussed in Section 4.6.

The morphologies of the low and high altitude limits of the Chapman profile are both consistent with the general form of energy deposition produced by particle precipitation (Fig. 1.1) and Joule heating (Fig. 2.11). In this context it thus represents some unknown mixture of these, and perhaps other, processes.

4.2.2 Horizontal distribution of energy

We use two horizontal energy distributions, both of which are illustrated in Fig. 4.2. That shown by the solid line is intended to represent a heating source confined to a narrow auroral oval. It is distributed as a Gaussian with FWHM 3°, centred at 14° colatitude (see Fig. 4.2). This is the distribution used for our standard runs. The dot-dash line represents a polar cap 'filled in' with heating: in a sense the opposite extreme to the narrow oval, a case that will be discussed in Section 4.6.

4.3 Details of model runs

Our thermosphere model has already been described in Chapter 3. For the work in this chapter we use 28 pressure levels with a vertical resolution of 0.4 pressure scale heights, and a resolution of 1° in latitude. We also assume zonal symmetry, but we calculate the EUV heating for a full

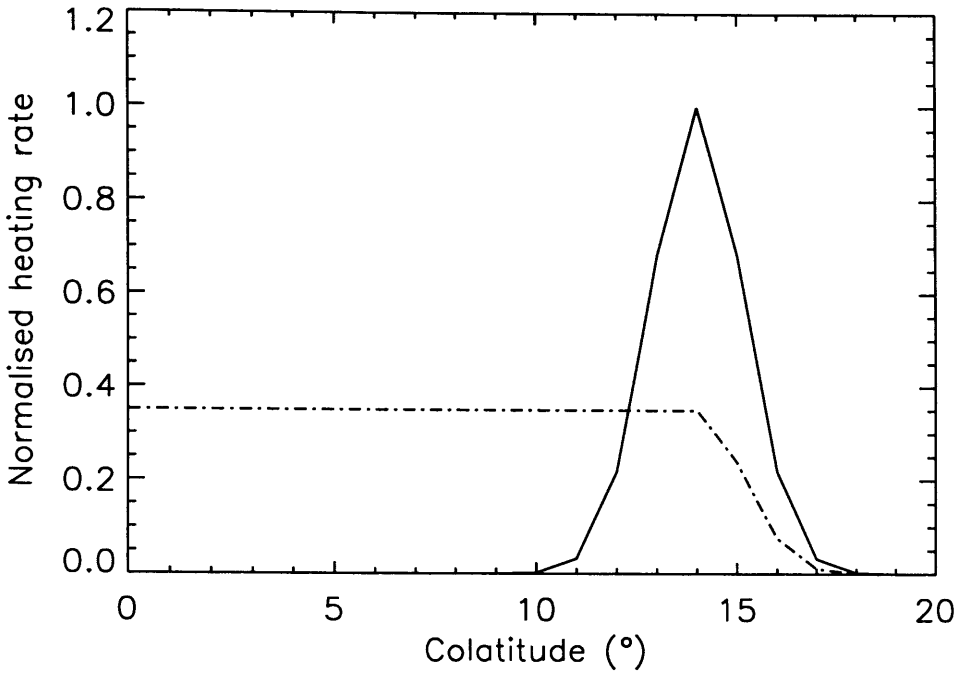

Figure 4.2: Latitude distribution of polar heating. The solid line is the heating distribution used for our standard runs. The dot-dash line is the 'filled in' polar cap distribution discussed in Section 4.6.3.

range of longitudes, and then use the zonal average as the input to the model. For several of the runs described below, validation runs using the full 3D model (including diurnally variable solar heating) indicate that the assumption of zonal symmetry has a very small influence on our results.

We have chosen to omit full composition transport calculations for reasons of computational efficiency. We have also set the eddy diffusion coefficient to zero in our standard calculations, such that the increased viscosity and thermal conduction associated with eddy diffusion processes is not included. These assumptions will be discussed briefly in Section 4.6.

The model was started with an initial uniform thermospheric temperature of 143K, corresponding to the fixed lower boundary temperature. It was then run for the equivalent of 800 Kronian rotations, in an equinox configuration, with solar EUV heating as the sole energy input. This long initial run ensured it had reached near steady-state before the inclusion of a polar heat source. The 'steady-state' exospheric temperature which this set-up run achieved was 180K at the equator and 160K at the poles. This confirms the estimates of Yelle and Miller (2004) discussed in Chapter 2. Similar results were reported in Müller-Wodarg et al. (2006).

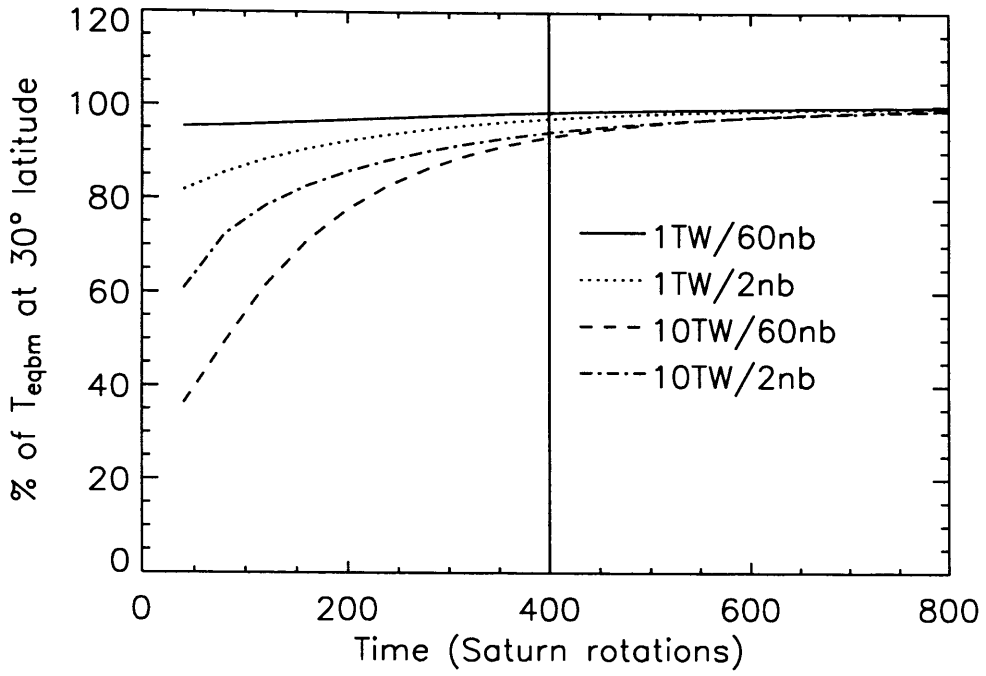

Figure 4.3: Convergence to steady state of models. Each line represents the time variation of the exospheric temperature at 30°N, as a percentage of its asymptotic value, for the energy inputs marked.

We then explore a parameter space of 25 runs, within which the total magnitude and peak altitude of the polar heating is varied. All runs are initialised using the 'steady-state' run described above. For each simulation, an identical polar heat source is imposed in each hemisphere. The polar heat source has the form described above in Section 4.2, using p_0 values of 60, 40, 20, 6, and 2 nbar (Fig. 4.1).

We calculate the total energy inputs by numerically integrating the normalised horizontal and vertical distributions across our model grid. We then set the parameter q_{h0} to give round values of the total energy input. Specifically, we use total polar energy inputs (integrated over both hemispheres) of 1, 2, 4, 6 and 10TW. For brevity in the following discussion we will describe a run with an input of xTW peaking at $y$nb as xTW/$y$nb.

Each model was run for 400 Kronian rotations. To check that 400 rotations is sufficient to represent steady state, we have run the models at the 'corners' of our parameter space — i.e. those representing inputs of 1 and 10TW at pressures of 60 and 2 nbar — for 800 rotations. We find that by 800 rotations the model temperatures are exponentially approaching an asymptote. Fig. 4.3 shows the time development of the exospheric temperature at 30°N as a percentage

of this asymptotic value. By 400 rotations the temperatures all lie well within 10% of the asymptote. We also note that in all cases this is a systematic *underestimate* of the temperature. An error of 10% is perfectly acceptable given the general nature of our modelling.

4.4 General response

The general response of the model is illustrated for the 6TW/40nb run in Fig. 4.4. The colour contours represent temperature in Fig. 4.4a and zonal wind velocity in Fig. 4.4b. In both figures the vertical and meridional velocities are plotted as arrows. The vertical scale has been stretched for clarity, and the vertical wind speeds have been scaled accordingly to preserve the geometry of the flow. Thus it should be made clear that in the plot shown vertical velocities are typically <5m/s, whereas peak meridional velocities are of the order of 300m/s. The thickness of the arrows represents the combined vertical/meridional wind speed; this is dominated by the meridional component.

The model grid points are shown as dots. Note that the altitude of the upper pressure level of the model falls off strongly towards the equator, as a simple consequence of the thermal structure. The two crosses indicate the location of the energy inputs. The co-latitude of the crosses corresponds to the peak of the horizontal distribution shown in Fig. 4.2. The lower cross shows the location at which the heat input per scale height q_h peaks (see Fig. 4.1). The upper cross shows the altitude at which the heat input per unit mass q_m has risen to ~90% of its asymptotic value $q_{m\infty}$; for brevity we will refer to this point as the 'shoulder' of q_m.

The general behaviour is as follows. The heated zone at 14° colatitude exhibits strong upwelling driven by the heating. There is a temperature peak here at about 2000km altitude. Below the peak the only significant energy input comes directly from the imposed heating profile. The atmosphere is cooled by a combination of downwards thermal conduction and adiabatic cooling of the rising gas. Above the peak, thermal conduction transfers heat upwards, and this is almost as important an energy source as the topside of the imposed heating profile.

The temperature peak does not correspond in altitude to the peak of q_h, but rather to the 'shoulder' of q_m. This suggests that q_m is a more useful measure of the heating rate than q_h for determining the thermal structure. The vertical temperature profile follows that of q_m quite closely: below the 'shoulder' both T and q_m increase with altitude; above the 'shoulder' they are both approximately constant.

At low altitudes, pressure gradients drive meridional winds both poleward and equatorwards of the heated zone. The polewards flow is convergent as a consequence of the spherical geometry, and this forces a sinking cell to form inside the polar cap. The sinking gas undergoes adiabatic heating. This heating almost 'fills in' the polar cap with the same temperatures observed in the main oval, although there is still a small residual temperature gradient driving the flow.

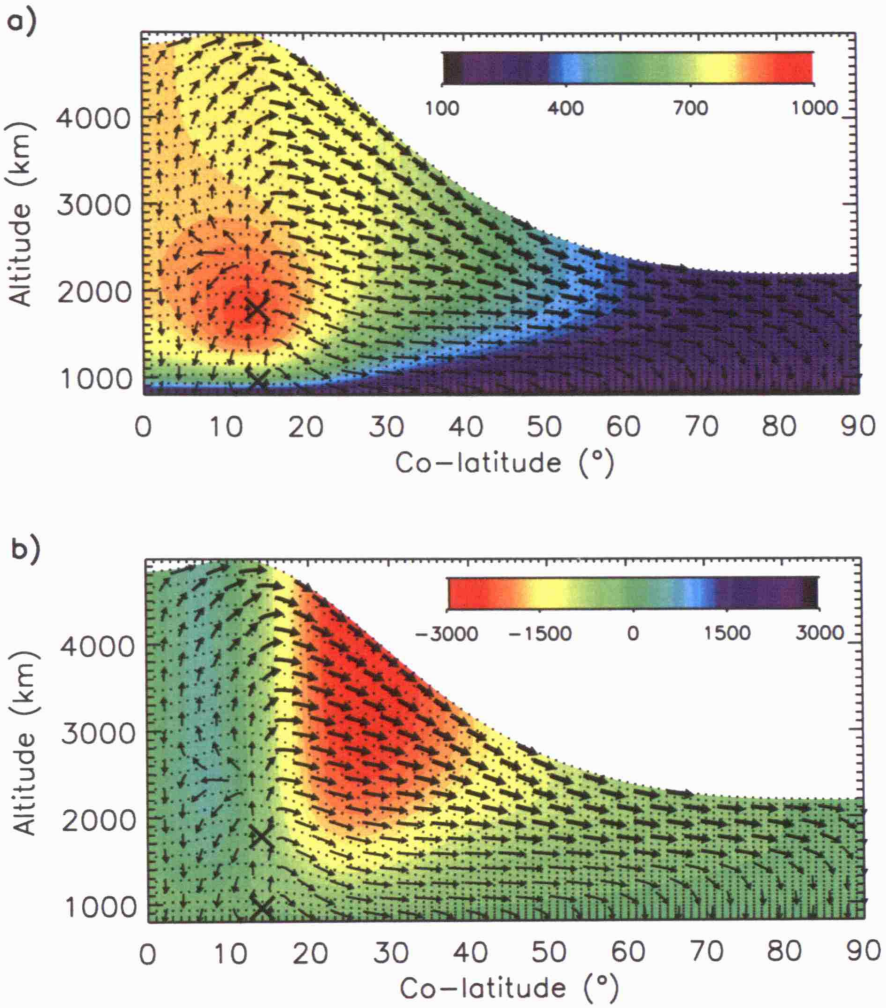

Figure 4.4: Temperatures and winds from the pole on the left to the equator on the right, for a run with an input of 6TW peaking at 40nbar. Arrows indicate the vertical and meridional circulation of the gas. The thickness of the arrows corresponds to the wind speed; the thickest arrows represent a speed of ~300m/s. (a) Colour scale: temperature (K). (b) Colour scale: zonal winds (m/s). Negative speeds (red/yellow) represent westwards (sub-corotating) flows; positive speeds (turquoise/blue) represent eastwards (super-corotating) flows. The crosses indicate the location of the energy input. The lower cross is at the peak of the energy input per scale height (q_h). The upper cross is at the altitude where the energy input per unit mass (q_m) has risen to approximately 90% of its asymptotic value $q_{m\infty}$.

The equatorwards flow is driven by a much steeper meridional pressure gradient. This flow is divergent, again as a consequence of the geometry. The divergence of the flow reduces the heating efficiency of the gas as it moves to lower latitudes, since the energy must be spread over a wider area. The gas is also cooled efficiently by thermal conduction as it moves to lower latitudes. The result is a persistent sharp pressure gradient equatorwards of the oval. At higher altitudes, the behaviour is essentially identical, except that the highest temperatures are found at the pole and one single equatorwards flow develops. The high-altitude hotspot at the pole results largely from upwards thermal conduction from the hot polar cap beneath.

The flows away from the oval are driven by pressure gradients, but are substantially modified by the Coriolis force to generate zonal winds (Fig. 4.4b). The polewards flow inside the main oval is forced into weak super-corotation (eastwards flow). The much stronger equatorwards flow outside the oval is driven into a fast sub-corotating (westwards) flow. We find that vertical viscous drag is the principle force limiting this zonal flow. In total, the Coriolis force is thus in balance with the combined meridional pressure gradient and vertical viscous drag forces. The importance of viscosity in controlling this behaviour will be discussed further in Section 4.6.

As the flow moves towards lower latitudes the pressure gradient, and thus the flow velocity, reduces significantly. As the gas slows it sinks, and this leads to some adiabatic heating of the low-latitude region. The adiabatic heating at the equator is significant, accounting for $\sim 0.04 \mathrm{mWm}^{-2}$ compared to only $\sim 0.01 \mathrm{mWm}^{-2}$ from solar heating.

4.5 Exploring parameter space

An important advantage of a GCM as compared to a one-dimensional model is that it allows the sparse and spatially separated observations of the Kronian thermosphere to be tested simultaneously. To compare the available observations with the model-derived temperatures it is, of course, necessary to associate each measurement with specific grid points within the model. In the case of the spacecraft occultation data we associate the measured exospheric temperatures of 400K at 30°N (Smith et al., 1983) and 800K at 4°N (Festou and Atreya, 1982) with the model-derived temperatures at the topmost pressure level and at the appropriate latitude. In the case of the ground-based spectroscopic measurements we assume that the observed emission is associated with the peak of the ionosphere, and that this in turn is, approximately, spatially coincident with the peak of q_h. Thus we associate the observed ionospheric temperatures with the model-derived temperatures at the pressure p_0 where q_h peaks vertically. The spectroscopic measurements represent an average temperature across the polar cap, so we average the temperature at the peak altitude across the whole polar cap within 14° colatitude. Henceforth we will refer to this polar cap average as the 'auroral' temperature.

The results of the complete grid of 25 model runs are summarised in Figs. 4.5 and 4.6. Fig-

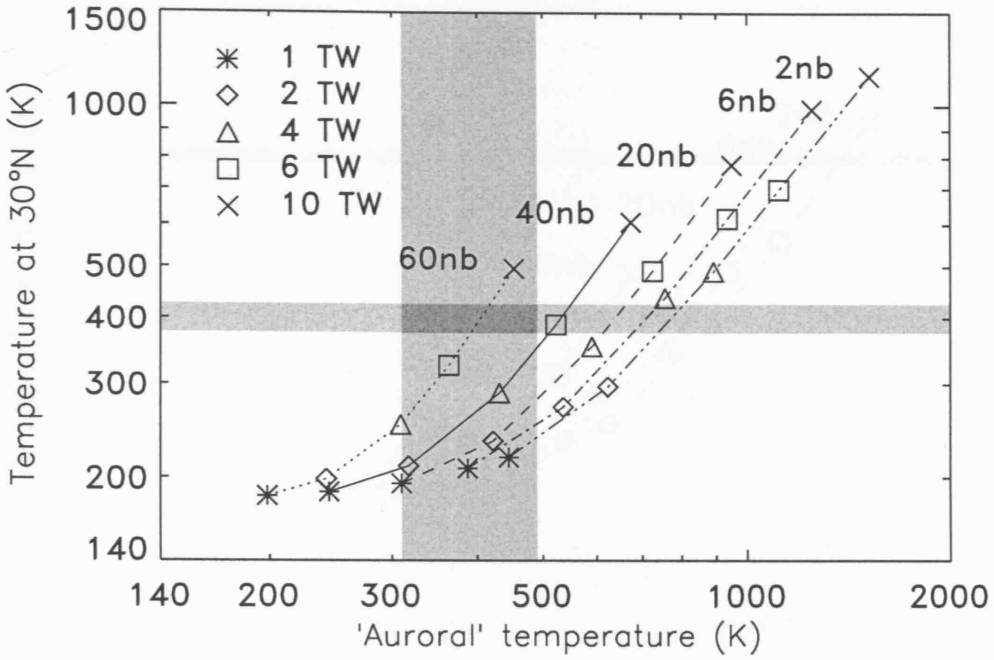

Figure 4.5: Comparison between 'auroral' temperature (x-axis) and temperature at 30°N (y-axis). The grey horizontal band represents the Voyager solar occultation measurement of ~400K (Smith et al., 1983), with a range of ±25K. The vertical band represents the auroral temperature range of 310-490K determined by Melin (2006).

ure 4.5 plots the auroral temperature for each model run along the x-axis and the corresponding 30°N temperature along the y-axis. Figure 4.6 is identical, but with the 4°N temperature plotted along the y-axis. Note the log scales. Points corresponding to the same height distribution are connected by lines (the line formats correspond to those in Fig. 4.1); the energy input is represented by the plot symbol, as shown.

The observational constraints are indicated by the horizontal and vertical grey bands. The horizontal band in Figure 4.5 represents the Smith et al. (1983) temperature of 400K at 30°N, with a width of ±25K. This range is intended not as an error bar, but as a guide to the scale of the plot and the closeness of the model-derived points to the constraint. The horizontal band in Figure 4.6 represents the 800K at 4N measurement of Festou and Atreya (1982) in the same way.

The vertical bands on both of Figs. 4.5 and 4.6 represent the 'auroral' temperature measurements of Melin (2006). As shown in Table 1.5, Melin (2006) determined two temperatures of 380K and 420K, both with an error of ±70K. These temperatures are determined by fitting theoretical H_3^+ emission spectra to data. The error is not a formal statistical error, but is de-

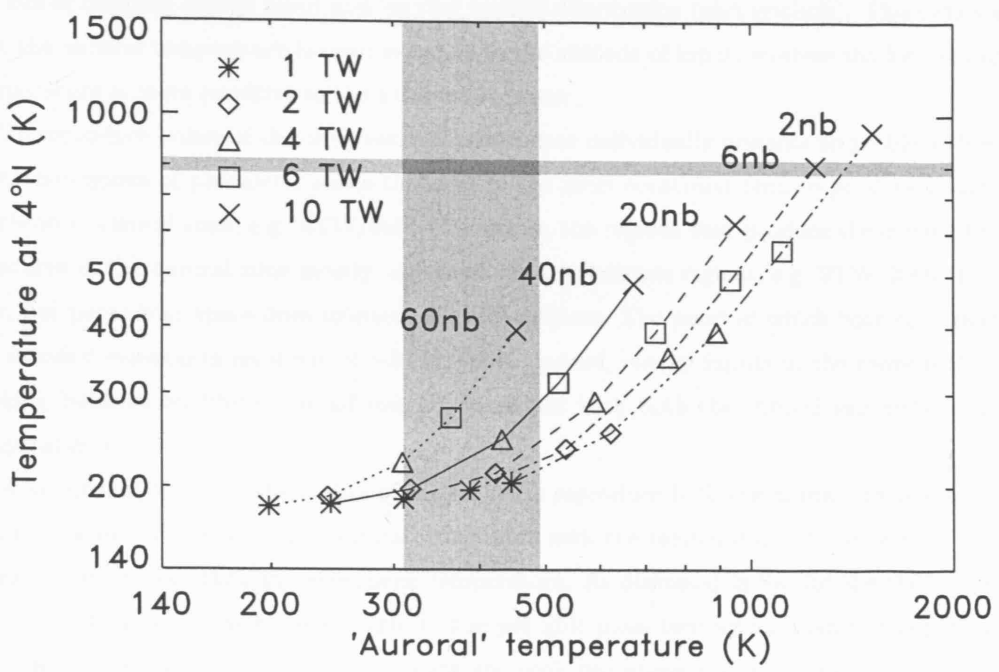

Figure 4.6: Equivalent to Figure 4.5 for the Voyager stellar occultation measurement of ~800K at 4°N (Festou and Atreya, 1982).

termined by estimating the temperatures either side of the best fit at which the fit begins to become poor. We thus consider the whole range 310-490K to be reasonably consistent with the measurements, and plot this range as the vertical grey band in Figs. 4.5 and 4.6. This should be interpreted with the understanding that the most probable values are towards the centre at ~400K. The dark grey box where the horizontal and vertical bands cross then represents the 'target' region within which both constraints are satisfied.

Focusing now on Fig. 4.5, we can see that our parameter space covers situations in which the atmosphere is both much colder and much hotter than the observations. For the 1TW/60nb run — which has the lowest power input at the lowest altitude — the auroral and mid-latitude temperatures are barely discernible from the case where there is no auroral input. At the other extreme the 10TW/2nb run exhibits an auroral temperature which approaches 2000K and a mid-latitude temperature greater than 1000K.

It is also clear that the temperature distribution is sensitive both to the total power input and to the vertical distribution. Increasing either the total input power or the altitude of the input increases both temperatures. This is unsurprising, since in both cases the ratio of the energy input to the heat capacity of the gas being heated increases (since at higher altitude the gas is less dense and thus has a lower heat capacity). However, the loci of constant vertical

distribution and varying energy input (connected by lines) generally have steeper gradients than the loci of constant energy input and varying vertical distribution (plot symbols). This indicates that the auroral temperature is most sensitive to the altitude of input, whereas the low latitude temperature is more sensitive to the total input power.

To reproduce either of the observational constraints individually presents no problem. However, the regions of parameter space that satisfy the 30°N constraint tend to produce a rather overheated auroral zone, e.g. 4TW/6nb. Conversely, the regions that produce the correct temperatures in the auroral zone mostly underheat the low-latitude regions, e.g. 2TW/20nb. However, our parameter space does intersect the observations. The point at which both constraints are satisfied represents an input of ~8TW/60nb. Indeed, energy inputs in the range 6-10TW peaking between 60-40nbar are all roughly consistent with both the auroral and mid-latitude temperatures.

A significant factor in the ability of the model to reproduce both constraints simultaneously is the decision to associate the 'auroral' constraint with the temperature at the point of peak energy input, rather than the exospheric temperature. As discussed in Section 4.4 the temperature structure responds more strongly to the per unit mass heating q_m than to the per unit scale height heating q_h. Thus the temperature peak lies above the peak of q_h. This is also partly a consequence of the proximity of the peak of q_h to the cold (143K), fixed temperature mesopause. This allows the region of peak energy input to be cooled efficiently by thermal conduction. Meanwhile, as described above, the upper altitude ranges are heated both directly by the topside of the heating profile, and indirectly through upwards thermal conduction from the temperature peak. Thus we find that the polar exospheric temperature may be considerably higher, by as much as hundreds of degrees Kelvin, as the auroral temperature (at the peak of q_h). It is thus, in principle, possible for the auroral temperature to be colder than the equatorial exospheric temperature while a pressure gradient still exists in the upper thermosphere to drive a redistributive wind system. This means that there is no *a priori* inconsistency between an auroral temperature of ~400K and an exospheric temperature at 4°N of 800K as reported by Festou and Atreya (1982).

However, looking now at Fig. 4.6, we see that when we try to reproduce the Festou and Atreya (1982) measurement at 4°N, this situation does not arise. To reach 800K at 4°N we require an input of 10TW/6nb or, visually interpolating from the graph, ~9TW/2nb, and this gives an auroral temperature three times the constraint. It is not possible to find a combination in our parameter space which gives both measurements simultaneously.

The recent reanalysis of the Voyager occultations by Vervack et al. (2005, in preparation), suggests that the exospheric temperature at 30° latitude may be closer to 450K. This only represents an increase of 50K over the constraint marked on Fig. 4.5, and it is clear that to achieve this temperature we require slightly more energy input at a slightly lower altitude: for

example ~9TW/60nb produces a good match between the new mid-latitude temperature and the 400K auroral constraint.

4.6 Discussion

4.6.1 Comparison to likely energy inputs

We have employed a general polar heating distribution rather than a specific physical heating mechanism because of the uncertainty in the exact nature of the polar heating. We now briefly assess the physical reasonableness of these inputs.

Joule heating

We may estimate the peak altitude of the Joule heating, which should occur near to the peak of the Pedersen conductivity, using Eqn. 2.27. This shows that the peak occurs close to the altitude where $r_i = 1$. To calculate r_i we take a nominal value of $B \simeq 60,000$nT, appropriate for the polar regions of Saturn. We find that for the full parameter space of 25 runs $r_{H^+} = 1$ in the range 50-80nbar and $r_{H_3^+} = 1$ in the range 20-60nbar. These ranges correspond well to the regions of parameter space in which we find best agreement between our model and the observations.

We have shown in Chapter 2 that the ionisation — and thus the conductivity — is more likely to peak close to the 10nbar level (Fig. 2.7). This is controlled by the location of the homopause, which ensures that below 10nbar H^+ and H_3^+ are destroyed by charge exchange with hydrocarbons. This suggests that any energy input from Joule heating may peak at too high an altitude to reproduce both constraints. However, the calculations shown in Fig. 2.11 indicate that the distribution of neutral winds tends to push the Joule heating peak below the peak of Pedersen conductivity. Thus it may plausibly occur at the correct altitude. The total polar heating powers of 6-10TW that give best agreement between our models and the data are also similar to the Joule heating powers predicted by Cowley et al. (2004b).

However, these estimates all neglect the complex influence of ion drag on the neutral atmosphere. This will be discussed in Chapter 5.

Particle heating

Cowley et al. (2004b) estimated a total global particle heating power of ~0.1-0.2TW. This is derived from a model of the auroral precipitation parameters that is reasonably consistent with observations of the UV aurora. It thus seems unlikely that heating associated with the UV aurora can provide our required heating powers.

However, Stallard et al. (2004) report observations of the IR aurora which indicates strong emission by the H_3^+ molecular ion across the whole polar cap. The presence of significant H_3^+

emission inside the polar cap indicates either that there is a local ionisation source, or that the H_3^+ is transported inwards from the main oval. If the former is the case, the ionisation is probably accompanied by heating.

For transport to explain the presence of H_3^+ there would need to be strong polewards thermospheric winds that were capable of transporting H_3^+ across the polar cap within its recombination timescale. This timescale is given by $\tau \sim [10^{-13} n_e]^{-1}$, such that if the electron density is $n_e \sim 10^9 \mathrm{m}^{-3}$ then $\tau \sim$ 10,000 seconds. The radius of Saturn's polar cap is approximately 15,000 km. Thus wind speeds of the order of 1.5km/s would be required to fill the polar cap with H_3^+. It is not clear whether these wind speeds are plausible, nor how they would be generated. In Chapter 5 we describe a mechanism for the generation of polewards flowing winds, but the calculated speeds do not approach 1.5km/s.

Furthermore, the ions would need to be fully coupled to the neutrals for this transport to be effective. This requires the ratio r_i discussed above to be greater than 1, so that ion-neutral collisions dominate over electromagnetic forces. This occurs below the level where $r_i = 1$, i.e. below the 20nbar level (see above). In this region the hydrocarbon densities are high enough to rapidly destroy both H_3^+ and H^+ (Moses and Bass, 2000). Thus the only region where significant ion transport is likely to occur lies in the region of the thermosphere where ion lifetimes are extremely short. For this reason it seems that the H_3^+ densities are unlikely to be explained by transport.

The H_3^+ must therefore be produced by local ionisation. If this exists it must be soft precipitation that does not produce a bright UV aurora. Soft precipitation is consistent with the generation of H_3^+ since it would result in ionisation above the homopause, where hydrocarbon densities are low and the H_3^+ lifetime is therefore relatively long. The mechanism for generating such precipitation is unclear, however there seems to be no other known mechanisms that can explain the H_3^+ observed in the polar cap.

Such precipitation would presumably deposit energy above the homopause at pressures less than 10nbar. There is no reason why it should not also deposit some energy at lower altitudes, but it is difficult to place any sound limits on the distribution or quantity of this energy source.

Other heat sources

In the introduction we also discussed the possibility of heating due to the dissipation of kinetic energy associated with ion drag, and increased levels of Joule heating caused by fluctuations about the mean electric field. We defer detailed discussion of these energy sources to Chapters 5 and 6.

4.6.2 Sensitivity to vertical energy distribution

As described in Chapter 3, the functions that we have chosen to describe the vertical distribution of our polar heating source have a very specific form. In particular the shape of the topside heating, which tends asymptotically to a constant per unit mass heating rate in the upper thermosphere, represents a very specific case.

In order to test the importance of the topside heating rate, we have repeated the 6TW/40nb run with modified vertical heating profiles (Fig. 4.7). We modify the topside by altering the exponential decay constant of the heating rates above the peak such that the total heating rate is either increased or decreased by 1TW (dotted lines); we modify the peak by adding or subtracting a Gaussian from the peak, again to increase or decrease the total rate by 1TW (dashed lines).

The results are shown in Fig. 4.8, which plots the same parameters as Fig. 4.5. The solid line is equivalent to the solid line in Fig. 4.5, i.e. it represents the parameter space of 40nb runs. The dotted lines join the runs with modified topside heating, and the dashed lines join the runs with modified peak heating.

The most striking feature of Fig. 4.8 is that the dotted lines are almost vertical. Thus the topside modification has a negligible effect on the auroral temperature, and a large effect on the exospheric temperature at low latitudes: the exospheric temperature is, to an extent, decoupled from the auroral temperature. Furthermore, adding or subtracting 1TW from the topside changes the exospheric temperature at mid-latitudes by ~100K. This represents a modification of less than 20% to the total heating rate, but a change of ~40% in the temperature contrast with the mesopause. The principal conclusion to draw from this observation is that it is essential to correctly quantify topside heating when assessing the effectiveness of a polar heat source. It is common in the literature to quote values for the total or height-integrated energy input: however these are clearly unhelpful if the structure of the topside — which represents a relatively small percentage of the total energy input — is improperly constrained.

The peak modification has a strong effect on the auroral temperature: this is unsurprising as we have defined the auroral temperature as the temperature at the heating peak. However, it has a similar effect on the exospheric temperature. Thus changes to the peak heating rate have a similar influence throughout the thermosphere. This is unsurprising, since the peak heating is at low altitude, and the rest of the thermosphere thus 'sits' on top of it.

4.6.3 Sensitivity to horizontal energy distribution

Latitudinally, our polar heat source is concentrated in a thin oval close to the observed UV auroral oval at ~14° colatitude. However, it is possible that the polar heating may be distributed more widely across the polar cap. For example, the Joule heating calculated by Cowley et al. (2004b) is distributed between the pole and ~25° colatitude. Similarly, the possible soft precipitation

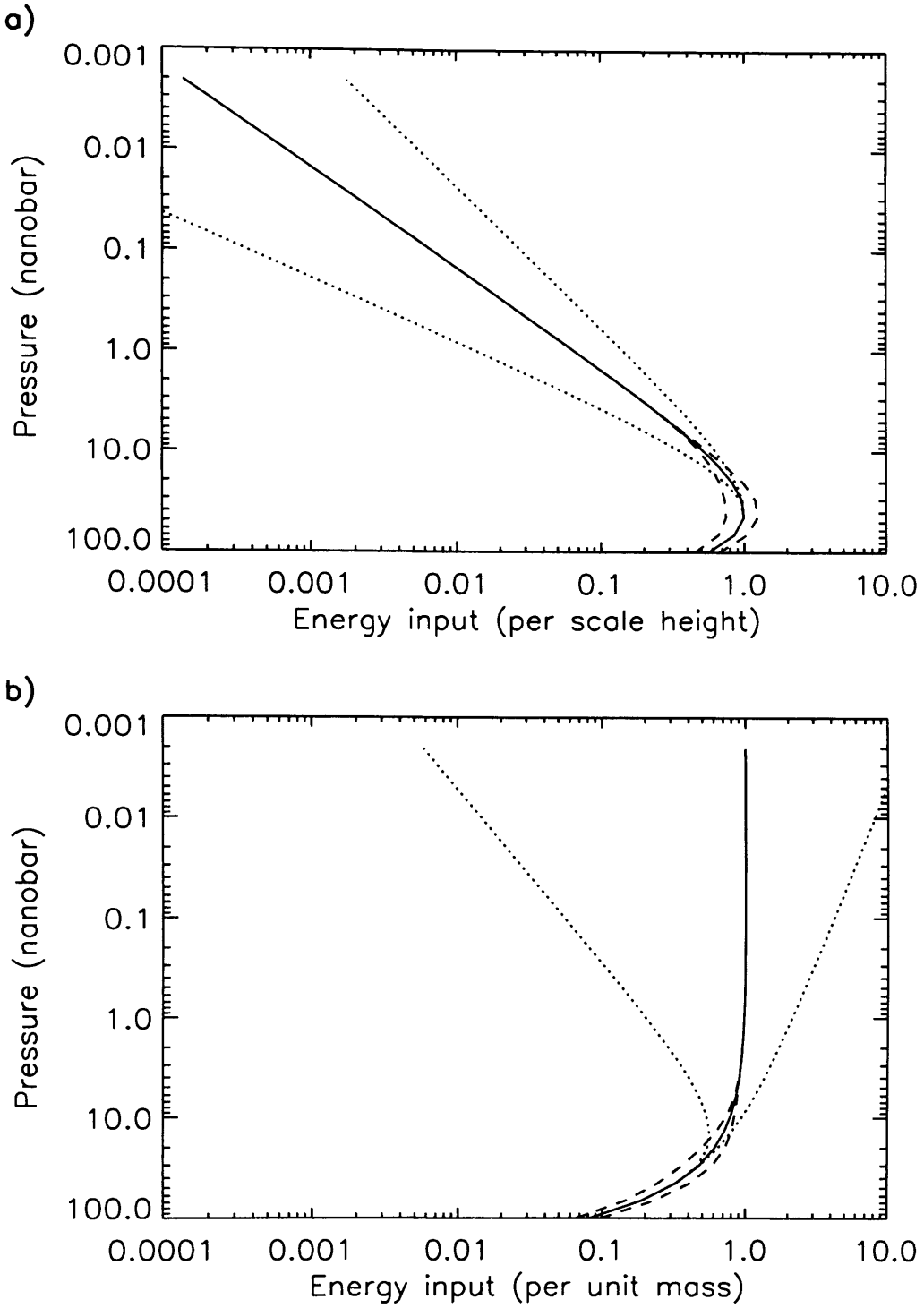

Figure 4.7: Modified Chapman profiles. Dotted lines: Chapman profiles with modified topside. Dashed lines: Chapman profiles with modified peak intensities. (a) per unit scale height rates. (b) per unit mass rates.

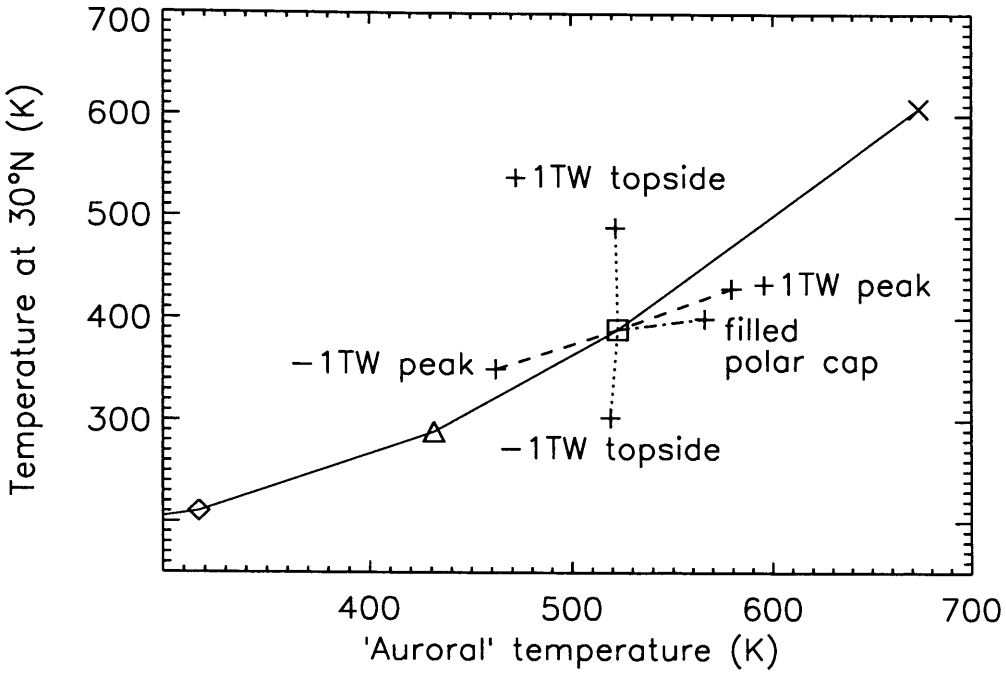

Figure 4.8: Effect of modifying the heating distribution. The solid line represents the parameter space of 40nb runs in the same manner as Fig. 4.5. Thus the square represents our standard 6TW/40nb run. The plus signs show the temperatures produced by modifying the heating distributions, as marked. Dotted lines join together runs with modified topside heating. Dashed lines join together runs with modified peak heating. The dot-dash line is joined to the run using a 'filled in' polar cap distribution.

within the polar cap, on which we have speculated above, would presumably generate heating across the whole polar region.

We have investigated the effect of a more distributed polar heat source by repeating the 6TW/40nb run using a latitudinal distribution representing a polar cap 'filled in' with uniform heating. This represents the opposite extreme to concentrating the heating in a narrow oval. The distribution is shown in Fig. 4.2 by the dot-dash line. In the runs using this distribution, we rescaled our peak heating rate q_{h0} to produce identical total energy inputs. The effect of this modification upon the auroral and mid-latitude temperatures is marked on Fig. 4.8 by the cross that is connected to the dot-dash line.

We find that the only significant effect of this modification is to alter the thermal structure and dynamics of the polar cap. Instead of the temperature peak just within the main oval, the temperature peak develops at the pole; and the two circulation cells redistributing heat into and away from the oval are replaced by a single circulation cell which redistributes heat

equatorwards. The auroral temperature, which we defined as an average across the polar cap, increases slightly (Fig. 4.8) because the hotspot generated by the heating lies fully within the region over which we average. This is thus largely a consequence of our definition of the auroral temperature.

The effect on the low latitude temperature is more interesting, in that it stays almost exactly the same. There is a slight increase but it is only of the order of 10-20K. This insensitivity to the polar cap energy distribution appears to be a consequence of the behaviour of the winds within the polar cap, which, as described in Section 4.4, almost 'fill in' the polar cap with a uniform temperature. The roughly uniform polar cap temperature then 'feeds' the global circulation. The exact polar cap energy distribution has a small effect on the resultant mid-latitude temperatures, but it is effectively negligible.

Thus we conclude that while the mid-latitude thermal structure is very sensitive to the vertical distribution of energy, it is almost entirely decoupled from the horizontal distribution of energy in the polar cap.

4.6.4 Importance of thermal conduction and viscosity

In the thermosphere mean free paths are large and molecular diffusion processes dominate the physics (see Section 2.5). Of particular importance are molecular thermal conduction (diffusion of heat energy) and molecular viscosity (diffusion of momentum and kinetic energy).

Thermal conduction is important because, in the absence of significant radiative cooling, it is the principle coolant of the thermosphere. The thermal conductive flux F (positive downwards) in the thermosphere is given by Eqn. 2.68. The altitude, z, depends on T because if the atmosphere is heated it will expand (Eqn. 1.5). Thus heating the thermosphere does not significantly change dT/dz. If κ_m was independent of temperature then the ability of thermal conduction to remove energy from the thermosphere would remain approximately constant as temperatures increased. However, κ_m is given by an expression of the form $\kappa_m = \lambda T^s$ where λ is a constant and $s \sim 0.7$ (Eqn 2.69 and Appendix A). Thus the thermal conductivity increases with temperature, but the non-linearity of the dependence means that the thermal conductivity increases more slowly with temperature than the internal energy of the gas $u = c_p T$. Due to this non-linearity, heating the thermosphere has a weak insulating effect, because higher temperatures lead to less efficient thermal conduction relative to the energy stored in the gas.

The consequence of this is that at higher temperatures the redistribution of energy by winds is more efficient, because conduction cools the gas less before it reaches mid-latitudes. This may explain the upwards curve of the lines in Figs. 4.5 and 4.6 as greater amounts of energy are input: the hotter models are closer to a situation in which the global temperature distribution is uniform.

The viscosity is also of importance to the effectiveness of the redistribution. The zonal

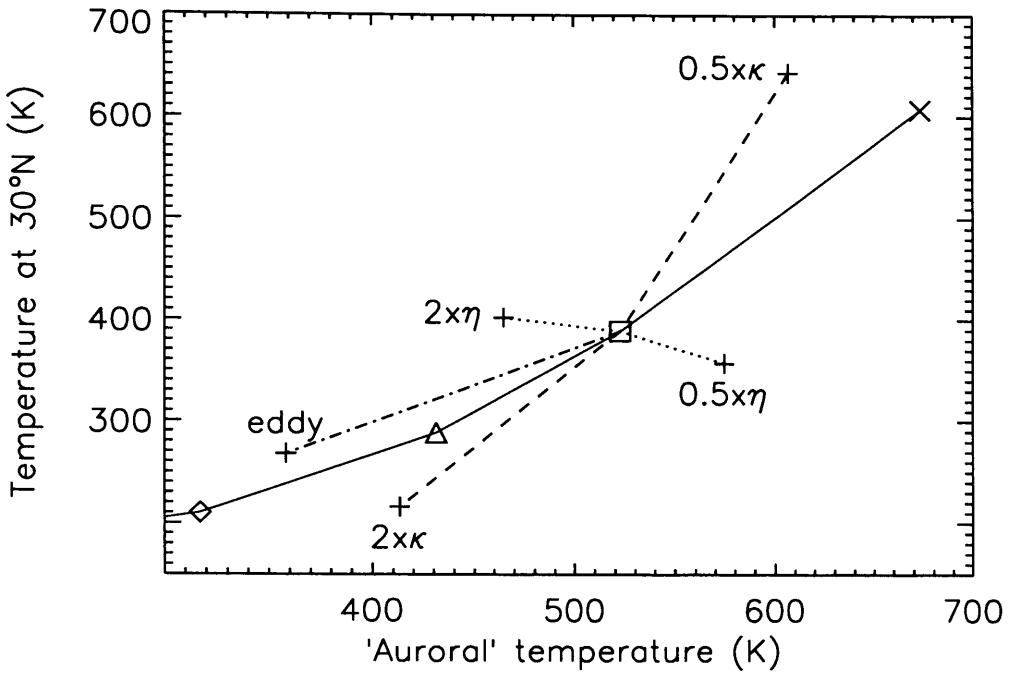

Figure 4.9: Effect of artifically altering the thermal conduction and viscosity. The square represents the standard 6TW/40nb run. The dotted line joins together the runs with modified viscosity η_m, as marked. The dashed line joins together the runs with modified thermal conductivity κ_m. The dot-dashed line shows the effects of including eddy diffusion effects in the conductivity and viscosity calculations.

force balance at high altitudes between vertical viscous drag and Coriolis forces is important in determining the speed of meridional winds. If the viscous drag is reduced a faster westward flow develops, increasing the poleward Coriolis forces, which slow the equatorwards flow. Thus a lower viscosity leads, perhaps counterintuitively, to less effective redistribution.

It is worth asking whether we may have underestimated the viscosity. The molecular viscosity μ is given by expressions of the form $\eta_m = \mu T^\beta$, where $s \sim 0.7$ (Eqn. 2.73 and Appendix A). For molecular hydrogen, the major gas in our model, $\mu = 1.46 \times 10^{-7}$ and for atomic hydrogen, the only other gas important at high altitudes, $\mu = 2.07 \times 10^{-7}$ (although see discussion in Appendix A). Note that the units of η_m are $\mathrm{kg\,m^{-1}s^{-1}}$. Thus atomic hydrogen is approximately 40% more viscous than molecular hydrogen. In our startup profiles atomic hydrogen represents no more than ~10% of the gas in the upper altitude ranges. This does not change because we run the models with fixed composition profiles. To significantly increase the viscosity would require a greater proportion of atomic hydrogen by tens of percent. However, the strong vertical winds in the auroral regions are likely to mix greater quantities of molecular hydrogen into

the high altitude regions, thus reducing the viscosity. To test this hypothesis we repeated the 6TW/40nb run with full composition transport calculations switched on. As expected, molecular hydrogen is transported into the high altitude regions. However, the effect on the thermal structure is negligible: temperature differences are of a few degrees Kelvin or less throughout the thermosphere. This justifies our decision to run the models with composition transport switched off.

To investigate the effect of different viscosities and thermal conductivities, we have repeated the 6TW/40nb run with the viscosity and thermal conductivities artificially modified. We have increased and decreased both parameters by a factor of 2. The effect of this is illustrated in Fig. 4.9. Increasing (decreasing) thermal conduction simply results in globally lower (higher) temperatures, as expected. The effect of altering the viscosity is more interesting. We expect a higher (lower) viscosity to enhance (inhibit) the redistribution of energy. This is the case: the temperature at mid-latitudes increases (decreases) by ~10-20K. However, the effect on the auroral temperature is much stronger. It decreases (increases) by about 50K. Thus the strongest effect that the viscosity has on the redistribution is to mediate the degree to which winds remove energy from the auroral regions. It has a weaker effect on the temperatures at mid-latitudes.

Finally we have investigated the effect of including eddy diffusion processes in our calculations of thermal conductivity and viscosity, applying a uniform eddy coefficient $K_\tau = 1.0 \times 10^3 \mathrm{m^2 s^{-1}}$as discussed by Müller-Wodarg et al. (2006). The result of this is shown in Fig. 4.9 by the cross connected to the dot-dash line. The resultant temperature distribution is uniformly cooler, but remains close to the locus of 40nb runs (the solid line). Thus the effect of including eddy processes seems to be an increase in the total energy required, but not in the distribution of that energy. The simple reason for this is that the eddy contribution to thermal conduction and viscosity is only important at very low altitude. The effect of the eddy viscosity is negligible, since the wind shears are small anyway at these altitudes. The eddy conduction is more important, but only has an influence very close to the mesopause. The result is that the eddy conduction simply makes the base of the thermosphere colder, and the temperatures throughout the rest of the thermosphere are uniformly shifted accordingly.

4.6.5 Angular momentum transport

Another perspective on the importance of viscosity is apparent if we consider the conservation of angular momentum. In our rotating frame, the axial angular momentum of a parcel of gas consists of two components: its angular momentum due to the rotation of the planet, and that due to its own velocity relative to the planet, i.e. that due to the zonal winds. In the absence of viscosity, the sum of these components must be conserved (see Read (1986) for a detailed discussion). To move gas from the polar regions (where the angular momentum due to the rotation of the planet is small) to the equatorial regions (where the angular momentum due to the

rotation of the planet is much greater) would thus require a reduction in the angular momentum due to the zonal winds. This implies the generation of fast westwards winds—comparable in magnitude to the rotation velocity of the planet—to keep the total angular momentum constant. In practice there is considerable viscosity in the thermosphere, and this supplies extra angular momentum from the lower atmosphere, allowing the gas to move equatorwards without the generation of unexpectedly fast zonal winds. Thus a higher viscosity leads to improved energy redistribution because it is able to supply more angular momentum to the thermosphere.

This analysis motivates us to consider two other possible mechanisms for supplying angular momentum to the thermosphere: gravity waves from the lower atmosphere and ion drag. The influence of gravity waves on the upper atmospheric flows are complicated at Earth and, given the very different nature of the deep atmosphere at Saturn, they are likely to have a different, and unknown, effect upon the upper atmosphere. It is possible that although supplying little energy to the upper atmosphere, gravity waves are able to provide a zonal drag that improves redistribution from the polar regions.

The effects of ion drag are slightly better understood. It is established that the inner magnetosphere almost corotates with Saturn (Richardson, 1986). It is driven into corotation by forces exerted by magnetosphere-ionosphere coupling currents. These currents transfer angular momentum from the conducting layer of the ionosphere to the magnetosphere. One would expect the same transfer of angular momentum to occur to high altitude regions of the thermosphere that also sub-corotate. Thus the existence of a significant Pedersen conductivity at high altitudes may allow the corotating lower thermosphere, where the conductivity is high, to transfer angular momentum to higher altitudes, where the conductivity is lower, but non-negligible.

4.6.6 Electrodynamics

One possibility for explaining the high low-latitude temperatures may lie in the electrodynamics of the equatorial region. The Earth's equatorial ionosphere is complex, due to the juxtaposition of a horizontal magnetic field and neutral wind-induced electric fields. The electron density is a minimum at the magnetic equator, and maximises each side of it due to the 'fountain effect' (Ratcliffe, 1972). Also there is a greatly enhanced conductivity in the E-region leading to the equatorial electrojet. Solving for these effects self-consistently is complex due to the global nature of the electrodynamical coupling (see e.g. Millward et al., 2001). The extent of these effects at Saturn is not known, although, like the Earth, Saturn has a strong equatorial magnetic field. It is possible there is substantial equatorial heating from electrojet currents. However, there is no *a priori* reason to think this might be the case, as the wind-induced electric fields on Saturn are not well-constrained. This will hopefully be investigated in the future with a more sophisticated version of the model.

4.7 Comparison with Jupiter

We will discover in Chapters 5 and 6 that the approach taken in this chapter of considering a pure input of thermal energy is probably rather naïve. For this reason we will not engage in a similar systematic study of polar heating inputs for the Jovian case. Instead, we will attempt to gain some insight into the differences between the planets by briefly investigating the importance of various parameters that govern the behaviour of the thermosphere.

Specifically, we investigate the importance of the planetary radius, rotation rate and surface gravity, and of the pressure of the mesopause. The radius and rotation rate are greater at Jupiter by less than 20%, the surface gravity by a factor ~2, and the mesopause pressure by a factor of ~20. These widely differing variations make it difficult to untangle the effect of each of these parameters if we simply convert the model directly to Jupiter. Hence we increase each of these parameters by 20%, in various combinations (detailed in Table 4.1, and described in more detail below) and investigate the differential effect of each of these small alterations on the output of our standard 6TW/40nb run. In each of these cases we fix the vertical distribution of the energy input relative to the mesopause, equivalent to fixing the ratio p_0/p_m.

Since the relative temperatures at low and high latitudes are largely determined by competition between conductive cooling of the atmosphere and energy redistribution by winds, we might expect the modified parameters to alter the global thermal structure by changing the balance between these processes. Inspecting the terms of the energy and momentum equations, we can divide them into three groups that scale with changes in different parameters:

$$\begin{aligned} \text{diffusive terms} &\sim g/p^2 \\ \text{Coriolis} &\sim \Omega \\ \text{hydrodynamic terms} &\sim 1/R \end{aligned} \tag{4.3}$$

where 'diffusive terms' refers to vertical thermal conductivity and viscosity, and 'hydrodynamic terms' refers to advection, pressure gradients and curvature terms.

Altering the balance between these terms will also change the equilibrium time constant of the thermosphere in complicated ways. We can thus not be sure that runs with modified parameters are equally close to steady state. However, experience with the model indicates that as models approach steady state they heat up at both low and high latitudes. Thus, on our temperature comparison plots, they move, roughly speaking, along the loci of constant energy input. Most of the error caused by non-equilibriation will therefore be in the direction from bottom-left towards top-right on our plots.

4.7.1 Radius and rotation rate

First we investigate the importance of the radius (run A) and rotation rate (run B). Note that run B has been run for 480 rotations, rather than the standard 400, since this corresponds to the same

	A	B	C	D	E	F
planetary radius (R)	$\times 1.2$					
angular velocity (Ω)		$\times 1.2$				
mesopause pressure (p_m)			$\times 1.2$	$\times 1.2$	$\times 1.2$	$\times 1.2$
gravity (g)			$\times 1.2$			
column mass (M_m)				$\times 1.2$	$\times 1.2$	$\times 1.2$
energy input (per kg)					$\div 1.2$	$\div 1.2$
energy input (per m^2)				$\times 1.2$		
run length						$\times 1.2$

Table 4.1: Modified planetary parameters for runs A-F. Spaces left blank indicate that the parameter is unaltered.

run time for a rotation rate increased by 20%. The results of these runs are shown in Fig. 4.10, in the usual format. Both of these runs produce very similar perturbations, increasing the auroral temperature by ~50K and decreasing the mid-latitude temperature by 10-20K. Intuitively, this is because increasing both the radius and rotation rate increases the importance of the Coriolis force, which is the principle barrier to redistribution by winds.

This is clearly the correct interpretation in the case of the increased rotation rate. However the Coriolis term is not proportional to the radius of the planet, so at first glance our intuitive understanding does not make sense. This is resolved if we consider that the hydrodynamic terms scale inversely with R, and are thus reduced relative to the Coriolis term by the increased radius. Thus, relatively speaking, the Coriolis force does become a more important term in the momentum equation.

This interpretation also explains the discrepancy between the change in temperature produced by runs A and B. The diffusive terms do not scale with either rotation rate or radius, and are thus unaffected in both of these runs. In the case of run A, the reduction in the importance of the hydrodynamic terms increases the relative importance of the diffusive terms. In the case of run B, the increase in the importance of the Coriolis term reduces the relative importance of the diffusive terms. Thus diffusive terms are more important in run A than in run B. We know that the main effect of enhancing the diffusive terms is to cool the model at all latitudes (see Fig. 4.9). This then explains why run A is slightly cooler than run B.

4.7.2 Mesopause pressure and gravity

The mesopause pressure p_m, the gravity g, and the column mass of the atmosphere above the mesopause M_m are related by the equation

$$p_m = gM_m \tag{4.4}$$

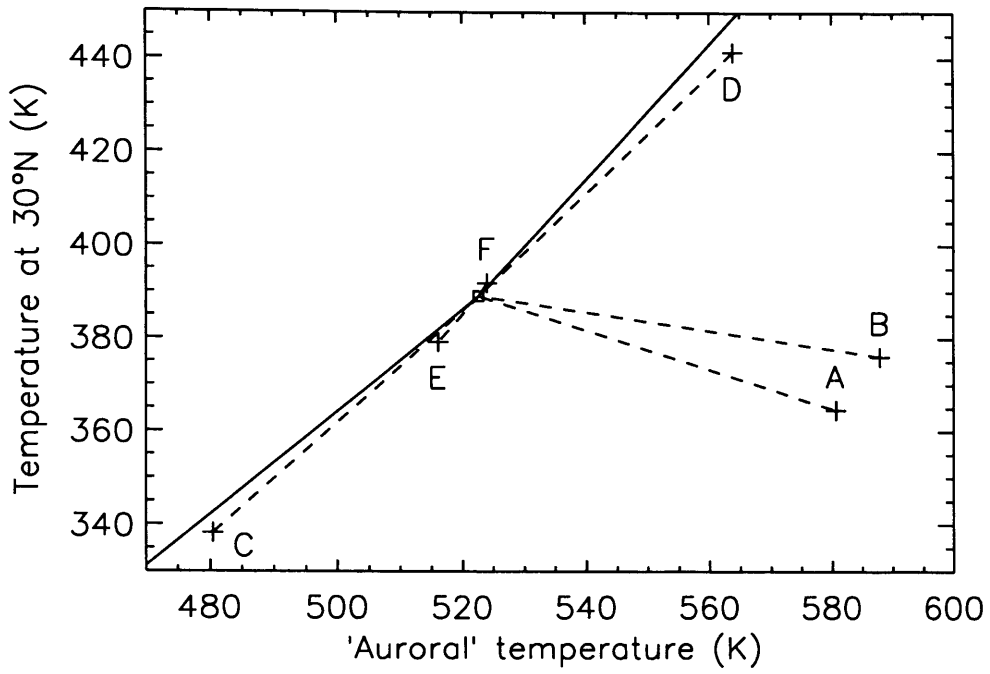

Figure 4.10: Sensitivity to modified planetary parameters. The square represents the standard 6TW/40nb run, and the solid line the locus of standard 40nb runs. The plus signs joined to the dashed lines then represent runs with modified parameters, as described in Table 4.1.

which follows from hydrostatic equilibrium. Thus we cannot change either the mesopause pressure or gravity without also changing the column mass, which is an important parameter in itself.

Our initial approach to these parameters is therefore to increase the mesopause pressure by changing g and M_m in turn. Run C thus represents an atmosphere with g and p_m increased by 20%, and run D an atmosphere with M_m and p_m increased by 20%. In both cases we keep the energy input per unit mass fixed; in the case of run D this obviously requires increasing the total energy input. The results of these runs are plotted in Fig. 4.10.

These two runs have almost exactly opposite effects. Run C shows cooling at all latitudes, close to the locus of 40nb runs, and run D shows heating at all latitudes, following the locus of 40nb runs in the opposite direction. We can understand this behaviour by observing that the scaling relations above (Eqn. 4.3) indicate that only the diffusive terms depend directly on the pressure and gravity, scaling as the quantity

$$g^2/p_m = g/M_m \tag{4.5}$$

and thus increasing g increases the importance of diffusion and increasing M_m decreases the im-

portance of diffusion. Again we note from Fig. 4.9 that the main effect of increasing (decreasing) diffusive processes is to uniformly cool (heat) the atmosphere. This then explains rather easily the behaviour of runs C and D.

It is worth offering some simple physical explanations for this dependence of the diffusive terms on g and M_m. In the case of an increased value of g, this leads to smaller atmospheric scale heights, so the atmosphere is considerably more compressed in the vertical direction. This makes diffusive processes more effective, since given a fixed thermal structure with respect to pressure, the vertical temperature and velocity gradients are increased.

In the case of an increased value of M_m, with gravity fixed, this is equivalent to increasing the number of particles present in the thermosphere, while keeping its physical dimensions fixed. The hydrodynamic and Coriolis terms are unaffected by this: inertial forces, advection and pressure gradients all act with twice the magnitude but on twice as much mass. The efficiency of diffusive processes is affected differently, because although mean free paths are reduced by the greater number density, there are now more particles present to participate in diffusive transport, so the diffusive fluxes of energy and momentum remain the same.

Thus, whereas the actual quantity of energy and momentum transported in the bulk flow processes increases with the mass density, the quantity of energy and momentum transported by diffusive processes remains unchanged. If the energy per unit mass is fixed, then we have a greater amount of energy entering the thermosphere, but no equivalent increase in the efficiency of conductive cooling. This explains the higher temperatures.

This observation motivates us to carry out two further runs. In Section 2.4, we showed that if thermal conduction is the only energy transfer process, then the thermal structure depends only on the gravity, the total energy input, and the pressure contrast between the mesopause and the energy input (Eqn. 2.72). It does not depend on the absolute pressure or column mass. For run E we therefore repeat run D, but do not scale the energy input with the column mass. The only difference between run E and the standard 6TW/40nb run is then that the column mass M_m, mesopause pressure p_m, and peak heating pressure p_0 are all 20% greater.

The result of this run is shown on Fig. 4.10. It is clear that it produces very nearly the same thermal structure as the standard run, in good agreement with Eqn. 2.72. The offset is only of the order of $\sim$10K in both temperatures, much less than the effect of any of the other modifications described above. This suggests that the implication of Eqn. 2.72 that the thermal structure depends more strongly on the quantity of energy than on the quantity of mass is a good approximation even when redistribution of energy by winds is an important process.

However, increasing the mass must increase the equilibriation time constant even if it does not significantly effect the resultant thermal structure. We would expect the time constant to increase approximately in proportion to the column mass. To test this, run F is identical to run E but has been run for a further 80 planetary rotations, increasing its runtime by 20%. As

shown in Fig. 4.10, this results in almost identical conditions to the standard run, supporting the notion that the thermal structure is almost independent of the total mass of the thermosphere. It is interesting that, even in the presence of winds, a theory based on energy transfer by thermal conduction alone still describes quite accurately a basic property of the thermosphere.

4.7.3 Consequences for Jupiter

These experiments show that the greater mesopause pressure at Jupiter does not, by itself, imply that greater energy inputs are required to reproduce the temperatures observed at Saturn. However, the higher gravity will improve the efficiency of thermal conduction, and taken together with the requirement of higher temperatures at Jupiter ($\sim$ 1000K globally) this implies that the energy inputs must be substantially greater than 6TW to resolve the energy crisis. The effect of the larger radius and rotation rate will exacerbate this situation. We will not attempt an explicit assessment of Jupiter's thermal structure here, but will return to the issue in Chapter 6, in which we will examine the specific possibility that the component of Joule heating due to rapid fluctuations in the electric field may be responsible for the high thermospheric temperatures.

4.8 Conclusions

The simulations described in this chapter have examined the effect of a general polar heating input on Saturn's thermosphere. We find that for our chosen heating distributions an input of $\sim$8TW peaking at 60nb can explain both the Smith et al. (1983) determination of temperature at 30°N and auroral H_3^+ temperatures (Melin, 2006). However, it is not possible to find a reasonable energy input distribution which is consistent with both the auroral measurements and the Festou and Atreya (1982) determination for 4°N. By seeking to match both auroral and mid-latitude constraints we have been able to constrain the possible heating distributions more narrowly than would have been possible with one constraint only.

We have also indicated the sensitivity of the thermal structure to the topside heating profile, and shown that the latitudinal structure of the polar heating is less important than the total heating powers and vertical heating profile for determining the mid-latitude thermal structure.

More detailed considerations of the sensitivity of the model to thermal conduction and viscosity showed that a higher viscosity tends to improve redistribution of energy by winds, by enhancing the upwards transfer of angular momentum that opposes the Coriolis force. Unfortunately, any process that might increase the viscosity is likely to be accompanied by an increase in the thermal conductivity, which uniformly cools the thermosphere. Thus an enhanced eddy coefficient cannot be invoked to improve the efficiency of the redistributive winds.

A further analysis of planetary parameters that differ between Jupiter and Saturn has been carried out, demonstrating the importance of the complex balance between energy transport by

winds and by diffusion. This analysis demonstrates clearly that polar energy inputs at Jupiter must be considerably greater than those required at Saturn to explain the observed thermospheric temperatures.

This study has also raised many open questions concerning the complex effects of Joule heating and ion drag on the thermospheric temperature and circulation, and it is to these that we turn in the next two chapters.

Chapter 5

Saturn

We now focus on the specific case of energy and momentum inputs directly associated with the magnetosphere-ionosphere coupling currents, i.e. Joule heating and ion drag. We use the magnetosphere and conductivity models described in Chapter 2 and the magnetic field model described in Appendix C to simulate these processes. We run the thermosphere model with a latitudinal resolution of 0.2° and with 55 pressure levels at a 0.2 scale height spacing. As before, we use a lower boundary condition of zero neutral wind velocity and 143K. Our standard runs employ an eddy coefficient $K_\tau = 10^3 \mathrm{m}^2\mathrm{s}^{-1}$. We calculate both viscosity and thermal conductivity due to eddy processes, but, as discussed in Chapter 2, we omit the second term in the eddy conduction flux. Each model has been run for 400 rotations to ensure it is almost in thermal equilibrium.

We again assume zonal symmetry, but also introduce the additional assumption of hemispheric symmetry. This latter assumption is motivated by the observation that in an equinox configuration the northern and southern hemispheres of the planet exhibit almost identical behaviour. We thus calculate winds for the northern hemisphere only. Our equatorial boundary condition is that the zonal winds just south of the equator are identical to the zonal winds just north of the equator, and that the meridional winds at the equator are zero.

5.1 Initial observations on ion-neutral coupling

As discussed in Chapter 2, the coupling between the magnetosphere and thermosphere that leads to Joule heating (direct thermal energy input) and ion drag (kinetic energy input) can be viewed as analagous to a frictional interaction mediated by the coupling currents. This frictional interaction is not only the source of the energy inputs to the thermosphere, it is also the cause of the rotation of the magnetosphere. This motivates us to analyse both of these problems in as unified a manner as possible.

With this approach in mind, our initial model run exposes an interesting physical inconsis-

tency in our magnetosphere model, which at present is a fixed model represented by Eqn. 2.8. This model for Ω_M and the rotational velocity of the thermosphere Ω_T resulting from our initial model run are shown in Fig. 5.1a. We also show the torque on the thermosphere (Fig. 5.1b), the field-aligned currents in the ionosphere (Fig. 5.1c) and K (Fig. 5.1d).

Evidently the thermosphere does not respond to the magnetospheric forcing with a constant value of K at all latitudes. Polewards of 70° latitude it lies consistently in the range 0.3 to 0.9, but there is substantial structure, especially close to the boundaries of region B (the grey shaded area). The cause of these sharp peaks and troughs in K can be traced to the neutral angular velocities in Fig. 5.1a. The latitude profile of the neutral velocity is substantially smoothed compared to the profile of plasma velocity. We will show in Section 5.3 that this smoothing is largely the result of advection related to the thermospheric wind systems that will be described in Section 5.2. This smoothed neutral velocity field results in a 'wiggly' profile of K. In particular, K exhibits peaks just inside region B and troughs just outside region B.

This is clearly a very different situation from that arising if K is a constant, shown with the dotted line. In this simple situation, the neutral atmosphere follows the sharp gradients in the plasma velocity exactly, by definition.

The physical consequence of this latitudinal smoothing of the neutrals relative to the plasma is illustrated in Fig. 5.1b, which shows the corotational torque exerted on the magnetosphere by the thermosphere at each co-latitude. In steady state this must of course be equal to the anti-corotational torque exerted on the thermosphere by the magnetosphere. The troughs and peaks of K are replicated in the latitudinal profile of torque. In particular, the torque drops to small values close to the inner edges of region B (labels 2 and 3). Just outside the poleward edge, the torque is strongly peaked (label 1), and just outside the equatorwards edge there is a small but distinct shelf (label 4). These structures are not observed if K is constant, as shown by the dotted line.

These peaks and troughs are important because the model we have constructed is intended to represent the mean, steady state configuration of the coupled thermosphere-magnetosphere system. If the thermosphere exerts the complex corotational torque shown in Fig. 5.1b upon the magnetosphere, an equally complex anti-corotational torque must be exerted on the magnetosphere by some other process to ensure steady-state. This anti-corotational torque must either be an inertial effect — i.e. a result of mass-loading or radial motions of plasma — or associated with solar-wind coupling.

To support the model of Cowley et al. (2004b) requires us to postulate the existence of such a torque — of precisely the form shown — in order to maintain the regions of constant rotational velocity. We have no reason to suppose that such a torque exists. The data on which the Cowley et al. (2004b) model is based is rather scattered (see Fig. 2.1), and the inclusion of approximately constant regions of flow was made for reasons of simplicity. Our initial study of

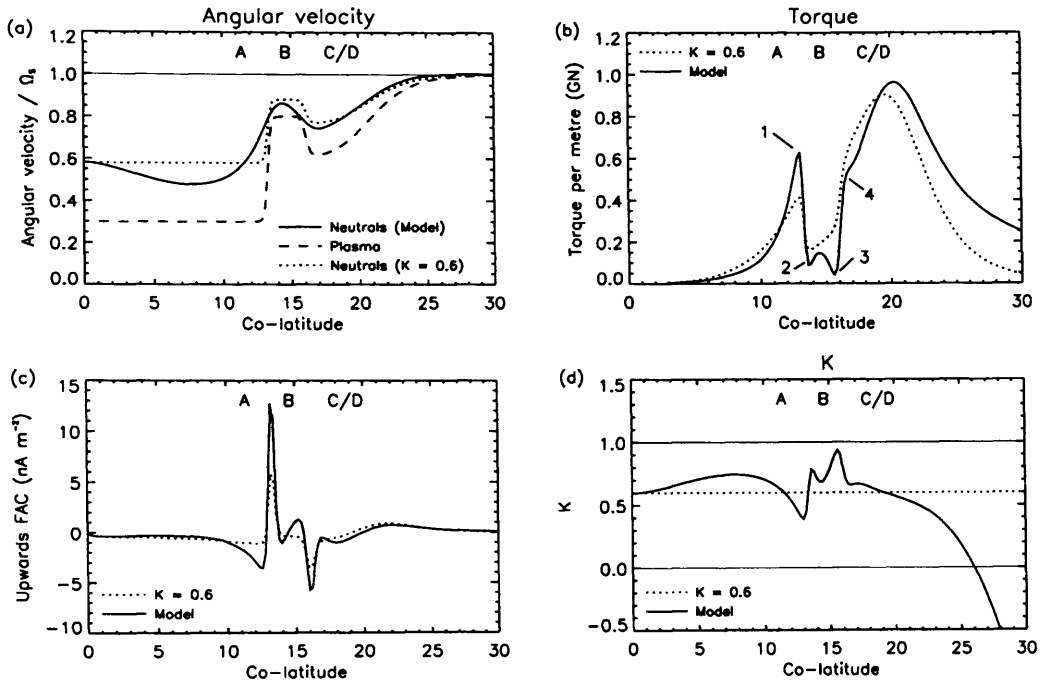

Figure 5.1: Parameters for our initial magnetosphere model (Ω-model). In each plot the grey shaded area represents region B of the magnetosphere model. (a) Angular velocities. Solid line: height-integrated thermospheric angular velocity Ω_T, calculated using the thermosphere model. Dashed line: plasma angular velocity Ω_M. Dotted line: height-integrated thermospheric angular velocity Ω_T inferred from Ω_M if $K = 0.6$. (b) Anti-corotational (corotational) torque exerted by the magnetosphere (thermosphere) on the thermosphere (magnetosphere), as a function of latitude in the thermosphere. The torque is expressed in units of torque per metre of latitude. Solid line: torque calculated using thermosphere model; dotted line: torque inferred if $K = 0.6$. (c) Upwards field-aligned currents in the ionosphere calculated using the thermosphere model (solid line) and the assumption that $K = 0.6$ (dotted line). (d) The thermospheric slippage parameter K, as a function of latitude. Solid line: K calculated from thermospheric model. Dotted line: $K = 0.6$.

the neutral atmospheric response shows that for the apparently simple model to be correct, it must be supported by finely tuned complex processes for which we have no evidence.

We are thus motivated to improve the plasma velocity model such that the behaviour of the neutrals is taken into account. Our improved model follows from two observations. Firstly, the torque required to maintain a rotation velocity Ω_M should be roughly proportional to that rotation velocity; secondly, the torque exerted by the thermosphere that might maintain this rotation velocity is proportional to $\Omega_T - \Omega_M$. We can thus equate these two quantities, with some suitable constant of proportionality α:

$$\Omega_M = \alpha(\Omega_T - \Omega_M) \tag{5.1}$$

We expect this quantity α to depend on the physical conditions in the magnetosphere and ionosphere that correspond to each shell of flux tubes. A large value of α means that a relatively small velocity difference $\Omega_T - \Omega_M$ is required to enforce rotation at the velocity Ω_M: this might correspond, for example, either to a large ionospheric conductivity or to very low mass-loading of the magnetosphere.

We may re-express this relation:

$$\Omega_M = \Omega_T \frac{\alpha}{1+\alpha} \tag{5.2}$$

Thus, if $\alpha \rightarrow \infty$, then $\Omega_M \rightarrow \Omega_T$ and the magnetosphere corotates with the thermosphere. If $\alpha \rightarrow 0$, then $\Omega_M \rightarrow 0$ and the magnetosphere acquires a negligible rotation velocity.

It is convenient to write the ratio between the magnetospheric and thermospheric velocities as a parameter which we call χ:

$$\chi = \frac{\Omega_M}{\Omega_T} \tag{5.3}$$

This parameter is conceptually somewhat similar to K. The traditional description of the thermospheric behaviour using a constant value of K packages a variety of complex thermospheric processes into a single parameter which represents 'slippage' from the thermosphere's natural state of perfect corotation. The new parameter χ likewise parameterises the complex behaviour of the magnetosphere, representing 'slippage' of the magnetosphere from its natural state of almost zero corotation. (Note that this simple theoretical description of the magnetospheric slippage happens to correspond exactly to the physical model of the polar cap (region A) plasma angular velocity due to Isbell et al. (1984) (see Appendix B), in which the dimensionless conductivity parameter σ is equivalent to the parameter α briefly introduced above.)

To improve the plasma flow model, we now make the assumption that this quantity χ is approximately constant across each of the flow regions defined by Cowley et al. (2004b). This is, of course, a simplification. However, given the lack of better physical models for the plasma flow, especially in region B, such a simplification seems justified, and indeed still represents a significant improvement over a fixed plasma flow model. For region A we do possess a physical model of the plasma flow: this will be discussed further in Section 5.5.

We then simply replace Eqn. 2.8 with an equivalent model for χ:

$$\begin{aligned}\chi(F) &= \chi_A \\ &+ (\chi_B - \chi_A)T_{AB}(F) \\ &+ (\chi_C - \chi_B)T_{BC}(F) \\ &+ (\chi_D - \chi_C)T_{CD}(F) \end{aligned} \tag{5.4}$$

where the functions T_{XY} are unchanged. We may then determine Ω_M at any point by combining Eqns. 5.3 and 5.4. From henceforth we will refer to this modified model as the 'χ-model' and the original model as the 'Ω-model'.

It is clear that we also require values for the parameters χ_{A-D} that define the actual flow velocities generated by the model. It is important that we continue to be guided by the empirical considerations that determine the flow velocities in the Cowley et al. (2004b) model. Thus we define three 'anchor points' F_{A-C} in each of the flow regions A-C. We demand that the flow velocity at each of these points is identical to that in the original model. This is enough to specify the parameters χ_{A-C}. We set $F_A = 700\text{nTR}_S^2$ and $F_B = 1900\text{nTR}_S^2$ such that the anchor points lie approximately in the 'middle' of each region in terms of magnetic flux. We set $F_C = 2400\text{nTR}_S^2$ such that the minimum rotational velocity in this region lies at approximately the same latitude as in the original model. Finally we fix $\chi_D = 1$ such that the inner magnetosphere perfectly corotates with respect to the thermosphere. We recalculate the flow velocities implied by this model after each timestep of the thermosphere model, such that the magnetospheric rotation is continually updated with reference to any changes in the thermospheric flow.

Fig. 5.2 shows the resultant structure of both Ω_M and Ω_T in the same format as Fig. 5.1. It can be seen that the thermospheric response is very similar. However, the sharp gradients in the magnetosphere model have been smoothed in response to the thermospheric structure. The basic shape of Ω_M remains similar to the previous fixed model, and is still consistent with the rather scattered data points (see Fig. 2.1 and discussion in Section 5.6). The torque (Fig. 5.2b) is now a smooth function in each region, consistent with our desire to represent approximately uniform physical properties in each region of the magnetosphere. Note that K (Fig. 5.2d) still exhibits peaks and troughs, but is considerably more smooth as a function of latitude.

This smoothing of the magnetosphere by the thermosphere indicates an alternative perspective on the interaction. Looking again at Fig. 5.1b, and in particular at the boundary between regions A and B, it is clear that on the polewards side of the boundary the torque exerted by our thermosphere model is greater than that exerted by the $K = 0.6$ model; on the equatorwards side the situation is reversed. Thus, if we suppose that the torque supplied to the magnetosphere by inertial effects and the solar wind interaction is similar to the $K = 0.6$ curve — i.e. similar to the torque implied by the original Cowley et al. model — the complex thermospheric torque will act to spin up the region polewards of the boundary and spin down the region equatorwards of the boundary, thus smoothing the transition between the two plasma regimes. This has the

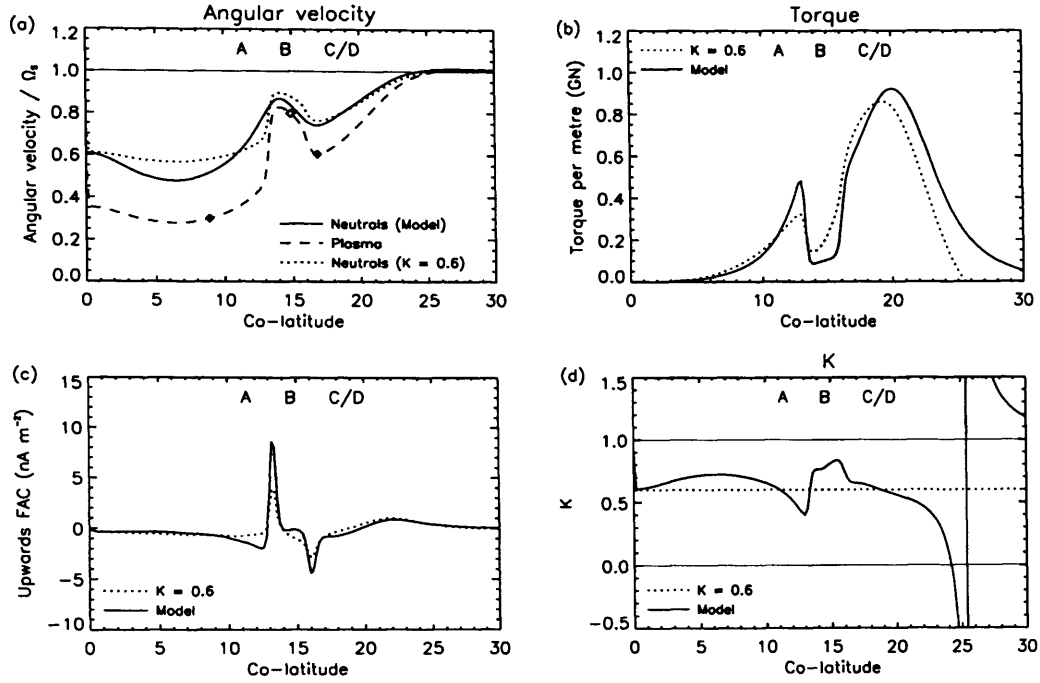

Figure 5.2: Parameters for our modified magnetosphere model (χ-model) in the same format as Fig. 5.1.

appearance of a viscosity acting between adjacent regions of the magnetosphere — or, in this particular case, between the outer magnetosphere and field lines open to the solar wind.

A not dissimilar situation to this was described by Pontius (1995) in the Jovian context, who argued that the 'flywheel' of the neutral upper atmosphere would smooth out structure in the Io plasma torus. However, our argument is more general. Any large scale change in the rotation velocity in some region of the magnetosphere will, inevitably, lead to a corresponding alteration in the rotation velocity of the neutrals connected to that region. This changed rotation velocity will be communicated by internal thermospheric processes (in Section 5.3 we will show that the principle process is transport by meridional winds) to nearby regions of the neutral atmosphere, which in turn will exert a torque back on a different region of the magnetosphere or connected solar wind. Thus motions in the neutral atmosphere mediate a viscous-like interaction between otherwise unconnected regions of the magnetosphere and solar wind.

The behaviour of the model at colatitude greater than 25° is also interesting. At these latitudes two apparently peculiar situations occur. Firstly K drops below zero. This indicates 'negative slippage'. K is intended to represent the extent to which the neutrals slip below corotation. Thus, when it becomes negative it means that the neutrals have been accelerated above corotation. This super-corotation is due to thermospheric effects that will be discussed in

greater detail below. At 26° colatitude, K goes towards negative infinity and then 'flips over' to values much greater than positive unity. This occurs because this is the region in which the magnetosphere is assumed to corotate with the neutrals. Thus, if the neutrals cross over the corotation line to super-corotation — implying $K < 0$ — there is also likely to be a point at which the plasma velocity curve crosses over perfect corotation. At this point $K \rightarrow \infty$, since the denominator in its definition (Eqn. 2.56) is zero. Equatorwards of this point both the neutrals and plasma slightly super-corotate, and K becomes positive again. The strange behaviour of K is thus just a consequence of its definition in terms of the planetary rotation velocity Ω_S and the assumption that all rotation velocities in the system must represent sub-corotation with respect to this reference velocity. When the situation is complicated by the inclusion of a full dynamical model of the thermosphere, the usefulness of K is perhaps questionable.

Nevertheless, the super-corotation is interesting in itself in that it indicates that magnetospheric super-corotation can arise naturally as a result of thermospheric dynamics. This offers the possibility that points in the Voyager data that appear to super-corotate may not be anomalous or a consequence of fluctuations, but may be persistent features with a simple physical explanation. The Voyager 2 data shown in Fig. 2.1 exhibit super-corotation in the inner magnetosphere of perhaps ~5%. Our results do not show super-corotation of this magnitude, but we do reproduce this effect qualitatively.

A corollary advantage of our modified model is that it is now extremely unlikely that a situation will arise in which the magnetosphere rotates more quickly than the thermosphere ($\Omega_M > \Omega_T$). (If we do not modify the model this situation does arise in some of the runs described later in the chapter.) If $\Omega_M > \Omega_T$ we would require an extra corotational torque on the magnetosphere to make it rotate more quickly than the thermosphere. To rule this out we need only repeat the arguments exercised above, but in this case we would require a complex torque containing both corotational and anti-corotational regions. This is clearly an even more improbable situation than those that have already been rejected.

Finally we comment on the field-aligned currents (FACs) generated by the models described above (Figs. 5.1c and 5.2c). In each figure, the solid line represents FACs calculated using our thermospheric model, and the dotted line FACs calculated using the assumption that $K = 0.6$ and the plasma velocities shown. Firstly, we note that the magnitude of these currents is much less than that predicted by Cowley et al. (2004b); this is simply because our solar-produced conductivity model has height-integrated conductivities much less than 1 mho. This will be discussed further in Section 5.4.

More interestingly, the FACs calculated with the thermosphere model are greater in both cases than those calculated assuming $K = 0.6$. This is because the 'smoothed' thermosphere responds slowly to changes in the plasma velocity, such that the *relative* velocity of plasma and neutrals changes much more quickly. This leads to a greater divergence of the Pedersen current,

and a greater FAC.

Our thermospheric calculations thus have an important influence on the intensity of current sheets that may generate aurorae. In general our thermosphere model acts to intensify current sheets compared to the normal assumptions. The introduction of the χ-model reduces this effect slightly. It is clear that an accurate characterisation of both the plasma and neutral velocities at these boundaries is necessary to calculate accurate intensities for FACs.

In practice it is not possible for all modelling of auroral current sheets to include full neutral atmosphere models; nor can such models be considered reliable given the lack of data available for validation studies. However, since the smeared thermospheric response has been shown to intensify the current sheets, it would not be unreasonable to calculate the parameters of auroral current sheets using a constant K model: the intensities so calculated would then constitute the lower limit of a full calculation.

5.2 Thermospheric response

We now embark on an analysis of the thermospheric response to the magnetospheric drag. Our approach is first to give a qualitative summary of the thermospheric structure, and then to give a more detailed quantitative analysis of the behaviour.

5.2.1 Qualitative behaviour

The basic response is summarised in Figure 5.3, which shows the temperature field and neutral winds in the polar regions of the planet when the thermosphere is forced using the χ-model described above. Regions where the Joule heating exceeds 2 W/m are hatched; closed contours of ion drag energy input are also shown at -2 W/m (dotted) and +2 W/m (dashed). The solid line shows the altitude of the peak of the per unit mass Pedersen conductivity s_P.

It is worth noting the similarities and differences between this model output and the pure heating case described in Chapter 4. Firstly, the temperature distribution peaks at the pole, not in the region of peak energy input. Furthermore, there is no super-corotation at the pole — polewards of 25° colatitude the atmosphere almost exclusively sub-corotates. This latter effect is an unsurprising consequence of the imposition of a sub-corotational ion drag. A second interesting feature is the cool region at low altitudes between 20° and 25° colatitude. This is associated with a polewards flow, whose driving force is not immediately apparent.

Indeed, the flow patterns in the polar cap region are very different to those in the pure heating case. In particular, there is a strong polewards flow everywhere at low altitudes, and polewards of 24° colatitude this flow is against the pressure gradient. At high altitudes there is a fast equatorwards flow in the direction of the pressure gradient, familiar from the pure heating case. To untangle this behaviour we attempt to separate the influence of ion drag and Joule

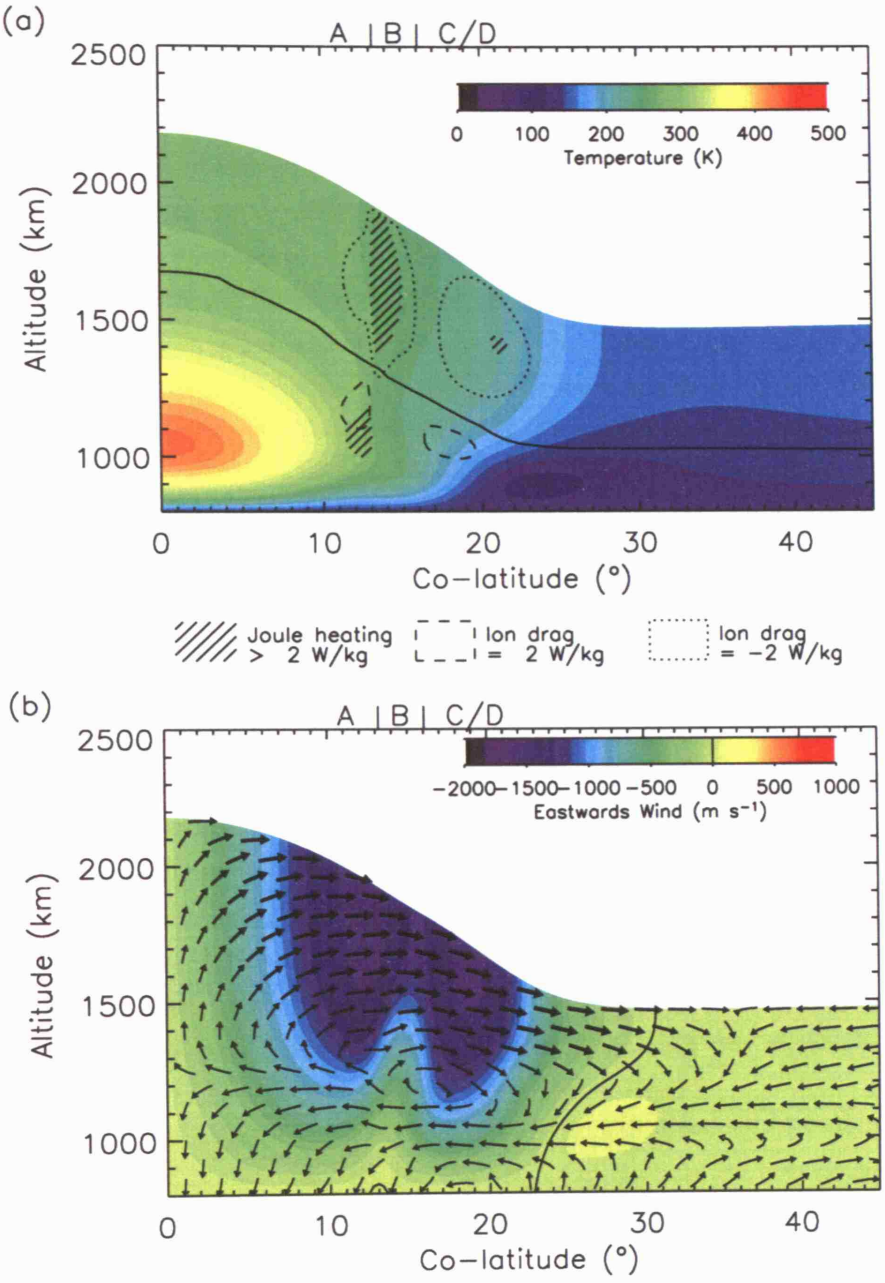

Figure 5.3: Thermal and dynamical structure of the polar cap for the χ-model, in a similar format to Fig. 4.4. In the upper plot regions where the Joule heating exceeds 2 W/kg are hatched and closed contours of ion drag energy input are shown at -2 W/kg (dotted) and +2 W/kg (dashed). The solid line indicates the peak altitude of the Pedersen conductivity per unit mass s_P.

heating by performing two further 'thought experiment' model runs in which each, respectively, is switched off.

Switching off ion drag entails omitting the inputs of both energy and momentum that it provides. If we do this in the simplest conceivable manner — by simply artificially setting these terms to zero in the model — we find that the Joule heating becomes very large and heats the model to temperatures of the order of ~1000K. This is because, as discussed in Chapter 2, the Joule heating represents thermalisation of the relative K.E. of the neutrals and plasma. If this thermalisation is allowed to occur without the K.E. of the neutrals being correspondingly reduced by ion drag, we introduce a situation in which thermal energy may be extracted from the neutral winds *ad infinitum*. To avoid this situation we instead take the Joule heating inputs calculated using the full model — i.e. those illustrated in Fig. 5.3 — and impose them on the model using the same method as the runs described in Chapter 4, with the ion drag set to zero.

The result of this run is shown in Fig. 5.4, in the same format as Fig. 5.3. These results are rather different from those with ion drag included. The temperatures are somewhat lower than in the full model run, and the temperature peak now lies close to the energy inputs. The circulation looks much more like that described in Chapter 4, with upwelling in the heated region, a double circulation cell towards and away from the pole, and a super-corotating jet inside the polar cap.

The striking difference between Figs. 5.3 and 5.4 suggests that it may be the ion drag, not the Joule heating, that dominates the thermal structure. In Fig. 5.5 we therefore show the results of a third run in which the Joule heating has been switched off. In this case there is no conceptual difficulty in artificially switching off the Joule heating; we need only imagine that the Joule heating is perfectly balanced by a very fortuitous distribution of radiative cooling, thus rendering the net thermal energy input zero. Indeed, were we to fix the ion drag energy and momentum inputs in the manner just described for the Joule heating, we might generate dangerous inconsistencies. For example, the region of corotational ion drag at high altitudes around 20° colatitude exists as a consequence of the sub-corotational winds at this altitude. If this ion drag were simply imposed on the model, it could potentially generate an unphysical super-corotational flow. Thus for the run with ion drag inputs only we simply set the Joule heating to zero and calculate the ion drag inputs self-consistently.

Initial inspection of the resultant circulation (Fig. 5.5) shows it to be very similar to the full model (Fig. 5.3). We again observe the hotspot at the pole, the cool region around ~20° colatitude, and a poleward flow at low latitudes. Temperatures, in general, are slightly lower than in the full model.

This picture indicates strongly that the ion drag dominates the thermal structure, while the Joule heating contributes a small additional increase in temperature across the polar region. One interesting effect of this small additional heating is that the thermally driven high-altitude wind (the wind driven by the meridional pressure gradient) in the full model (Fig. 5.3) penetrates

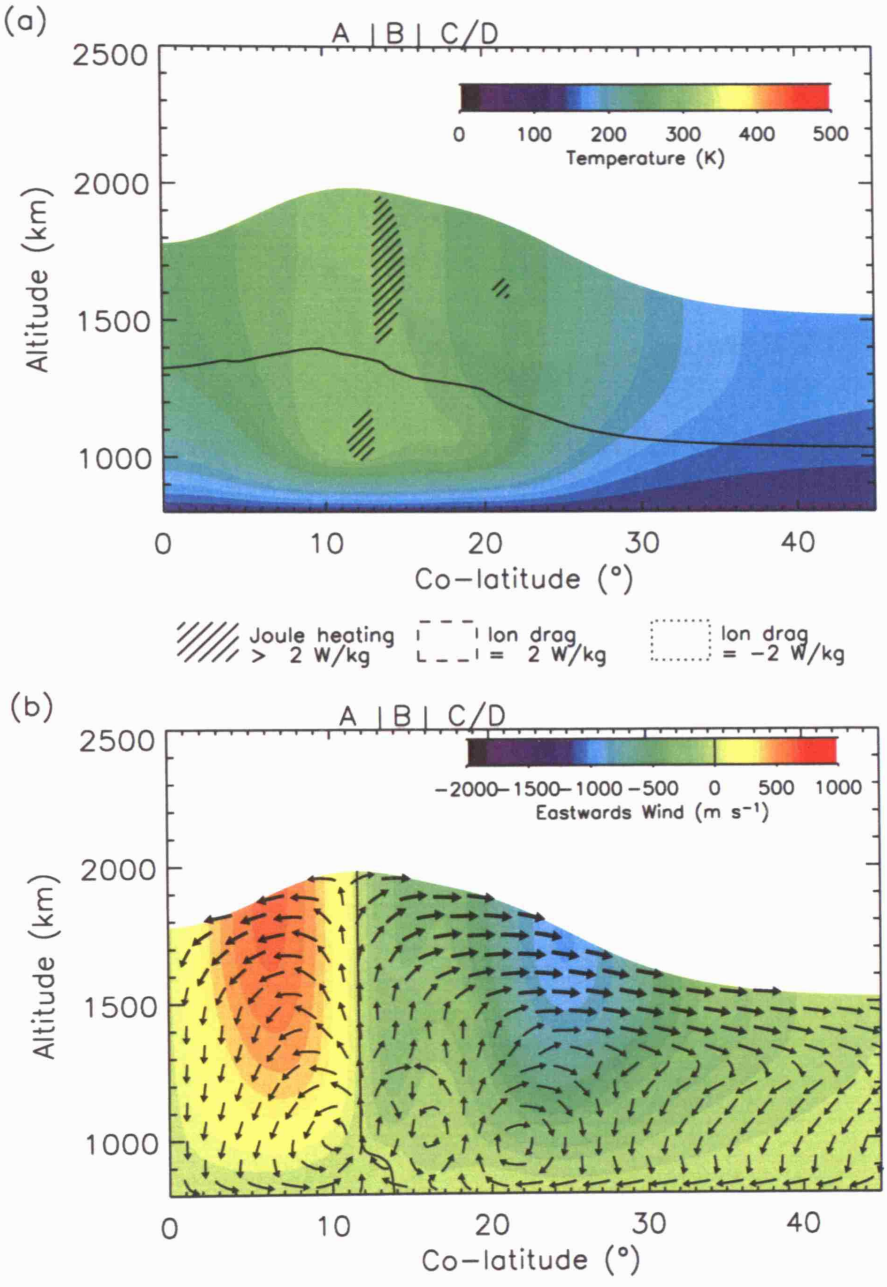

Figure 5.4: Polar circulation with ion drag switched off, in the same format as Fig. 5.3.

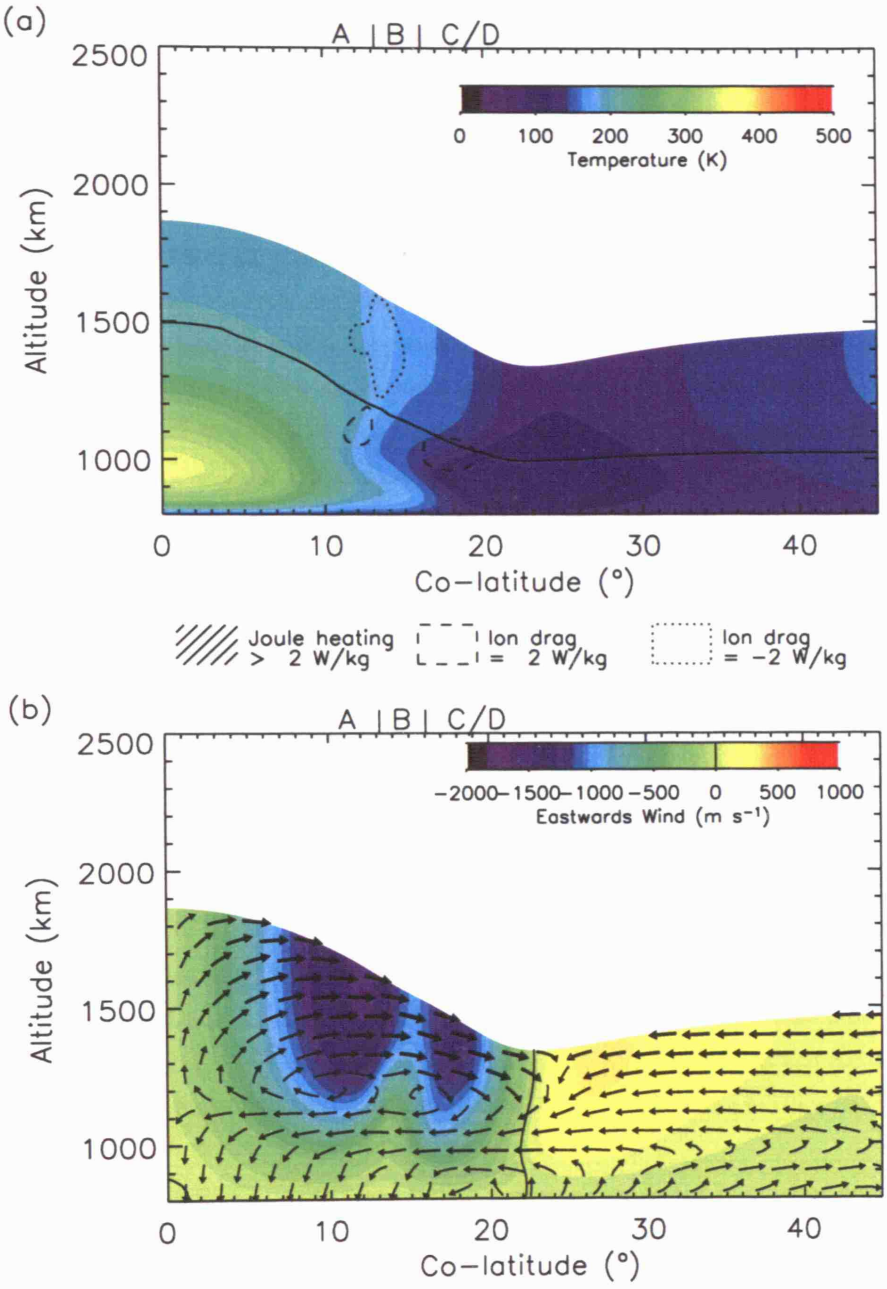

Figure 5.5: Polar circulation with Joule heating switched off, in the same format as Fig. 5.3.

to lower latitudes than in the model without Joule heating (Fig. 5.5). This thermally driven wind generates the patch of negative ion drag energy and positive Joule heating at high altitude around 20° colatitude that has already been mentioned. This represents thermalisation of the thermally driven wind — in other words the dynamics driven by the Joule heating generate further Joule heating at lower latitudes. Ultimately, this energy has presumably entered the system as thermal energy and has been stored as gravitational potential as the atmosphere has thermally expanded. It is then converted into K.E. as it drives winds down the pressure gradient; this K.E. is then rethermalised by the action of ion drag. During this transport process the thermal energy is degraded in the sense that it is associated with lower temperatures. This is thus a classic example of a thermally driven heat engine generating mechanical motion and then dissipating this energy as low level heat.

As further evidence that ion drag dominates the thermal structure, Fig. 5.6 illustrates a fourth run in which net energy inputs from Joule heating and ion drag are removed entirely, but momentum inputs from ion drag are retained. Since the energy input from ion drag is kinetic energy, and a momentum input necessitates a kinetic energy input, we achieve a net energy input of zero by adding a negative thermal energy component equal to the positive kinetic energy input due to ion drag. Again this may be thought of, conceptually, as a very fortuitous distribution of radiative cooling.

This run continues to show the basic features of the full model: a hotspot at the pole, a cool region around 20° colatitude, and a polewards flow at low altitudes. It is particularly striking that even though the net energy input is zero, the polar hotspot develops. For this to occur the winds driven by ion drag must be acting to extract energy from the cool region around 20° colatitude and move it towards the pole. This mechanism — which will be analysed in more detail below — clearly dominates the thermal structure of the polar region.

5.2.2 Quantitative analysis

Above we have described the principle features of the thermospheric response to Joule heating and ion drag. We now attempt to explain the origin of these features more quantitatively. For the purposes of this discussion we will refer extensively to Figs. 5.7, 5.8 and 5.9, which plot the various terms in the momentum and energy equations corresponding to the circulation shown in Fig. 5.3.

Figure 5.7 shows the acceleration terms corresponding to the meridional component of the momentum equation. Unshaded regions represent positive (equatorwards) values; shaded regions negative (polewards) values. The contours are separated at 50mm s^{-2} intervals between -500mm s^{-2} and 500mm s^{-2}; dashed lines are positive contours, dotted lines negative, and the zero line solid. Note that the balance is dominated by the Coriolis and pressure gradient terms. There is considerable structure in the zero contour of the other two terms shown, but most of this

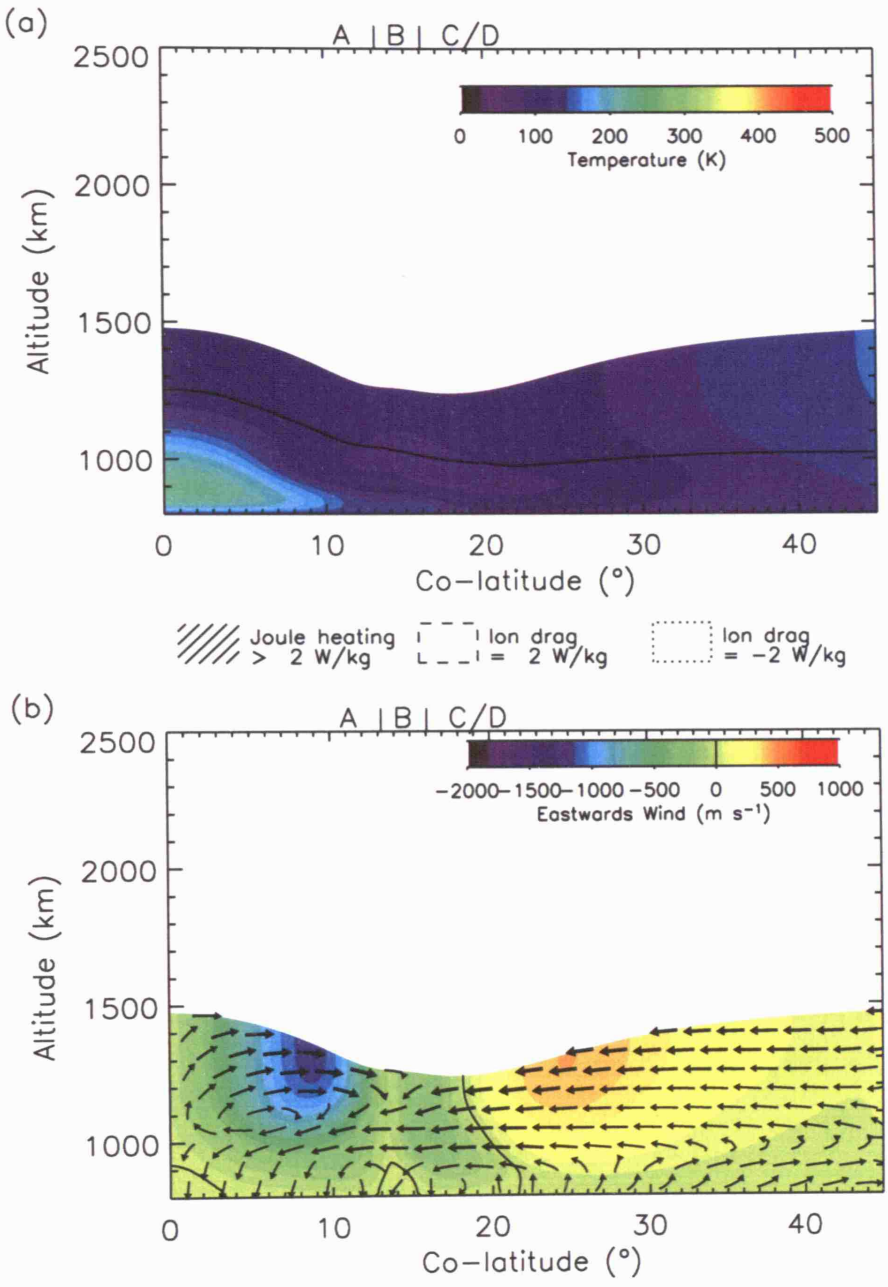

Figure 5.6: Polar circulation with Joule heating and ion drag energy switched off, in the same format as Fig. 5.3.

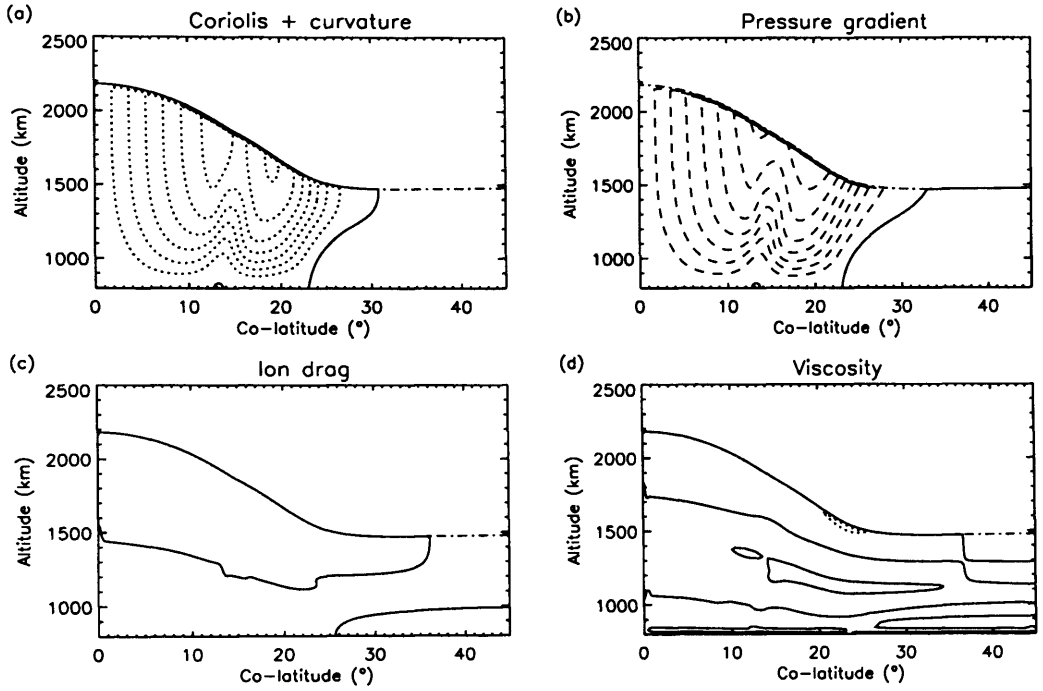

Figure 5.7: Meridional momentum terms corresponding to the circulation plotted in Fig. 5.3. (a) Coriolis and curvature. (b) Pressure gradient. (c) Ion drag. (d) Viscosity. Advection terms are almost negligible and are not shown. Solid contours: zero. Dashed contours: positive values separated by 50mm s^{-2} intervals up to 500mm s^{-2}. Dotted contours/shaded region: negative values separated by 50ms^{-2} intervals down to -500mm s^{-2}. The dot-dash line is the upper boundary of the model.

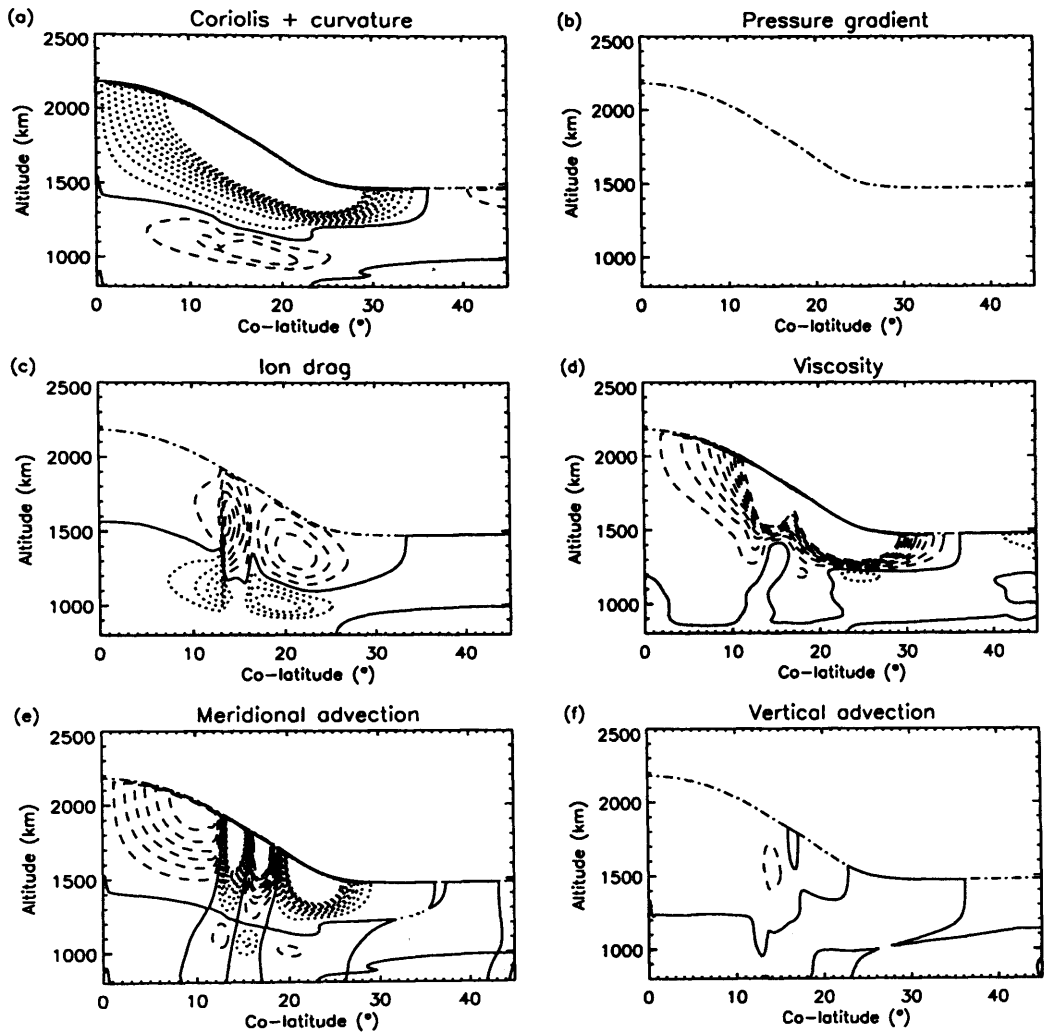

Figure 5.8: Zonal momentum terms corresponding to the circulation plotted in Fig. 5.3. Solid contours: zero. Dashed contours: positive values separated by 1mm s^{-2} intervals up to 10mm s^{-2}. Dotted contours/shaded region: negative values separated by 1mm s^{-2} intervals down to -10mm s^{-2}. The dot-dash line is the upper boundary of the model.

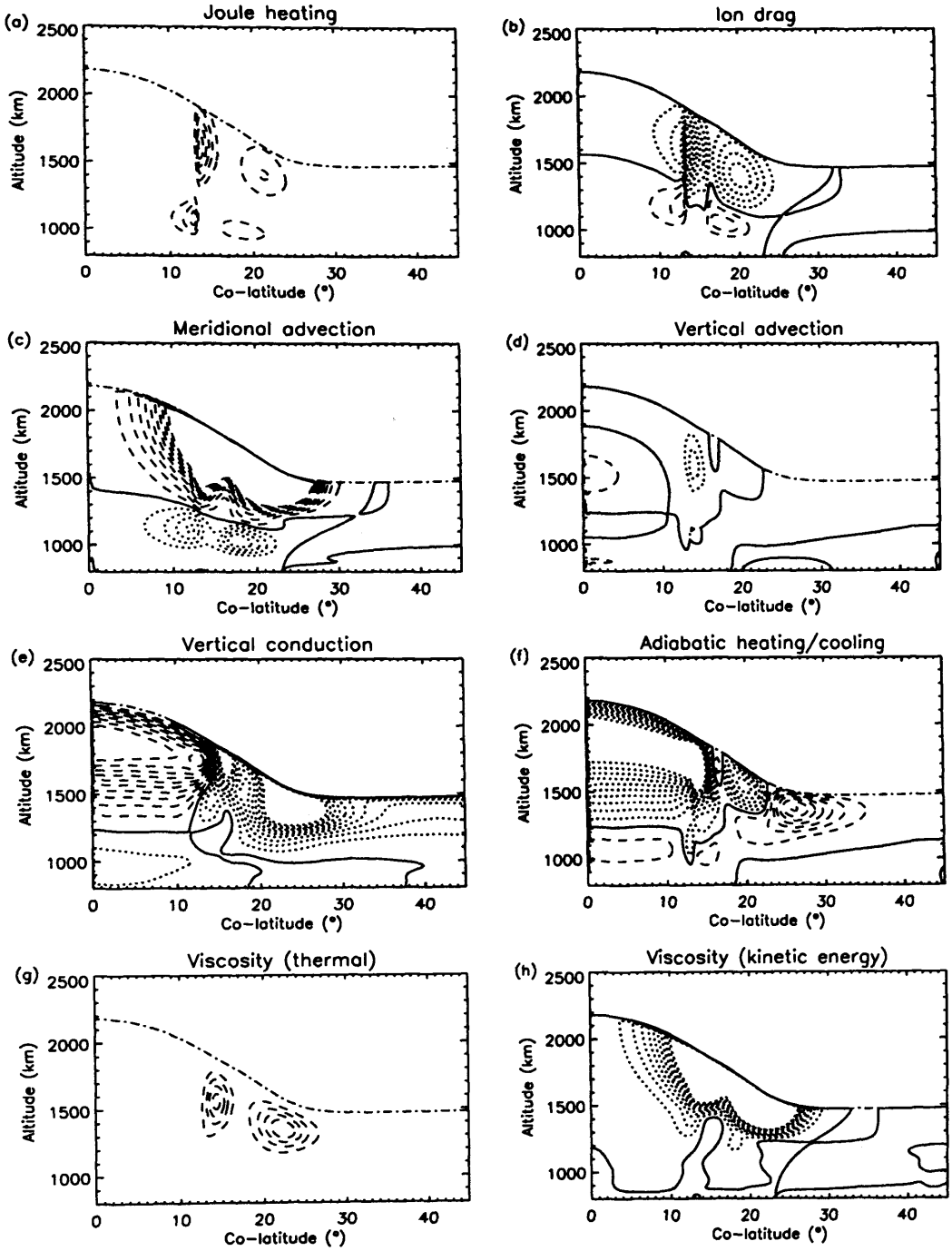

Figure 5.9: Energy terms corresponding to the circulation plotted in Fig. 5.3. Solid contours: zero. Dashed contours: positive values separated by 1 W/kg intervals up to 10 W/kg. Dotted contours/shaded region: negative values separated by 1 W/kg intervals down to -10 W/kg. The meridional and vertical advection terms influence the combined thermal and kinetic energy; all other terms influence the thermal or kinetic energy alone, as appropriate. The dot-dash line is the upper boundary of the model.

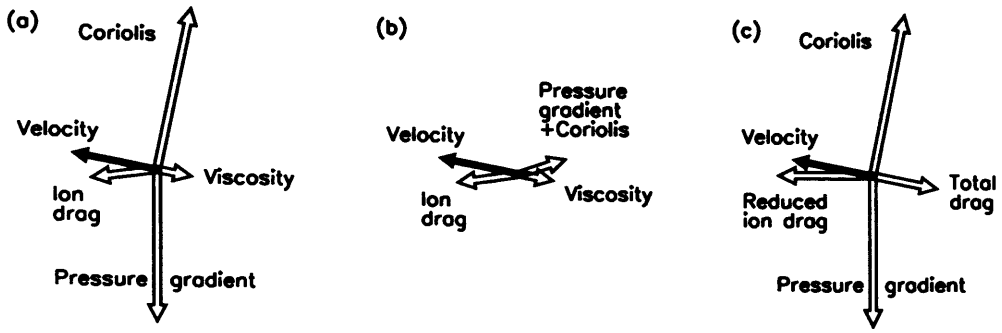

Figure 5.10: Schematic diagrams of force balance in the conducting layer. (a) Balance between ion drag, Coriolis, pressure gradient and viscosity. (b) Balance if pressure gradient and Coriolis are combined. (c) Balance if the plasma velocity component of ion drag ('reduced ion drag') is considered separately and the neutral velocity component is combined with the viscous drag.

structure represents values smaller than 50mm s^{-2} which make a negligible contribution to the acceleration balance.

Figure 5.8 shows the zonal terms in the same way, except that in this case the magnitude of the acceleration balance is smaller, so contours of 1mm s^{-2} ranging from -10mm s^{-2} to 10mm s^{-2} are plotted. Figure 5.9 shows the terms of the energy equation, again in a similar format. In this case contours of 1W/kg are shown ranging from -10 W/kg to 10 W/kg.

We begin our discussion with an analysis of the polewards flow observed at low altitudes. Looking at the meridional momentum terms (Fig. 5.7) it is clear, as mentioned above, that the dominant force balance is between Coriolis and the strong equatorwards pressure gradient. However, this force balance does not tell us anything about the resultant direction of the wind unless we also take into account the zonal force balance (Fig. 5.8). This shows that the principle force opposing ion drag in this low latitude region is Coriolis. For this Coriolis to act in the correct direction — towards corotation — requires a polewards wind. If there were no poleward wind, the westwards zonal wind would increase under the action of ion drag. This in turn would increase the polewards meridional Coriolis, and a poleward wind would be generated. This production of a polewards wind by westwards ion drag and Coriolis is a possibility already mentioned in Chapter 2 (see Fig. 2.13).

In Figure 5.10 we show this force balance schematically in three different ways. Fig. 5.10a shows the balance between ion drag, Coriolis, pressure gradient and viscosity (note we assume in this discussion that viscosity provides a drag antiparallel to the velocity, which is not always the case). The Coriolis-pressure gradient balance dominates the behaviour, but the ion drag and viscosity have an important role to play in determining the orientation of the velocity vector.

In Fig. 5.10b we combine the Coriolis and pressure gradient forces, which are almost exactly

balanced, to show a balance of three forces. The residual of the Coriolis force now acts towards the pole and eastwards, counteracting the westwards ion drag. Ion drag acts both westwards — driving the system — and equatorwards, resisting the polewards motion of the gas. The only role of the viscosity is now to slightly modify the balance between Coriolis and ion drag.

Finally, Fig. 5.10c shows the effect of separating the ion drag into two terms — the part proportional to the plasma velocity, which acts in a pure westwards direction (we call this the 'reduced ion drag'), and the part proportional to and antiparallel to the neutral velocity, which acts in approximately the same direction as viscous drag. We thus combine this second part with the viscous drag to produce a 'total drag' force.

The situation is now rather simple, with the reduced ion drag and pressure gradient fixed by definition to point westwards and equatorwards, and the Coriolis and total drag pointing perpendicular and antiparallel to the velocity respectively. Notice that this force balance does not require a viscous drag at all, provided that the ion drag on the neutral winds is non-zero. The magnitude of the 'total drag' determines the orientation of the velocity vector. If the 'total drag' is very small, we expect the reduced ion drag and pressure gradient to be opposed by Coriolis alone; if it is very large we expect an almost perfectly zonal wind to develop, with Coriolis balancing the pressure gradient in the meridional direction and 'total drag' balancing 'reduced ion drag' in the zonal direction.

Note that in this discussion we have ignored the effects of advection, which are complex (see e.g. Fig. 5.8e). It is to precisely to account for complicated effects such as this that we require a numerical model!

From the preceding discussion we may draw two interesting physical insights. Firstly, the supply of angular momentum to the polar regions that supports the neutral flow against sub-corotation is apparently not mediated by vertical viscous transfer, as supposed by Huang and Hill (1989) and all subsequent discussion of the situation. The angular momentum is supplied by the flow, which is spun up by Coriolis as it moves towards the pole. Our evidence for this assertion is Fig. 5.8, in which viscous drag is negligible at low altitudes where the conductivity layer lies.

Secondly, the magnitude of the westwards wind is now determined by the meridional pressure gradient that opposes the polewards flow. A greater meridional pressure gradient must be balanced by a greater meridional Coriolis force, which requires a faster westwards velocity. Thus heating and cooling processes in the polar cap region that are unrelated to the dynamics — for example heating by particle precipitation or radiative cooling — may play a crucial role in regulating the response of the neutral atmosphere to ion drag. There is also the possibility that the pressure gradient itself may be determined by the form of the ion drag, i.e. the temperature structure of the polar cap may be regulated by the magnetosphere. This is suggested by the form of the pressure gradient term plotted in Fig. 5.7, which assumes a double-lobed form familiar

from the two regions of greatest sub-corotation (A and C) in the magnetosphere model.

We turn now to the situation at 25° colatitude, where the low-altitude cooling occurs. It is clear from Fig. 5.8 that the zonal ion drag is only significant poleward of 25°. This is because equatorward of this region the plasma is required to corotate with the neutrals. It will, therefore, exert little sub-corotational drag on the almost corotating neutrals close to the base of the model. Thus the ion drag cuts off at 25°, and it therefore cannot combine with Coriolis to drive a polewards wind anywhere equatorward of this point.

This cut-off in the ion drag-driven poleward wind at 25° generates a positive divergence of the horizontal winds, which must be balanced by upwelling to ensure mass conservation. (The divergence might also be balanced by downwelling, but this would require the horizontal winds at higher altitudes to be very strongly convergent, which they are not.) This upwelling is evident in Fig. 5.3. The upwelling gas at 25° cools adiabatically, as evidenced by Fig. 5.9f, and it is this process that produces the cool temperatures. Equatorwards of this cool region there is now a polewards pressure gradient (see Fig. 5.7), and referring again to Fig. 2.13 we can see that this will generate a polewards wind with a tendency to super-corotate. This is exactly what we observe in this region. This is the cause of the super-corotation in the angular velocity curves shown in Fig. 5.2.

The second peculiar feature generated by ion drag is the polar hotspot. With a little thought we can see that this is in turn a consequence of the polewards winds. Since our model is axisymmetric, the polewards wind is generated at all longitudes, producing a strong convergence at the pole. This must be balanced by downwelling. The result is that the gas in the polar cap sinks and heats adiabatically. This heating generates the polar hotspot.

We can see with reference to Fig. 5.9 that adiabatic heating is indeed the only significant positive thermal energy term in this region, balanced largely by vertical thermal conduction. Viscous heating, Joule heating and vertical advection are all positive in the low altitude polar region, but only adiabatic heating exhibits powers greater than 1W/kg.

The net effect of ion drag is thus to pull gas upwards at the equatorwards boundary of the polar cap region, cooling it in the process (a cooling that is akin to storing some of its internal energy as gravitational potential energy), transport this cooled gas towards the pole, and then release the stored energy by forcing it downwards again. This has the effect of pumping heat polewards across a temperature gradient.

This behaviour is analagous to that of a mechanical heat pump or refrigerator. These devices usually contain a working fluid which undergoes a cycle of heating, compression, cooling and expansion. Suppose we wish to extract heat from a space C at temperature T_C (e.g. the interior of the refrigerator) and pump it to a space H at a higher temperature T_H (e.g. the room containing the refrigerator). The working fluid is initially forced to undergo expansion to reduce its temperature to $T < T_C$. It is then placed next to the space C and extracts heat via thermal

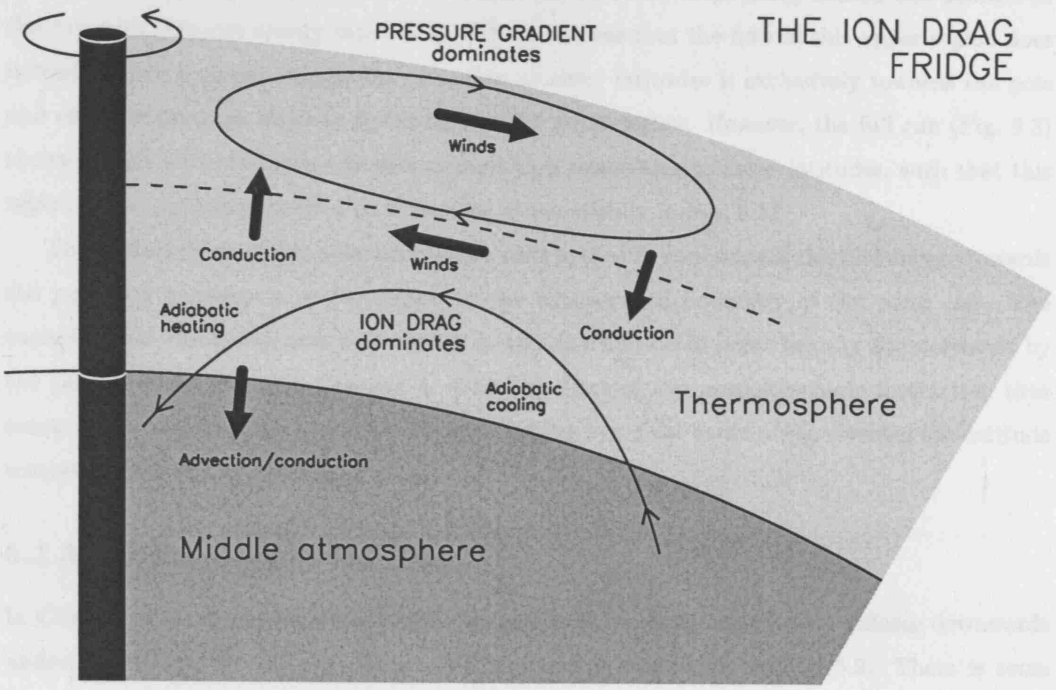

Figure 5.11: Schematic diagram of the 'ion drag fridge'. Thin arrows indicate gas flows. The dashed line indicates the separatrix between the low altitude region — the 'fridge' — and the high altitude flow that it cools. Block arrows indicate major energy flows.

conduction. It is then mechanically compressed such that its temperature rises to $T > T_H$ and placed next to the space H, where it may then cool by radiation or conduction. It is then compressed again and the cycle repeated. In this process energy is forced to flow from C to H against a temperature gradient. This requires an input of mechanical energy, and the net effect on the whole system is that some work is converted to heat.

The polar thermosphere in our model apparently operates in a similar fashion, illustrated schematically in Fig. 5.11. Cold gas is drawn into the system at the equatorward boundary of the polar cap. This gas is cooled by expansion and extracts heat conductively from the warmer upper thermosphere. This gas is then 'pumped' towards the pole by the ion drag/Coriolis driven wind system. At the pole it is compressed and heated. It then loses heat conductively both to the upper thermosphere and the lower atmosphere.

The upper thermosphere behaves as an almost hydrodynamically isolated system. The gas is cooled by conduction at the equatorwards edge and then flows polewards, also driven by the ion drag/Coriolis effect. It is then heated conductively by the lower thermosphere. At the highest altitudes the ion drag becomes insignificant to the extent that the equatorwards pressure gradient generated by the polar hotspot may drive gas back towards the equator. Thus the gas

in this region undergoes a continual circulation in which it is repeatedly heated and cooled. In the run with zero net energy input (Fig. 5.6) we can see that the flow in this upper region does indeed exhibit a closed circulation. The flow at lower latitudes is exclusively towards the pole and confines the high altitude circulation to the polar region. However, the full run (Fig. 5.3) shows a high altitude thermally driven wind that penetrates to lower latitudes, such that this region is not perfectly isolated as illustrated schematically in Fig. 5.11.

The overall effect of the polar circulation cells is thus to concentrate thermal energy towards the pole and generate a cooled region at the equatorward boundary of the polar cap. The cooled region effectively acts as a barrier to the distribution of polar heating equatorwards by the processes described in Chapter 4. The net effect of the magnetospheric interaction thus seems to be to reduce the likelihood of polar heating being the cause of the elevated low-latitude temperatures.

5.2.3 Dissipation of ion drag

In Chapter 2 we discussed the thermal dissipation of ion drag energy as it diffuses downwards under the action of viscosity. No such dissipation is discernible in Fig. 5.9. There is some viscous heating at high altitudes associated with the broad sub-corotational jets in this region, but at low altitudes it is negligible, certainly relative to the adiabatic heating associated with the convergent flow.

This raises the question of where the ion drag energy is dissipated. It must be dissipated within the model, since the zero velocity boundary condition means that kinetic energy cannot diffuse or advect through the lower boundary. The apparent insignificance of viscosity in determining the dynamics suggests that it may not be viscously dissipated at all.

If we consider the motion of a parcel of gas that undergoes acceleration by ion drag, the energy that enters the system is associated with a westwards flow. However, this flow is continually turned polewards by the action of the Coriolis force. Thus the flow that is accelerated by ion drag is altered by the Coriolis force to flow against the equatorwards pressure gradient in the polar region.

The effect of this flow against the pressure gradient can be understood in two ways, depending on whether we interpret the behaviour in terms of Fig. 3.1a or Fig. 3.1b. In the case of Fig. 3.1a, in which we envisage a horizontal flow against a pressure gradient, the gas is presumably slowed and compressed by the pressure gradient, and by this process its K.E. is thermalised.

In the case of Fig. 3.1b, the flow of gas against the pressure gradient is envisaged as a flow along a tilted pressure level. In this case the K.E. is converted to gravitational potential energy as it moves up the gradient of the pressure level; as the winds converge and sink at the pole this G.P.E. is then thermalised by adiabatic heating of the gas.

Either interpretation leads to the same conclusion: the conversion of ion drag to heat is a

dynamical, rather than a viscous, process. Furthermore, ion drag is now seen to be an important contributor of energy towards the generation of the polar hotspot itself.

5.2.4 Importance of centrifugal accelerations

The observed behaviour of the winds in the polar cap can also be interpreted in terms of the centrifugal acceleration of the gas. In the rotating frame of our model, we assume that the associated centrifugal acceleration (which in the polar regions is small and almost horizontal) is part of the gravitational acceleration term. If the model is unforced — i.e. isothermal and perfectly corotating — it represents an atmosphere in hydrostatic equilibrium. This means that internal pressure gradients perfectly balance the combined gravitational and centrifugal accelerations.

Alternatively we may consider this balance of forces from the perspective of an inertial frame, in which case the rotation of any part of the planet is maintained by a centripetal force provided by the combined gravitational and pressure gradient forces.

We have found that when a westwards zonal wind is introduced by the action of ion drag this wind is turned polewards. We can interpret this behaviour in terms of the balance of forces in both the rotating and inertial frames. In the rotating frame, this is interpreted simply in terms of the Coriolis force acting on a westwards velocity. However, we can gain greater insight into this behaviour by considering the perspective of the inertial frame. In this case, the westwards motion of a packet of gas reduces its rotational velocity in the inertial frame. However, the centripetal acceleration acting on the gas due to the gravitational and pressure gradient forces is instantaneously unchanged. It is thus subject to a centripetal force greater than that required to maintain its rotation velocity, and this causes it to spiral inwards towards the axis of rotation.

Now consider a situation in which the entire planet began to rotate at a reduced velocity. In this case one would expect the whole planet to contract slightly towards the pole and assume a less oblate profile. In the same way, one would expect the sub-corotating polar thermosphere to move towards a steady state in which it exhibits a slightly less oblate profile. Indeed, the altitude profile of Fig. 5.3 clearly shows that the atmosphere has become distended at the pole, increasing its curvature in latitude.

Because this increased curvature at the pole must be supported above the fixed altitude profile at the mesopause, it is necessary for the gas to be heated to provide the necessary increase in altitude. The adiabatic heating of the convergent meridional flow at the pole provides a natural, self-regulating mechanism for this heating. If the hotspot is too cool, meridional winds will increase to provide the necessary heating. If it is too hot, they will decrease until the temperature has reached the appropriate level.

5.3 Analysis of latitudinal 'smearing'

Having discussed thermospheric dynamics in some detail we now provide justification for the assertion in Section 5.1 that the latitudinal 'smearing' of the thermospheric zonal winds is a direct result of advection associated with the meridional circulation.

To convince ourselves that this is the most important mechanism we need to rule out possible model-related smoothing effects. There are two non-physical effects in the model that may generate latitudinal smoothing of the zonal winds. Firstly, the latitude grid step size provides a limit to the scale size of processes that can be accurately represented by the model. Attempting to force the model to produce gradients or shears with scale sizes smaller than the latitude grid step will produce a 'smoothed' response.

Secondly, the model incorporates a numerical smoother-desmoother algorithm to filter out numerical noise at the spatial frequency of the latitude grid step size (Fuller-Rowell et al., 1996). If there is a sharp gradient in the zonal winds that occurs on a spatial scale close to the grid step, the gradient will contain spatial frequencies close to the grid step size, and these will be filtered by the smoothing algorithm, effectively smoothing out the gradient.

Both of these processes are, ultimately, consequences of an over-large grid step size. Since the transitions in the plasma velocity at the inner and outer edges of region B occur over a spatial scale of $\sim 1°$, and our standard grid resolution is $0.2°$, our resolution is close to the region in which it may fail to resolve the velocity shears correctly. To check that non-physical processes are not responsible for the latitudinal smearing, the model has therefore been run for a further 10 rotations, at a latitude grid step of $0.025°$, through the latitude range 70-80°, using the previous, lower resolution run as a startup atmosphere and boundary condition. We find that 10 rotations is enough for this model to make the (very small) adjustment required for it to reach near steady-state.

The results of this run are shown in Fig. 5.12. Fig. 5.12a shows the quantities Ω_M (dashed line) and Ω_T (solid line). The value of Ω_T calculated with the standard model is shown with the triple dot-dash line. This figure shows that using the very high resolution model does not eliminate the latitudinal smearing effect. The Ω_T curve is slightly less smeared in the high-resolution case, exhibiting a slightly sharper peak at 13.5° colatitude. We may ascribe this to a slight reduction in the importance of the non-physical smoothing effects. However, the profile is still substantially smeared, and it is clear that these non-physical effects are not the dominant contribution to the smearing effect.

In Fig. 5.12b we show the height-integrated balance of the various zonal momentum terms in the high-resolution run. We group the terms into ion drag (solid line), Coriolis and curvature (dotted line), advection (short dashed line) and viscosity (long dashed line). In addition to plotting these four groups of physically meaningful terms we also plot their residual, i.e. the imbalance of the momentum terms (dot-dash line). This residual represents deviations from

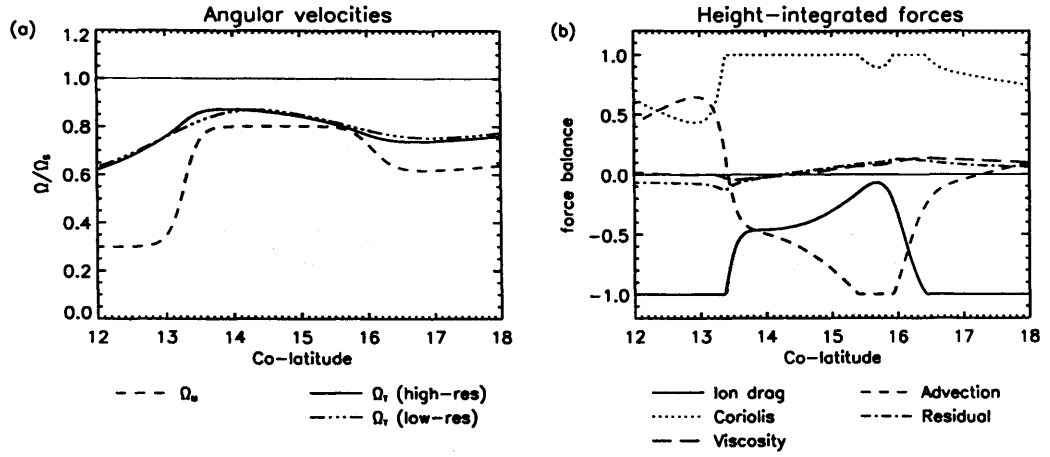

Figure 5.12: Parameters of nested grid Ω-model. (a) Angular velocities. Neutral velocities are shown by the triple dot-dash and solid lines for the low- and high-resolution models respectively. The dashed line shows the fixed model of Ω_M. (b) Height-integrated, normalised zonal momentum terms: Coriolis and curvature (dotted line), advection (short dashed line), viscosity (long dashed line) and residual (dot-dashed line).

equilibrium caused either by the model not having run to steady state, or by the non-physical smoothing terms.

We height-integrate each group of terms at each co-latitude to calculate the total torque that each supplies. We then normalise to the term with the largest absolute magnitude at each latitude. This means that on one plot we can examine the relative balance of the terms at each latitude, even though the absolute values of the terms vary significantly across the range shown.

It is clear first of all that the residual is relatively insignificant, lying close to zero throughout the range shown. This immediately indicates, as suggested by Fig. 5.12, that the smearing is a real physical process, not a modelling artefact. Secondly, we can see that the viscosity term is also almost insignificant, again lying close to the zero line.

The significant terms are therefore ion drag, Coriolis and advection. Before we describe the balance between these three components the reader is reminded that the prevailing wind at low altitudes, where most of the inertia and conductivity are located, is towards the pole (Fig. 5.3). Thus advection tends to transport quantities from right to left in the figures. Starting from the right hand side (18° colatitude) it is clear that Coriolis is the most important term balancing ion drag. As the wind moves into region B (the shaded area) it encounters a reduced ion drag, due to the rise in the plasma velocity. This reduction in ion drag makes advection a more important sub-corotational term. This is because the gas arriving at the edge of region B is sub-corotating to a greater extent than the plasma to which it is about to become connected. As it moves into and across region B it accelerates gradually towards corotation, driven by the Coriolis force.

This slow spin-up as the gas moves into and then through region B is the process that generates the smearing at this first boundary.

At the polewards boundary of region B the same process occurs, but in the opposite sense. Gas that has moved back towards corotation moving through region B suddenly encounters much more strongly sub-corotating plasma in the polar cap (region A). At this juncture advection acts to support the flow, as the inertia of the polewards flowing gas prevents the neutral velocity dropping as quickly as the plasma velocity. Thus the neutral velocity falls off slowly — almost linearly — towards the pole, as the neutrals are gradually accelerated into sub-corotation by the plasma.

This smoothing of the neutral profile by the combined influence of advection and Coriolis leads to a profile that is not only smoothed but also slightly shifted towards the pole. Thus the deviation from a constant K value (as illustrated in Fig. 5.1) is greater on the poleward side of each shear in the plasma velocity. This is evident in Fig. 5.1d, in which the peak in K at the poleward edge of the B-C boundary is greater than the corresponding trough at its equatorward edge, and the trough in K at the poleward edge of the A-B boundary is greater than the corresponding peak at its equatorward edge.

Finally, note that the difference between the neutral angular velocity profiles calculated with the low and high resolution models is consistent with this description of the origin of the smearing. If the smearing is caused by meridional advection, then a parcel of neutral gas should only respond to a shear in the plasma velocity *when it reaches it.* Thus at the A-B boundary, the neutral velocity of the gas moving towards the pole should not begin to drop before the plasma velocity, since it has no mechanism with which to 'feel' the change in the plasma velocity any earlier. The high resolution model does indeed exhibit this behaviour, whereas the neutral velocity in the low resolution model clearly begins to drop before the plasma velocity. This is presumably a result of the numerical smoothing, which, by acting diffusively, allows the gas to detect the change in the plasma velocity before it reaches the boundary.

It does no harm to emphasise that the low resolution model — which we use for the rest of this study — will always present this minor deficiency. However, the basic 'smearing' behaviour, and all other characteristics of the flow, are perfectly adequately described by the model, such that this small problem does not have much impact upon the majority of our results.

For comparison, we also show the same quantities as plotted in Fig. 5.12 for the modified χ-model in Fig. 5.13. Essentially identical behaviour is observed in this improved model, although the ion drag has adopted a simpler form, in accordance with our justification for introducing the χ-model.

In conclusion, the smearing is clearly a real physical effect caused by meridional winds, and these must be taken into account in calculating the response of the neutral atmosphere. Although this apparently introduces great complexity into the problem of the neutral atmosphere's be-

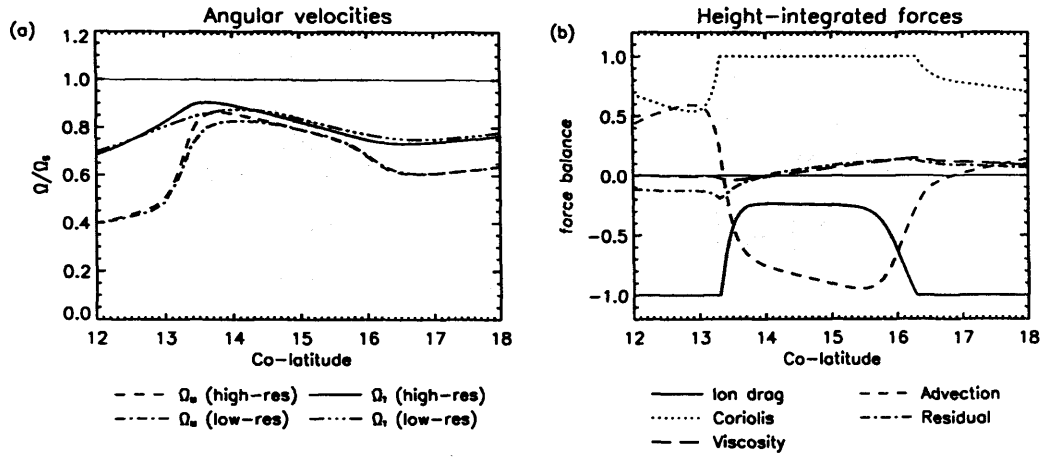

Figure 5.13: Parameters of nested grid χ-model, in the same format as Fig. 5.12. In the left-hand plot the dotted and dashed lines indicates the plasma angular velocity calculated in the low- and high-resolution models respectively.

haviour, the physical mechanism — transport of angular momentum by meridional winds — is relatively simple, and it may be desirable in the future to build analytic or semi-analytic models of this transport which allow for greater flexibility compared to our relatively cumbersome numerical modelling.

5.4 Polar conductivity enhancement

The previous discussion has been based solely on runs carried out using the solar produced conductivity model. Parameters for this model are plotted in Fig. 5.14 — including angular velocities (Fig. 5.14a), true and effective Pedersen conductivities (Fig. 5.14b), field-aligned current intensities (Fig. 5.14c) and the K and χ parameters (Fig. 5.14d). Note that some of the parameters plotted here have already been shown in Fig. 5.2.

There are two discrepancies between this model output and the theoretical considerations of Cowley et al. (2004b) upon which our plasma velocity model is based. Both these discrepancies stem from the observation, mentioned earlier, that the conductivity in the polar regions is much less than 1mho; Fig. 5.14b shows that it lies in the range 0.05-0.5 polewards of 30° colatitude. We might choose to rectify this by simply scaling the conductivities up to produce the required value: but since they are derived from a non-linear model of solar-produced ionisation, this approach would be somewhat unhelpful. Unless the Moore et al. (2004) model of solar-produced ionisation is incorrect by an order of magnitude, solar radiation is apparently unable to produce the required value of 1mho at high latitudes.

Furthermore, the effective conductivity — which is the value actually set to 1mho by Cowley

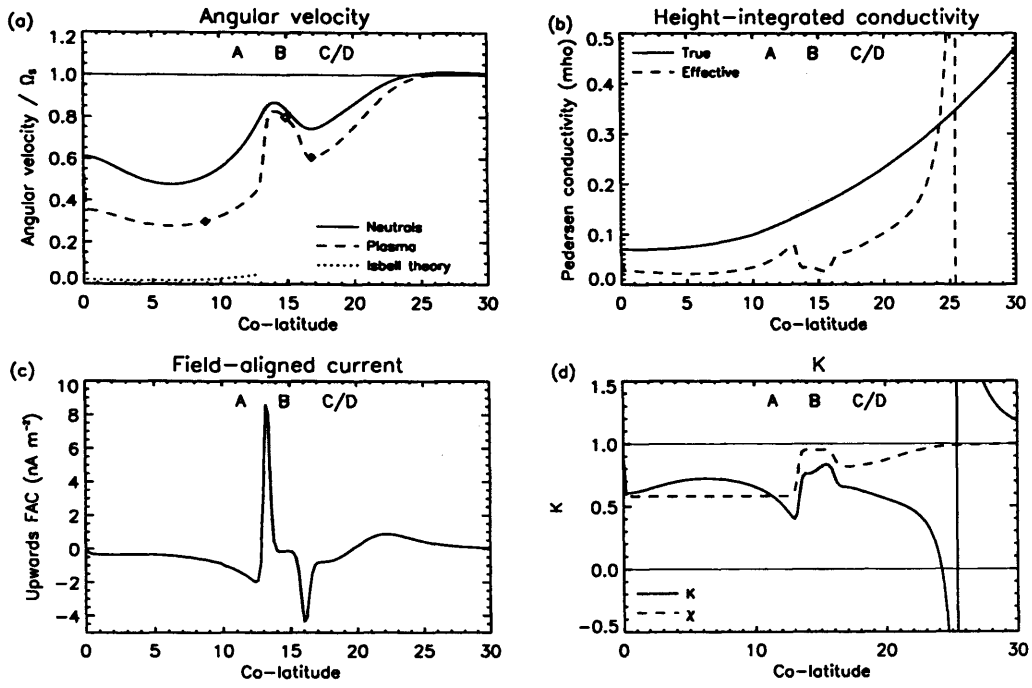

Figure 5.14: Parameters for χ-model using solar produced conductivity only. (a) Angular velocities. Solid line: Ω_T; dashed line: Ω_M; dotted line: Ω_M predicted by Isbell theory based on Ω_T and Σ_P. Diamonds mark the 'anchor points' for the χ-model. (b) Pedersen conductivities. Solid line: true; dashed line: effective. (c) Field-aligned currents (positive upwards). (d) K: solid line; χ: dashed line.

et al. (2004b) — is approximately half that of the true conductivity from the pole down to 25° colatitude, exacerbating the discrepancy.

This reduced conductivity leads to two problems: firstly, the intensity of the current sheet at the A-B boundary (the boundary between open and closed field lines) is only $\sim$10nAm^{-2}, approximately one tenth of the intensity calculated by Cowley et al. (2004b) to be necessary for the generation of auroral emissions comparable to those observed. It is clear that the intensification of the current sheet resulting from the smearing of the thermospheric slippage is nowhere near great enough to compensate for the lower conductivity.

The second problem is that the rotation velocity of the plasma in the polar cap, observed to be $\sim 0.3\Omega_S$ by Stallard et al. (2004), is the same as that predicted by the theory of Isbell et al. (1984) only if the effective conductivity $\Sigma_P^* = 1$mho. The polar cap angular velocity predicted by this theory using the values of Σ_P and Ω_T derived from the solar-produced conductivity model applied to our thermosphere model is shown by the dotted line in Fig. 5.14a. This velocity lies very close to zero. There is thus a mutual inconsistency between the results of our model,

the predictions of the Isbell theory, and the observations. We have chosen to force our plasma angular velocity profile to be reasonably consistent with the observations, but in the present situation this implies a greater angular velocity than that predicted by the Isbell theory. We might equally choose to specify the angular velocity in the polar cap directly using the Isbell theory, but in this case we would end up forcing the thermosphere model with polar cap angular velocities much lower than those actually observed. Ideally, we would like to find a situation in which the data-constrained plasma angular velocity profile used in the model is consistent with that predicted by the Isbell theory.

These various inconsistencies motivate us to investigate enhanced conductivities in the polar cap, as suggested by the considerable H_3^+ emission observed across the whole of the region polewards of the main auroral oval (Stallard et al., 2004; Melin, 2006). We suppose this observed enhancement to correspond to region A of our model. If some of the conductivity is generated by particle precipitation, it seems perfectly feasible for it to change over a relatively short spatial scale at the open-closed field line (A-B) boundary, since flux-tubes either side of this boundary may be connected to very different plasma regimes which imply very different precipitation parameters.

To enhance the conductivity by, for example, 1 mho over the solar-produced conductivity model, we scale the H_3^+ densities described in Section 2.4 such that the conductivity is enhanced by 1 mho at the pole. We then apply the same H_3^+ distribution across the whole of the polar cap, calculating the conductivity at each latitude dependent upon the local magnetic field strength. This leads to a very slight increase in the conductivity enhancement moving away from the pole.

This method ensures that we apply a constant column density of H_3^+ across the polar cap that we may then readily compare with the observed column densities (Table 1.5). We find that for an enhancement of 1 mho we require a column density of $\sim 1 \times 10^{16}\mathrm{m}^{-2}$. Melin (2006) found a range of $\sim 2 - 8 \times 10^{16}\mathrm{m}^{-2}$ (Table 1.5), indicating that we should expect a conductivity enhancement of between 2 and 8 mho. With this in mind we calculate the effect of conductivity enhancements of 1, 2, 4, 8, and 16 mho, giving us coverage of the region consistent with the measurements and a spread either side.

5.4.1 Thermospheric effects

We show in Fig. 5.15 the temperatures and winds in the low latitude polar cap generated by enhancements of 1 mho and 8 mho, alongside those generated by the unenhanced model, in a similar format, and using the same colour and contour scales, as Fig. 5.3. Figures 5.16 and 5.17 show the energy and zonal momentum terms for the same runs. Note that the solid line in Fig. 5.15, which shows the peak altitude of the per unit mass Pedersen conductivity s_P, exhibits a pronounced drop in altitude of 1-2 scale heights in the region of enhanced conductivity. This is because, as noted in Section 2.4, the peak of our enhanced conductivity model lies slightly

lower than that of the solar produced conductivity model.

Looking first at the thermal structure shown in Fig. 5.15, we can see that the most pronounced effect of the 1 mho conductivity enhancement is to shift the polar temperature peak to lower altitudes. This is clearly partly related to the lower altitude of the peak in the conductivity. However, the downwards shift of the temperature peak is greater when the conductivity is enhanced to 8 mho, indicating that the magnitude of the conductivity is as important in determining this behaviour. The temperature peak is also slightly hotter for the model with greater conductivity, and confined to a smaller region.

The winds plotted in the right hand panels give us some insight into why the temperature peak moves downwards. As the conductivity is enhanced, the sub-corotating jet in region A penetrates to deeper levels of the atmosphere. This is presumably because the enhanced conductivity implies a greater torque, allowing the magnetosphere to drive deeper — and thus denser — layers of the atmosphere into sub-corotation.

Given this behaviour, we can understand the change in the morphology and intensity of the temperature peak in terms of the adoption by the polar thermosphere of a less oblate profile, as discussed above. If lower altitude regions of the thermosphere are significantly sub-corotating, then it is necessary for the less oblate profile to be adopted at lower altitudes. To sustain a bulge of the appropriate curvature at lower altitudes which are only one or two scale heights above the mesopause — the temperature of which is assumed to remain fixed — requires a more intense temperature peak than at higher altitudes, since there is less vertical space available to build up a convex altitude profile.

To emphasise this, suppose we need an altitude contrast δh between two colatitudes θ_1 and θ_2 to generate the required altitude profile. If there are n scale heights available to support this altitude contrast, then the average scale height contrast required is

$$H_1 - H_2 = \frac{\delta h}{n} \tag{5.5}$$

The smaller the value of n, the greater the scale height contrast required. Assuming an approximately constant composition, a greater scale height contrast implies a greater temperature contrast.

For large conductivity enhancements, this has interesting consequences if the temperature at the pole is regulated by some other process. Suppose, for example, that the temperature is kept cool by radiative cooling or thermal conduction. In this case, the atmosphere must cool below the mesopause temperature somewhere towards the equator to provide the necessary scale height contrast across the polar cap. Since we do have efficient thermal conduction acting to extract thermal energy from the polar hotspot, this situation does indeed occur, and the generation of the cool region at the A-B boundary (Fig. 5.15) can be interpreted in these terms.

The energy terms (Fig. 5.16) and the zonal momentum terms (Fig. 5.17) support this picture. Firstly, the energy inputs from the magnetosphere (Fig. 5.16a) are clearly pushed downwards to

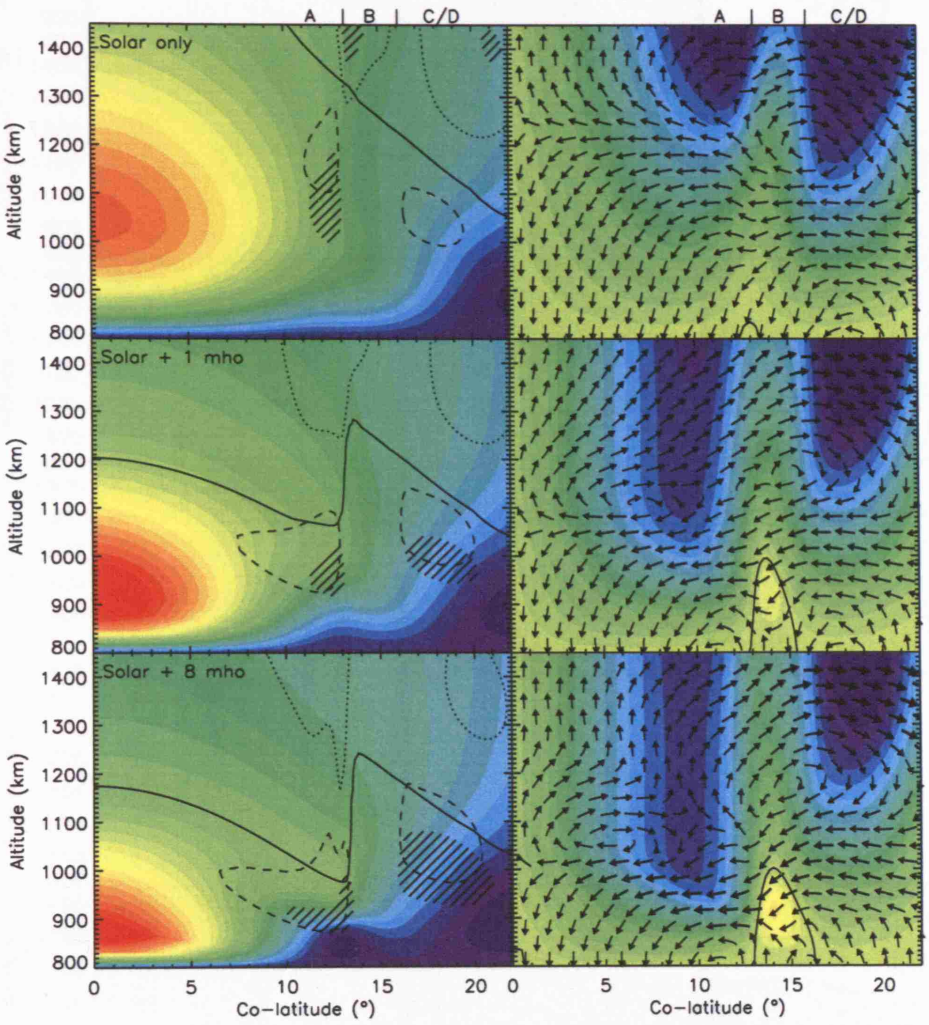

Figure 5.15: Temperatures and winds for the unenhanced conductivity model (top row) and for models with enhanced polar conductivities of 1 mho (centre row) and 8 mho (bottom row). Left: temperatures and selected energy terms, using the same colour and contour scales as Fig. 5.3a. The solid line represents the peak altitude of the Pedersen conductivity per unit mass (s_P). Right: zonal winds (colour scale) and meridional and vertical winds (arrows) using the same colour scale as Fig. 5.3b.

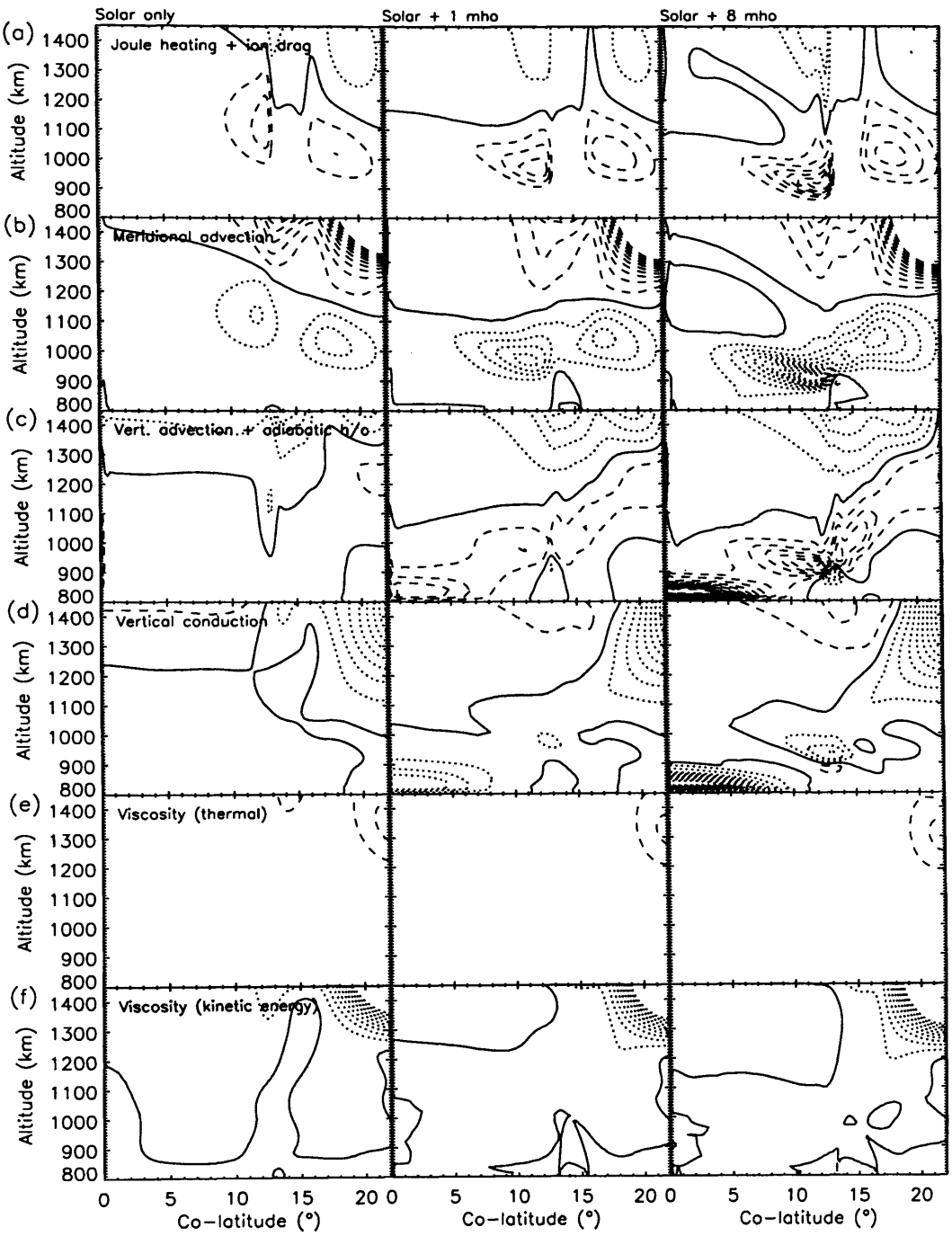

Figure 5.16: Energy terms for conductivity enhancement runs, in a similar format to Fig. 5.9. Contour are plotted every 2 W/kg between -20W/kg and 20 W/kg. Dotted lines, grey shading: negative contours; dashed lines: positive contours; solid line: zero contour.

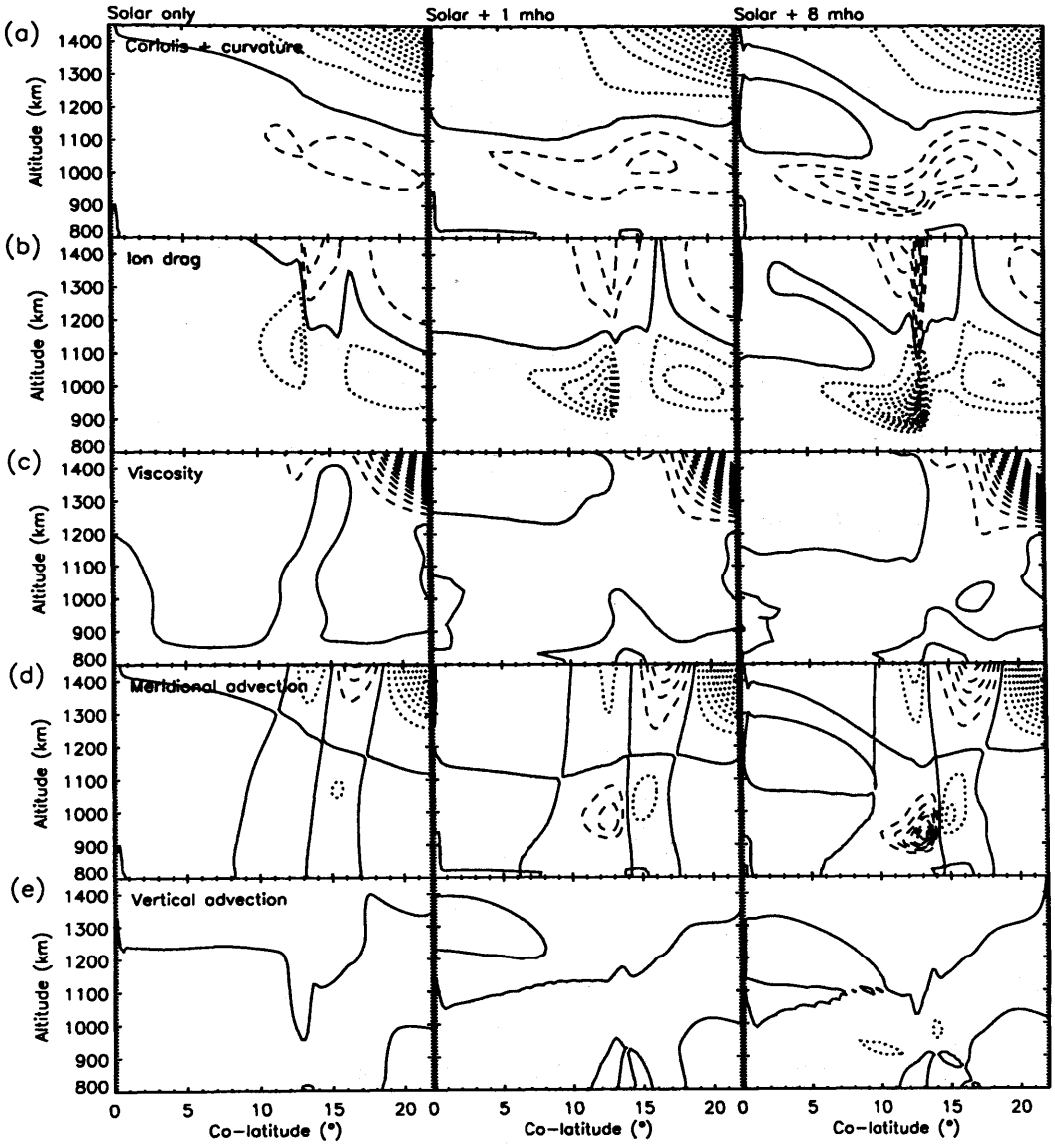

Figure 5.17: Zonal terms for conductivity enhancement runs, , in a similar format to Fig. 5.8. Contour are plotted every 2mm $s^{-2}2$ between -40mm s^{-2} and 40 mm s^{-2}. Dotted lines, grey shading: negative contours; dashed lines: positive contours; solid line: zero contour.

lower altitude by the conductivity enhancement. This is indicative of the region that is almost fully sub-corotating — in which $k \sim 1$ and the Joule heating and ion drag energy are almost zero — penetrating to lower altitudes and confining the energy inputs beneath it.

The enhanced meridional flow evident in Fig. 5.15 also leads to an enhanced cooling of the region by meridional advection of cool gas from lower latitudes (Fig. 5.16b). This advection largely balances the Joule heating and ion drag input.

The most dramatic alteration, though, is in the magnitude of the vertical advection/adiabatic heating term (Fig. 5.16c) close to the pole. In the 8 mho case this becomes intensely concentrated close to the lower boundary at the pole — corresponding to the hotspot — and is aggressively counteracted by downwards thermal conduction (Fig. 5.16d). This is the situation already discussed in which thermal conduction restricts the generation of an oblate profile at the pole. Meanwhile, the viscosity plays a negligible role at low altitudes (Figs. 5.16e and f).

The zonal momentum terms (Fig. 5.17) are interesting because they maintain essentially the same balance as previously noted between Coriolis, ion drag and meridional advection, but the accelerations comprising this balance become much greater in magnitude. Since the ion drag is opposed by the polewards wind — through the advection and Coriolis effects that it engenders — it seems to be a natural consequence of enhanced ion drag that the polewards wind should increase in intensity.

5.4.2 Magnetosphere-atmosphere coupling effects

We now move on to examine the consequences of the conductivity enhancement for the plasma flows and auroral current systems. The appropriate parameters for this analysis, for the 1, 2, 4, 8 and 16 mho runs, are shown in Figs. 5.18 - 5.22 in the same format as Fig. 5.14.

Looking first at Fig. 5.18, representing a relatively modest enhancement of the conductivity, we can see that the penetration of the sub-corotating jets to lower altitudes shown in Fig. 5.15 also results in greater sub-corotation in a height-integrated sense. The height-integrated lag of the neutrals to corotation increases such that it is comparable to that of the plasma velocity; the difference between plasma and neutrals is of the order of less than $0.05\Omega_S$, corresponding to $K > 0.9$.

As a direct consequence of this high K value the effective conductivity remains small, and the polar cap rotation velocity predicted by the Isbell theory remains much smaller than the observed value of $\sim 0.3\Omega_S$. This initial enhancement clearly does little to resolve the mutual inconsistency between our data-constrained model and the predictions of the Isbell theory.

However, the current sheet at the A-B boundary is considerably enhanced by the increase in the polar conductivity. This is unsurprising: the current sheet in the constant conductivity model of Cowley et al. (2004b) results from a drop in equatorwards Pedersen current at the A-B boundary due to a change in the plasma velocity; we reproduce a similar drop through

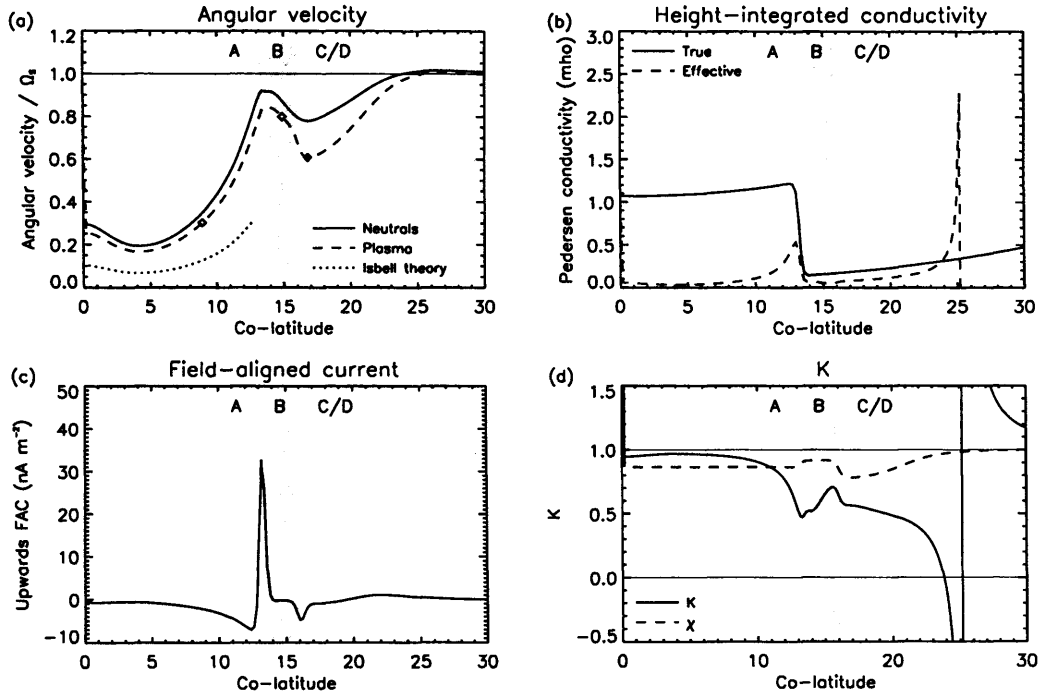

Figure 5.18: Coupling parameters for polar conductivity enhancement of 1mho.

a combination of small changes in the plasma and neutral velocities and a large drop in the Pedersen conductivity.

Note that while the total integrated upward current at this boundary depends simply upon the difference in the Pedersen currents flowing on either side, the intensity of the current sheet is highly dependent upon the exact location and spatial scale of the drop in the Pedersen conductivity. Since we do not attempt to resolve any additional conductivity enhancement associated with the rather narrow UV main oval, which is likely to complicate the structure of the currents at this boundary, the current sheet intensities shown here should be considered to be indicative only.

Figs. 5.19-5.22 then show the effect of further enhancing the polar conductivity. It is worth briefly mentioning that for the 8 mho and 16 mho runs the intensity of the current sheet is roughly the same (150nA m^{-2}) as calculated by Cowley et al. (2004b). Bearing in mind the caveats above, this simply indicates that if the solar-produced conductivity is much less than 1 mho, invoking an appropriate enhancement in the polar regions is able to restore consistency with the notion that the main auroral oval is located at the open-closed field line (A-B) boundary.

Furthermore, it is clear that the main cause of the current sheet may be the change in the conductivity, *not* the change in the plasma and neutral velocities. In the 16 mho case, the relative velocities of plasma and neutrals *increases* across the A-B boundary, indicating a downwards

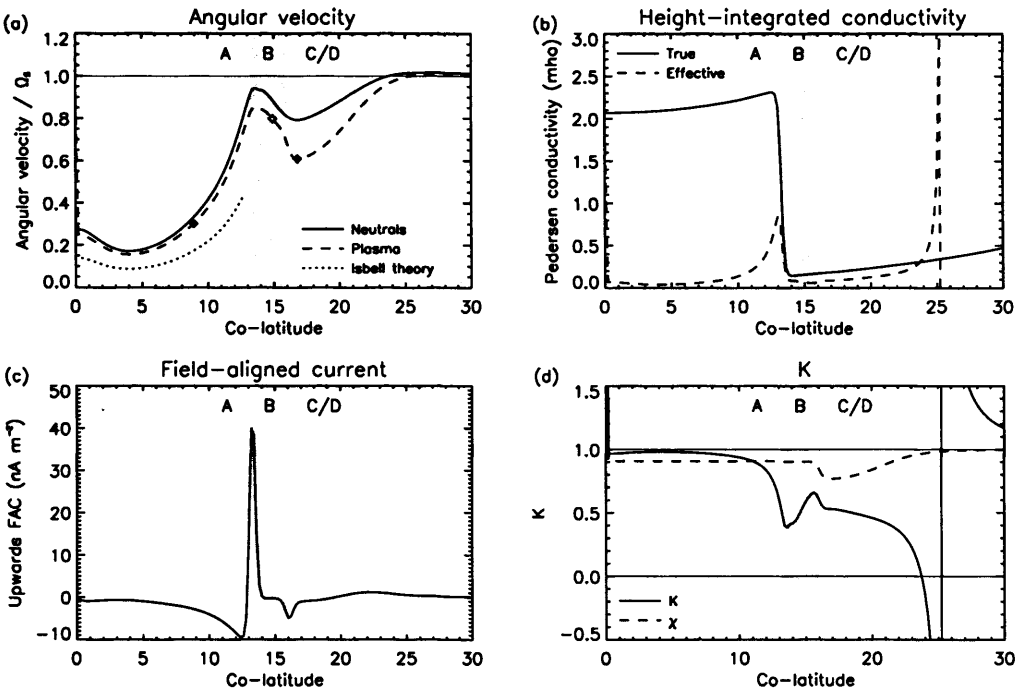

Figure 5.19: Coupling parameters for polar conductivity enhancement of 2mho.

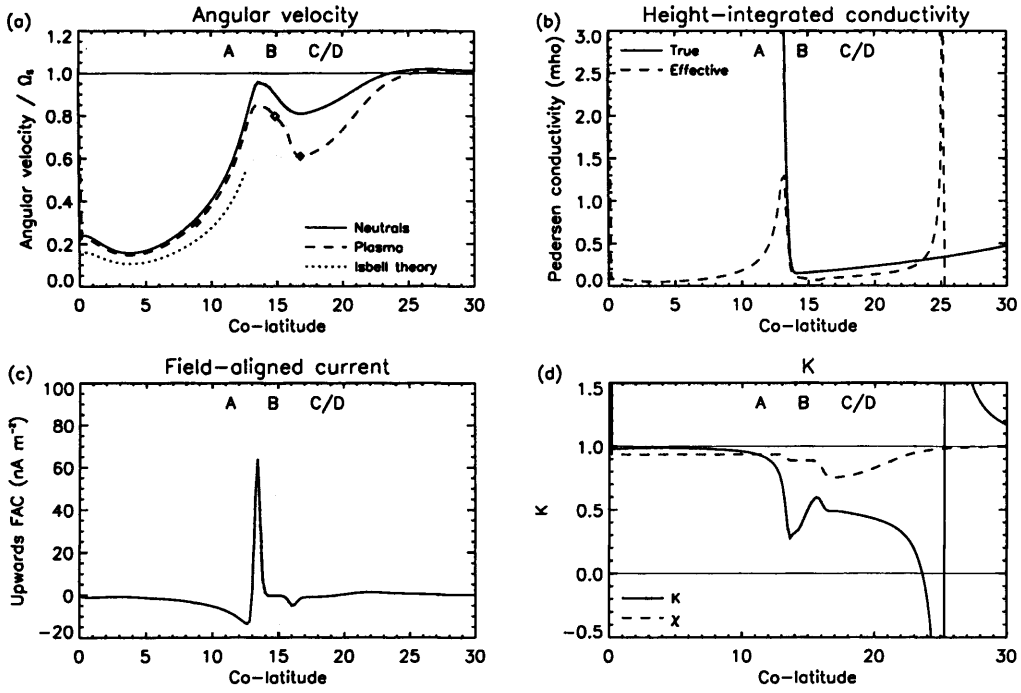

Figure 5.20: Coupling parameters for polar conductivity enhancement of 4mho.

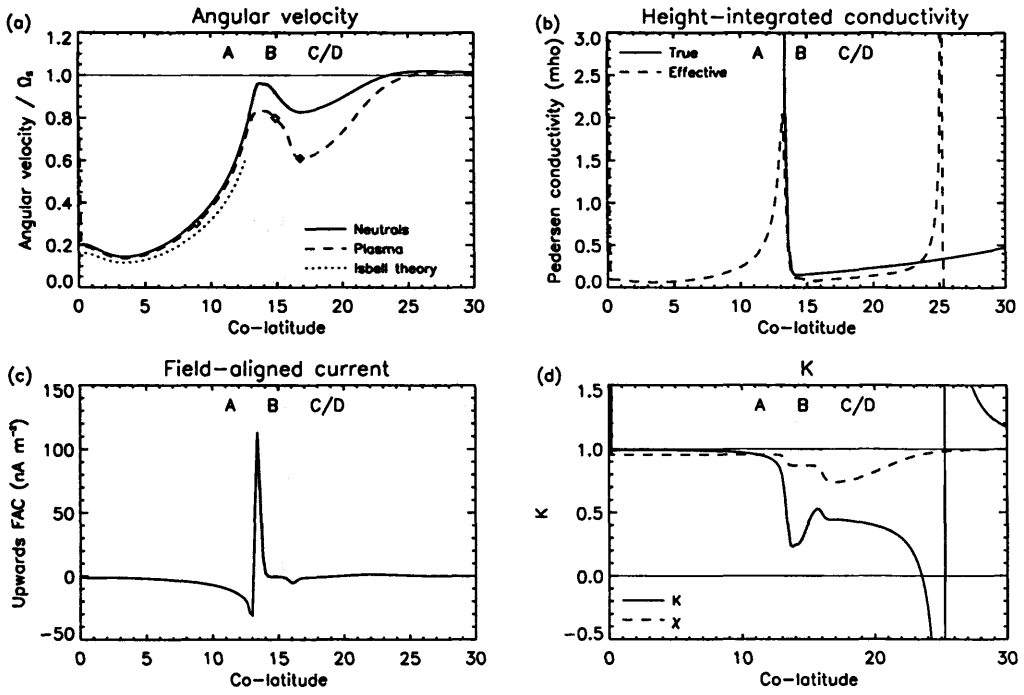

Figure 5.21: Coupling parameters for polar conductivity enhancement of 8mho.

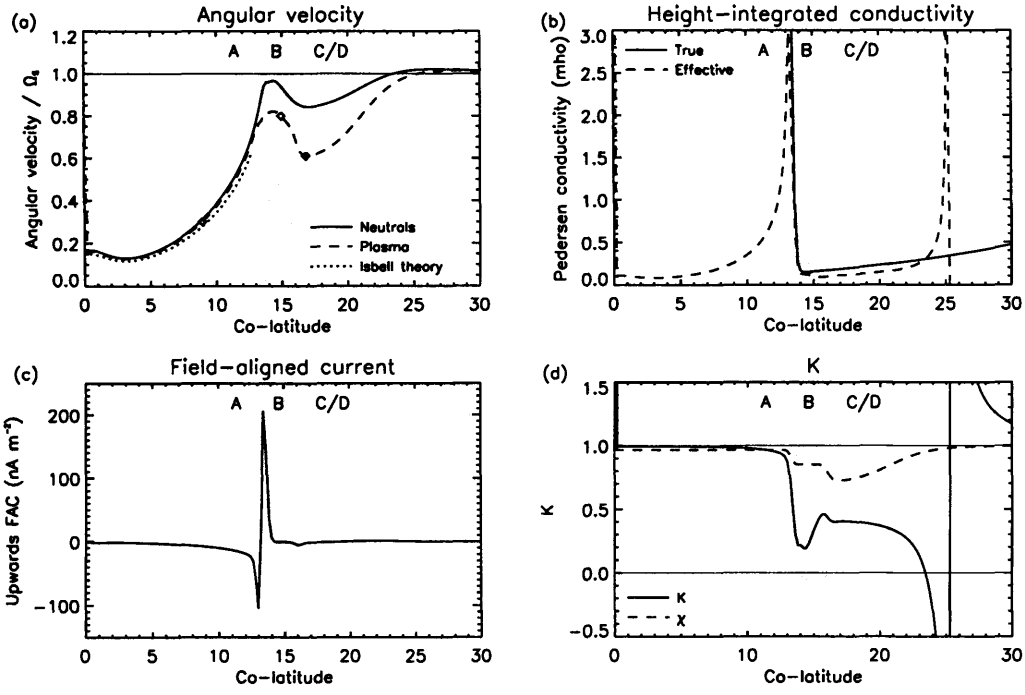

Figure 5.22: Coupling parameters for polar conductivity enhancement of 16mho.

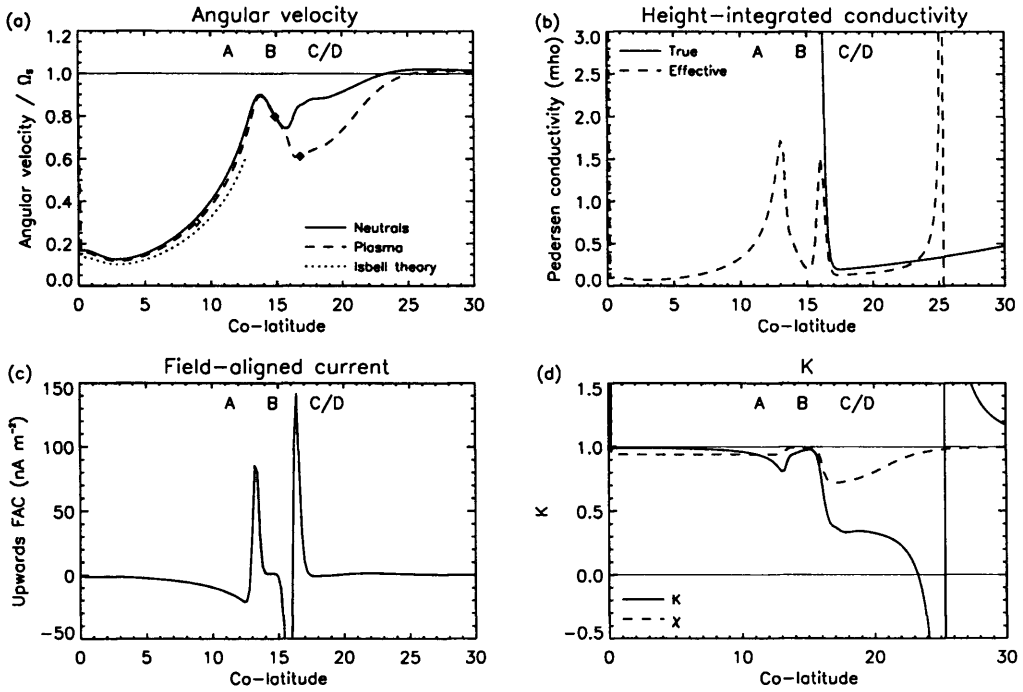

Figure 5.23: Coupling parameters for polar conductivity enhancement of 8mho extending from the pole to the B-C boundary.

current sheet if the conductivity were constant. The upwards current sheet is generated only because the conductivity drops so precipitously across the boundary.

This suggests that the auroral oval might conceivably be generated not by a shear in the plasma velocity, but by a change in the conductivity of the ionosphere. To illustrate this, Fig. 5.23 shows the same parameters again, but for a case in which an enhancement of 8 mho is applied between the pole and the B-C boundary. In this case a more intense current sheet is generated at the B-C boundary than at the A-B boundary.

Of course, there are other elements to the argument that the location of the main oval corresponds to the A-B boundary (see e.g Cowley et al., 2004a), and we will not argue here that it is actually located at the B-C boundary. However, this experiment illustrates that if there is a conductivity enhancement in the polar regions, an auroral oval may be generated in the absence of appropriate plasma velocity shears. Indeed, if the auroral precipitation generates conductivity enhancements itself, one might envisage a situation in which it becomes a self-sustaining phenomenon.

Returning to the plasma angular velocity in the polar regions, it is clear that enhancing the conductivity beyond 1mho still fails to improve consistency between our data-constrained model and the predictions of the Isbell theory. A good measure of this consistency is the value of

the effective conductivity Σ_P^* in the polar cap. Since we know that $\Sigma_P^* = 1$mho produces the observed angular velocity of $0.3\Omega_S$, we require this value — or close to this value — across the whole polar cap to be consistent with both the theory and the data. For the range of conductivity enhancements, this never occurs — although for the runs enhanced by 4, 8 and 16 mho a small region of $\Sigma_P^* > 1$mho does occur close to the A-B boundary. This is simply due to the neutral flow being supported by advection from region B: it does not improve the situation over the majority of the polar cap.

The essential problem seems to concern a deficit in the supply of angular momentum to the polar thermosphere. The Isbell theory, as described in Appendix B, is based on the following argument:

1. Suppose the plasma in the polar cap rotates at angular velocity Ω_A.
2. To what extent does this rotation velocity cause the field lines in the magnetotail to become twisted?
3. What is the tail current required to sustain this twisting?
4. What is the polar cap neutral velocity Ω_T required to sustain this tail current?

This argument yields a relationship between Ω_A and Ω_T. However, it implicitly assumes that, given these values of Ω_A and Ω_T, the thermosphere is able to maintain the angular velocity Ω_T against the resultant ion drag. This is simply a question of whether enough angular momentum can be supplied to the thermosphere in the polar cap to balance the torque exerted by the magnetotail.

It is clear that the inconsistency between our data-constrained model and the theory is a consequence of insufficient angular momentum being supplied to the polar thermosphere. If we run the model with the polar cap angular velocities explicitly determined in terms of the Isbell formulation, we find that both the plasma and neutrals 'collapse' to almost zero corotation, indicating that the angular momentum of the polar thermosphere has fallen almost to zero. Now, since the supply of angular momentum must, presumably, take place principally either by meridional advection or upwards vertical viscous transfer, it seems natural to invoke either enhanced meridional flow or enhanced eddy viscosity to restore consistency between the data-constrained model and the theory. We will explore this further in Section 5.5. There remains the possibility, of course, that the Isbell theory is not a full treatment of the physics governing the plasma angular velocity in the polar cap. If this is the case then the theory must be updated to explain the observations.

5.5 Sensitivity to eddy coefficient

In an attempt to resolve the contradiction between our data-constrained model and the Isbell theory, we now show the results of several runs in which we enhance the value of the eddy diffusion coefficient K_T. The physical justification for such an enhancement is the presumed increase in vertical mixing driven by auroral processes at high latitudes. Such enhancements have previously been invoked in the Jovian context by Huang and Hill (1989) in an attempt to match their model to the available data.

We explore two possible enhancements over our 'standard' value of $K_T = 10^3 \mathrm{m}^2\mathrm{s}^{-1}$. Firstly we apply a global enhancement by a factor of 10 such that $K_T = 10^4 \mathrm{m}^2\mathrm{s}^{-1}$. This brings the eddy coefficient into line with the homopause eddy coefficient determined by Atreya (1982) (see Appendix A). We then investigate a further enhancement in which the eddy coefficient in region A is increased to $K_T = 10^5 \mathrm{m}^2\mathrm{s}^{-1}$ while it remains fixed at $K_T = 10^4 \mathrm{m}^2\mathrm{s}^{-1}$ elsewhere. We show the results of three runs with these eddy parameters and a conductivity enhancement in region A of 8 mho.

5.5.1 Thermospheric effects

First, in Figs. 5.24, 5.25 and 5.26 we show the temperatures and winds, energy terms, and zonal momentum terms for these three runs. It is clear from Fig. 5.24 that enhancing the eddy coefficient has the opposite effect of enhancing the conductivity. The polar hotspot moves to slightly higher altitudes and becomes less intense; the penetration depth of the sub-corotating jet is also confined to slightly higher altitudes.

This indicates that enhancing the eddy processes restricts the ability of ion drag to induce sub-corotation at low altitudes. The most obvious interpretation of this effect is that the enhancement in the eddy viscosity has allowed a more efficient upwards transport of angular momentum to the conducting layer. However, if the eddy viscosity dominated the behaviour, we would not expect the intensification in the meridional wind speed clearly observed in Fig. 5.24. Indeed, we would expect the opposite.

A more palatable interpretation emerges if we also consider the effect of the enhanced eddy conductivity, which will tend to increase the conductive cooling of the polar hotspot. This leads to a greater inflow of gas from lower latitudes to generate the adiabatic heating that is necessary to generate a convex altitude profile. However, this inflow of gas is of course able to counteract ion drag both by advection and by the action of Coriolis. This acts to reduce the sub-corotation of the polar thermosphere and thereby also reduce the altitude contrast required in the polar cap.

Thus it seems that the conductive influence of the enhanced eddy coefficient may be indirectly responsible for the lower rotation velocities observed. This interpretation is borne out somewhat

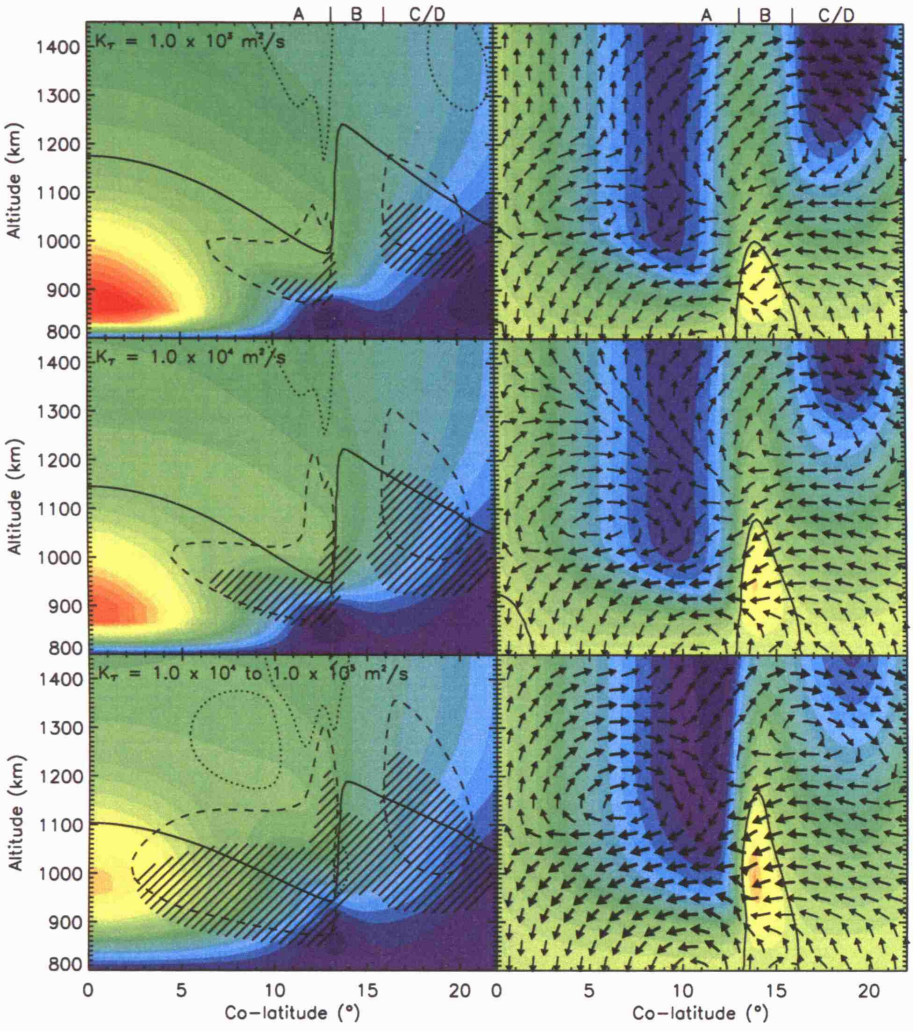

Figure 5.24: Temperatures and winds for eddy enhancement runs, in the same format as Fig. 5.15.

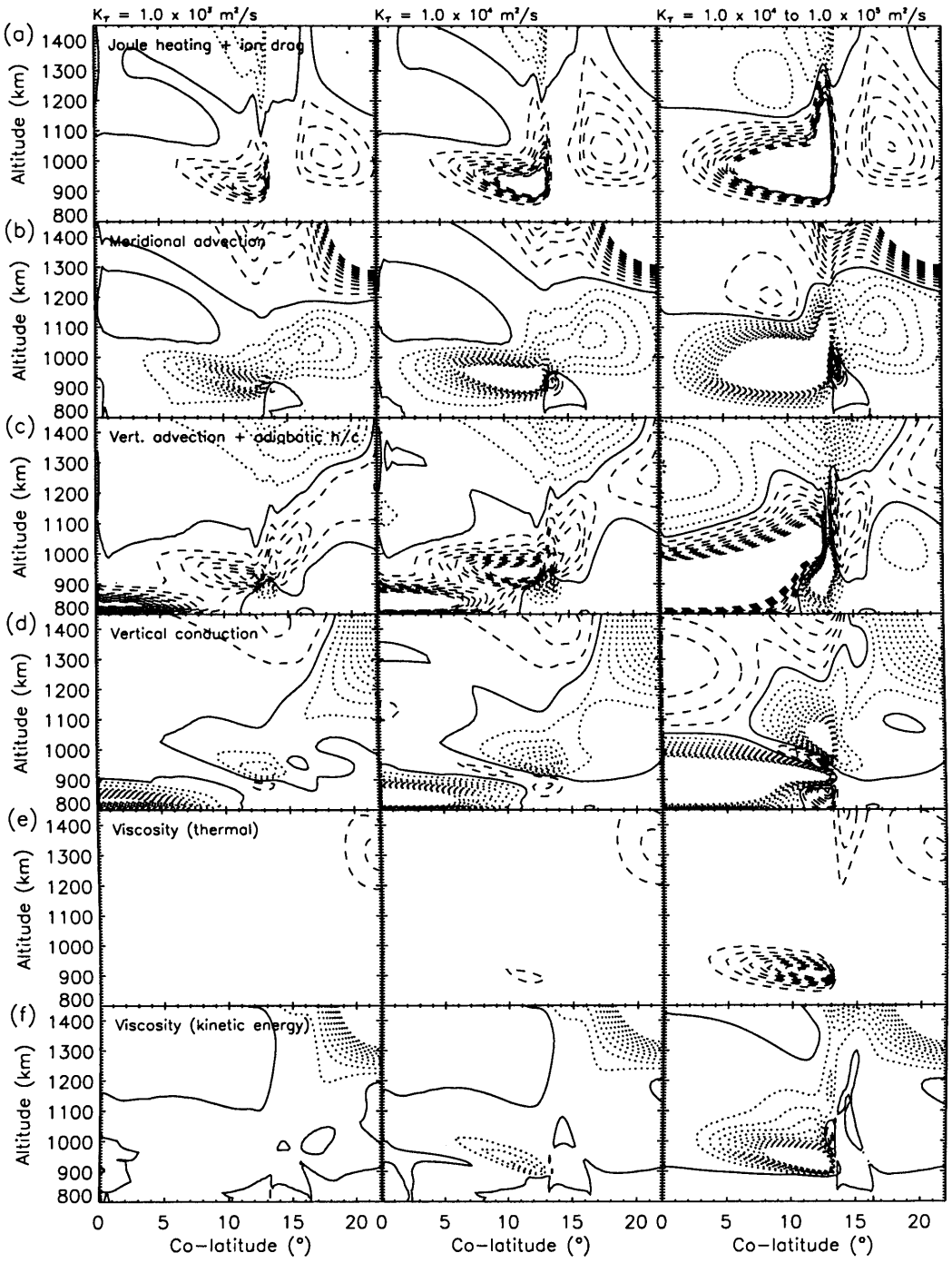

Figure 5.25: Energy terms for eddy enhancement runs, in the same format as Fig. 5.16.

by Fig. 5.25, which shows that both the adiabatic heating and thermal conduction both increase greatly close to the pole for the runs with an enhanced eddy coefficient. Meridional advection also increases, and it is this that largely balances the increased inputs of Joule heating and ion drag.

The viscosity seems to have a relatively unimportant influence, although by the run with an enhanced eddy coefficient of $10^5 m^2 s^{-1}$ the viscous heating term is beginning to become important in region A. However, it is still small compared to the adiabatic heating.

Looking now at the zonal momentum terms (Fig. 5.26), we can see that in the momentum balance the enhancement in the eddy viscosity is important. The zonal balance between Coriolis, advection and ion drag is maintained — the Coriolis and advection intensifying due to the faster meridional flow, and the ion drag intensifying due to the slower zonal flow relative to the plasma velocity — however, the viscosity is now an important extra component of this balance. In the run with an enhanced eddy coefficient of $10^5 m^2 s^{-1}$ the viscous drag is, at its peak, the most important term balancing the ion drag.

This evidence leads to the conclusion that enhancing the eddy coefficient promotes corotation of the polar regions through two mechanisms. Firstly, it restricts the temperature of the polar hotspot via eddy conduction, and thus it restricts the degree of convexity that may be sustained in the polar cap. This in turn restricts the degree to which the polar thermosphere may sub-corotate, due to the continual inwards 'collapse' of the polar thermosphere that supplies angular momentum. Secondly, it explicitly restricts the sub-corotational velocity of the polar thermosphere through the enhanced supply of angular momentum by eddy viscosity. We can see that the improvement in the corotational velocity is driven by a mixture of Coriolis, advection, and viscosity. It is not trivial to separate these terms and treat them separately, since their behaviour is intimately interlinked.

5.5.2 Magnetosphere-atmosphere coupling effects

Given that the eddy enhancement has increased the rotational velocity of the neutrals in the polar regions of the model, does this resolve the inconsistency between the data-constrained model and the Isbell theory? We show the plasma flow and auroral parameters for the eddy enhancement runs in Figs. 5.27 and 5.28 which should be compared to Fig. 5.21, the run with the equivalent conductivity enhancement of 8 mho but with the standard eddy coefficient.

The first enhancement (Fig. 5.27) increases the rotational velocity of the neutrals such that the rotational velocity of the plasma predicted by the Isbell theory comes very close to matching the observations. At first sight, this seems a very good match between the theory and the data. However, the (dotted) Isbell line still lies below the (dashed) data-constrained line. This means that, were we to replace the data-constrained plasma rotation velocity with the Isbell plasma rotation velocity, the sub-corotational drag on the neutrals would increase, and both the plasma

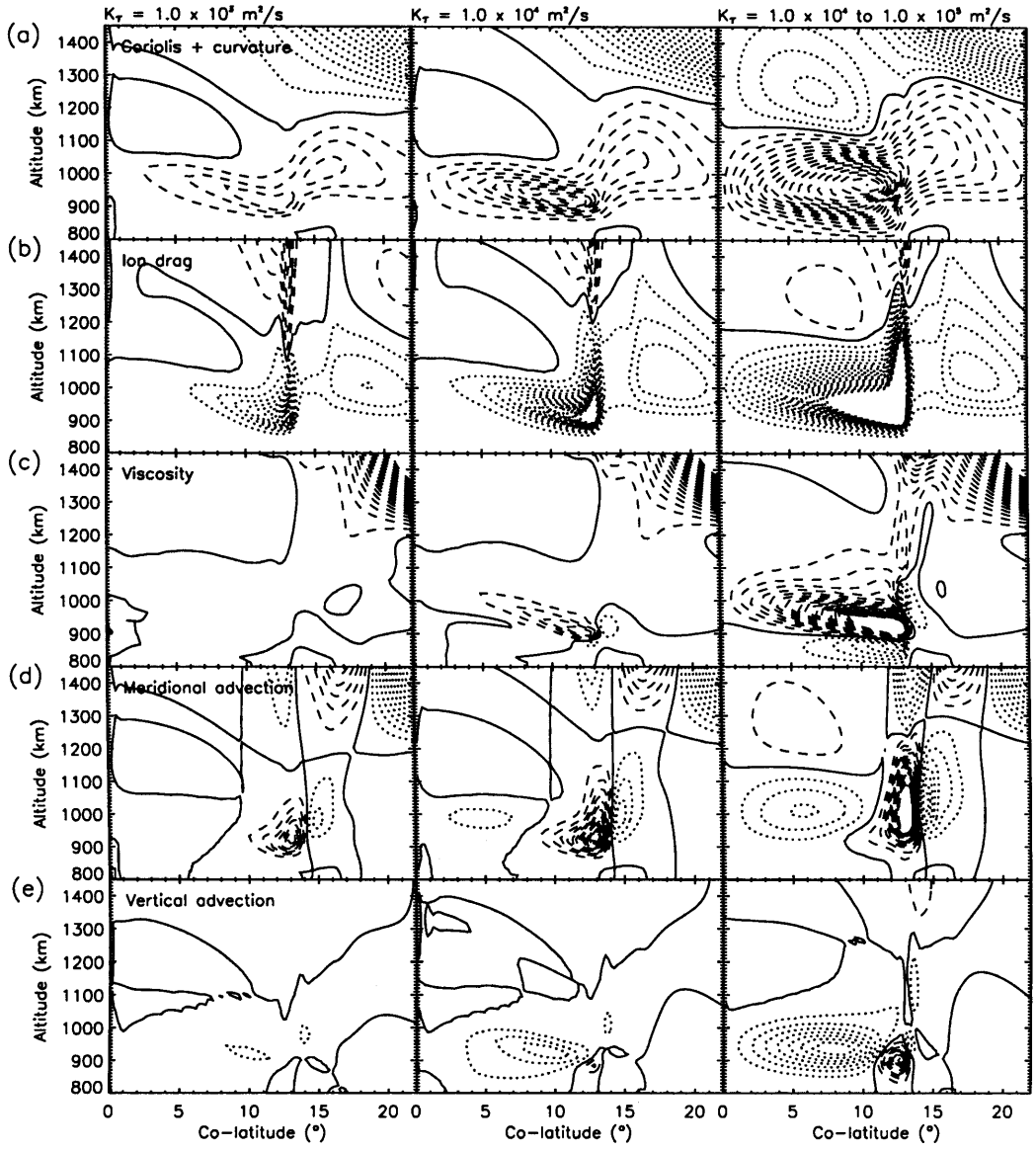

Figure 5.26: Zonal terms for eddy enhancement runs, in the same format as Fig. 5.17.

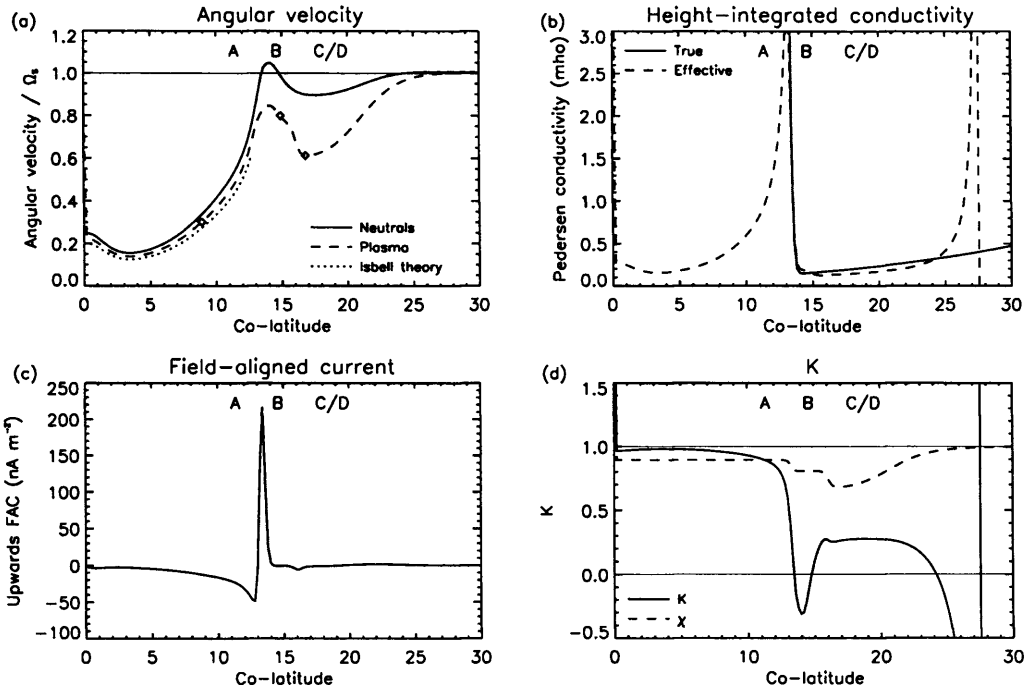

Figure 5.27: Coupling parameters for polar conductivity enhancement of 8mho and eddy coefficient of $10^4 m^2 s^{-1}$.

and neutral velocities would move towards the zero line. The plasma velocity profile would then not closely match the observations. Thus we are not yet supplying sufficient angular momentum to match the data to the Isbell theory.

Interestingly, this run also exhibits super-corotation of the neutrals in region B — a phenomenon previously only observed in region D — due to spin up of the polewards flow of gas driven by the eddy conductive cooling of the polar cap.

The further enhancement (Fig. 5.28) intensifies this latter behaviour, generating super-corotation of $\sim$ 10% in region B. It also succeeds in supplying sufficient angular momentum to match the data with the Isbell theory: the prediction of the Isbell formula in region A (the dotted line in Fig. 5.28c) now lies between the neutral and plasma rotation velocity curves. This means that the neutral atmosphere is able to provide more than enough angular momentum to sustain the plasma velocity postulated by the Isbell theory. We conclude that, with a suitably enhanced eddy coefficient, it is possible for conditions to prevail in the thermosphere such that the predictions of the Isbell theory are consistent with the observations.

Finally, in Fig. 5.29, we show this consistency check between our data-constrained model and the Isbell formula for a range of conductivities and the three eddy coefficient enhancements described above. The solid line indicates the empirical plasma angular velocity of $0.3\Omega_S$. The dotted, dashed and dot-dash lines respectively then correspond to eddy coefficients of 10^3, 10^4

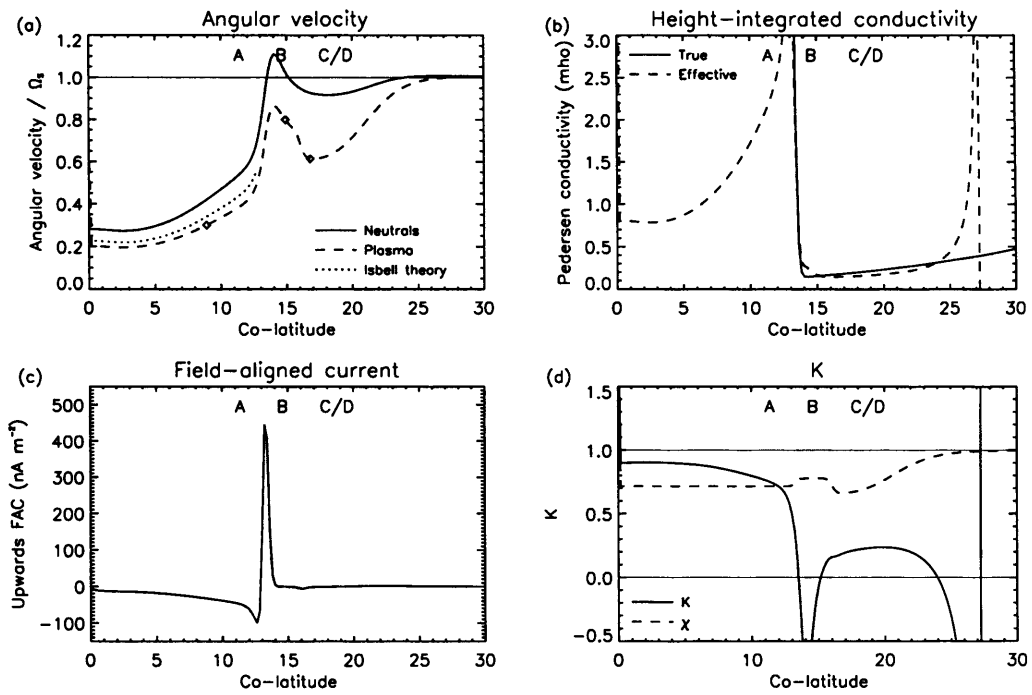

Figure 5.28: Parameters for polar conductivity enhancement of 8mho and eddy coefficient of $10^4 m^2 s^{-1}$ enhanced to $10^5 m^2 s^{-1}$ in region A.

and $10^5 m^2 s^{-1}$respectively. The triple-dot dash line is identical to the third case, but with only the eddy conductivity enhanced: the eddy viscosity is calculated using the 'standard' value of $10^3 m^2 s^{-1}$.

This plot shows that for the range of conductivities considered — and this range was guided by empirical considerations — we must enhance the eddy coefficient above at least $10^4 m^2 s^{-1}$ to find situations in which enough angular momentum is supplied to the thermosphere. Indeed, such situations only arise here in the case of the runs with the greatest eddy enhancement, for which we also require greater than 2 mho of conductivity to produce situations in which enough angular momentum is supplied to satisfy the theory. This conductivity enhancement is not implausible.

The runs without an enhanced eddy viscosity (the triple dot-dash line in Fig. 5.29), which show angular velocities only slightly below the equivalent runs including enhanced eddy viscosity, indicate that it is the effects due to the enhanced eddy thermal conductivity that dominate the supply of angular momentum. Thus, even though the eddy viscosity plays a part in the increased supply of angular momentum, it is very much in a supporting role.

We have shown that the theory can be reconciled with our data-constrained model if we enhance the eddy coefficient. However, we must ask whether it is reasonable to infer the existence

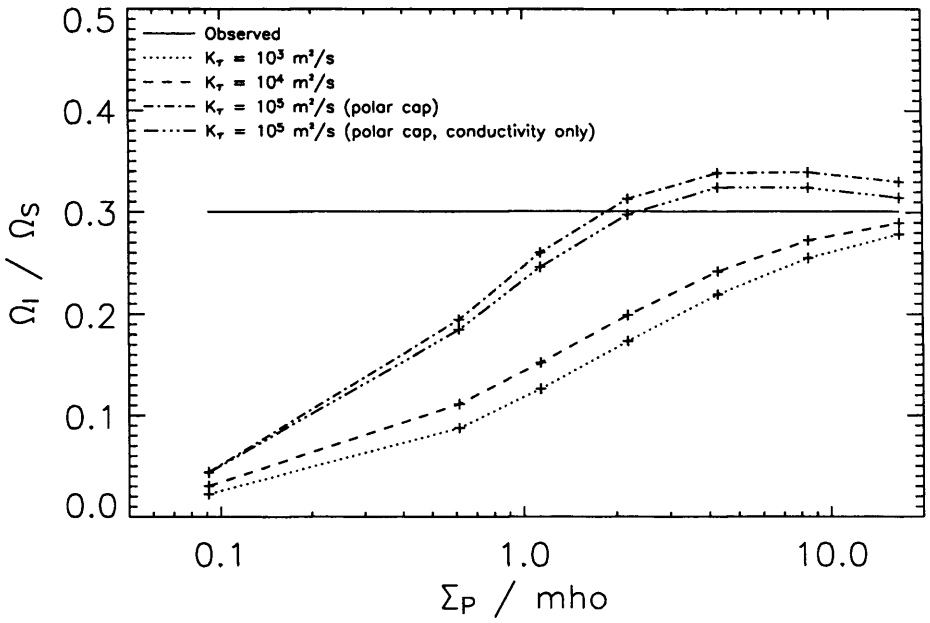

Figure 5.29: Consistency between observed rotation velocities and the Isbell theory at the anchor point in region A (colatitude ~9°). Solid line: observed rotation velocity of $0.3\Omega_S$; dotted line: prediction of Isbell formula for $K_T = 10^3 \mathrm{m}^2\mathrm{s}^{-1}$; dashed lines: for $K_T = 10^4 \mathrm{m}^2\mathrm{s}^{-1}$; dot-dash line: for $K_T = 10^4 \mathrm{m}^2\mathrm{s}^{-1}$, enhanced to $10^5 \mathrm{m}^2\mathrm{s}^{-1}$ in region A. The triple dot-dash line shows the situation for an unenhanced eddy viscosity (calculated using $K_T = 10^3 \mathrm{m}^2\mathrm{s}^{-1}$) but a maximally enhanced eddy conductivity (calculated using $K_T = 10^4 \mathrm{m}^2\mathrm{s}^{-1}$, enhanced to $10^5 \mathrm{m}^2\mathrm{s}^{-1}$ in region A).

of such an enhancement based on this evidence. It must be remembered that the eddy coefficient is, ultimately, a 'fudge factor' introduced to account for processes that are not modelled. It is possible to rescue almost any theory with an appropriate fudge factor, so we should not take too much encouragement from the fact that we have rescued this one.

Nevertheless, the two processes by which an enhanced eddy coefficient is able to supply angular momentum may both be considered proxies for other processes. The increased conductive cooling in the polar cap that encourages a greater meridional influx of angular momentum might be replaced with enhanced radiative cooling there, either from hydrocarbons at low altitudes in the thermosphere or from H_3^+ at ionospheric altitudes. Likewise, the increased drag induced by enhanced eddy viscosity might be replaced by momentum dumped by breaking atmospheric gravity waves. Further investigation of these processes here is beyond the scope of this study.

5.6 Comparison with data

Before concluding, it is worth checking that the χ-model used throughout this chapter is consistent with the available observations. For this purpose we refer the reader back to Fig. 2.1 on which the original Ω-model and the spacecraft and ground-based data are plotted. The dark grey shaded region on the lower plot represents the range explored by the plasma velocity in all of the runs described in this Chapter (excepting the 'thought experiment' runs, described in Section 5.2, in which Joule heating and/or ion drag were omitted). Several features of this are exactly as we expect: the anchor points, for example, exhibit identical flow velocities to the Ω-model, by definition.

Comparing the dark grey shaded region to the scattered data points it is clear that the match between the data and any of the χ-model curves is no worse than that of the Ω-model curve. In regions C and D the χ-models follow the Ω-model closely, and the new model barely alters the predicted behaviour.

In regions A and B the deviations are much greater, but still consistent with the data. In particular, some of the χ-models exhibit significantly greater flow velocities than the Ω-model in the range $\sim 9 - 15°$ co-latitude, i.e. between the anchor points for regions A and B. This is entirely a consequence of the smeared nature of the neutral response, already described in Section 5.3, which supports the zonal flow of both neutrals and plasma just polewards of the A-B boundary. The behaviour at this boundary is of particular interest since it is here that the main auroral oval is believed to be generated. The A-B boundary is also supposed to represent the boundary between open and closed field lines, in which case the relationship between the plasma flows either side of this boundary is complex. The actual behaviour in this region is thus likely to be considerably more complicated than that represented by either of the Ω- or χ-models.

Nevertheless, looking at the overall behaviour, it is apparent that in introducing the χ-model we have been successful in matching the plasma flows to the data while also satisfying the consistency arguments presented in Section 5.1.

5.7 Conclusions

We have shown that the dynamics of Saturn's polar thermosphere are dominated by the influence of ion drag, which unexpectedly generates a strong polewards flow in the conducting layer that acts to concentrate energy at the pole. We have described this flow as analagous to a heat pump extracting energy from the thermosphere, and pointed out that this process acts as a barrier to the possible redistribution of polar heating to the rest of the planet, both by directly cooling the polar regions and by restricting the equatorwards flow of energy.

This behaviour has also been interpreted in terms of thermospheric dynamics. The polar

hotspot is generated by necessity to support a less oblate profile in the sub-corotating polar regions of the planet. An enhancement in the conductivity in the polar regions has the effect of intensifying both the polar hotspot and the sub-corotational behaviour of the thermosphere, and these two effects are interlinked. The polewards flow is also responsible for a region of super-corotation equatorwards of the regions subject to sub-corotational ion drag. This leads to effective conductivites greater than the true conductivity, and suggests that there is no inconsistency in regions of the magnetosphere rotating more quickly than the nominal planetary rotation velocity.

Importantly, we find that this meridional flow is able to provide angular momentum to the polar regions, such that the conventional picture in which angular momentum is supplied by vertical viscous transfer is seen to be incomplete. We have investigated the effect on this behaviour of enhancing the eddy coefficient. This increases the supply of angular momentum to the polar thermosphere, by an explicit increase in upwards vertical viscous transfer — as anticipated by previous studies — but also, more importantly, by an increase in polewards meridional flow caused by increased conductive cooling of the polar cap which encourages inwards 'collapse' of the polar thermosphere.

We also examined the consistency of our data-constrained model with the theoretical considerations of Isbell et al. (1984). We showed that under most circumstances, the Isbell theory predicts plasma angular velocities below those that are observed. This inconsistency between data and theory arises because the thermosphere is unable to supply sufficient angular momentum to sustain the neutral rotation velocity against ion drag. However, in some cases with an enhanced eddy diffusion coefficient, it was possible to restore consistency. More generally, the response of the neutrals to forcing by the sub-corotating magnetosphere was shown to be substantially smeared latitudinally. We showed that this was a consequence of advection by meridional winds, a process not previously considered in this context, and suggested that this smearing necessitated the adoption of a magnetosphere model more responsive to the neutral angular velocity profile. We proposed a very simple model along these lines, and have used it throughout this study.

Finally, we have discussed the influence of these various behaviours on the generation of auroral current sheets. We showed that although our solar conductivity model did not imply current sheets of sufficient intensity to generate an aurora, the solar conductivity model combined with a polar conductivity enhancement did. The conductivity gradient, rather than the plasma flow gradient, dominated the generation of this current sheet, and therefore we suggested that a gradient in the plasma flow velocity might not be necessary for the generation of the aurora.

It must be emphasised that the work in this Chapter has been based on a model generated specifically to fit data collected by the two Voyager spacecraft, which encountered Saturn close to equinox. For this reason, and for simplicity, we have assumed hemispheric symmetry and an

equinox configuration of the solar produced conductivity. The data currently being collected during the early phase of the Cassini mission corresponds to solstice. A useful future extension of this work must therefore be to develop a model that incorporates, either in a fully three-dimensional or zonally-averaged sense, the ionospheric and magnetospheric consequences of a solstice configuration.

Chapter 6

Jupiter

The Jupiter model exhibits essentially the same features as the Saturn model described in the previous chapter, in particular the ion drag 'fridge' behaviour and the supply of angular momentum to the polar regions by advection and Coriolis. We shall briefly analyse these processes again in the following chapter. However, to avoid too much repetition, we will focus mostly on those processes that the slightly different structure of the Jupiter model allows us to study more easily. In particular, the coupling to the Nichols and Cowley (2004) model of the middle magnetosphere allows us to critically examine their assumption that $K = 0.5$. We are also able to assess the eddy viscosity enhancement proposed by Huang and Hill (1989) and examine the effect of Joule heating from electric field fluctuations on the behaviour of the magnetosphere.

At present, the Jupiter model employs a latitudinal resolution of 0.2°, with 30 pressure levels at a resolution of 0.4 pressure scale heights. We again assume zonal and hemispheric symmetry. The model is initiated with zero neutral winds and a constant global temperature of 260K, corresponding to the fixed mesopause temperature (see Chapter 3). It is then run for 200 rotations with a 3 second timestep. This is enough time for the model to reach very good dynamical equilibrium. The magnetosphere model is recalculated ten times per rotation using the current thermospheric wind field as its atmospheric boundary condition, and the conductivities and plasma velocities so calculated are then imposed on the thermosphere model until the next recalculation of the magnetosphere. This allows the magnetosphere and thermosphere to gradually converge on a joint steady state.

6.1 Response of nominal model

6.1.1 General thermospheric behaviour

The basic response of the model is illustrated in Fig. 6.1 in terms of the rotation velocities of the plasma and neutrals and height-integrated conductivity. Regions A and B exhibit fixed plasma

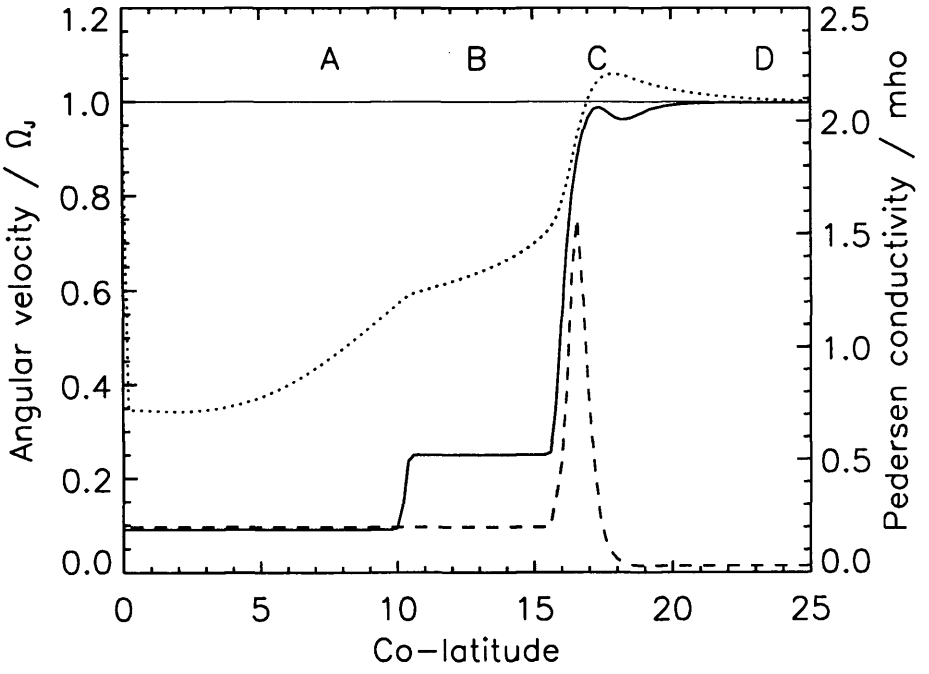

Figure 6.1: Rotation velocities and conductivities in the ionosphere. Dotted line: Ω_T. Solid line: Ω_M. Dashed line: Σ_P.

velocities as required by the model. Regions C and D, for which the plasma velocity is explicitly calculated, exhibit greater structure, which will be discussed in detail below. The conductivity shows a sharp peak at the polewards edge of region C; this is the conductivity enhancement due to the particle precipitation that forms the main auroral oval.

The neutrals show corotation of ~50% in regions A and B. Just equatorwards of the main oval, in region C, is a region of super-corotation. The physics of this super-corotation have aleady been discussed in Chapter 5. Further towards the equator the neutral velocity returns to the planetary rotation velocity.

A more detailed view of the thermospheric dynamics is shown in Figs. 6.2, which shows the temperatures, winds, Joule heating and ion drag energy in the same format as the figures in Chapter 5. The temperature structure is essentially identical to that described for Saturn, with a hotspot at the pole and rather inefficient redistribution of thermal energy to regions equatorwards of the main oval. While the polar temperatures peak at ~700K, which approaches the H_3^+ temperature measurements in this region (Table 1.5), the low latitudes retain cool temperatures that are only slightly elevated above those generated by absorption of sunlight.

The winds also exhibit similar structures. Most importantly, the polewards flow at low

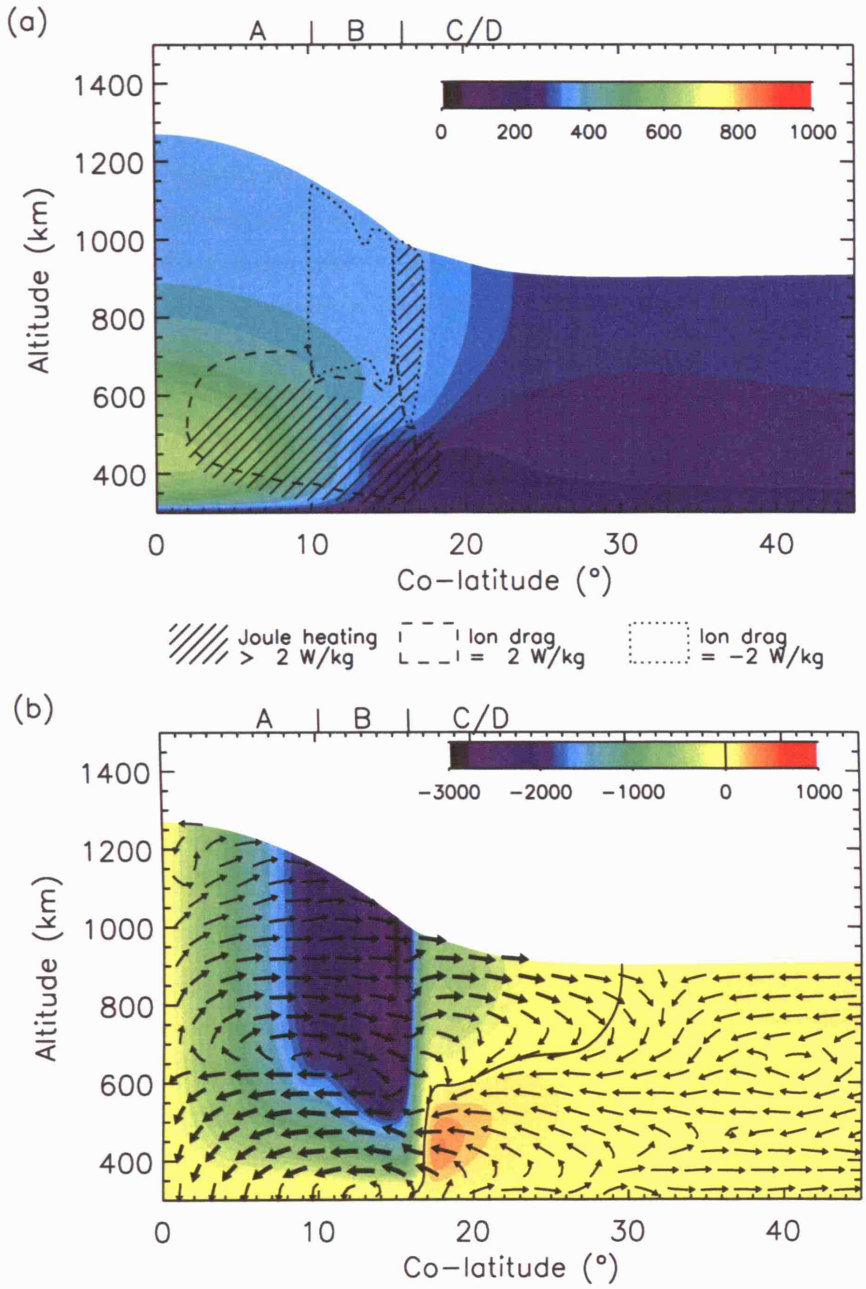

Figure 6.2: Temperatures and winds for normal conditions, in the same format as Fig. 5.3.

altitudes and equatorwards flow at high altitudes that constitute the ion drag 'fridge' are clearly present, indicating that this dynamical process is a feature common to Jupiter and Saturn. The zonal winds exhibit a single broad sub-corotating jet in regions A and B; this terminates rather sharply at the boundary with region C. This is associated with the sudden change in the plasma velocity in the region of the main oval. This will be discussed in greater detail below.

The distribution of energy inputs is also interesting. Regions A and B exhibit significant Joule heating and ion drag powers at low altitudes. This is simply due to the action of the magnetospheric frictional drag in the region that has the highest conductivity. At high altitudes there are areas of negative ion drag energy in both of regions B and C. Both of these patches of ion drag represent extraction of kinetic energy stored in the thermally-driven high-altitude winds that are sub-corotating relative to the plasma. Some of the K.E. from these regions is thermalised — generating a patch of Joule heating at high altitudes in region C — and some is redistributed, either to the magnetosphere or to lower altitudes.

The high altitude patch of Joule heating in region C is also interesting because it is partly a conductivity enhancement effect. Thermally-driven winds blowing through the main auroral oval encounter resistance from the enhanced conductivity in this region, which slows the winds and extracts kinetic energy as heat. Were the conductivity not enhanced, the Joule heating in this region would be relatively unimportant.

Indeed, the most interesting aspect of the energy input distributions shown is that the Joule heating due to the main oval — i.e. due to the middle magnetosphere corotation breakdown currents — is much less significant than that due to the greater sub-corotation rates over a much greater area that are present inside the polar cap. This indicates that the main oval itself may be relatively unimportant in terms of the thermal structure: a surprising result.

6.1.2 Momentum balance

We now summarise the momentum balance of the thermosphere. Fig. 6.3 shows the height-integrated velocities of the plasma and neutrals in the upper panel and the corresponding height-integrated zonal momentum terms in the lower panel. The upper panel has been shaded to give an impression of the height-integrated conductivity at each co-latitude. Thus the darkest shaded region corresponds to the conductivity enhancement due to the main auroral oval.

The velocities in the upper panel are velocities, not angular velocities, related to the angular velocities Ω_T and Ω_M by Eqn. 2.51. The height-integrated terms in the lower panel then represent the total zonal momentum supplied to the thermosphere at each latitude by the various processes, which we group together into advection (horizontal and vertical) viscous drag (horizontal and vertical), inertial terms (Coriolis and curvature) and ion drag.

It is clear from these diagrams that the behaviour is very similar to that observed at Saturn. The viscous drag is almost entirely unimportant. Everywhere ion drag acts to increase K —

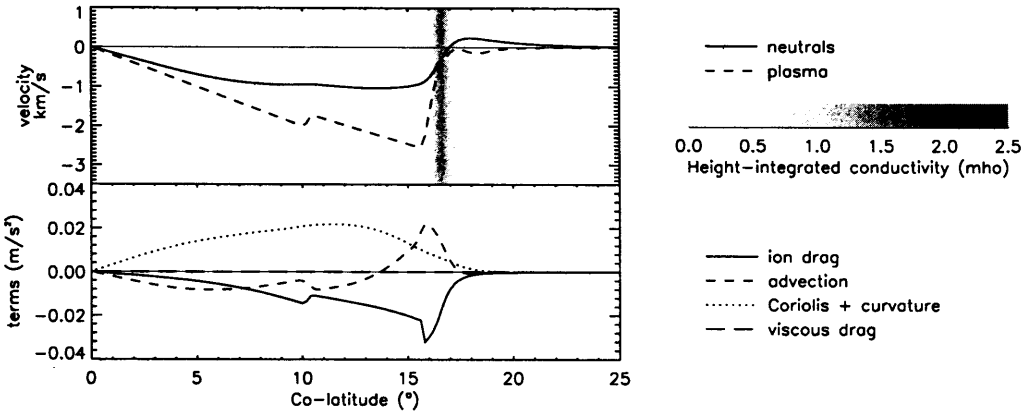

Figure 6.3: Height-integrated zonal velocities and momentum terms for normal conditions. Upper plot: height-integrated zonal neutral velocity (solid line) and zonal plasma velocity (dashed line). Shading represents the value of the height-integrated Pedersen conductivity. Lower plot: height-integrated zonal momentum terms.

i.e. to increase the 'slippage' of the neutrals — and this is opposed almost everywhere by the Coriolis force. Across most of the region shown advection acts in the same direction as ion drag, i.e. towards sub-corotation. This is simply because the sub-corotational zonal velocity decreases towards the pole, and the prevailing meridional wind is polewards. In the region of the main oval advection becomes important in supporting the flow against slippage, since in this region the zonal velocity increases towards the pole. Gas that is advected poleward across the main oval supports the flow against slippage because it has arrived from a region where both the plasma and neutrals almost corotate. There is a lag before it acquires the greater sub-corotation typical of the polar regions A and B.

Just equatorwards of the main oval Coriolis again becomes more important than advection, and, as at Saturn, it is this that generates the small region of super-corotation in the neutral velocity profile.

6.1.3 Response of magnetosphere

Whereas the thermospheric response is clearly similar to that calculated for Saturn, the use of a physical model of the middle magnetosphere allows us to directly assess the influence of the thermospheric winds on the plasma flows in this region. Our approach in constructing the coupled model (see Chapter 2) was to keep the model as similar as possible to the original Nichols and Cowley (2004) model, to facilitate direct comparison. Thus, in the following, we will always plot our results alongside a reference model corresponding to the assumptions of Nichols and

Cowley. In general we plot the results of the reference model as a dashed line and those of our full model as a solid line.

The reference model is calculated using an almost identical model of the true ionospheric conductivity, but with the neutral rotation velocity calculated assuming that $K = 0.5$. The only small difference between the conductivity model used for the reference model and that used for our full model runs, is that the reference model assumes an effective background conductivity of $\Sigma_P^* = 0.0275$mho ($\Sigma_P = 0.055$mho, $K = 0.5$) whereas the full model uses a true background conductivity of $\Sigma_P = 0.0275$mho, the effective conductivity Σ_P^* then following from the value of K that is implied by the thermosphere model (see discussion in Section 2.4). We will discuss the effect of our assumed background conductivity further below.

Fig. 6.4 shows the standard format in which we present our results. The data are plotted as a function of radial distance in the magnetosphere. Our model extends from $4R_J$ to $100R_J$; within $4R_J$ we assume $\Omega_M = \Omega_T$. The left hand column represents parameters associated with the rotation velocities of the plasma and neutrals, and the right hand column parameters associated with currents and conductivities. Fig. 6.4a is the height-integrated thermospheric angular velocity (Ω_T). This, of course, includes the (small) component due to meridional motions coupled to the Hall conductivity (see Section 2.2.4). The dashed line shows the thermospheric velocity implied by the reference model. Since the reference model assumes $K = 0.5$, this is calculated by halving the plasma corotation lag.

Fig. 6.4b shows the plasma angular velocity Ω_M. Again, the reference model is represented by a dashed line. Fig. 6.4c shows our calculated value of K mapped into the magnetosphere. The horizontal dashed line represents the reference model assumption that $K = 0.5$. Fig. 6.4d shows the sub-corotation parameter $\chi = \Omega_M/\Omega_T$ introduced in Chapter 5.

Figs. 6.4e-h show, respectively, the field-aligned current in the ionosphere (mapped to the magnetosphere), the resulting height-integrated conductivity, the effective height-integrated conductivity, and the radial current in the magnetosphere, respectively. Fig. 6.4g also includes a dotted line which indicates the effective conductivity that we would calculate if we halved our true conductivity calculated with the full model. This gives an indication of the features in the effective conductivity that are due to structure in K rather than structure in the true conductivity.

Finally, the dotted line in Fig. 6.4h shows values of the radial current deduced from Galileo magnetometer data (Khurana, 2001). This is the same data shown by Nichols and Cowley (provided by K. K. Khurana, private communication, 2006). For further details of the origin of this data, the reader is referred to Nichols and Cowley (2004).

Initial inspection of Fig. 6.4 indicate that the introduction of coupling to the neutrals has only a small effect on the majority of the magnetospheric parameters. In particular, the plasma angular velocities calculated using the full model are effectively identical to the reference model

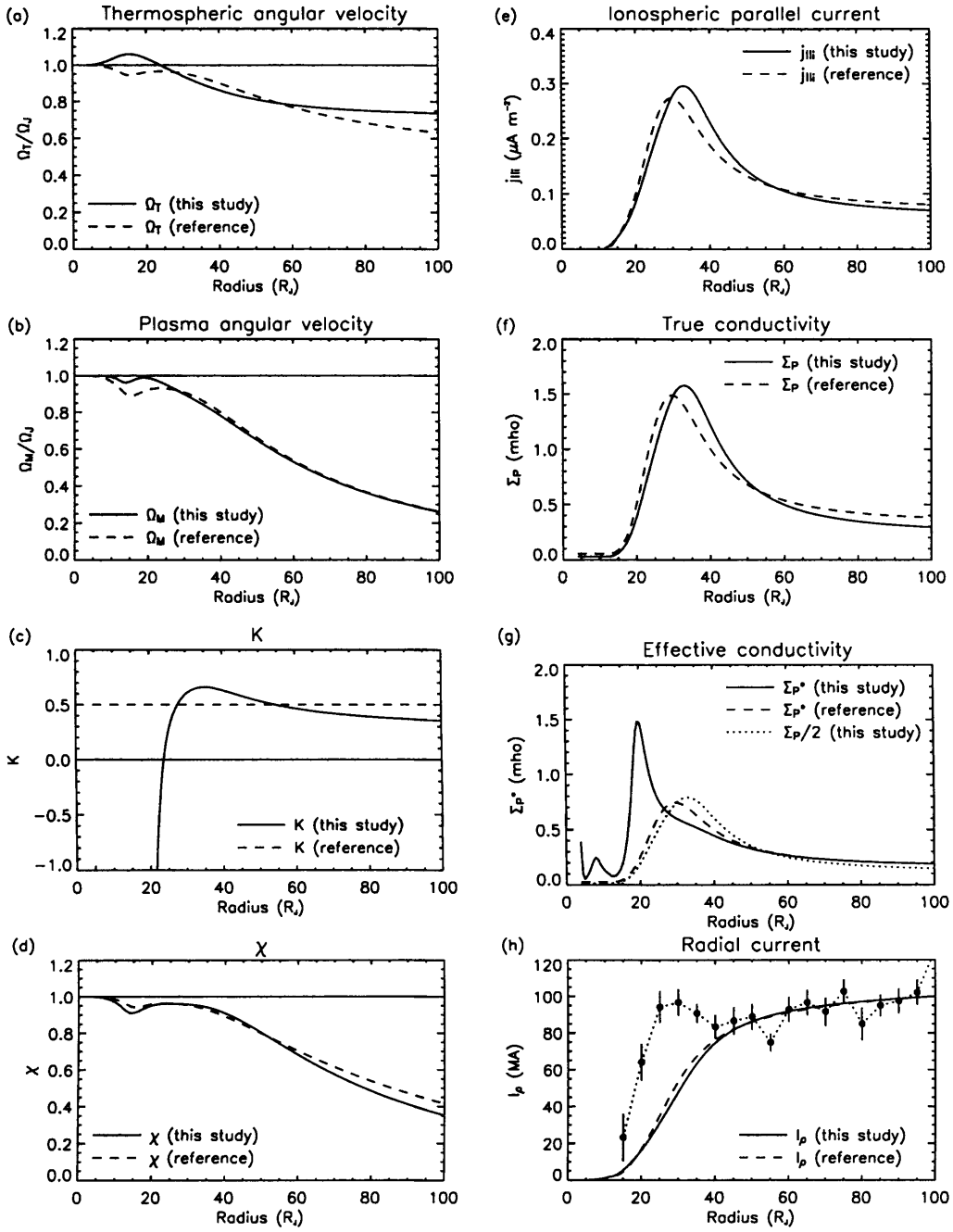

Figure 6.4: Magnetospheric parameters for normal conditions. Solid lines: full model. Dashed lines: reference model. (a) Ω_T, (b) Ω_M, (c) K, (d) χ, (e) $j_{\parallel i}$, (f) Σ_P, (g) Σ_P^* (dotted line shows $\Sigma_P/2$ for the full model), (h) I_ρ (dotted line shows values deduced from the data of Khurana (2001)).

beyond $\sim 30R_J$. At smaller radial distances our plasma angular velocity is considerably greater than that in the reference model, lying much closer to corotation. These two regimes divide the model naturally into 'outer' and 'inner' regions respectively. The region within $30R_J$ is shaded grey to represent this division.

Looking first at the 'outer' region, beyond $30R_J$, we can see that although the plasma angular velocity is almost unchanged, each of the other parameters differs, at least marginally, from the reference model. These differences can be traced to the differing behaviour of the neutral atmosphere, which rotates slightly more slowly than in the reference model between $30R_J$ and $55R_J$, and then slightly more quickly beyond $55R_J$. This slight difference in the neutral rotation velocities is of course because there is no requirement for our neutral atmosphere model to generate radially constant profiles of K, and it is thus unsurprising that we do not exactly reproduce the reference model. However, the model does produce values of K in the range 0.35-0.7 throughout the whole outer region. This suggests that the assumption $K \sim 0.5$ is reasonable in this part of the magnetosphere. This is presumably because, as is clear from Fig. C.1, most of the magnetosphere beyond $20R_J$ maps to a very confined range of latitudes in the thermosphere, implying a fairly homogeneous behaviour.

In the outer region our currents are distributed very slightly differently from the reference model. The auroral oval maps to a slightly larger radius, and consequently the radial current is concentrated very slightly more in the outer regions of the magnetosphere. However, these small changes do not seem particularly significant, and are simply minor consequences of K not being exactly equal to 0.5.

The inner region is considerably more interesting. To aid our discussion of this region, Fig. 6.5 shows the same parameters as Fig. 6.4, but across the range 0-$40R_J$ only. This region maps to latitudes just equatorwards of the main auroral oval, which exhibit super-corotation via the mechanism described in Chapter 5. Super-corotation was not envisaged when the parameter K and the concept of effective conductivity were introduced (Huang and Hill, 1989), so the consequences of this behaviour are somewhat peculiar, as we saw in Chapter 5. Firstly K becomes strongly negative, representing 'negative slippage' of the thermosphere. There are two deep troughs in K in this region, each of which corresponds to peaks in the plasma angular velocity. As the plasma angular velocity approaches corotation, the denominator in the formula for K (Eqn 2.56) approaches zero, while the numerator is negative. This generates strongly negative values of K, whose only physical significance is that the plasma angular velocity is close to corotation. This structure in K is similar to that observed in Chapter 5, since it is ultimately a consequence of Ω_T behaving partly independently of the profile of Ω_M, behaviour that the constant K model cannot account for.

The effect of these negative values of K on the effective conductivity is to enhance it significantly, since the factor $(1 - K)$ becomes strongly positive. This explains the two peaks in

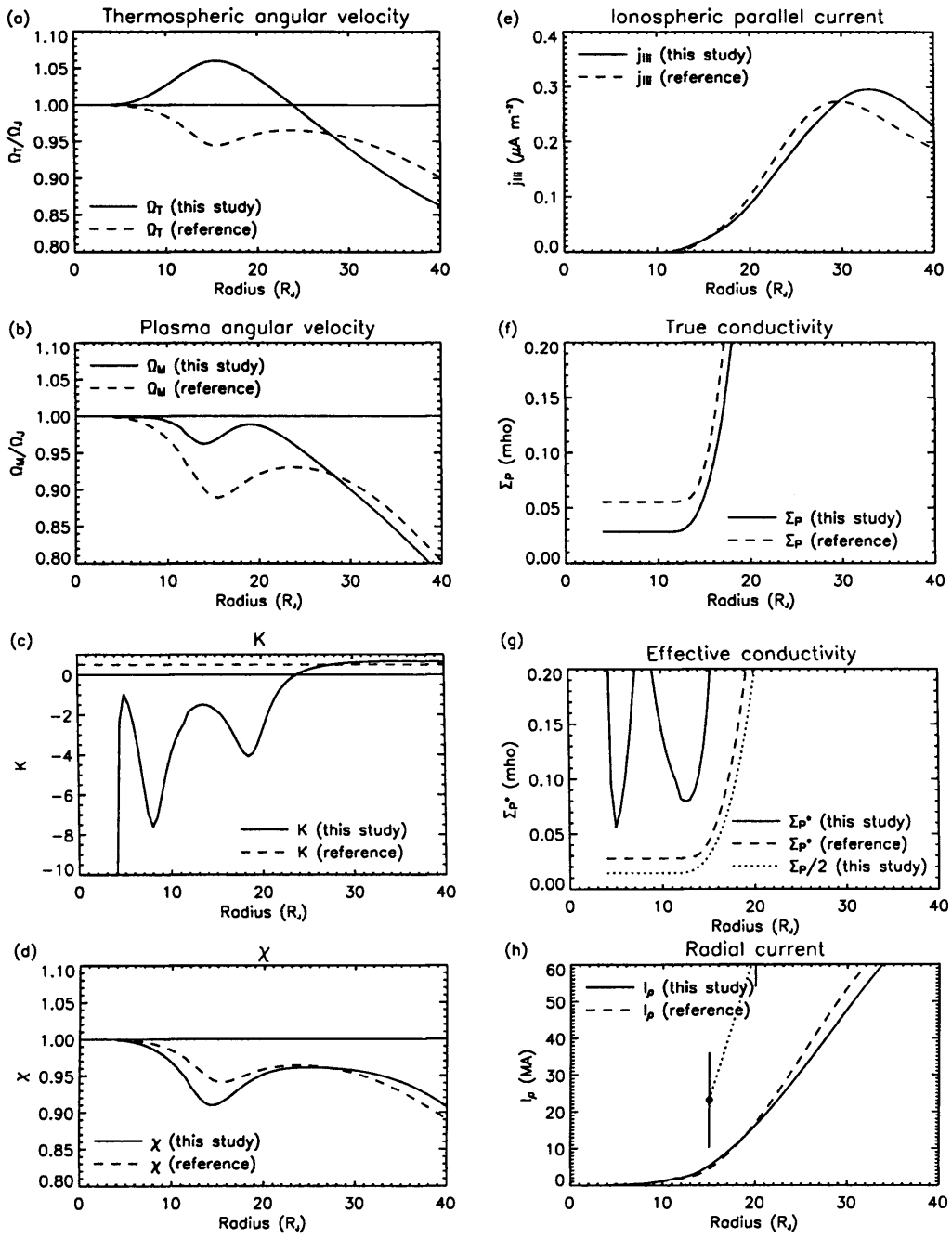

Figure 6.5: Magnetospheric parameters for normal conditions in the inner region, in the same format as Fig. 6.4.

Fig. 6.4g. Since the effective conductivity represents the effective ability of the thermosphere to enforce corotation, it is not surprising that when the thermosphere super-corotates it is able to enforce corotation more effectively.

This interpretation is borne out by the behaviour of the sub-corotation parameters χ, which lies very close to that calculated from the reference model. This indicates that the sub-corotation of the plasma relative to the neutrals is relatively model-independent — introducing internal dynamics of the thermosphere merely shifts the absolute value of the plasma angular velocity.

The negative K values also enhance our effective conductivity in the inner region above that in the reference model, even though we assume a lower true background conductivity. The effective conductivity is the empirically constrained parameter in this region (Hill, 1980), and we are currently overestimating it. This suggests that we may require a still lower true background conductivity.

To investigate this, the model has been run with the true background conductivity reduced by a factor of two to $\Sigma_{P0} = 0.01375$mho, the results of which are shown, for the inner region, in Fig. 6.6. This reduction in the conductivity has an almost imperceptible effect on the super-corotating thermospheric angular velocity profile in the inner region. This is unsurprising, since the very fact that the thermosphere super-corotates in this region shows that its behaviour is not governed by sub-corotational ion drag. We showed in Chapter 5 that super-corotation is generated by pressure gradients equatorwards of the region of greatest plasma sub-corotation. It thus seems that the degree of super-corotation in the part of the thermosphere connected to the inner magnetosphere is governed not by the background conductivity in that region but by the elevated conductivities and plasma sub-corotation in the main oval and polar cap, which are connected to the middle and outer magnetospheres. It is interesting that the sub-corotation of the outer regions of the magnetosphere should, indirectly, be responsible for supporting the corotation of the inner regions.

Although the thermospheric rotation velocity is almost unaffected by the reduced background conductivity, the plasma velocity within $\sim 20R_J$ drops by approximately a factor of two. Thus the background conductivity is important in this region in terms of determining the degree of corotation of the magnetosphere. Within $\sim 13R_J$ our model now reproduces the reference model almost exactly, and this corresponds to our effective conductivity matching the reference model well. Thus, by appropriately choosing the background conductivity, we can reproduce the empirical effective conductivity in the inner region.

However, we will see in the experiments that follow that the effective conductivity of the inner region is also sensitive to other parameters. Therefore no single value of the true conductivity can definitively give the correct effective conductivity under all conditions. Given this complexity we will use our original assumed background conductivity of $\Sigma_{P0} = 0.0275$mho for the remainder of the study.

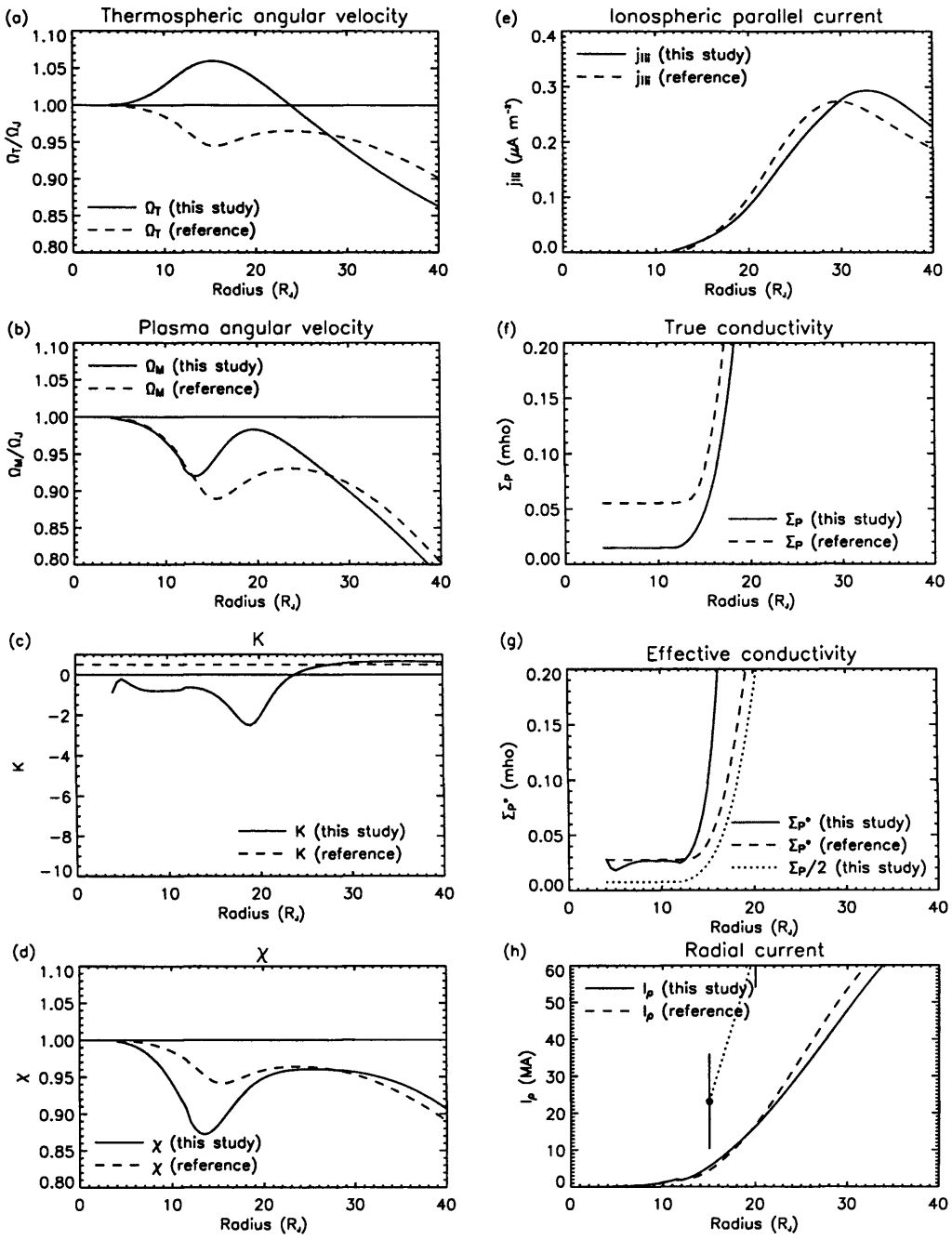

Figure 6.6: Magnetospheric parameters for the inner region, with the true background conductivity reduced to $\Sigma_{P0} = 0.01375$mho.

6.2 Effect of fluctuating electric fields

The above establishes that the basic behaviour of the middle magnetosphere and auroral oval is relatively unaffected by our standard thermospheric model. Other than the super-corotation in the inner magnetosphere, previous studies have described the behaviour well.

We now examine the sensitivity of this basic response to the parameters that define the thermospheric model. Firstly we introduce extra Joule heating in the polar cap, such as may be induced by small-scale fluctuations in the electric field (see Section 2.2.4). Our approach is to add a component to the Joule heating as described by Eqn. 2.50. We assume that, as at Earth, the fluctuations originate in the solar wind and thus apply to the regions coupled, to some extent, to the solar wind, i.e. regions A and B. It may be that fluctuations are also important in the inner and middle magnetosphere regions, but for the purposes of this study we confine ourselves to the solar wind coupled regions.

We show the results of four runs with r.m.s. fluctuations in the electric field of $\Delta E = 0.3$, 0.5, 0.7 and 1.0 V/m. Since the extra Joule heating goes as the r.m.s. electric field fluctuation squared, this set of runs spans about one order of magnitude of extra Joule heating, from heating that makes a very small difference to the temperatures to heating that produces temperatures in the polar cap that are at the upper limit of the available observations. Note that we explicitly specify the electric field fluctuation, rather than the relative electric field fluctuation determined by the parameter s. If the mean field magnetospheric electric field is E_θ then $s = \Delta E / E_\theta$.

6.2.1 Distribution of fluctuation heating

Before showing the detailed results of these runs, we show in Fig. 6.7 the vertical distribution of Joule heating, ion drag energy and fluctuation heating at 5° colatitude from the model run with $\Delta E = 0.3$V/m, plotted against the vertical distribution of the parameter k and the Pedersen and Hall conductivities per unit mass.

Firstly, note in the left hand panel the dominance of the Pedersen conductivity compared to the Hall. This difference is much clearer when the conductivites are plotted against a linear scale, compared to the log scale in Fig. 2.6. The centre panel then shows the neutral wind parameter k, but also plots the two components k_θ and k_ϕ (Eqns. 2.40 and 2.41). These are simply the meridional and zonal neutral winds respectively, normalised to the zonal plasma velocity. It is clear from this plot that the zonal wind is much greater than the meridional wind at all altitudes where the conductivity is significant. Since, according to Eqn. 2.44, the meridional component must be coupled to a significant Hall component to influence the coupling with the magnetosphere, and the Hall conductivity is, as just discussed, rather low, the meridional wind makes a tiny contribution to k.

Thus k_ϕ coupled to the Pedersen conductivity is very much the dominant contribution, and

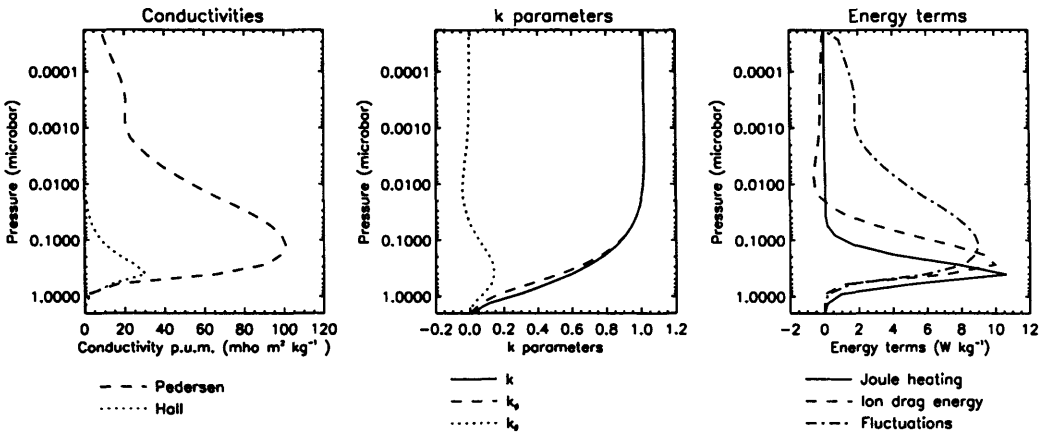

Figure 6.7: Vertical distribution of conductivity, normalised neutral rotation velocities and selected energy terms at 5° colatitude, for a run with $\Delta E = 0.3$V/m. Left: Pedersen (dashed line) and Hall (dotted line) conductivities. Centre: k (solid line), k_ϕ (dashed line), k_θ (dotted line). The plot is shaded for regions > 1 and < 0. Right: mean field Joule heating (solid line), ion drag energy (dashed line), fluctuation Joule heating (dot-dash line). The plot is shaded for regions < 0.

$k \simeq k_\phi$. If k_ϕ were constant with altitude, then we would expect all three energy inputs to peak with the Pedersen conductivity. However, the neutral wind response goes from $k = 0$ at the lower boundary (our boundary condition) to $k \sim 1$ at the upper boundary. This is very similar to the vertical distribution of neutral winds discussed in Section 2.5.3 in the context of a one-dimensional viscosity dominated thermosphere. Although we have seen that viscosity does not dominate in this context, the velocity profiles are similar, and therefore the same analysis applies to the vertical distribution of Joule heating and ion drag. The two energy inputs are thus confined below the conductivity peak, the former lying at a slightly lower altitude. However, the fluctuation heating has no dependence on the neutral winds, and its peak thus lies exactly coincident with the conductivity peak. Hence the fluctuation heating peaks above both the Joule heating and ion drag.

In Chapter 4 we demonstrated the importance of the altitude of the energy input for its efficiency as an energy source for lower latitudes. Since the fluctuation heating lies at much higher altitudes than the mean field Joule heating it is expected to heat lower latitudes more efficiently. Its altitude above the ion drag layer should also protect this energy input somewhat from the effect of the ion drag 'fridge'.

It is also interesting to analyse the behaviour at high altitudes. At these altitudes k is marginally greater than unity, since the thermally driven equatorwards wind in this region is driven into sub-corotation by the Coriolis force. The fact that k is only slightly greater than

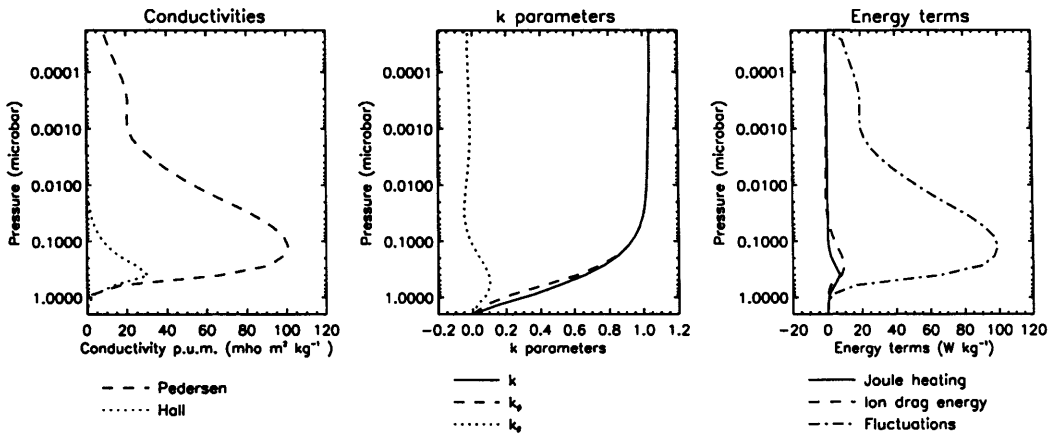

Figure 6.8: Vertical distribution of conductivity, normalised neutral rotation velocities and selected energy terms at 5° colatitude, for a run with $\Delta E = 1.0$V/m, in the same format as Fig. 6.7.

unity indicates that the ion drag is limiting the sub-corotation of this wind system. The ion drag energy is slightly negative at high altitudes, demonstrating that kinetic energy is being extracted from the thermally driven winds. However, there is very little Joule heating associated with this negative ion drag energy, such that at this latitude very little of this kinetic energy is thermalised, and most of it is redistributed, either to lower altitudes or to the magnetosphere.

Finally, for comparison, we show the equivalent diagram for a fluctuation electric field of 1.0V/m in Fig. 6.8. The fluctuation heating has increased by about an order of magnitude, but the other characteristics are almost unchanged, in terms of the ordering of the three components of energy input with altitude. Increasing the fluctation field by only a factor of ~3 has entirely changed the balance of the energy inputs, from one in which mean field Joule heating, ion drag energy, and fluctuation heating are about equal to one in which the fluctuation heating is dominant. This suggests that the behaviour of the thermosphere is very sensitive to the parameter ΔE.

6.2.2 Thermospheric response

We now show in Figs. 6.9 and 6.10 the equivalent plots to Fig. 6.2 for the 0.3 and 1.0 V/m runs. The extra Joule heating term due to fluctuations is shown by horizontal hatching, while mean field Joule heating is still represented by diagonal hatching. Again, the energy input due to each process inside the corresponding hatched regions is greater than 2 W/kg.

Looking firstly at Fig. 6.9, it is clear that despite the relatively high altitude of the fluctuation energy these relatively small fluctuation powers have only a minimal effect on the thermal structure and circulation. This suggests that the ion drag still dominates the thermal structure,

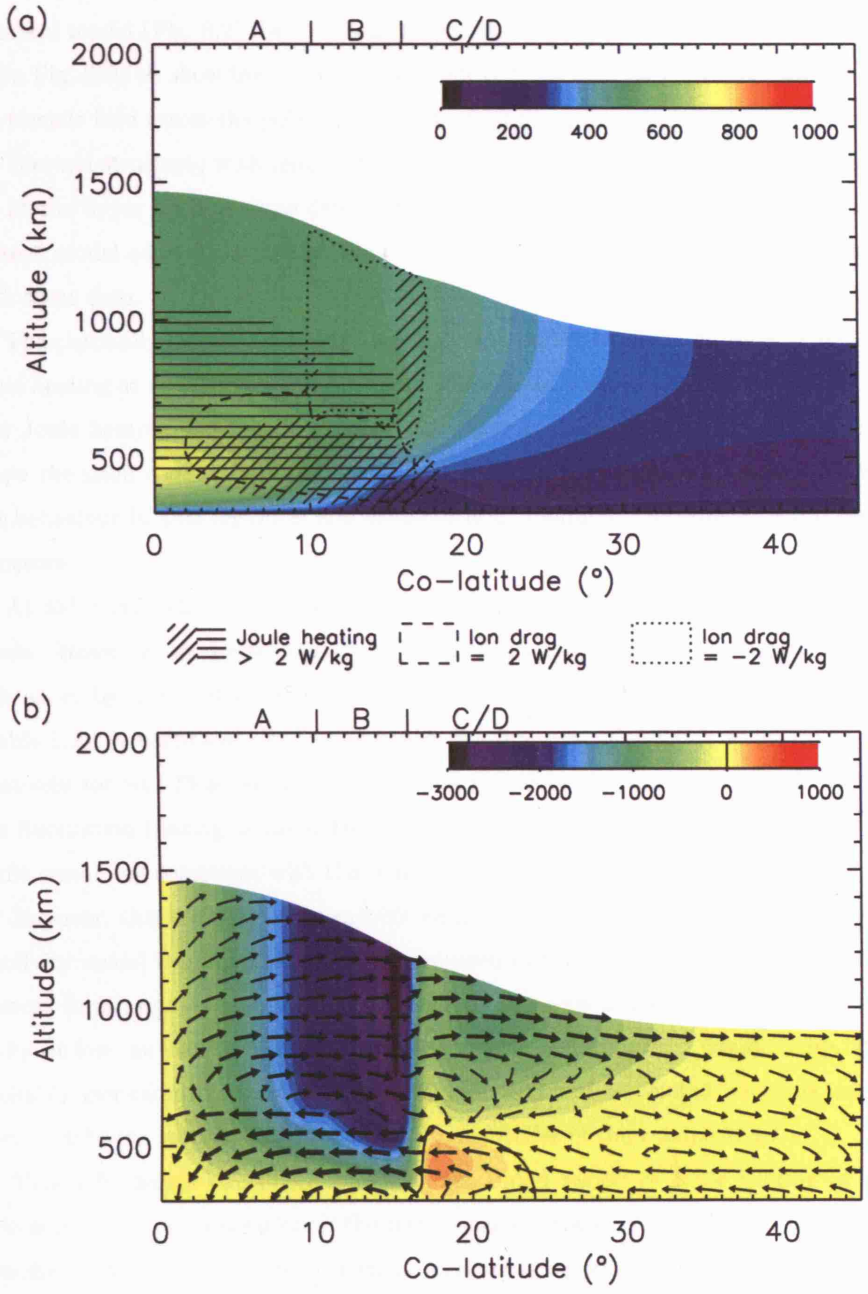

Figure 6.9: Temperatures and winds for r.m.s. fluctuations of 0.3V/m, in a similar format as Fig. 6.2. Diagonal hatching represents regions in which the mean field Joule heating is greater than 2 W/kg; horizontal hatching represents regions in which the fluctuation Joule heating is greater than 2 W/kg.

and indeed the polewards flow that characterises this behaviour is still strongly present at low altitudes.

However, the polar cap is slightly warmer, and, importantly, this intensifies the high altitude thermally driven meridional wind. This now penetrates as far as 45° colatitude, whereas in our standard model (Fig. 6.2) the thermally driven winds only penetrate to 30°.

In Fig. 6.10 we show the equivalent plots for the run with an r.m.s. fluctuation of 1.0V/m in the electric field across the polar cap. The fluctuations now begin to have a significant effect on the thermal structure, with temperatures in the polar cap of up to 1500K. These temperatures are at the upper limit of those determined from spectroscopy of H_3^+ (Table 1.5), so within our current model adding any further fluctuation heating would lead to temperatures inconsistent with these data.

The thermally driven winds now dominate the high altitude behaviour. There is significant Joule heating at all latitudes equatorwards of the main oval as ion drag thermalises these winds. The Joule heating and ion drag energy in the polar cap are confined to very low latitudes, below the main conductivity peak, and in this region there is still a polewards flow. However, the behaviour in this region is now apparently of minimal importance to the overall thermal structure.

At 45° colatitude the exospheric temperature is raised to ~800-1000K by the redistributive winds. However, at the equator (not shown) the exospheric temperature is only 400K. This falls short by a considerable margin of the ~1000K established by numerous measurements (Table 1.3), in particular the Galileo probe measurement of ~900K, which must be considered relatively robust. Thus our initial conclusion is that neither mean field Joule heating/ion drag nor fluctuation heating in the polar cap can account for the elevated low latitude temperature while remaining consistent with the temperatures at high latitudes.

However, this conclusion comes with an important caveat. Our low- and mid-latitude conductivity model is unrealistic, since, as discussed in Chapter 2, the magnetosphere model in its current form requires a conductivity profile that is constant with latitude. Thus the conductivity at low- and mid-latitudes has the same form as the auroral conductivity. In reality it is probably generated by absorption of solar radiation and associated photoelectrons. This may lead to different vertical distributions and magnitudes of the conductivity.

This will change two effects. Firstly, the broad region of Joule heating at mid-latitudes associated with thermalisation of the meridional wind will take a different form. Depending on how the conductivity is different it might increase or decrease. Secondly, the influence of the ion drag on the winds will be altered. As discussed in Chapter 4, the ion drag may have the effect of supplementing the viscosity in supplying angular momentum to the high altitude winds, thus allowing them to penetrate to lower latitudes. However, it may also have the effect of directly slowing the meridional winds.

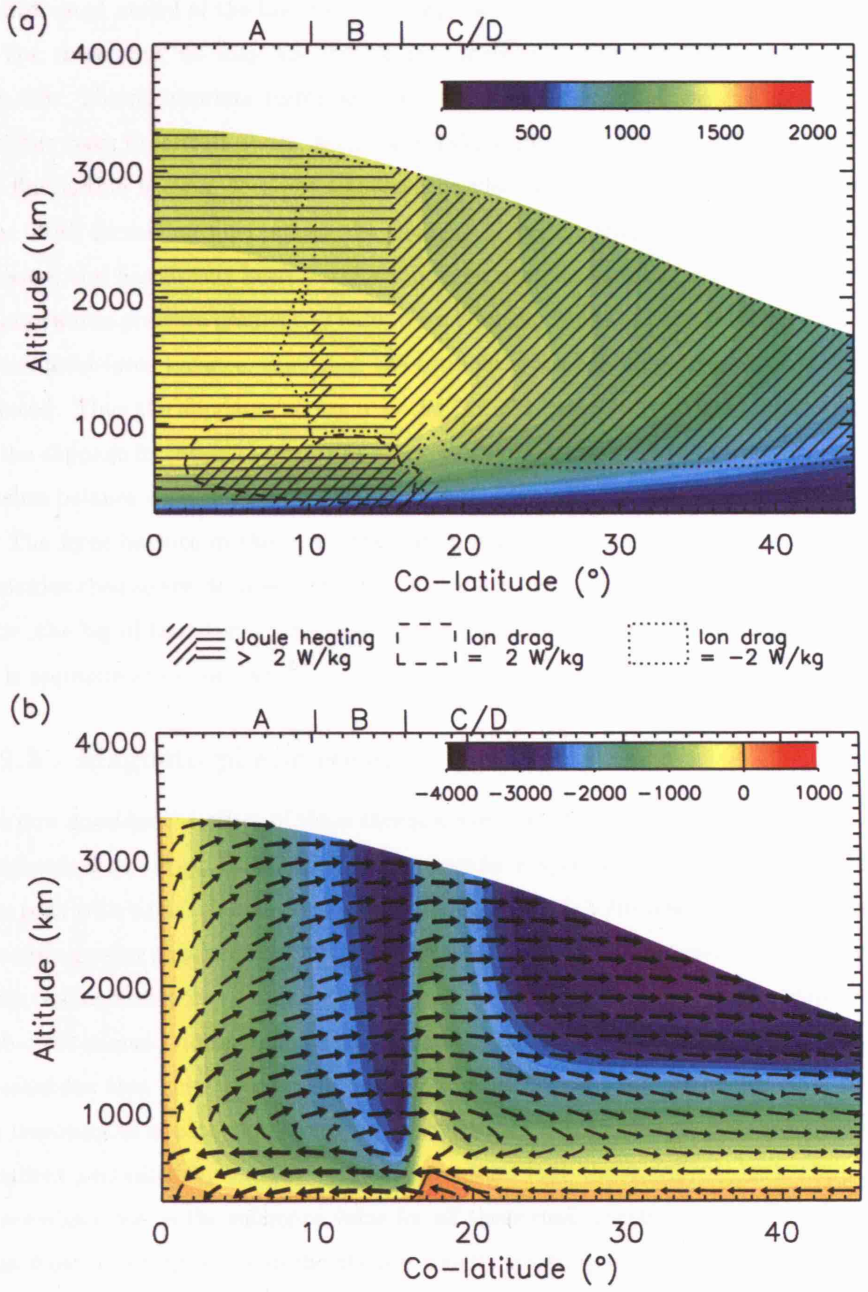

Figure 6.10: Temperatures and winds for r.m.s. fluctuations of 1.0V/m, in the same format as Fig. 6.9.

Another effect that would alter the thermal structure would be the inclusion of H_3^+ radiative cooling in the polar regions. This might permit an energy input in the polar regions great enough to heat the equatorial regions without overheating the polar regions themselves. Separating these various effects is non-trivial, and we leave this issue for a future study to resolve using a more sophisticated model of the low- and mid-latitude conductivity.

For these runs we may also repeat the analysis of the momentum terms represented by Fig. 6.3. The appropriate terms are shown in Fig. 6.11 for the case of zero fluctuations and the four cases described above, each panel taking the same format as Fig. 6.3. It is clear that the fluctuation heating does not significantly affect the velocities or force balance in the polar cap. With increasing fluctuations the slippage of the neutrals in the polar cap does gradually increase: this has already been described in terms of sub-corotating winds driven by the enhanced equatorwards pressure gradient. These sub-corotating winds at high altitudes contribute slightly to the total force balance, such that the total corotational force exerted by Coriolis is slightly reduced. Thus the slippage increases as the Coriolis can no longer support the flow. However, as the slippage increases the ion drag is correspondingly reduced until such time as it once more reaches balance with the Coriolis.

The force balance in the main oval region itself is remarkably stable, even though the flow velocities themselves drop somewhat. This is because, even though the flow velocities drop a little, the lag of the plasma compared to the neutrals — which largely determines the ion drag — is approximately constant.

6.2.3 Magnetospheric effects

We now consider the effect of these thermospheric wind systems on the behaviour of the middle magnetosphere. Figs. 6.12-6.15 show the middle magnetosphere model parameters for each of the runs with r.m.s. fluctuations of 0.3, 0.5, 0.7 and 1.0 V/m respectively. The general trend is towards greater sub-corotation in both the thermosphere and magnetosphere. This is consistent with the increasing importance of the high altitude thermally driven winds, which are exclusively sub-corotational. Adding greater and greater quantities of fluctuation heating slowly erodes the mechanism that generates super-corotation in the region mapping to the inner magnetosphere, by imposing an equatorwards pressure gradient that is much greater than any polewards pressure gradient generated by the ion drag 'fridge'. Note that the magnetospheric slippage parameter χ remains close to the reference value for all these runs, consistent with our earlier observation that most of the structure in the plasma velocity is simply due to the magnetosphere responding almost identically to a different neutral velocity profile.

Another interesting consequence of the thermally driven sub-corotating winds is that the parallel current moves to greater radial distances in the magnetosphere and becomes slightly less intense. The results of Nichols and Cowley (2004) imply that the region of parallel current

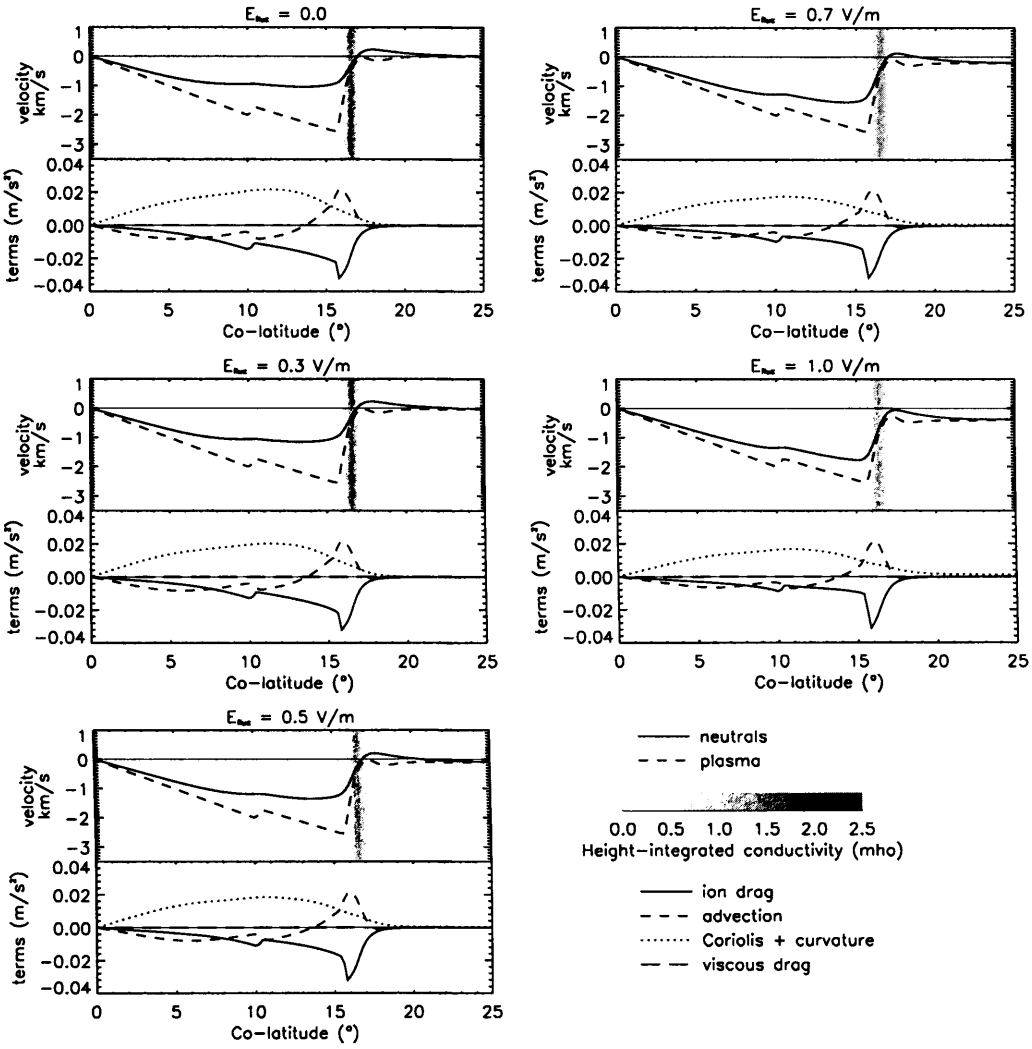

Figure 6.11: Momentum terms for runs with a fluctuating component of the electric field. Each panel is in the same format as Fig. 6.3.

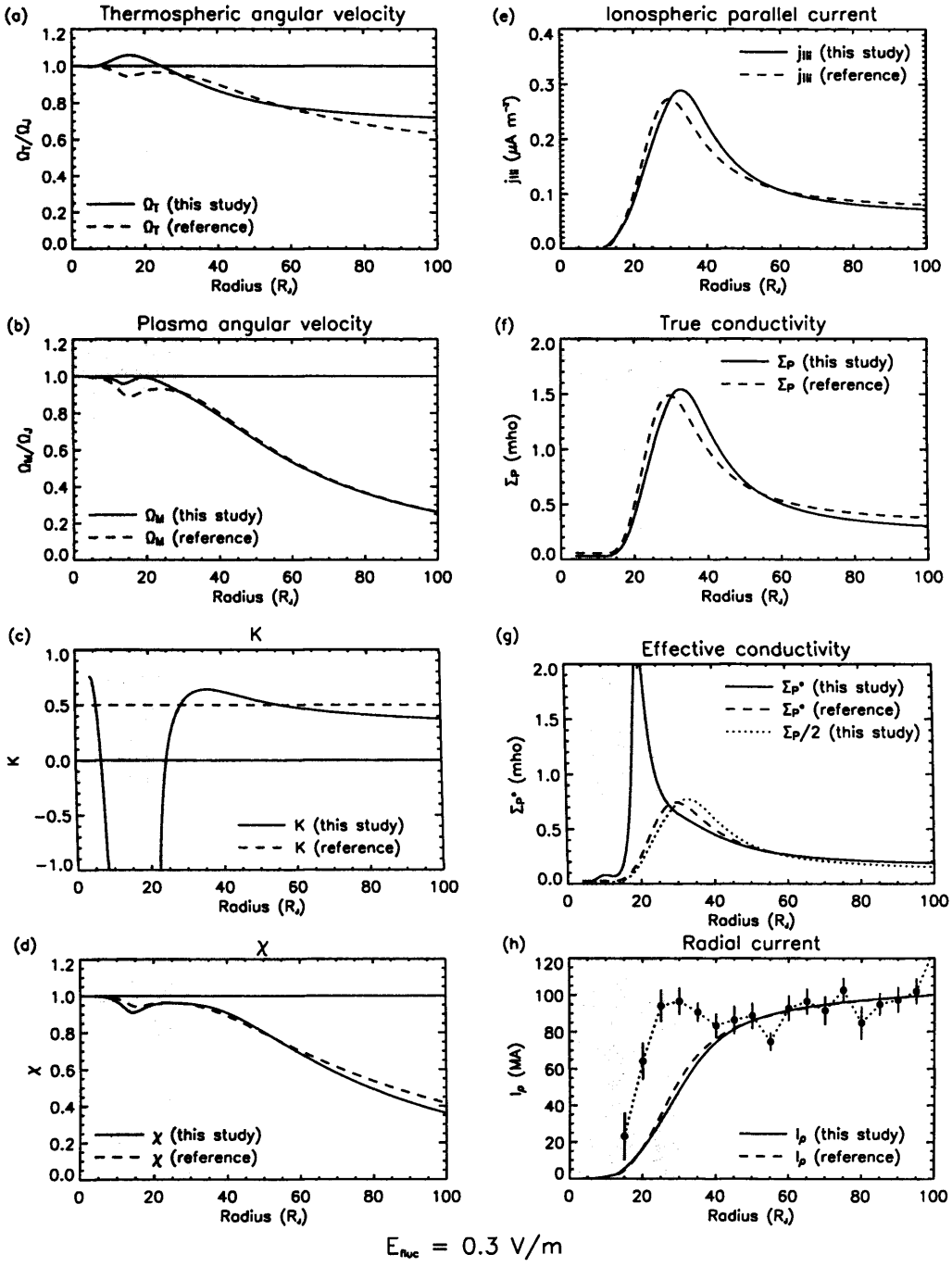

Figure 6.12: Parameters for r.m.s. fluctuations of 0.3V/m, in the same format as Fig. 6.4.

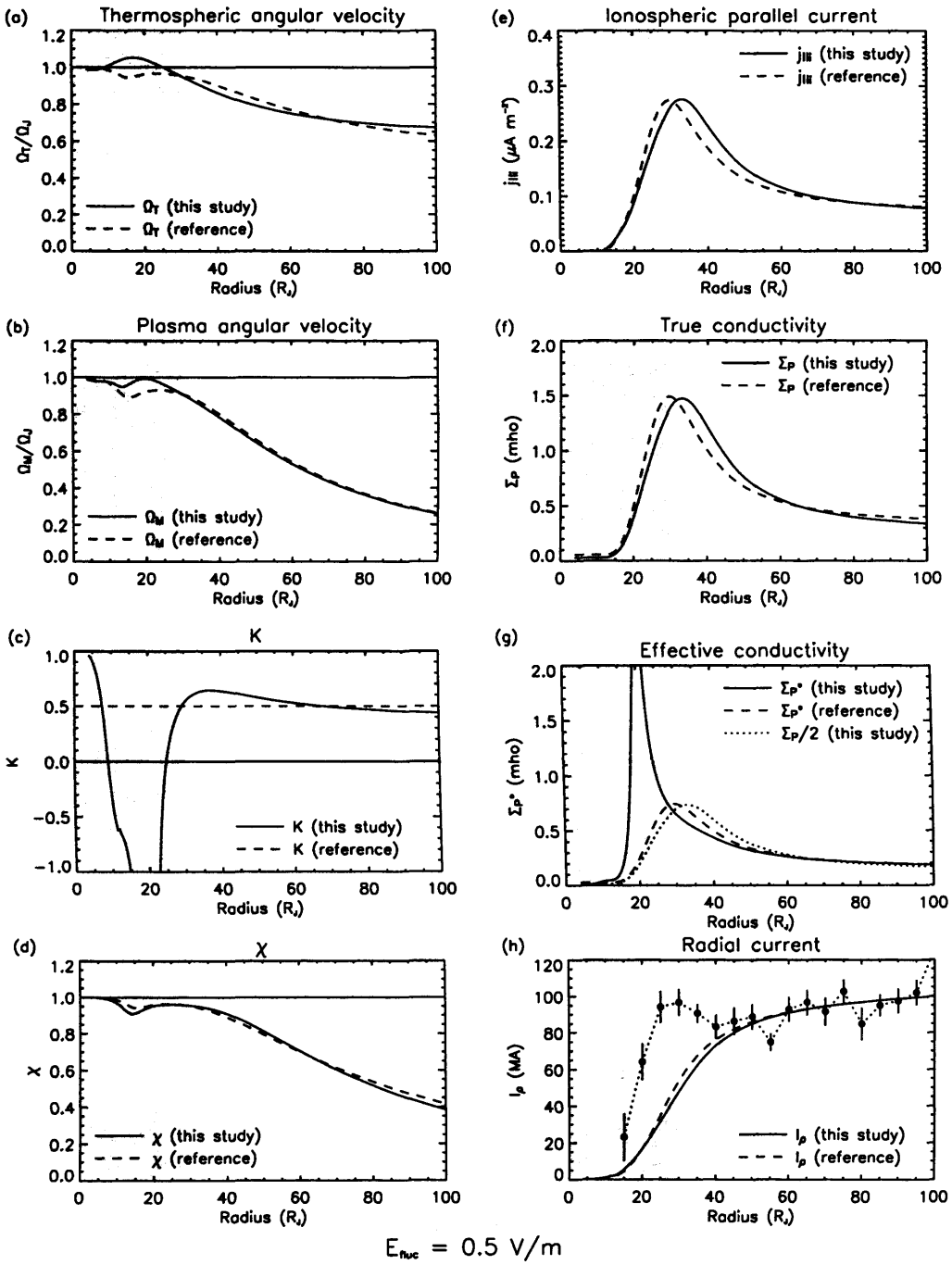

Figure 6.13: Parameters for r.m.s. fluctuations of 0.5V/m, in the same format as Fig. 6.4.

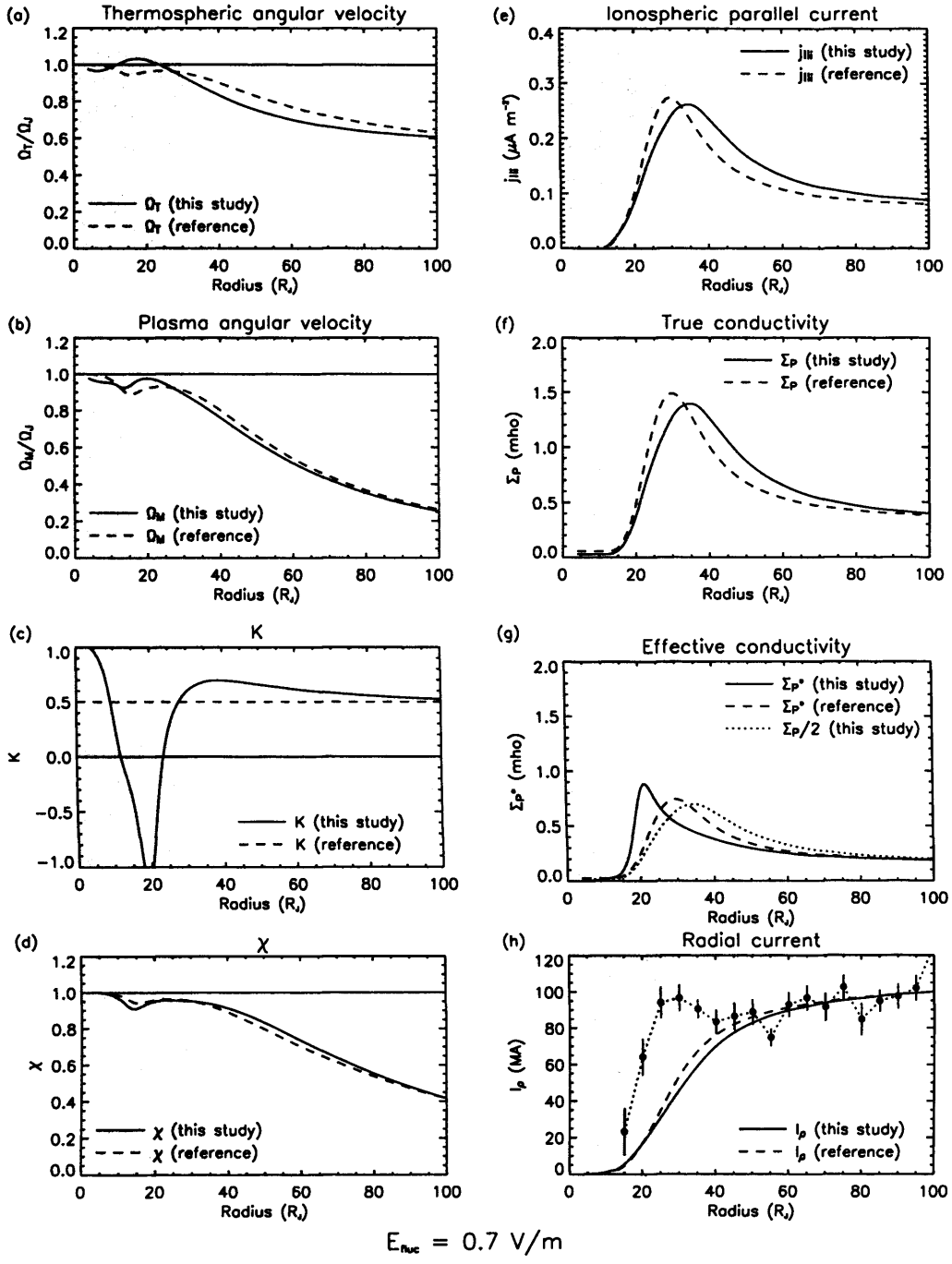

Figure 6.14: Parameters for r.m.s. fluctuations of 0.7V/m, in the same format as Fig. 6.4.

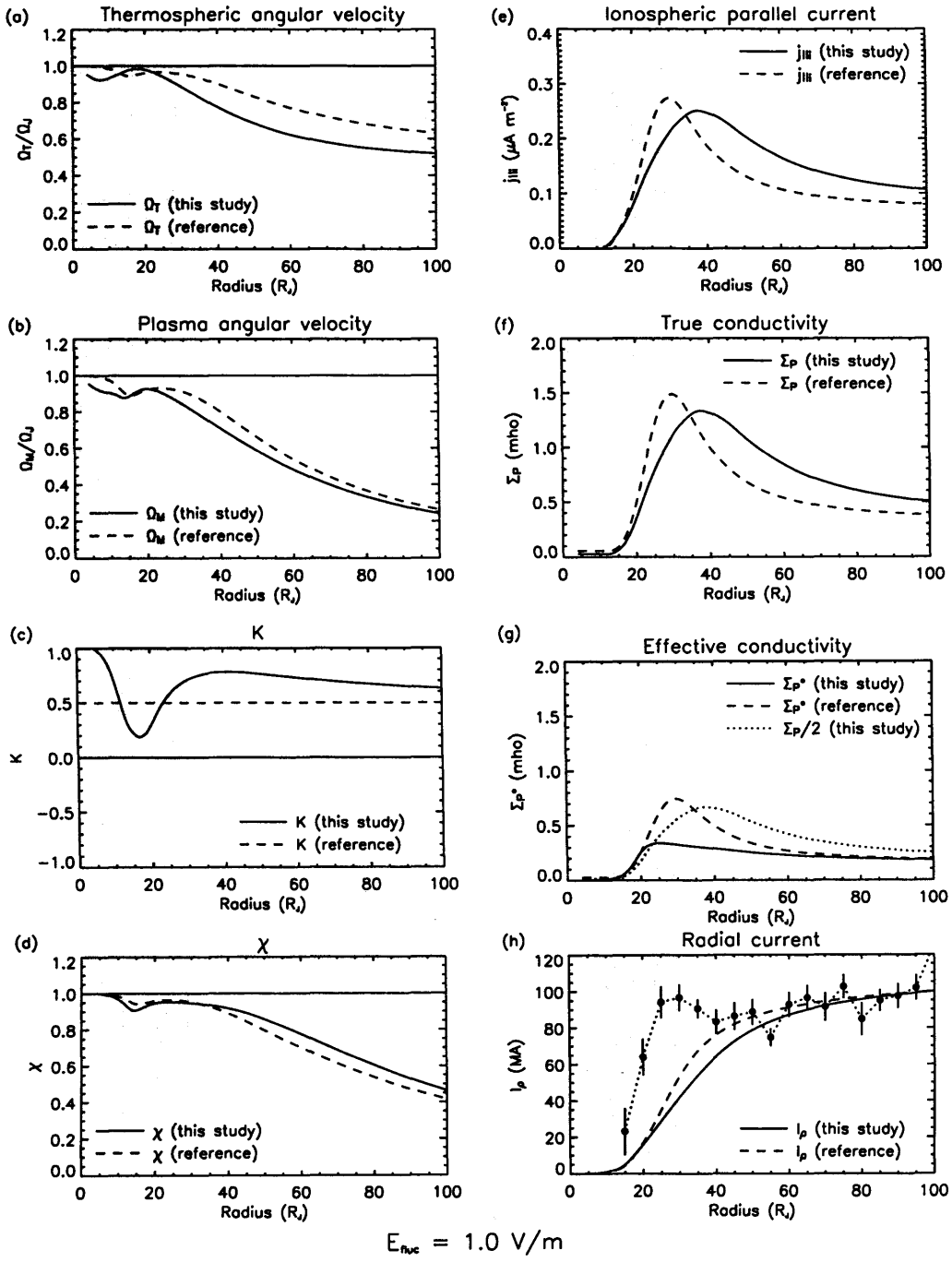

Figure 6.15: Parameters for r.m.s. fluctuations of 1.0V/m, in the same format as Fig. 6.4.

behaves in this manner if the mass outflow rate of iogenic plasma $\dot{M}$ is decreased. We can interpret this in terms of a decrease in the intensity of the current systems required to enforce corotation when the mass outflow rate is lower. In our situation, the entire thermosphere is sub-corotating considerably due to its internal dynamics. Thus the magnetosphere 'sees' a planet that is (differentially) rotating much more slowly than the full rotation rate of Jupiter. This produces an effect similar to a decrease in the mass outflow rate, since the amount of angular momentum required for 'corotation' with the sub-corotating thermosphere is of course much less.

While this interpretation provides an explanation for the observed change in the coupling currents, the change itself does nothing to improve consistency with the available data. Nichols and Cowley (2004) attempted to improve the fit between their model and the data of Khurana (2001) (the dotted line in plot (h) in the figures) by *increasing* the mass outflow rate, thus intensifying and pushing inwards the peak in the parallel current. This in turn pushed inwards the rise in the radial current that occurs in the range 20-40R_J in the reference model. In the data this rise occurs rather steeply at $\sim 20R_J$. The influence of the thermally driven winds is to delay this rise in the radial current, thus making the mismatch between the data and the model worse. We can view this as indirect evidence against the hypothesis that redistribution of polar heating is responsible for the high equatorial thermospheric temperatures.

Nevertheless, having established that equatorwards, sub-corotating winds may push the coupling currents to larger magnetospheric radii, this opens up the possibility that polewards, super-corotating winds might push the coupling currents in to smaller radii, thus improving the match between the model and the data. Such winds might develop if there were strong polewards pressure gradients. These might be caused either by a large equatorial energy source that caused low-latitude temperatures to exceed those in the polar region, or alternatively by significant cooling in the polar regions, perhaps due to enhanced eddy conduction (as discussed in Chapter 5) or significant H_3^+ radiative cooling. This is a possibility that should be investigated in the future.

6.3 Effect of a globally enhanced eddy coefficient

Previous studies have understood the supply of angular momentum in terms of upwards transfer by eddy viscosity (Huang and Hill, 1989; Pontius, 1995). These studies required an enhanced value of the eddy coefficient for their theory to match observations. Indeed, this requirement was cited by Huang and Hill as indirect evidence for the existence of an enhanced eddy coefficient in the polar regions of Jupiter. Contrary to these studies, we have shown that it is not necessary to invoke an enhanced eddy coefficient to supply angular momentum to the polar thermosphere. Nevertheless it is interesting, for comparison, to study the effect of an enhanced eddy coefficient on the behaviour of our model. We have already seen in Chapter 5 the effect of enhancing

both the eddy conduction and eddy viscosity, in the context of Saturn. We can expect similar behaviour at Jupiter — thus, in this section, to avoid too much repetition, we enhance the eddy viscosity only, and analyse the consequences.

Our standard eddy coefficient is $K_T = 1.4 \times 10^2 \mathrm{m^2 s^{-1}}$, consistent with the precipitation model of Grodent et al. (2001) whose H_3^+ profiles consitute our model of the auroral ionosphere. Enhancing this eddy coefficient without recalculating the profiles of H_3^+ is clearly not a self-consistent approach. The bottomside of the H_3^+ density profile is largely determined by hydrocarbon chemistry, which dominates below the homopause. Enhancing the eddy coefficient will move the homopause upwards, and the H_3^+ layer will correspondingly move to higher altitudes. We neglect this effect, and assume the H_3^+ profiles to be unaffected by an enhanced eddy coefficient. This allows us to test the dynamical implications of the eddy viscosity independent of its influence on the ionospheric chemistry.

We enhance the eddy coefficient by factors of 10^2, 10^3, 10^4 and 10^5. Note that these enhancements are very large. The greatest enhancement considered by Huang and Hill (1989) was by a factor of 10^2 (although it should be noted that their eddy coefficient increases with altitude as $n_n^{-1/2}$, such that for most of the range covered by our model their eddy coefficient is slightly greater than ours for a similar degree of enhancement). Recently, as noted in Appendix A, Parkinson et al. (2006) have used Cassini UVIS observations of the Jovian aurora to show that the eddy coefficient in the auroral regions is 'at least' $8 \times 10^2 \mathrm{m^2 s^{-1}}$ and 'possibly greater than' $4 \times 10^3 \mathrm{m^2 s^{-1}}$. Thus our minimum enhancement by a factor of 10^2 already exceeds the empirical constraints. The results of this section thus very much represent a series of 'thought experiments' investigating the behaviour of the thermosphere in the limit of an improbably large viscosity, while all other variables are held constant.

6.3.1 Thermospheric response

We show the temperatures and winds for enhancements of 10^3, 10^4 and 10^5 in Figs. 6.16-6.18. Note that the temperature and velocity scales differ between these plots.

We do not show the results for an enhancement of 10^2 because the differences between this run and the standard run shown in Fig. 6.2 are minimal. Even the larger enhancement by a factor of 10^3 (Fig. 6.16) only alters the details of the thermospheric behaviour: the basic pattern remains the same as that seen in Fig. 6.2. In particular, the enhanced viscosity does not significantly alter the pattern of sub-corotational winds in the polar cap. The temperatures in the polar cap do increase by ~200K, and this increases the equatorwards pressure gradient at high altitudes, such that the mid-latitude redistributive winds are much stronger. This temperature increase seems to be a consequence of the increase in viscosity slightly slowing both the zonal and meridional winds in the polar region. Slowing the zonal wind increases the velocity difference between plasma and neutrals and increases the Joule heating. Slowing the meridional wind reduces the

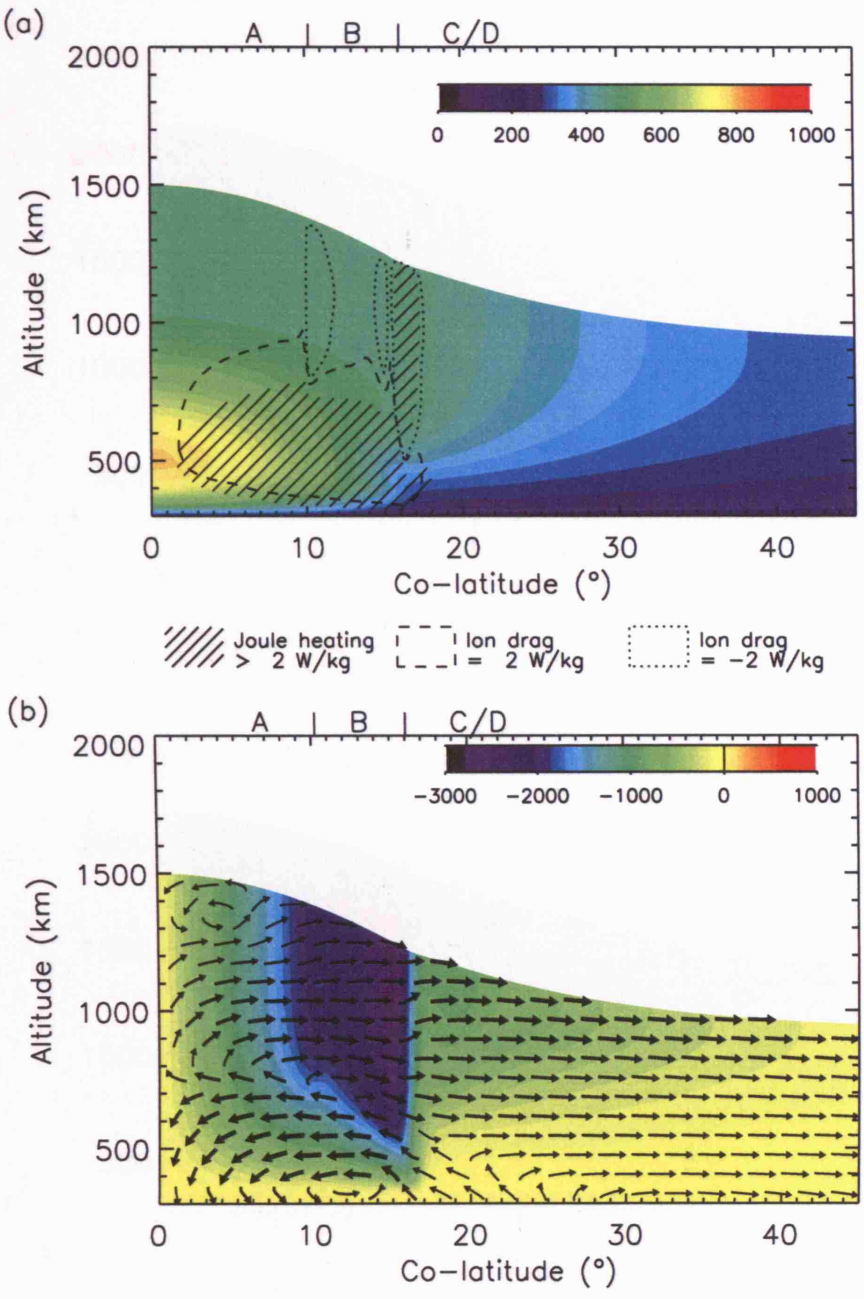

Figure 6.16: Temperatures and winds for an eddy coefficient enhanced by a factor of 10^3, $K_\tau = 1.4 \times 10^5 \mathrm{m}^2\mathrm{s}^{-1}$, in the same format as Fig. 6.2.

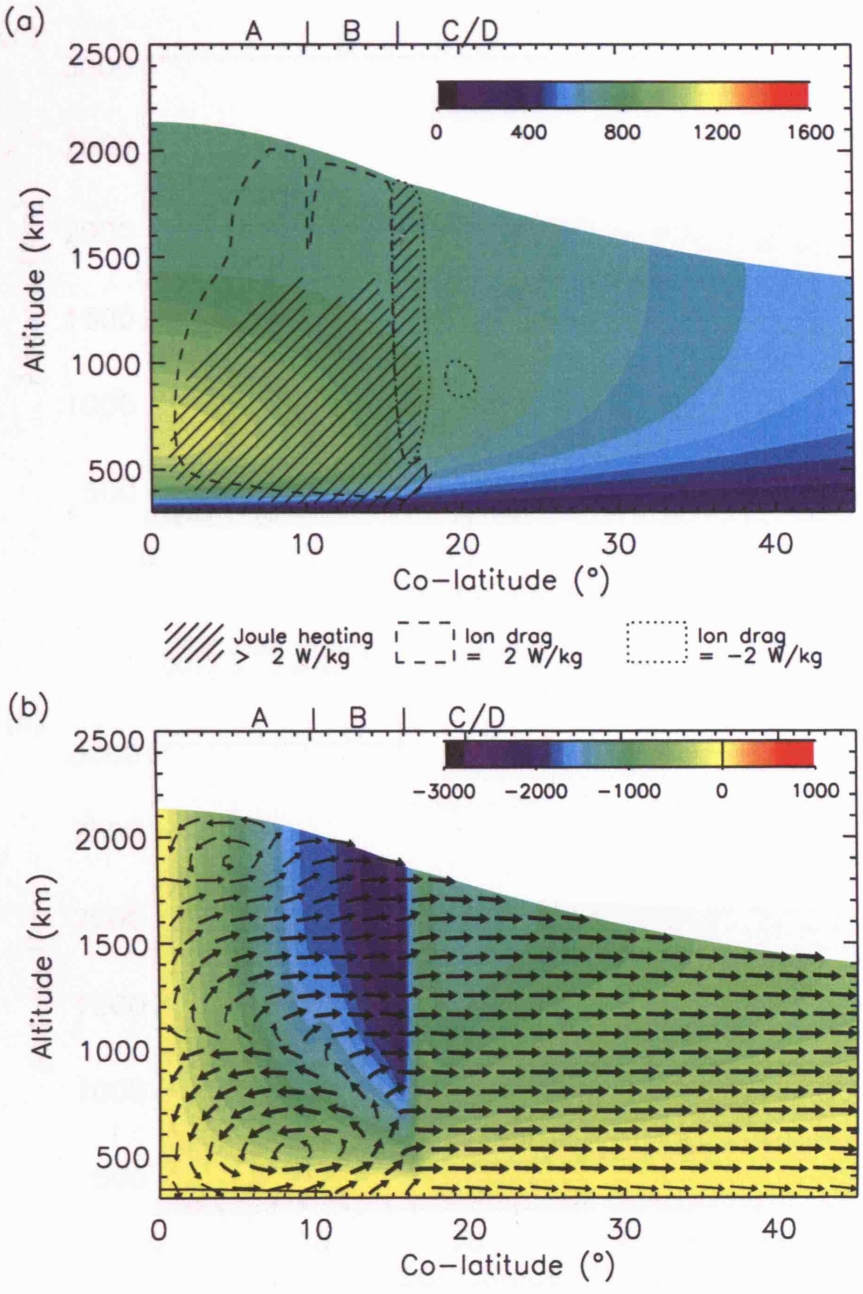

Figure 6.17: Temperatures and winds for an eddy coefficient enhanced by a factor of 10^4, $K_\tau = 1.4 \times 10^6 \mathrm{m^2 s^{-1}}$, in the same format as Fig. 6.2.

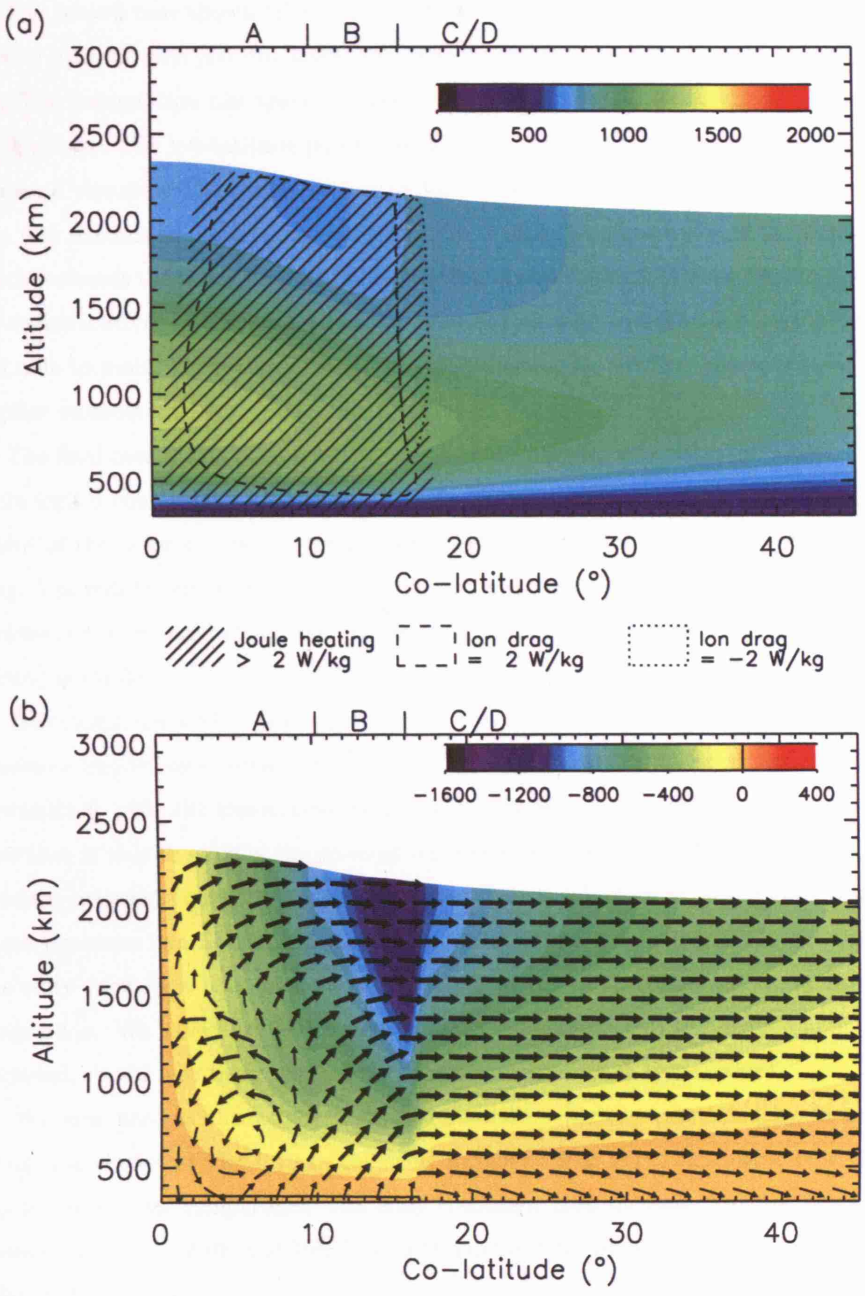

Figure 6.18: Temperatures and winds for an eddy coefficient enhanced by a factor of 10^5, $K_\tau = 1.4 \times 10^7 \mathrm{m}^2\mathrm{s}^{-1}$, in the same format as Fig. 6.2.

supply of cool gas from mid-latitudes by the polewards ion drag 'fridge' flow, thus allowing Joule heating to warm the gas for longer before it passes out of the system. The combination of these two effects elevates the temperature. Other than these small differences the behaviour is not radically different.

The second case shown (Fig. 6.17) is for an enhancement by a factor of 10^4, i.e. 10 times greater than the case just discussed. The thermal structure and flow are now clearly quite different. The temperature has again increased significantly and the zonal winds are now noticeably much slower. The low-latitude polewards flow of the 'fridge' has also become disrupted by the increased viscosity. The region subject to Joule heating and significant ion drag in the polar region now extends to much higher altitudes; this is again a consequence of the slower zonal winds which increases the relative velocities of the plasma and neutrals. Equatorwards of the main oval the redistributive meridional flow has become very strong, driven by the large pressure gradient and able to maintain itself against the Coriolis barrier by efficient upwards viscous transfer of angular momentum.

The final case shown (Fig. 6.18), for an enhancement by a factor of 10^5, takes this behaviour to its logical conclusion. The zonal winds are so restricted by viscosity that the entire vertical extent of the polar cap is subject to significant energy input from both Joule heating and ion drag. The redistributive winds are very efficient and the exospheric temperature at 45° colatitude is close to the required equatorial temperature of 1000K. The equatorial temperature itself (not shown) is similar.

Enhancing the eddy viscosity thus has two interrelated implications: firstly to alter the dynamics implied by a particular thermal structure, and secondly for the heating implied by these dynamics to alter the thermal structure itself. The result is a radically different thermospheric flow that is able to explain the elevated equatorial temperatures. However, as indicated above, it seems extremely unlikely that the eddy coefficient is enhanced to such a great degree, and that these processes can be invoked to explain the observed temperatures. In the final run shown the eddy coefficient is so great that it flatly contradicts the observations by several orders of magnitude. We have also deliberately omitted enhancement of the eddy conduction, which, if included, would inevitably restrict the temperatures to much lower values.

We now analyse the height-integrated rotation velocities calculated by these model runs. These are shown in Fig. 6.19 in the same format as Fig. 6.11. We also replot Fig. 6.3 in the top left panel, for comparison. The eddy coefficient then increases moving down the left hand column by factors of 10^2 and 10^3. The right hand column shows the results from eddy coefficients enhanced by 10^4 and 10^5.

The initial enhancement (by 10^2) makes very little difference to the behaviour. The neutral rotation velocity continues to be supported largely by Coriolis and advection, although the contribution from viscosity is now distinguishable from zero. The main features of the response

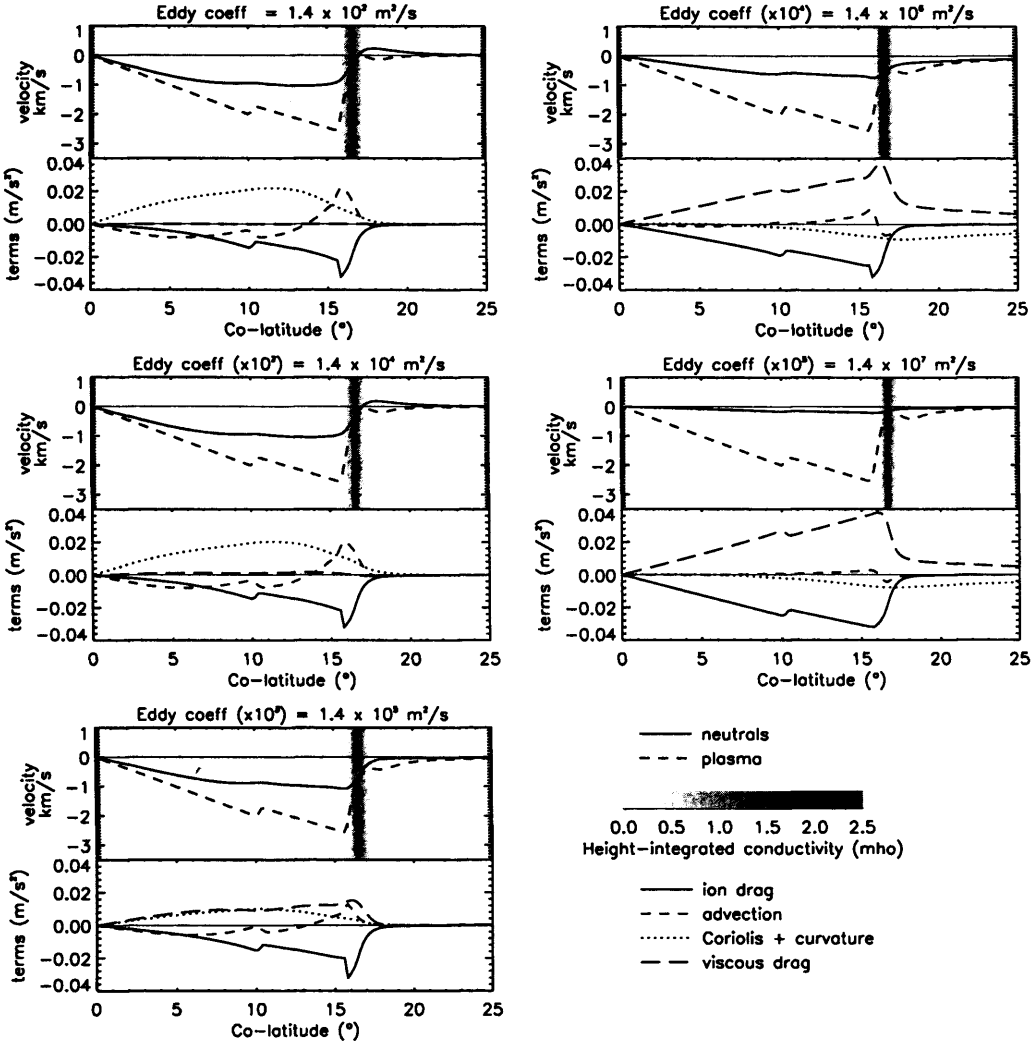

Figure 6.19: Terms for eddy enhancement runs. Each panel is in the same format as Fig. 6.3.

— in particular the super-corotation equatorwards of the main oval — are identical.

The second enhancement (by 10^3), corresponding to Fig. 6.16, now begins to alter the behaviour. Viscosity becomes as important as Coriolis in opposing ion drag across most of the polar cap, and is more important close to the main oval. The region of super-corotation, which is generated by the dominance of Coriolis, is damped out by the viscosity.

The third enhancement (by 10^4), corresponding to Fig. 6.17, shows viscosity as the dominant force opposing ion drag. Coriolis now acts in the same direction as ion drag due to the importance of thermally driven equatorwards winds, which are driven into sub-corotation by Coriolis. Indeed, the region equatorwards of the main oval, which previously exhibited super-corotation, now sub-corotates somewhat. It is interesting that in this region the introduction of an enhanced viscosity *increases* the lag of the neutrals relative to the plasma by restricting the supply of angular momentum by advection and Coriolis. Only when it is enhanced still further is it able to supply comparable quantities of angular momentum by itself.

This further and final enhancement (by 10^5), corresponding to Fig. 6.18, shows the almost total dominance of viscosity to the extent that the thermospheric rotation velocity is almost exactly that of corotation. The velocity just equatorwards of the main oval has now risen back to corotation. Note that there is still some sub-corotation of the neutral winds, due to the small component of sub-corotational Coriolis acting on the thermally driven equatorwards winds. Thus, even when viscosity is almost totally dominant, there is still some complicated background behaviour driven by the Coriolis force.

6.3.2 Magnetospheric response

It is now interesting to examine the consequences of this behaviour for the middle magnetosphere region. Parameters for the four eddy enhancement runs are shown in Figs 6.20-6.23.

The neutral rotation velocities exhibit the behaviour described in the previous section, initially slipping into greater sub-corotation as the viscosity is increased, and then for very high viscosities returning almost to perfect corotation. As in the previous experiments, the slippage parameter χ is fairly stable, such that the plasma rotation velocity decreases and increases alongside the neutrals.

Note that in the run with the greatest viscosity, we have almost restored a situation analagous to that studied by Huang and Hill (1989), in that the response of the thermosphere is (almost) constant everywhere. There are certainly no regions where $K < 0$, a situation that could not arise in their model. The most conspicuous deviation from this behaviour is the peak in K at a radius of $30R_J$. This is associated with the peak in the plasma velocity related to the enhanced conductivity in the main oval. However, since the remaining 'slippage' in the neutrals is approximately flat across this region (or at least changing slowly, with no strong maximum or minimum) the rise in the plasma velocity comes close to the neutral velocity, increasing K at

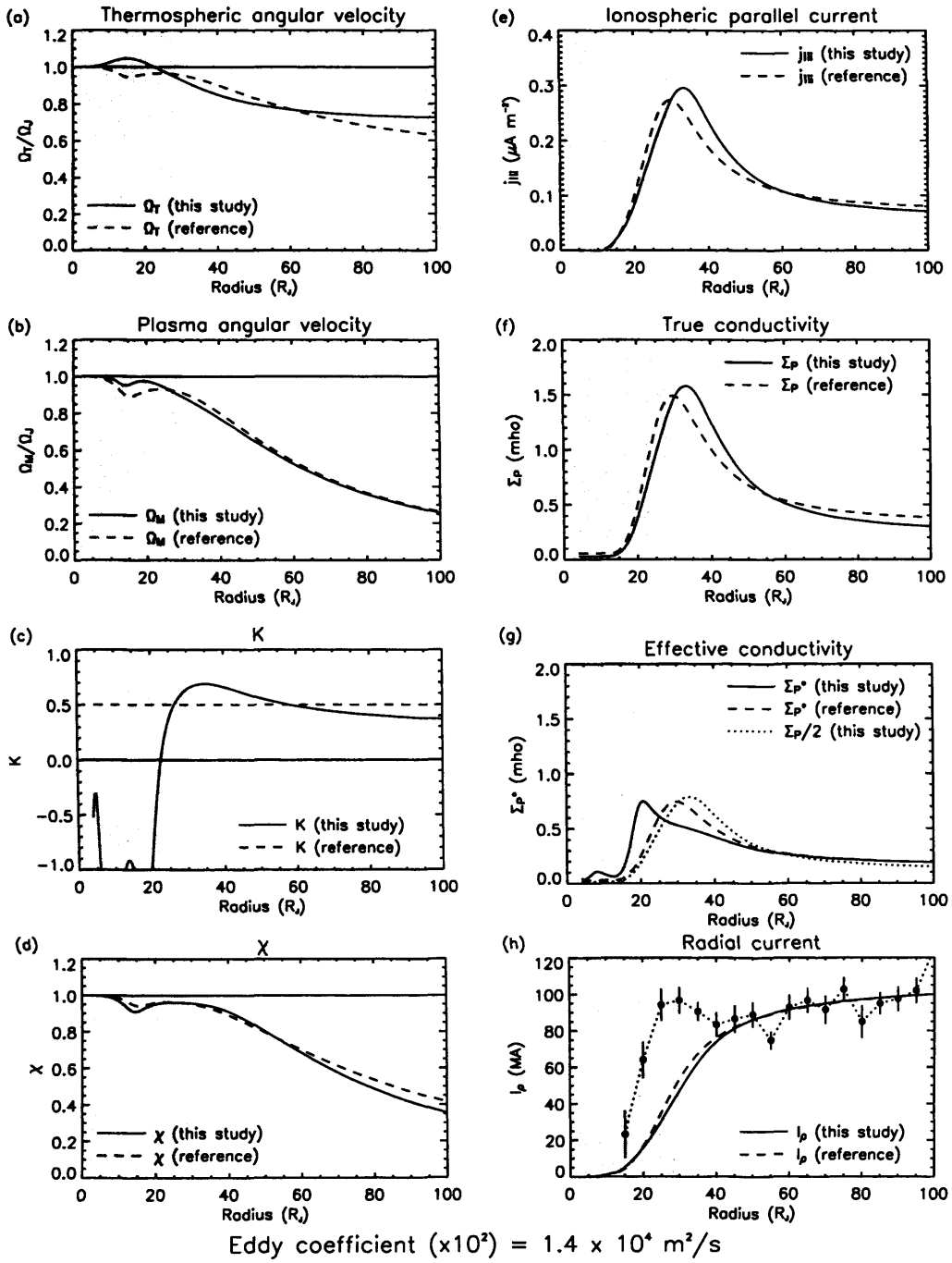

Figure 6.20: Parameters for eddy coefficient enhanced by a factor of 10^2, $K_\tau = 1.4 \times 10^4 \mathrm{m^2 s^{-1}}$, in the same format as Fig. 6.4.

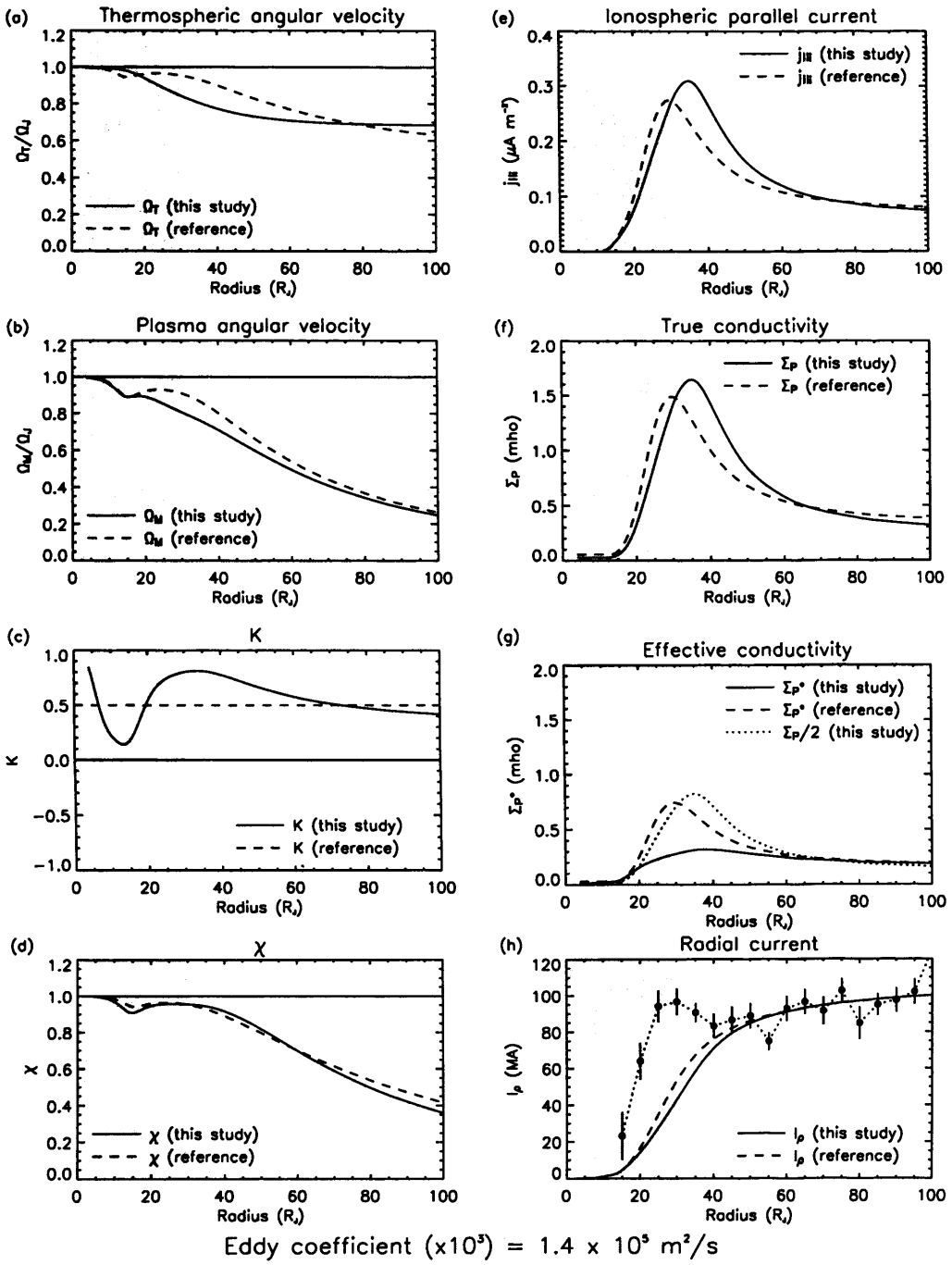

Figure 6.21: Parameters for eddy coefficient enhanced by a factor of 10^3, $K_\tau = 1.4 \times 10^5 \mathrm{m}^2\mathrm{s}^{-1}$, in the same format as Fig. 6.4.

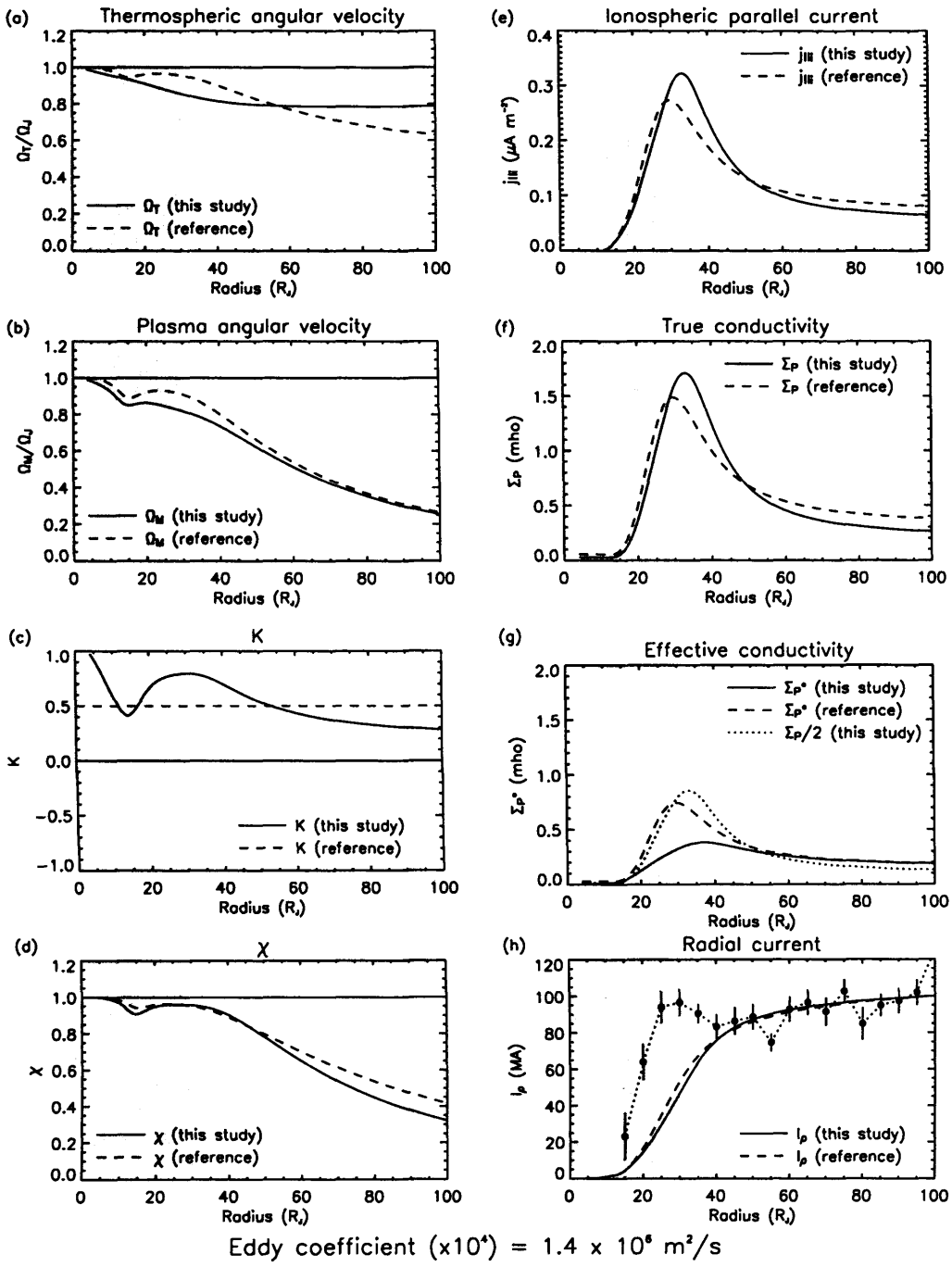

Figure 6.22: Parameters for eddy coefficient enhanced by a factor of 10^4, $K_\tau = 1.4 \times 10^6 \mathrm{m^2 s^{-1}}$, in the same format as Fig. 6.4.

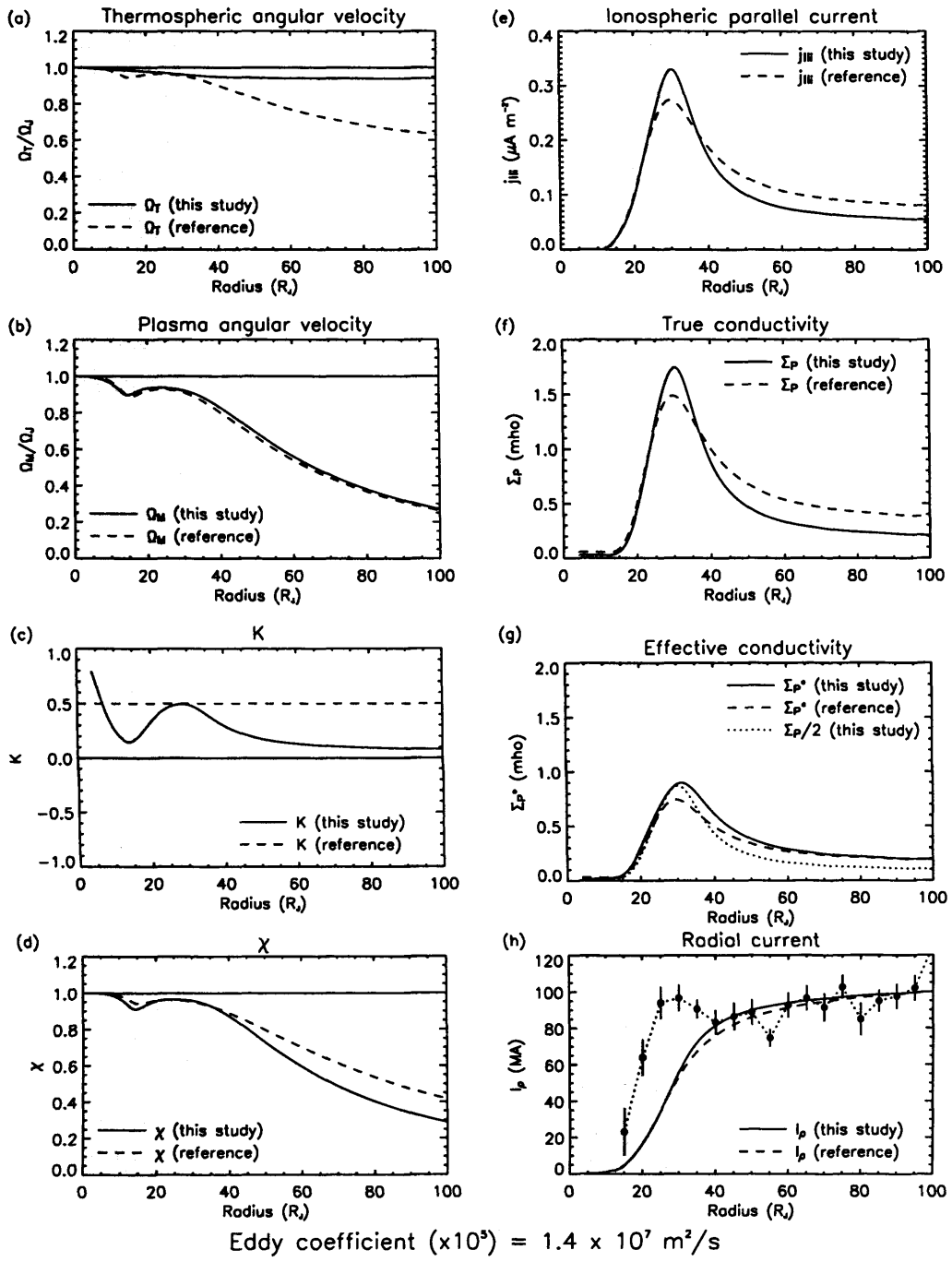

Figure 6.23: Parameters for eddy coefficient enhanced by a factor of 10^5, $K_T = 1.4 \times 10^7 \mathrm{m^2 s^{-1}}$, in the same format as Fig. 6.4.

this point to 0.5.

The neutral velocity is approximately flat because, as mentioned above, the residual 'slippage' is driven by the Coriolis force acting on the thermally-driven meridional winds. Since this 'slippage' is not directly controlled by the plasma flow, it does not respond to the peak. Indeed, internal thermospheric dynamics will always generate small zonal winds that are important when the details of almost corotating plasma are in question. Thus thermospheric dynamics are likely to always play an important role in this inner region where the plasma is close to corotation. This means that even in our limit of improbably high viscosity, the simple situation of Huang and Hill (1989) does not apply.

Due to the large changes to the neutral velocity profile induced by the eddy enhancements, the behaviour of the plasma velocity in the inner region is very variable. In our standard run (Fig. 6.4) and the first eddy enhancement run (Fig. 6.20), the plasma velocity in the inner region is greater than that implied by the reference model. This is due to our effective conductivity being slightly too large, as already discussed in Section 6.1.3. However, the next enhancement of the eddy coefficient (Fig. 6.21) induces greater slippage of the thermosphere due to thermally driven winds. In this case our plasma velocity matches the reference model well in the inner region, and thus matches reasonably well the data of Hill (1980).

Further enhancing the eddy coefficient, though, leads firstly to the slippage of the plasma increasing (Fig. 6.22) and then to it increasing again to values close to the reference model (Fig. 6.23). This complicated behaviour is dictated almost entirely by the form of the thermally driven winds, which are determined largely by processes inside the polar cap. Thus the effective conductivity linked to this inner region of the magnetosphere is critically dependent upon processes occuring elsewhere in the thermosphere, and it is thus not trivial to consistently reproduce the behaviour of the inner region in a model of the type presented here.

The position, width, and intensity of the peak in the field-aligned current and the form of the radial current are also slightly altered in response to the enhanced eddy coefficients. For example, in the run with the greatest eddy viscosity the peak in the field-aligned current and conductivity is at the same position as in the reference model, but is thinner and more intense. The peak corresponds almost precisely to the aforementioned peak in K, such that the effective conductivity is preferentially reduced in this region and thus has a very similar form to that in the reference model.

6.4 Conclusions

While the basic response of the Jupiter model is very similar to that of the Saturn model described in detail in Chapter 5, the unique nature of our coupled thermosphere-magnetosphere model has given us various useful insights into the coupling between the dynamics of the two

regions.

Principally, we have demonstrated the inadequacy of the constant K model used by numerous previous studies. While there is some justification for employing this model in the outer regions of the middle magnetosphere (between about 40 and $100R_J$), where we find $K \sim 0.5$, all previous physical justifications of this value are flawed in their neglect of effects due to meridional winds. In the inner region, it is not just the justification that is flawed: the results given by our model differ significantly from those given by the reference model, in that we are able to generate features such as super-corotation of the neutrals that previous models have not attempted to represent. Although we have not seen super-corotation of the plasma itself, this is clearly a possibility that might arise if, for example, the background conductivity was somewhat greater. Indeed, the behaviour in this inner region is very sensitive to the neutral winds, and any future theoretical treatment of this region that seeks to provide detailed comparisons with data must take this into account. Even in an extremely improbable scenario in which the eddy viscosity is enhanced by a factor of 10^5 over commonly accepted background values, the dynamics still play an important role in the structure of the magnetospheric response, since pressure gradients and Coriolis forces are still important.

More generally, we have also seen a situation similar to that mentioned in Chapter 5, in which widely separated regions of the magnetosphere are able to influence each other via coupling to the thermosphere. In the case of Saturn, this coupling took the form of a pseudo-viscous interaction in which the thermospheric response to the magnetosphere became 'smeared' by winds, and this smearing was then communicated back to the magnetosphere. In our Jupiter model, we see some other interesting effects. Firstly, the behaviour of the thermosphere corresponding to the main oval (region C) appears to be controlled not by the regions of the magnetosphere that map directly to this region, but to regions that map polewards of the main oval (regions A and B). These latter regions generate most of the Joule heating and ion drag that dominates the thermospheric dynamics. Thus much of the interesting behaviour observed in our model of the middle magnetosphere originates in the outer magnetosphere and solar wind driving the thermosphere. This cannot be simply characterised as a 'pseudo-viscous' interaction: it is much more complicated than that term implies.

Secondly, we have the interesting super-corotation observed in the thermosphere at latitudes that map to the inner magnetosphere. We showed in Chapter 5 that such regions of super-corotation are generated equatorwards of regions of significant ion drag. In the case of the inner magnetosphere, the ion drag that generates the super-corotation is due to the rest of the magnetosphere, which all sub-corotates to a greater or lesser extent. Thus we have a situation in which, via the thermospheric interaction, the sub-corotating middle and outer magnetospheres act to support the corotation of the inner magnetosphere. This is precisely the opposite of a viscous interaction, and illustrates the surprising behaviour that can arise when the full dynamics

of the thermosphere are considered.

We have also shown that if a properly coupled physical model of the thermosphere and magnetosphere is employed we may tentatively use magnetospheric data to make inferences concerning thermospheric dynamics. In particular, thermally driven winds that might redistribute energy from the poles to the equatorial regions tend to push the bulk of the coupling currents towards larger radii in the magnetosphere. This aggravates the mismatch between the predictions of the reference model and the radial currents implied by the data of Khurana (2001). Since thermospheric dynamics are able to aggravate the mismatch between model and data, this certainly opens up the possibility that, under certain circumstances, they may be able to mitigate it, a possibility that should perhaps be pursued in future studies.

This behaviour also offers indirect evidence against the heating of low latitudes by energy redistributed from high latitudes. However, this must be viewed as a very preliminary conclusion. The form of the radial currents are yet to be explained, and it may be that some process currently missing from the model may both explain the mismatch in the reference model and compensate for the effects due to the thermally driven winds. Nevertheless, even this rather weak inference indicates the usefulness of coupled models, in that we are able to place additional, indirect constraints on the thermospheric behaviour through our understanding of the magnetosphere.

Finally we must emphasise the many omissions and caveats that surround this work:

- we have yet to assess the consistency between our plasma angular velocity model and the predictions of the Isbell theory, nor have we considered whether it may be necessary to introduce a 'χ-model' for regions A and B, as discussed in Chapter 5,
- we continue to assume a corotating lower boundary with a fixed temperature. The precise location of this lower boundary and its parameters are somewhat arbitrary, and this must be considered a source of error,
- the neglect of radiative cooling means that its influence upon the thermal structure of the polar cap — which, as discussed in Chapter 5, is intimately linked to the dynamics — cannot yet be characterised,
- likewise, the influence of particle heating, which is likely to be particularly important in the main auroral oval, has not been investigated,
- in our studies of an enhanced eddy coefficient, we neglected effects due to enhanced eddy conduction, altered ionospheric chemistry, and latitudinal variations of the eddy coefficient. All of these issues need to be treated more completely in future modelling studies,
- our low-latitude ionosphere model is currently a scaled version of the auroral conductivity model. This was a necessary simplification to permit coupling to the Nichols and Cowley

magnetosphere model. Calculating a full low-latitude ionosphere model may have interesting consequences.

Correcting these issues, and others, is a difficult problem because there is simply not enough data to properly validate models of the thermosphere and ionosphere. For this reason the results in this chapter merely scratch the surface of a potentially extremely complex and interesting subject.

Chapter 7

Conclusions

7.1 General conclusions

The methodology that we have adopted in this study of the thermospheres of Jupiter and Saturn is representative of a relatively new approach to this area. The traditional approach is exemplified by the two extant Jovian thermosphere-ionosphere models, JIM (Achilleos et al., 1998) and JTGCM (Bougher et al., 2005). These models were generated by converting wholesale to the Jupiter case complex terrestrial models. They both produce interesting results, but their usefulness is clearly hampered by their complexity, which is far out of proportion to the data available for validation. Their complexity also prevents very long runs, and it is thus difficult to be sure that either model has reached steady state. In the context of the specific problem of understanding the energy crisis, this is a major flaw.

The new approach adopted here was arguably initiated by Müller-Wodarg et al. (2006), who began the construction of a Saturn thermosphere-ionosphere model 'bottom up' by generating a basic thermosphere model with simple energy inputs. Our initial study, detailed in Chapter 4, was the natural extension of this approach. We were able to build on Müller-Wodarg et al.'s initial study in three ways. Firstly, we considered results from a two-dimensional parameter space of runs. This allowed a range of plausible scenarios to be systematically assessed. Secondly, we carried out sensitivity studies on the details of our chosen energy distribution, allowing a critical assessment of which features of our energy input distribution determined the various features of the resultant thermal structure. Thirdly, we compared our results with observed temperatures at both high and low latitudes. Since a relatively narrow range within our parameter space satisfied both of the constraints, it is clear that attempting to match more than one data point is crucial if we are to reproduce realistic conditions.

However, it is arguable that the most important conclusion of this initial study was to establish the usefulness of simple, systematic modelling of these undoubtedly complex systems.

The actual results themselves almost certainly do not represent real conditions in the Kronian thermosphere, given the extremely simple nature of the model: but some of the simple physical insights that the simple model made possible are apparently applicable quite generally, for example our discussion of the relative importance of diffusion processes in different circumstances. General results such as these are likely to survive the inquisition of more sophisticated modelling which, with all probability, will show that the actual numerical results presented in Chapter 4 are imperfect.

Having established this methodology, the work presented in Chapters 5 and 6 explicitly sought to apply it to the more specific case of energy and momentum inputs from the magnetosphere. The additional complexity introduced by this specific case arises from the fact that winds generated by inputs of Joule heating and ion drag modify those inputs themselves. Furthermore, these inputs depend on the detailed structure of the ionosphere. Not only is the structure of the ionosphere not well understood, but winds driven by Joule heating and ion drag are likely to alter it. We are thus presented with a network of complicated, interdependent feedback loops, with barely any useful data to constrain our modelling.

For this reason we very deliberately resorted to a grossly simplified model of the ionosphere. Our approach aimed to neutralise the complexity of ionosphere modelling by treating the ionosphere as nothing more than a spatially variable coupling coefficient between the thermosphere and magnetosphere. This coupling coefficient is the ionospheric conductivity. By holding the conductivity fixed in a specific way we were then able to study the dynamical interaction between the thermosphere and magnetosphere rather more cleanly than would have been possible with a full thermosphere-ionosphere model.

Indeed, we might view our approach as a mid-way point between one-dimensional treatments in which the thermosphere fulfils the role of boundary condition for the magnetosphere (Huang and Hill, 1989; Pontius, 1995) and three-dimensional treatments in which the magnetosphere acts as a boundary condition for the thermosphere (Achilleos et al., 1998; Bougher et al., 2005). The former assume fixed profiles of thermal structure and conductivity and calculate only zonal winds; the latter perform detailed time-dependent calculations of both the thermospheric and ionospheric structure, including all three components of the neutral wind. Our two-dimensional model attempts to retain the simplicity of the one-dimensional studies while capturing some of the multi-dimensional dynamical complexity that the thermosphere must actually exhibit.

This approach has allowed us to analyse relatively easily various processes associated with the coupling between the thermosphere and magnetosphere that have not previously been considered, in particular:

1. the ion drag 'fridge' flow and its dominance of the high latitude thermal structure and dynamics

2. supply of angular momentum by advection

3. super-corotation of the thermosphere at sub-auroral latitudes

4. coupling between otherwise unconnected regions of the magnetosphere mediated by the thermosphere

These processes are all associated with meridional winds that are driven by the combined effect of sub-corotational ion drag and Coriolis. We can, in a sense, view the four processes listed above as 'discoveries', in that using the thermosphere model we have demonstrated for the first time the possibility of their existence. We can thus tentatively predict that signatures of these processes will be observed at some stage in the Jovian and Kronian systems. Our intermediate approach to the problem of thermospheric modelling has allowed us to include the physics that generates these effects without them becoming obscured beneath too many layers of complexity.

The recognition that eddy viscosity may not be the principle process by which the thermosphere replaces angular momentum extracted by the magnetosphere is particularly important. The eddy viscosity treatment of Huang and Hill is frequently used to justify the parameterisation of the upper atmosphere by an 'effective conductivity'. We have shown that this justification is flawed, but that despite this the Huang and Hill model is an adequate approximation under certain limited circumstances. In general the more complex the structure in the magnetospheric flows, the less likely it is that the Huang and Hill model will suffice. However, it is unreasonable to expect all studies of the magnetosphere to employ a full thermospheric model as their lower boundary condition. There is thus clearly a need for a compromise between the over-simple parameterisation of Huang and Hill and our rather complex model.

A major stumbling block in the development of such a compromise parameterisation must be our new understanding that the thermal structure of the thermosphere has an important influence on the zonal winds and thus on the coupling to the magnetosphere. A prime example of this is the thermal and dynamical structure of the polar thermosphere, which is determined by and in its turn influences the atmospheric layers below and the magnetosphere above. Thus the whole system from the mesosphere to the magnetopause is coupled together inseparably. The careful untangling of this coupling represents a considerable challenge for the future.

7.2 Status of the energy crisis

Largely as a consequence of this interdependency of the various components of the system, we are forced to leave several problems unanswered. Principal among these is the thermospheric energy crisis, which we have singularly failed to resolve. Although we presented results in Chapter 4 that matched the appropriate observations at Saturn, we were able to offer little conclusive evidence that the required heating distributions were realistic. Furthermore, the considerations of Chapter 5 exposed these initial experiments as rather naïve and inconclusive.

However, two aspects of this work present possible solutions to the energy crisis that have not been previously considered in detail. Firstly, we confined our discussion of fluctuation Joule heating to the Jupiter case, and even then we only imposed fluctuations polewards of the main auroral oval. However, it seems inevitable that the middle magnetosphere of Jupiter will not exhibit perfectly smooth plasma flows, since some asymmetry must exist to permit the flux-tube interchange motions that are proposed in order to allow outwards radial diffusion of iogenic plasma. At Saturn similar processes take place and the same argument applies.

Thus it is possible, as already noted by Smith et al. (2005), that fluctuations in the plasma flows extend to mid- or low-latitudes and thus directly heat the thermosphere in these regions. As a process this has the phenomenological advantage that it might function at all four gas giants, thus offering a single consistent explanation for the high thermospheric temperatures.

Secondly, we have shown that the time constants for thermal equilibriation of the thermosphere are of the order of hundreds of planetary rotations. Thus a continuous source of thermal energy may not be necessary to maintain the high temperatures. Instead, we might envisage periodic large heating events every $\sim$100 rotations, followed by periods of gradual thermospheric cooling. Such heating events might, for example, be related to structure in the solar wind driving the magnetosphere periodically.

In summary, our conclusions concerning the energy crisis must remain ambiguous. We have succeeded in describing and analysing numerous important aspects of the thermospheric structure, taking us a few small steps towards a comprehensive understanding of the system. However, the energy crisis remains a crisis.

7.3 Assumptions and omissions

While we have made progress in understanding these coupling processes, to do so we have had to neglect, ignore, simplify or otherwise eschew numerous important aspects of the system.

Many of these simplifying assumptions are geometric. At both Jupiter and Saturn we assumed a spherical planet permeated by vertical gravitational and magnetic fields. We further assumed that the gravitational and magnetic fields were constant across the vertical range of the model. The relaxation of any of these assumptions would undoubtedly change the details of our modelling. However, it is difficult to believe that it would significantly affect the basic physical behaviour of the model. Indeed, the introduction of a magnetic field tilted with respect to gravity would probably marginally increase the latitudinal 'smearing' effects that we observed in the Saturn case.

The other important geometric assumption is that the magnetic fields and plasma flows at both planets are axially aligned. This is particularly a problem at Jupiter, whose planetary dipole exhibits a significant tilt with respect to the rotation axis. A consequence of this is that a

wind that is zonal with respect to the rotational frame is a combination of zonal and meridional components in the magnetic field frame that defines the plasma drifts. Thus the tilted field at Jupiter may result in meridional winds being generated directly in the magnetic field frame by sub-corotational Coriolis forces that generate strong zonal winds in the rotational frame. For this reason meridional winds coupled to Hall conductivity may turn out to be considerably more important than the axisymmetric model implies.

A more fundamental simplification is our treatment of the ionosphere. While this simplification was deemed necessary to make progress, there are many interesting effects that full ionospheric calculations would allow us to study. In particular, the effect of winds on the ionospheric structure may be profound. As commented in Chapter 1, one outstanding problem that confronts ionosphere modelling at both Jupiter and Saturn is that the ionospheric peak in most models occurs at a lower altitude than that seen in the data. Equatorwards meridional winds such as those generated by polar heating have a significant component parallel to the magnetic field at low latitudes, which may induce upwards transport of the ionospheric plasma. This may help to explain the observations.

Motion of plasma associated with the neutral winds may also have an effect at high latitudes. The drift motions of ions relative to electrons that generate the Pedersen and Hall currents in the ionosphere also constitute bulk flow of the ionospheric plasma. In the case of H_3^+, which recombines relatively quickly, this transport is likely to be unimportant. However, longer lived ions such as H^+ may be transported considerable distances by these plasma drifts, and this continual reconfiguring of the ionosphere may have an important influence on the auroral current systems.

We have also not considered the possible importance of ionisation lying below the mesopause. Such structures are visible at very low altitudes in the occultation data presented in Figs. 1.6 and 1.7. These layers of the ionosphere are likely to supplement both the Pedersen and Hall conductivities, and will be coupled to mesospheric winds: they may have an important influence on the coupling currents.

An important omission related to our simplified ionosphere model is the neglect of radiative cooling. As we have commented at various junctures, the unknown influence of radiative cooling, especially that due to the H_3^+ molecule, is likely to alter many of our results. This is most problematic at Jupiter, where H_3^+ radiative cooling is believed to be important globally. However, the fact that we have failed to reproduce the observed high thermospheric temperatures somewhat negates this problem, since we are clearly omitting an (unknown) positive thermal energy source that must be greater in magnitude to any cooling we have omitted. Thus the neglect of radiative cooling can be seen as just another component of our incomplete understanding of the thermal structure.

Finally, we consider the consequences of our simplified magnetosphere models. Most pre-

vious treatments of the thermospheric response to the magnetosphere have assumed that the thermosphere is a largely quiescent flywheel driven by the magnetospheric rotation, a position implied in the 'slippage' model of Huang & Hill. Our treatment of the magnetosphere can be regarded as an inversion of this viewpoint. We regard the magnetosphere essentially as a flywheel driven by the planetary rotation. This viewpoint permitted the general arguments in Section 5.1 concerning the structuring of the magnetosphere by the thermosphere.

Just as we have shown that the magnetosphere-centred viewpoint neglects important thermospheric physics, so our thermosphere-centred viewpoint obviously neglects important magnetospheric physics. It would obviously be desirable to find a compromise position between these two extremes, for example coupling a simplified version of our thermospheric model to the physical model of Saturn's inner magnetosphere described by Saur et al. (2004).

7.4 Other planets

The most obvious extension of this work is to study, using similar models, Uranus and Neptune. Unfortunately such an extension is not trivial, for two reasons. Firstly, we have very little knowledge of the thermospheres and magnetospheres of Uranus and Neptune, since each has been studied only by a single spacecraft flyby and lie at such a great distance from the Earth that it is challenging to resolve details of their auroral emissions using Earth-based telescopes.

Secondly, the limited knowledge that we have indicates that the interaction between the planetary rotation, magnetic field and solar wind will be considerably more complicated than at Jupiter and Saturn. The magnetic fields at Uranus and Neptune both exhibit a significant tilt relative to the rotation axis and are offset considerably from the centre of the planet. At Uranus this is complicated by the peculiar orientation of the planetary rotation axis, which lies almost in the ecliptic plane. For this reason the simple axisymmetric models that we have described will probably not suffice. Progress in these circumstances is probably best served by three-dimensional models with low resolution and radically simplified geometry, in order to afford some initial insight into the thermospheric response.

A further application of this work could be found in the study of extrasolar planets. Many of these planets lie at small orbital distances, and the issue of their thermal structure and possible evaporation over a long time scale is an important research topic. Supposing that these planets exhibit fast rotation rates and the magnetospheres have substantial open field regions, we might discover that the ion drag 'fridge' flow is an important component of the thermal balance, regulating the temperature of the thermosphere and thus slowing the evaporation process.

7.5 Concluding remarks

This study has not succeeded in comprehensively explaining any of the problems that it has addressed. This initially seems somewhat disappointing. However, our adopted methodology made it almost inevitable that our conclusions would be laden with caveats. The willing acceptance of these caveats has allowed us to cut our way carefully through a thicket of complexity and hopefully, in the process, open up several new viewpoints on the subject that indicate some interesting directions for future research.

The most overarching of these seems to be the further characterisation of energy, momentum and plasma transport by meridional winds, and the consequences of this for the structure of the thermosphere, ionosphere and magnetosphere. In the context of the thermospheric energy crisis we have also raised but not completely addressed the importance of fluctuations in the magnetospheric plasma flows on the total Joule heating.

Arguably, though, the most important outcome of this study is the establishment of a simple, unified approach to the whole atmosphere-magnetosphere system. This approach has the potential, with further work, to provide a solid background to more detailed and specific studies.

Appendix A

Diffusion parameters

In this Appendix we discuss firstly our adopted values of molecular thermal conductivity and viscosity coefficients, and then briefly review determinations of the eddy coefficient at Jupiter and Saturn.

A.1 Molecular diffusion

Coefficients for molecular thermal conduction and viscosity are calculated using Eqns. 2.69 and 2.73. We adopt the same coefficients for these processes as Achilleos et al. (1998) and Müller-Wodarg et al. (2006). These parameters are shown in Tables A.1 and A.2.

These coefficients were determined by Achilleos et al. (1998) from the experimental data tabulated by Lide (1997) for H_2 and He. The H parameters were determined from the H_2 parameters through scaling procedures whose justification is not well documented. We take this opportunity to tentatively cast some doubt on these scaled parameters for H. Banks and Kockarts (1973) quote theoretical values of viscosity and thermal conductivity for H which are shown in the rightmost columns of Tables A.2 and A.1. Their μ is ~50% smaller than that of Achilleos et al. (1998) and their λ is ~50% greater. These discrepancies cannot be accounted for by the differences in β and s, which are small.

This clear inconsistency between the scaled parameters of Achilleos et al. (1998) and earlier theoretical determinations is worrying. However, we need not be overly concerned, since in our

	H_2	He	H	H (B. & K.)
λ	1.262×10^{-3}	3.7366×10^{-3}	2.585×10^{-3}	3.79×10^{-3}
s	0.876	0.648	0.716	0.69

Table A.1: Molecular thermal conductivity parameters. The units of λT^s are J s^{-1} m^{-1} K^{-1}. The fourth column is the H thermal conductivity quoted by Banks and Kockarts (1973).

	H_2	He	H	H (B. & K.)
μ	1.4648×10^{-7}	4.3338×10^{-7}	2.0715×10^{-7}	1.22×10^{-7}
β	0.716	0.670	0.716	0.69

Table A.2: Molecular viscosity parameters. The units of μT^{β} are kg s^{-1} m^{-1}. The fourth column is the H viscosity quoted by Banks and Kockarts (1973).

simulations H makes up at most approximately ~10% of the composition. Thus a 50% error in the H viscosity and conductivity parameters will translate into at most a 5% error in the total viscosity and conductivity. We thus retain the scaled parameters of Achilleos et al. (1998) in order that our model is consistent with their simulations, with subsequent studies that employed the same model (Achilleos et al., 2001; Millward et al., 2002, 2005), and with the work of Müller-Wodarg et al. (2006). However, an up to date review of available experimental and theoretical data is clearly highly desirable.

A.2 Eddy diffusion

Eddy diffusion coefficients for Jupiter and Saturn are in general determined by attempting to estimate the altitude at which hydrocarbon densities begin to drop rapidly. This corresponds to the onset of the heterosphere and diffusive separation, since the hydrocarbon species are several times heavier than the H_2 of which the upper atmosphere is largely composed.

Determinations of the eddy coefficient and homopause altitudes by different authors often differ due the use of different definitions and parameterisations that are not always unambiguously defined. It is, for example, common to describe the eddy coefficient as varying in altitude as some power of the number density $K \sim n^{-\gamma}$. Values of γ range from 0.3 (Moses et al., 2000) to 0.45 (Gladstone et al., 1996) and 0.5 (Atreya et al., 1981; Atreya, 1982). These are essentially empirical factors used to tune the behaviour of hydrocarbon chemistry. Since we are not interested in hydrocarbon chemistry in this study — the eddy coefficient serves largely to introduce some extra thermal conductivity and viscosity in the lower altitude ranges of our models — we simply adopt eddy diffusion coefficients that are fixed in altitude.

Jupiter

Using calculations of hydrocarbon chemistry and an analysis of the Voyager stellar occultation, Atreya et al. (1981) found a value of $K \simeq 1 - 2 \times 10^2 \mathrm{m}^2/\mathrm{s}$ for Jupiter. Later, Atreya (1982) refined this to $K = 1.4 \times 10^2 \mathrm{m}^2/\mathrm{s}$, locating the homopause at 1μbar. This value was adopted by the hydrocarbon chemistry study of Gladstone et al. (1996) and the auroral model of Grodent et al. (2001). We also adopt this value of K in our standard Jupiter model.

Recently, Parkinson et al. (2006) have analysed Cassini Ultraviolet Imaging Spectrograph

(UVIS) observations of the Jovian aurora performed during Cassini's flyby of Jupiter in 2000. They find that the eddy coefficient is enhanced in the auroral regions to values of 'at least $8 \times 10^6 \mathrm{cm}^2\mathrm{s}^{-1}$ [$8 \times 10^2 \mathrm{m}^2\mathrm{s}^{-1}$], and possibly greater than $4 \times 10^7 \mathrm{cm}^2\mathrm{s}^{-1}$ [$4 \times 10^3 \mathrm{m}^2\mathrm{s}^{-1}$]'. This provides a useful experimental constraint on the eddy coefficient enhancement experiments described in Chapter 6.

Saturn

Atreya (1982) also calculated a value of the homopause eddy diffusion coefficient at Saturn of $K = 1.0 \times 10^4 \mathrm{m}^2/\mathrm{s}$, placing the homopause at approximately 4nbar. However, the detailed study of Moses et al. (2000) adopts a complicated profile of eddy diffusion which places the homopause deeper in the atmosphere, below 10nbar. Müller-Wodarg et al. (2006), whose model we employ in this study, adopt a fixed value of $K = 1.0 \times 10^3 \mathrm{m}^2/\mathrm{s}$, placing the homopause close to 70nbar. For consistency with Müller-Wodarg et al. (2006) we also adopt this value in our standard Saturn model. However, in Chapter 5 we describe experiments to investigate the effect of an eddy coefficient enhanced above this value, both globally and in the auroral regions.

Appendix B

Twisting of tail field lines

Here we briefly summarise the theoretical calculations of Isbell et al. (1984), who estimated the expected angular velocity in the polar cap of plasma connected to a planet's magnetotail. We re-express their results in terms of the quantities Ω_M and Ω_T that we have used throughout this thesis. The argument follows from the notion that open field lines in the polar cap are constrained at one end by the antisunwards motion of the solar wind — to which they are magnetically connected — and at the other end by the rotational motion of the neutral atmosphere — to which they are coupled by the ionospheric conductivity. The result is that the field lines in the tail become twisted by the planetary rotation, as sketched in Fig. B.1.

We use a simplified geometry, shown in Fig. B.2. Each lobe of the magnetotail consists of a perfectly cylindrical bundle of magnetic flux of radius R_T with uniform flux density B_T. This

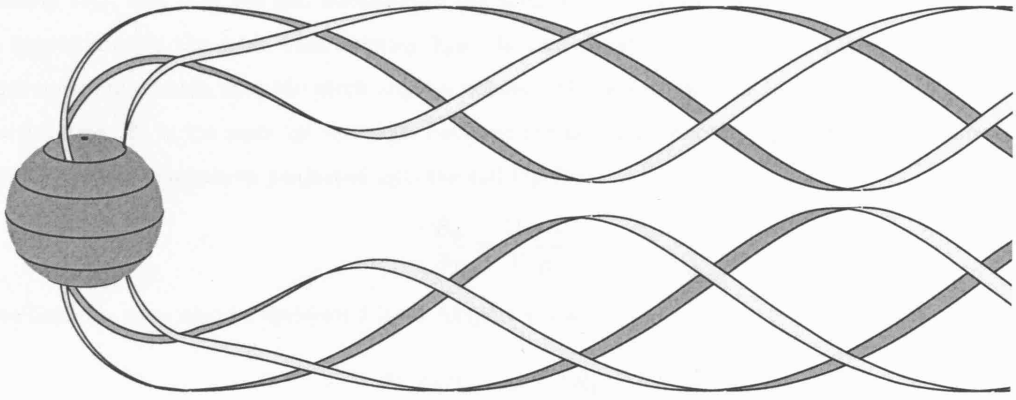

Figure B.1: Sketch of twisting tail field lines (after Isbell et al., 1984).

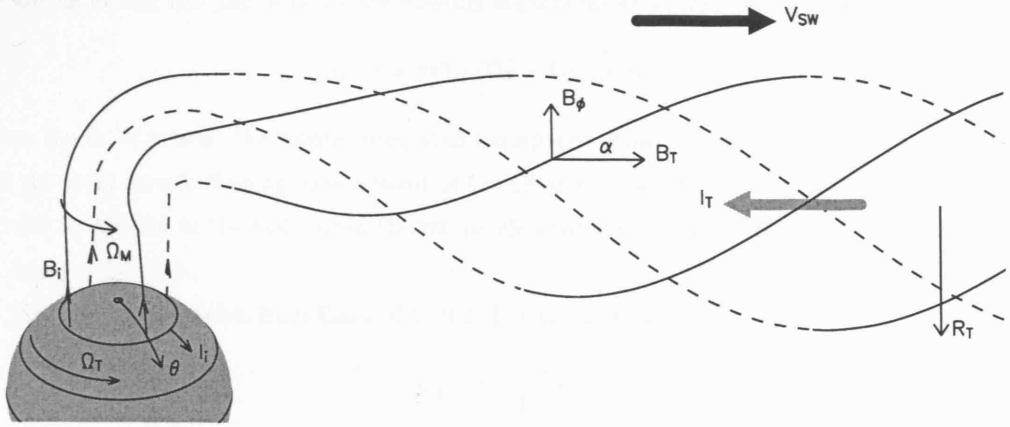

Figure B.2: Geometry of twisted tail field lines.

then maps to the polar ionosphere, where we assume a cylindrical bundle of flux tubes lying between the pole and some off-axis distance $\rho_i \simeq R_P\theta$, where R_P is the planetary radius and θ the colatitude. We assume that this region of the ionosphere can be approximated as flat, with a uniform vertical magnetic flux density B_i. Given this geometry, in which the tail and polar cap are just two connected cylinders of uniform flux density, we can map between a radius R_T in the tail and an off-axis distance ρ in the polar ionosphere with the flux conservation relation

$$B_T R^2 = B_i \rho^2 \tag{B.1}$$

We now consider the extent to which the flux tubes in the tail may be twisted by their connection to the spinning planet. We assume that the ionospheric end of a flux tube rotates at an angular velocity Ω_M, and that the end anchored in the solar wind does not rotate, travelling down tail at approximately the solar wind velocity V_{SW}. In this situation, as shown in Fig. B.2, the field lines must spiral such that the pitch angle α between the down-tail field B_T and the field due to the rotation B_ϕ is the same as the angle between the downtail velocity V_{SW} and the rotational velocity of the ionosphere projected into the tail $\Omega_M R_T$:

$$\frac{B_\phi}{B_T} = \frac{\Omega_M R}{V_{SW}} \tag{B.2}$$

The field B_ϕ may also be estimated from Ampère's law:

$$2\pi R_T B_\phi = \mu_0 I_T(R_T) \tag{B.3}$$

where I_T is the total current flowing in the tail within the radius R_T. For Jupiter and Saturn this current must flow towards the planet to generate the required direction of twist.

We may also relate Ω_M to currents flowing in the ionosphere in terms of the electric field generated there by the relative motions of the plasma and neutrals. If the plasma in the ionosphere

is rotating at Ω_M and the neutrals are rotating slightly faster at Ω_T, then we find:

$$I_i(\rho) = 2\pi\Sigma_P(\Omega_T - \Omega_M)\rho_i^2 B_i \tag{B.4}$$

where Σ_P is, of course, the height-integrated ionospheric Pedersen conductivity. The quantity I_i is the total current flowing equatorward at the off-axis distance ρ_i. This must be equal to the current I_T flowing in the tail within the radius R_T that maps to ρ_i by Eqn. B.1. Thus we can set $I_i(\rho_i) = I_T(R_T)$.

It is now easily shown from Eqns. B.1, B.2, B.3 and B.4 that:

$$\Omega_M = \Omega_T \frac{\sigma}{1+\sigma} \tag{B.5}$$

where σ is a dimensionless 'conductivity parameter':

$$\sigma = V_{SW}\mu_0\Sigma_P \tag{B.6}$$

It can further be shown, with a little manipulation, that

$$\Omega_M = \Omega_P \frac{\sigma^*}{1+\sigma^*} \tag{B.7}$$

where σ^* is the 'effective conductivity parameter':

$$\sigma^* = V_{SW}\mu_0\Sigma_P^* = V_{SW}\mu_0\Sigma_P(1-K) = \sigma(1-K) \tag{B.8}$$

and Ω_P is the planetary rotation velocity. Thus, while the true conductivity expresses the lag of the plasma relative to the actual neutral rotation velocity, the effective conductivity expresses the lag relative to the planetary rotation velocity. If $V_{SW} = 400$km/s, a typical value, then we find that

$$\sigma^* \simeq 0.5 \times \Sigma_P^* \tag{B.9}$$

so in the case of Saturn, an effective conductivity of 1mho corresponds to $\Omega_M \simeq 0.33\Omega_P$, roughly the value observed by Stallard et al. (2004).

This theory is clearly not perfect. Firstly, it is clear that the whole tail cannot be moving antisunwards at the solar wind velocity, otherwise it would become detached from the planet! There must be a region of the tail close to the planet that exhibits intermediate behaviour not described by the theory. Secondly, as discussed in Chapter 5, the theory assumes that the neutral atmosphere in the polar cap is able to supply enough angular momentum to effectively oppose the implied ion drag. It is not clear what must happen if it is unable to supply this angular momentum. Finally, if the flux in the magnetotail has been open for a very long time, then the region of the solar wind to which it is connected must lie many hundreds of planetary radii down tail. In this case it seems untuitively unlikely that the solar wind velocity would continue to control the rotation velocity of plasma at the planet.

Appendix C

Magnetic field models

We require models of the planetary field of Jupiter and Saturn for two purposes. Firstly, the magnetic field is an important parameters in determining the magnitude of Joule heating and ion drag in the thermosphere. Secondly, the form of the surface magnetic field determines the mapping of the magnetosphere models into the ionosphere. For the Jupiter model, we also require the magnetospheric flux function model described by Nichols and Cowley (2004).

Real planetary magnetic fields are complex, and for the purposes of magnetosphere and ionosphere modelling are often approximated by a dipole (Millward et al., 1996; Achilleos et al., 1998). In the case of Earth and Jupiter this dipole must be offset relative to the centre of the planet and tilted relative to the rotation axis to provide a reasonable match to the actual magnetic field. At Saturn the magnetic field is very nearly aligned with the planet, but quadrupole, octopole and higher terms make a dipole field alone a poor approximation.

One consequence of this complexity in the planetary magnetic fields is that the magnetic zenith angle (the angle between the magnetic field direction and the vertical) and the declination angle (the angle between the magnetic field direction and a meridian) are non-zero and take different angles at different latitudes, longitudes and altitudes. In this study we consider these variations to be a second order effect, since we are primarily interested in the high latitude regions where the magnetic field is almost vertical. In a dipole field, the magnetic field is within 16° of the vertical poleward of 30° colatitude and within 8° poleward of 15°. These are relatively small deviations which, given the numerous other simplifications in our modelling, are unlikely to change the substance of our results. We thus assume the magnetic field to be vertical everywhere.

The principle advantage of this assumption is that each grid point in our model corresponds both to a single column of gas and to a single magnetic field line. The height-integrations described in Chapter 2 can then be performed vertically at each location, without the insertion of trigonometric factors which would considerably complicate the calculations — while failing to usefully enrich the physics that the model represents.

The principle disadvantage of the assumption of vertical field is the situation at mid- and

low-latitudes. In these regions the tilt of the magnetic field is considerable, and our assumption is poor. However, in our studies of Joule heating and ion drag in Chapters 5 and 6 we almost entirely concern ourselves with the behaviour at high latitudes where the simplification is valid. The low latitudes essentially provide a largely quiescent boundary condition to the high latitude study.

Indeed, to accurately capture the behaviour of lower latitudes would require a completely different approach in which the full electrodynamics of the ionosphere were built in. This is beyond the scope of this study. It seems preferable to apply a very simple and transparent assumption to these low latitudes, and thus, with not a little queasiness, we maintain the assumption of vertical field all the way to the equator.

In the case of the Saturn model, we also switch off all Joule heating and ion drag equatorwards of 45° latitude. This means that the magnetic field has no influence whatsoever at low latitudes. Interestingly, the winds undergo a very slight change of direction at this cut-off point in the ion drag, reminiscent of refraction. This behaviour seems physically reasonable.

In the Jupiter model, we find that introducing such a cut-off generates waves in the wake of the cut-off point which propagate throughout the model and disrupt the flow at high altitudes in the polar regions. There almost certainly exists such wave activity in the thermosphere. However, this is not the subject of this study. To maintain the role of the low-latitudes as a quiescent boundary condition for our high latitude studies, we therefore extend Joule heating and ion drag all the way to the equator in the Jupiter model. This is clearly an inadequacy of the model at present, but the influence on the high-latitude behaviour appears to be negligible.

C.1 Saturn

The internal magnetic field of Saturn has been determined by Davis and Smith (1990) from a combination of Pioneer and Voyager data. This is known as the SPV model. The principle terms in the magnetic field are the dipole, quadrupole and octopole terms. The principal effect of the quadrupole term upon the field is to offset it vertically, such that the field strength in the northern polar regions is stronger than in the south. We neglect this asymmetry term, so our magnetic field is effectively an 'average' of the northern and southern hemispheres. The effect of the octopole term is to strengthen the magnetic field in the polar regions and weaken it in the mid-latitude and equatorial regions. We include this term, since it introduces no hemispheric asymmetries.

The values of the dipole and octopole terms in the SPV model are $g_1^0 = 21160$ and $g_3^0 = 2329$nT respectively. At a radius r this defines the radial and meridional components of the magnetic field (Cowley and Bunce, 2003):

$$B_r(r,\theta) = 2g_1^0 \cos\theta \left(\frac{R_S^*}{r}\right)^3 + 2g_3^0 \cos\theta(5\cos^2\theta - 3)\left(\frac{R_S^*}{r}\right)^5$$

$$B_\theta(r,\theta) = g_1^0 \sin\theta \left(\frac{R_S^*}{r}\right)^3 + \frac{3}{2} g_3^0 \sin\theta (5\cos^2\theta - 1) \left(\frac{R_S^*}{r}\right)^5 \quad \text{(C.1)}$$

and the flux function required in order to map the Cowley et al. (2004b) plasma flow model into the ionosphere is

$$F_i(r,\theta) = {R_S^*}^2 \sin^2\theta \left[g_1^0 \left(\frac{R_S^*}{r}\right) + \frac{1}{2} g_3^0 (5\cos^2\theta - 1) \left(\frac{R_S^*}{r}\right)^3 \right] \quad \text{(C.2)}$$

where $R_S^* = 60330$km, the radius of Saturn used by Davis and Smith (1990), which here is treated simply as a parameter in the magnetic field model. Note that elsewhere in this study the radius of Saturn is taken to be $R_S = 60268$km.

This defines these three parameters as a function of radius r and co-latitude θ. It is then necessary to define the radial surface to which our thermospheric model corresponds. Saturn is the most oblate of the planets, with a polar radius ~10% smaller than that at the equator. We thus follow Cowley and Bunce (2003) in defining the radius as an ellipse of revolution:

$$R_i(\theta) = \frac{R_e}{(1 + \epsilon \cos^2\theta)^{1/2}} \quad \text{(C.3)}$$

where the $R_e = 60268$km and the oblateness $\epsilon \simeq 0.22$. This defines the profile of the 1 bar level. We calculate the magnetic field parameters at this altitude and assume that they are constant with altitude across the range of our model. The greatest altitudes calculated above the 1 bar level are $\sim$ 2000km, representing $\sim$ 3% of the total radius. In the flux function, the octopole term is inversely proportional to the radius to the power 3, implying maximum errors of $\sim$ 9%; in the magnetic field strength, the octopole term is inversely proportional to the radius to the power 5, implying maximum errors of $\sim$ 15%. Note that the errors in the dominant dipole term are much less than this. These errors are of a similar order to those introduced by the assumption of a vertical magnetic field, and, crucially, they are not at a level where they affect the order of magnitude of the field. Since we are most interested in a simple model of the balance of physical processes in the thermosphere, this approximation is perfectly adequate.

This procedure provides us with values of B_r, B_θ and F_i as a function of co-latitude on an oblate planet. However, our thermospheric model does not currently take into account the oblateness of the planet. We thus map the magnetic field parameters determined using the oblate profile to the spherical model planet, keeping the values fixed as a function of co-latitude. We then use the *total* magnetic field $B = \sqrt{B_r^2 + B_\theta^2}$ as the vertical magnetic field in our model.

Finally, note that we do not require the value of the flux function in the magnetosphere in this study, since we simply use the parameters already provided by Cowley et al. (2004b).

C.2 Jupiter

For Jupiter our model of the ionospheric field is considerably simpler than at Saturn. We wish to retain maximal consistency with the Nichols and Cowley (2004) model, who assumed a constant

value of $B_i = 2B_J$ in the polar regions of the planet, where $B_J = 426400$nT. We follow this formulation. Since there is no obvious latitude at which to abandon this assumption, we extend a vertical magnetic field of $2B_J$ across the entire planet. This, of course, is an extremely poor model at co-latitudes greater than $\sim 30°$. However, as we have already discussed, the function of the low latitudes is largely to provide a quiescent boundary condition to the high-latitude coupling region, and we do not attempt to use our model to make any physical inferences concerning the behaviour of Joule heating and ion drag at low latitudes.

We do, however, require models of the magnetic field $B_{ze}(\rho_e)$ and flux function $F_e(\rho_e)$ in the equatorial magnetosphere, for which we again use the functions of Nichols and Cowley (2004), which represent analytic approximations to empirical models (Connerney et al., 1981; Khurana and Kivelson, 1993):

$$\begin{aligned} B_{ze}(\rho_e) &= -\left\{ B_o \left(\frac{R_J}{\rho_e}\right)^3 \exp\left[-\left(\frac{\rho_e}{\rho_{eo}}\right)^{5/2}\right] + A\left(\frac{R_J}{\rho_e}\right)^m \right\} \\ F_e(\rho_e) &= F_\infty + \frac{B_o R_J^3}{2.5\rho_{eo}} \Gamma\left[-\frac{2}{5}, \left(\frac{\rho_e}{\rho_{eo}}\right)^{5/2}\right] + \frac{A}{m-2}\left(\frac{R_J}{\rho_e}\right)^{m-2} \end{aligned} \tag{C.4}$$

where $B_o = 3.335 \times 10^5$nT, $\rho_{eo} = 14.501 R_J$, $A = 5.4 \times 10^4$nT, $m = 2.71$, $F_\infty \simeq 2.841 \times 10^4 \text{nT} R_J^2$ and $\Gamma(a, z) = \int_z^\infty t^{a-1} e^{-t} dt$ is the incomplete gamma function. Note that the second expression is derived from the first by integration. For further discussion of the origin of this model the reader is referred to Nichols and Cowley (2004).

Fig. C.1 shows the relation between ionospheric colatitude and magnetospheric radius that follows from this magnetic field model. One interesting consequence of this model is that the region of the magnetosphere lying in the range 20-100R_J maps to only 2° of co-latitude in the ionosphere.

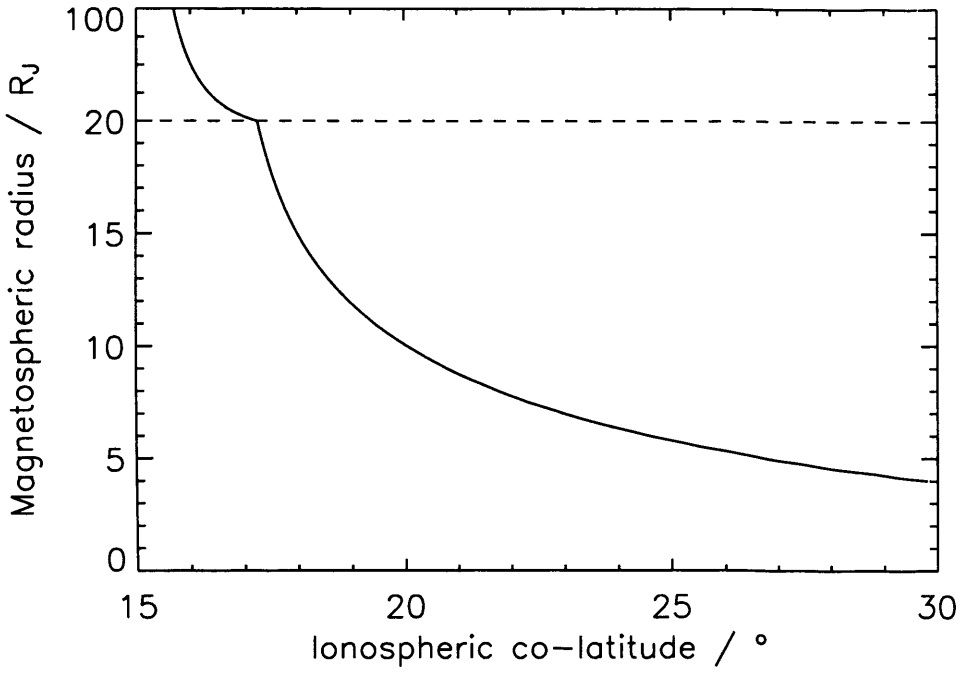

Figure C.1: Relation between ionospheric colatitude and magnetospheric radius implied by the Jovian magnetic field model. Note that the vertical scale changes at the horizontal dotted line.

Appendix D

Inertial Terms

Two sets of inertial terms enter the momentum equation: firstly the so-called curvature terms, which are a consequence of the spherical geometry of the model grid, and secondly the Coriolis and centrifugal forces, which are consequences of the rotating frame of the model.

As an unaccelerated particle moves through a rotating curvilinear coordinate system, the set of vectors that expresses its inertial motion slowly changes due to a combination of the non-Cartesian geometry and the rotation of the frame. From the point of view of the particle, this means that even though its velocity in an inertial frame is unaltered, the three numbers that represent its velocity must be adjusted to the new coordinate system. From the point of view of a point fixed in space — e.g. a model grid point — the particle arrives with its own set of unit vectors, and these must be corrected to suit the local coordinate system.

D.1 Method

If we substitute the advective derivative (Eqn. 3.11) into only the second term of Eqn. 3.10 then we can write the j-component of the the curvature term:

$$-\left[u_i u_k \frac{\partial \boldsymbol{e}_i}{\partial x_k}\right]_j = \dot{u}_j - a_j \tag{D.1}$$

where $\dot{u}_j$ is the total derivative with respect to time of the velocity component u_j. Clearly the LHS of the equation does not depend instantaneously on the value of the force a_j. Thus we can calculate the LHS by setting the force to zero and calculating the quantity $\dot{u}_j$ for a particle moving inertially.

There are various ways to perform this calculation. Here we use Lagrangian mechanics (e.g Hand and Finch, 1998), which produces the correct result surprisingly quickly. The reader is reminded that the Lagrangian $\mathcal{L}$ is defined as:

$$\mathcal{L} = \mathcal{T} - \mathcal{V} \tag{D.2}$$

where $\mathcal{T}$ is the kinetic energy and $\mathcal{V}$ is the potential energy. We consider a particle moving inertially so $\mathcal{V} = 0$. The equation of motion of the particle may then be derived by applying the Euler-Lagrange equation.

$$\frac{d}{dt}\left(\frac{\partial \mathcal{L}}{\partial \dot{q}_i}\right) - \frac{\partial \mathcal{L}}{q_i} = 0 \tag{D.3}$$

and the accelerations so derived from this process are the inertial terms that we require.

D.2 Curvature terms

We begin by deriving the curvature terms alone. Thus we consider a particle moving in a spherical polar coordinate system $q_i = (r, \theta, \phi)$, which does not rotate. We may write the total velocities u_i in the various coordinate directions as follows:

$$\begin{aligned} u_r &= \dot{r} \\ u_\theta &= r\dot{\theta} \\ u_\phi &= r\sin\theta\,\dot{\phi} \end{aligned} \tag{D.4}$$

These are the total velocities relative to the inertial (non-rotating) frame that is fixed with respect to the centre of the planet. From Eqns D.4 and D.2 we can express the Lagrangian $\mathcal{L}$ per unit mass:

$$\mathcal{L} = \frac{1}{2}\dot{r}^2 + \frac{1}{2}r^2\dot{\theta}^2 + \frac{1}{2}r^2\sin\theta^2\,\dot{\phi}^2 \tag{D.5}$$

and then apply the Euler-Lagrange equation for each of the three coordinates $q_i = (r, \theta, \phi)$. For r:

$$\begin{aligned} & \ddot{r} = r\dot{\theta}^2 + r\sin^2\theta\,\dot{\phi}^2 \\ \Rightarrow \quad & \dot{u}_r = \frac{(r\dot{\theta})^2 + (r\sin\theta\,\dot{\phi})^2}{r} \\ \Rightarrow \quad & \dot{u}_r = \frac{u_\theta^2 + u_\phi^2}{r} \end{aligned} \tag{D.6}$$

where we have used Equations D.4. We now perform the same procedure for θ:

$$\begin{aligned} & \dot{r}u_\theta + r\dot{u}_\theta = (r^2\sin\theta\cos\theta\,\dot{\phi}^2) \\ \Rightarrow \quad & u_r u_\theta + r\dot{u}_\theta = (r\sin\theta\dot{\phi})^2\cot\theta \\ \Rightarrow \quad & r\dot{u}_\theta = u_\phi^2\cot\theta - u_r u_\theta \\ \Rightarrow \quad & \dot{u}_\theta = \frac{u_\phi^2\cot\theta}{r} - \frac{u_r u_\theta}{r} \end{aligned} \tag{D.7}$$

and finally for ϕ:

$$\begin{aligned} & d(r^2\sin^2\theta\,\dot{\phi})/dt = 0 \\ \Rightarrow \quad & d(r\sin\theta\,u_\phi)/dt = 0 \\ \Rightarrow \quad & \dot{u}_\phi r\sin\theta = -u_\phi(\dot{r}\sin\theta + r\dot{\theta}\cos\theta) \\ \Rightarrow \quad & \dot{u}_\phi r = -u_\phi(u_r + u_\theta\cot\theta) \end{aligned}$$

$$\Rightarrow \qquad \dot{u}_\phi = -\frac{u_\phi u_r}{r} - \frac{u_\phi u_\theta \cot\theta}{r} \tag{D.8}$$

Having derived these expressions it is well worth discussing the physical effects that they represent. First, the radial term:

$$\dot{u}_r = \frac{u_\theta^2 + u_\phi^2}{r} \tag{D.9}$$

This represents an effect equivalent to the centrifugal force — the expression is, indeed, identical to the centrifugal force experienced in a rotating frame. Now, our model assumes hydrostatic balance, which, as described in Chapter 3, means that gravity and pressure are assumed to be dominant forces in the vertical direction. Hence we need to check that this radial acceleration does not compete with the gravitational acceleration. For gravity g to dominate we require the total horizontal velocity $U = \sqrt{u_\theta^2 + u_\phi^2}$ to obey the relation:

$$U^2/R \ll g \quad \Rightarrow \quad U \ll \sqrt{gR} \tag{D.10}$$

where R is the planetary radius. For Saturn, $\sqrt{gR} \sim 24$ km/s and for Jupiter $\sqrt{gR} \sim 40$ km/s. The highest velocities observed in the models are of the order of ~ 5 km/s, in extreme circumstances, so it seems safe to omit this term and retain the assumption of hydrostatic equilibrium. We now turn to the θ component:

$$\dot{u}_\theta = \frac{u_\phi^2 \cot\theta}{r} - \frac{u_r u_\theta}{r} \tag{D.11}$$

The first part of this term again represents a centrifugal force. In this case it is the equatorwards acceleration experienced by a particle moving at constant latitude. The second part of the term is a coupling between vertical and meridional motions. This represents conservation of angular momentum. If the particle has a radial velocity *and* a meridional velocity, then as it moves outwards radially, the meridional motion must slow to conserve angular momentum. Both of these terms are included in the model, although the second term is usually negligible.

Finally we examine the ϕ component:

$$\dot{u}_\phi = -\frac{u_\phi u_\theta \cot\theta}{r} - \frac{u_\phi u_r}{r} \tag{D.12}$$

These terms are both similar to the second θ term. The first term arises because a particle with a non-zero u_ϕ must accelerate if it moves towards the pole to conserve angular momentum. The second term is identical to the second θ term, but for u_ϕ.

D.3 Coriolis and centrifugal terms

The Coriolis and centrifugal forces may be derived by a slight modification to the above procedure. If we allow the curvilinear coordinate system defined above to now rotate in the posititve ϕ direction with an angular velocity Ω, we must redefine the total ϕ velocity as $u_{\phi'}$, where u_ϕ

remains the ϕ velocity relative to the coordinate system:

$$u_{\phi'} = u_\phi + \Omega r \sin\theta \tag{D.13}$$

If we replace u_ϕ with $u_{\phi'}$ in Eqn. D.5 and repeat the derivation we find that the inertial terms become:

$$\begin{aligned}
\dot{u}_r &= \frac{u_\theta^2 + u_\phi^2}{r} + 2\Omega u_\phi \sin\theta + r\Omega^2 \sin^2\theta \\
\dot{u}_\theta &= \frac{u_\phi^2 \cot\theta}{r} - \frac{u_r u_\theta}{r} - 2\Omega u_\phi \cos\theta + r\Omega^2 \sin\theta\cos\theta \\
\dot{u}_\phi &= -\frac{u_\phi u_\theta \cot\theta}{r} - \frac{u_\phi u_r}{r} + 2\Omega u_r \sin\theta + 2\Omega u_\theta \cos\theta
\end{aligned} \tag{D.14}$$

and we see that each of the curvature terms now has two extra terms involving Ω. Inspection shows that these may be written in total as a vector $\dot{\boldsymbol{u}}_\Omega$:

$$\dot{\boldsymbol{u}}_\Omega = -\boldsymbol{\Omega} \times (\boldsymbol{\Omega} \times \boldsymbol{r}) - 2\boldsymbol{\Omega} \times \boldsymbol{u} \tag{D.15}$$

which are familiar as the centrifugal and Coriolis forces respectively.

The centrifugal component is constant at a particular location and always acts perpendicular to the rotation axis. Since it is constant it is convenient to combine it with the gravitational acceleration to form one 'effective' gravitational force at each location. Indeed, the combined gravitational and centrifugal accelerations at a location determine the surface profile of a gas giant, since the fluid moves into a shape in which the surface is perpendicular to the force acting upon it. In the case of Saturn, the centrifugal force is comparable to gravity, and this results in a flattened or oblate profile. To include the centrifugal force and gravity correctly would require this profile to be adopted. However, this is non-trivial, so to present a model that is as physically self-consistent as possible we retain the spherical form of the terrestrial model and assume a uniform gravity across the entire planet. This results in errors of the order of 10-20% in the gravitational acceleration. In future the correct treatment of oblateness should be considered.

The Coriolis component is one of the most important in the model, introducing a tendency for winds to rotate in a sense opposite to the planet's rotation. Most of the winds in the model are substantially modified by this effect.

D.4 Summary

Neglecting the centrifugal terms due to the winds and the rotation, omitting the Coriolis term due to the (small) vertical wind u_r, and ignoring all vertical accelerations, which are assumed negligible relative to hydrostatic equilibrium, we are left with the form of the inertial terms used in the model:

$$\begin{aligned} \dot{u}_\theta &= \frac{u_\phi^2 \cot\theta}{r} - \frac{u_r u_\theta}{r} - 2\Omega u_\phi \cos\theta \\ \dot{u}_\phi &= -\frac{u_\phi u_\theta \cot\theta}{r} - \frac{u_\phi u_r}{r} + 2\Omega u_\theta \cos\theta \end{aligned} \tag{D.16}$$

Appendix E

Pressure Coordinates

Pressure coordinates are used in the thermosphere model to greatly simplify the continuity equation. The essential idea is to replace the vertical coordinate z with the coordinate p, using the equation of hydrostatic equilibrium:

$$\frac{dp}{dz} = -\rho g \tag{E.1}$$

where ρ is the mass density and g is the acceleration due to gravity. It is helpful to write this in terms of the gravitational potential Φ which is defined by the relation:

$$d\Phi = g dz \tag{E.2}$$

Combing equations E.1 and E.2 we obtain:

$$\frac{d\Phi}{dp} = -\frac{1}{\rho} \tag{E.3}$$

This represents the equation of hydrostatic equilibrium in pressure coordinates. We also introduce the vertical wind w in pressure coordinates, defined as:

$$w = \frac{dp}{dt} \tag{E.4}$$

Before continuing, it is necessary to state the relationship between partial derivatives in the z and p systems. For vertical derivatives:

$$\frac{\partial a}{\partial z} = \frac{\partial a}{\partial p}\frac{\partial p}{\partial z} = -\rho g \frac{\partial a}{\partial p} \tag{E.5}$$

and for horizontal derivatives:

$$da = \left.\frac{\partial a}{\partial x}\right|_z dx + \frac{\partial a}{\partial z} dz \tag{E.6}$$

We then take the derivative of both sides with respect to x keeping p fixed:

$$\left.\frac{\partial a}{\partial x}\right|_p = \left.\frac{\partial a}{\partial x}\right|_z + \frac{\partial a}{\partial z}\left.\frac{\partial z}{\partial x}\right|_p \tag{E.7}$$

We then rearrange and substitute equations E.3 and E.5:

$$\left.\frac{\partial a}{\partial x}\right|_z = \left.\frac{\partial a}{\partial x}\right|_p + \rho \frac{\partial a}{\partial p}\left.\frac{\partial \Phi}{\partial x}\right|_p \tag{E.8}$$

We can find a similar equation for time derivatives:

$$\left.\frac{\partial a}{\partial t}\right|_z = \left.\frac{\partial a}{\partial t}\right|_p + \rho \frac{\partial a}{\partial p}\left.\frac{\partial \Phi}{\partial t}\right|_p \tag{E.9}$$

and by replacing $(\partial/\partial x)_z$ with the operator $\boldsymbol{\nabla}_z$ and $(\partial/\partial x)_p$ with the operator $\boldsymbol{\nabla}_p$ we can write:

$$\boldsymbol{\nabla}_z a = \boldsymbol{\nabla}_p a + \rho \frac{\partial a}{\partial p} \boldsymbol{\nabla}_p \Phi \tag{E.10}$$

or for a vector $\boldsymbol{a}$:

$$\boldsymbol{\nabla}_z \cdot \boldsymbol{a} = \boldsymbol{\nabla}_p \cdot \boldsymbol{a} + \rho \frac{\partial \boldsymbol{a}}{\partial p} \cdot \boldsymbol{\nabla}_p \Phi \tag{E.11}$$

Armed with these mathematical tools, we can now make progress on reexpressing the physics in the p coordinate system. Firstly we require a relationship between the vertical wind v_z in the z system and the vertical wind w in the p system. To find this we write the total derivative of z in the p coordinate system:

$$\begin{aligned} u_z &= \frac{dz}{dt} \\ &= \left.\frac{\partial z}{\partial t}\right|_p + \boldsymbol{u} \cdot \boldsymbol{\nabla}_p z + w \frac{\partial z}{\partial p} \\ &= \left.\frac{1}{g}\frac{\partial \Phi}{\partial t}\right|_p + \frac{1}{g}\boldsymbol{u} \cdot \boldsymbol{\nabla}_p \Phi - \frac{w}{\rho g} \end{aligned} \tag{E.12}$$

The first term represents the vertical wind due to vertical motion of the isobaric surfaces through a point fixed in space. The second term represents the vertical component of the isobaric winds that blow along the slightly tilted pressure surfaces. The third term represents winds that blow vertically *relative* to the fixed pressure surfaces. Now we reexpress the continuity equation in terms of the p coordinate system. The simplification that results from this is the principle advantage of using pressure as the vertical coordinate. In the z system the continuity equation is given by:

$$\underbrace{\left.\frac{\partial \rho}{\partial t}\right|_z}_{A} + \underbrace{\boldsymbol{\nabla}_z \cdot (\rho \boldsymbol{u})}_{B} + \underbrace{\frac{\partial (\rho u_z)}{\partial z}}_{C} = 0 \tag{E.13}$$

Physically this expresses the notion that the change in density must be equal to the divergence of the flux in the absence of sinks or sources of mass. For clarity, we convert each term to pressure coordinates separately. To convert term A we use Eqn. E.9:

$$\underbrace{\left.\frac{\partial \rho}{\partial t}\right|_z}_{A} = \underbrace{\left.\frac{\partial \rho}{\partial t}\right|_p}_{A_1} + \underbrace{\rho \frac{\partial \rho}{\partial p}\left.\frac{\partial \Phi}{\partial t}\right|_p}_{A_2} \tag{E.14}$$

For term B we use Eqn. E.11:

$$\underbrace{\boldsymbol{\nabla}_z \cdot (\rho \boldsymbol{v})}_{B} = \underbrace{\boldsymbol{\nabla}_p \cdot (\rho \boldsymbol{u})}_{B_1} + \underbrace{\rho \frac{\partial (\rho \boldsymbol{u})}{\partial p} \cdot \boldsymbol{\nabla}_p \Phi}_{B_2} \tag{E.15}$$

and for term C we substitute Eqn. E.12 and then apply Eqn. E.5:

$$\begin{aligned}
\underbrace{\frac{\partial(\rho u_z)}{\partial z}}_{C} &= \frac{1}{g}\frac{\partial}{\partial z}\left(\rho\frac{\partial\Phi}{\partial t}\bigg|_p + \rho\boldsymbol{u}\cdot\boldsymbol{\nabla}_p\Phi - w\right) \\
&= -\rho\frac{\partial}{\partial p}\left(\rho\frac{\partial\Phi}{\partial t}\bigg|_p + \rho\boldsymbol{u}\cdot\boldsymbol{\nabla}_p\Phi - w\right) \\
&= \underbrace{-\rho\frac{\partial}{\partial p}\left(\rho\frac{\partial\Phi}{\partial t}\bigg|_p\right)}_{C_1}\underbrace{-\rho\frac{\partial}{\partial p}(\rho\boldsymbol{u}\cdot\boldsymbol{\nabla}_p\Phi)}_{C_2}\underbrace{+\rho\frac{\partial w}{\partial p}}_{C_3}
\end{aligned} \tag{E.16}$$

Now consider term C_1:

$$\begin{aligned}
C_1 &= -\rho\frac{\partial}{\partial p}\left(\rho\frac{\partial\Phi}{\partial t}\bigg|_p\right) \\
&= -\rho\frac{\partial\rho}{\partial p}\frac{\partial\Phi}{\partial t}\bigg|_p - \rho^2\frac{\partial}{\partial p}\left(\frac{\partial\Phi}{\partial t}\bigg|_p\right) \\
&= -A_2 - \rho^2\frac{\partial}{\partial t}\left(\frac{\partial\Phi}{\partial p}\right)\bigg|_p \\
&= -A_2 - \rho^2\frac{\partial}{\partial t}\left(-\frac{1}{\rho}\right)\bigg|_p \\
&= -A_2 - \rho^2\left(\frac{1}{\rho^2}\frac{\partial\rho}{\partial t}\bigg|_p\right) \\
&= -A_2 - A_1
\end{aligned} \tag{E.17}$$

and thus $A_1 + A_2 + C_1 = 0$. We can apply a similar procedure to term C_2:

$$\begin{aligned}
C_2 &= -\rho\frac{\partial}{\partial p}(\rho\boldsymbol{u}\cdot\boldsymbol{\nabla}_p\Phi) \\
&= -\rho\frac{\partial(\rho\boldsymbol{u})}{\partial p}\cdot\boldsymbol{\nabla}_p\Phi - \rho^2\boldsymbol{u}\cdot\boldsymbol{\nabla}_p\frac{\partial\Phi}{\partial p} \\
&= -B_2 - \rho^2\boldsymbol{u}\cdot\boldsymbol{\nabla}_p(-1/\rho) \\
&= -B_2 - \rho^2\boldsymbol{u}\cdot\boldsymbol{\nabla}_p\rho\,(1/\rho^2) \\
&= -B_2 - \boldsymbol{u}\cdot\boldsymbol{\nabla}_p\rho \\
&= -B_2 - \left[\boldsymbol{\nabla}_p\cdot(\rho\boldsymbol{u}) - \rho\boldsymbol{\nabla}_p\cdot\boldsymbol{u}\right] \\
&= -B_2 - B_1 + \rho\boldsymbol{\nabla}_p\cdot\boldsymbol{u}
\end{aligned} \tag{E.18}$$

so that $C_2 + B_1 + B_2 = \rho\boldsymbol{\nabla}_p\cdot\boldsymbol{u}$. Returning to the continuity equation we have from Eqn. E.13:

$$\begin{aligned}
A_1 + A_2 + B_1 + B_2 + C_1 + C_2 + C_3 &= 0 \\
\Rightarrow (A_1 + A_2 + C_1) + (C_2 + B_1 + B_2) + C_3 &= 0 \\
\Rightarrow 0 + \rho\boldsymbol{\nabla}_p\cdot\boldsymbol{u} + \rho\frac{\partial w}{\partial p} &= 0
\end{aligned} \tag{E.19}$$

This reduces to the final form of the continuity equation in the p coordinate system:

$$\boldsymbol{\nabla}_p\cdot\boldsymbol{u} + \frac{\partial w}{\partial p} = 0 \tag{E.20}$$

Bibliography

N. Achilleos, S. Miller, R. Prangé, G. Millward, and M. K. Dougherty. A dynamical model of Jupiter's auroral electrojet. *New Journal of Physics*, 3:3–20, April 2001.

N. Achilleos, S. Miller, J. Tennyson, A. D. Aylward, I. Mueller-Wodarg, and D. Rees. JIM: A time-dependent, three-dimensional model of Jupiter's thermosphere and ionosphere. *J. Geophys Res.*, 103:20089–20112, September 1998.

R. A. Akmaev. Simulation of large-scale dynamics in the mesosphere and lower thermosphere with the Doppler-spread parameterization of gravity waves 2. Eddy mixing and the diurnal tide. *J. Geophys Res.*, 106(15):1205–1214, 2001.

A. L. Aruliah, E. M. Griffin, A. D. Aylward, E. A. K. Ford, M. J. Kosch, C. J. Davis, V. S. C. Howells, S. E. Pryse, H. R. Middleton, and J. Jussila. First direct evidence of meso-scale variability on ion-neutral dynamics using co-located tristatic FPIs and EISCAT radar in Northern Scandinavia. *Ann. Geophys.*, 23:147–162, January 2005.

O. Ashihara and M. Shimizu. The effect of electron precipitation on the Jovian ionosphere - Analysis of Pioneer 10 and 11 S-band radio occultation data. *Astronomy & Astrophysics*, 57: 85–96, May 1977.

S. K. Atreya. Eddy mixing coefficient on Saturn. *Planetary & Space Science*, 30:849–854, August 1982.

S. K. Atreya. *Atmospheres and Ionospheres of the Outer Planets and their Satellites.* Springer-Verlag, 1986.

S. K. Atreya, T. M. Donahue, and M. Festou. Jupiter - Structure and composition of the upper atmosphere. *Astrophysical Journal*, 247:L43–L47, July 1981.

S. K. Atreya, T. M. Donahue, and J. H. Waite. An interpretation of the Voyager measurement of Jovian electron density profiles. *Nature*, 280:795, August 1979.

S. K. Atreya, P. R. Mahaffy, H. B. Niemann, M. H. Wong, and T. C. Owen. Composition and origin of the atmosphere of Jupiter-an update, and implications for the extrasolar giant planets. *Planetary & Space Science*, 51:105–112, February 2003.

S. V. Badman, E. J. Bunce, J. T. Clarke, S. W. H. Cowley, J.-C. Gérard, D. Grodent, and S. E. Milan. Open flux estimates in Saturn's magnetosphere during the January 2004 Cassini-HST campaign, and implications for reconnection rates. *J. Geophys Res.*, 110(A9):11216, November 2005.

P. M. Banks and G. Kockarts. *Aeronomy.* Academic Press, 1973.

R. Baron, R. D. Joseph, T. Owen, J. Tennyson, S. Miller, and G. E. Ballester. Imaging Jupiter's aurorae from H_3^+ emissions in the 3-4 micron band. *Nature*, 353:539–542, October 1991.

S. W. Bougher, J. H. Waite, T. Majeed, and G. R. Gladstone. Jupiter Thermospheric General Circulation Model (JTGCM): Global structure and dynamics driven by auroral and Joule heating. *J. Geophy. Res.*, 110(E9):4008, April 2005.

D. Brunt. The transfer of heat by radiation and turbulence in the lower atmosphere. *Proc. Roy. Soc. London, A*, 124:201–218, 1929.

E. J. Bunce, S. W. H. Cowley, and J. A. Wild. Azimuthal magnetic fields in Saturn's magnetosphere: effects associated with plasma subcorotation and the magnetopause-tail current system. *Ann. Geophys.*, 21:1709–1722, 2003.

R. H. Chen. Studies of Jupiter's lower ionospheric layers. *J. Geophys Res.*, 86:7792–7794, September 1981.

A. F. Cheng and J. H. Waite. Corotation lag of Saturn's magnetosphere - Global ionospheric conductivities revisited. *J. Geophys Res.*, 93:4107–4109, May 1988.

J. T. Clarke, J.-C. Gérard, D. Grodent, S. Wannawichian, J. Gustin, J. Connerney, F. Crary, M. Dougherty, W. Kurth, S. W. H. Cowley, E. J. Bunce, T. Hill, and J. Kim. Morphological differences between Saturn's ultraviolet aurorae and those of Earth and Jupiter. *Nature*, 433: 717–719, February 2005.

M. V. Codrescu, T. J. Fuller-Rowell, and J. C. Foster. On the importance of E-field variability for Joule heating in the high-latitude thermosphere. *Geophys. Res. Lett.*, 22:2393–2396, 1995.

M. V. Codrescu, T. J. Fuller-Rowell, J. C. Foster, J. M. Holt, and S. J. Cariglia. Electric field variability associated with the Millstone Hill electric field model. *J. Geophys Res.*, pages 5265–5274, March 2000.

M. Combes, L. Vapillon, and J. Lecacheux. The occultation of beta Scorpii by Jupiter. IV - Divergences with other observers in the derived temperature profiles. *Astronomy & Astrophysics*, 45:399–403, December 1975.

J. E. P. Connerney, M. H. Acuna, and N. F. Ness. Modeling the Jovian current sheet and inner magnetosphere. *J. Geophys Res.*, 86:8370–8384, September 1981.

S. Cowley, E. Bunce, and R. Prangé. Saturn's polar ionospheric flows and their relation to the main auroral oval. *Ann. Geophys.*, 22:1379–1394, April 2004a.

S. W. H. Cowley, I. I. Alexeev, E. S. Belenkaya, E. J. Bunce, C. E. Cottis, V. V. Kalegaev, J. D. Nichols, R. Prange, and F. J. Wilson. A simple axisymmetric model of magnetosphere-ionosphere coupling currents in jupiter's polar ionosphere. *J. Geophys Res.*, 110:A11209, 2005.

S. W. H. Cowley, S. V. Badman, E. J. Bunce, J. T. Clarke, J.-C. Gérard, D. Grodent, C. M. Jackman, S. E. Milan, and T. K. Yeoman. Reconnection in a rotation-dominated magnetosphere and its relation to Saturn's auroral dynamics. *J. Geophys Res.*, 110(A9):2201, February 2005.

S. W. H. Cowley and E. J. Bunce. Origin of the main auroral oval in Jupiter's coupled magnetosphere-ionosphere system. *Planetary & Space Science*, 49:1067–1088, August 2001.

S. W. H. Cowley and E. J. Bunce. Corotation-driven magnetosphere-ionosphere coupling currents in saturn's magnetosphere and their relation to the auroras. *Ann. Geophys.*, 21:1691–1707, 2003.

S. W. H. Cowley, E. J. Bunce, and J. M. O'Rourke. A simple quantitative model of plasma flows and currents in Saturn's polar ionosphere. *J. Geophys Res.*, A18:5212, May 2004b.

S. W. H. Cowley, E. J. Bunce, T. S. Stallard, and S. Miller. Jupiter's polar ionospheric flows: Theoretical interpretation. *Geophys. Res. Lett.*, 30:24–1, March 2003.

L. J. Davis and E. J. Smith. A model of Saturn's magnetic field based on all available data. *J. Geophys Res.*, 95(14):15257–15261, September 1990.

P. Drossart, J.-P. Maillard, J. Caldwell, S. J. Kim, J. K. G. Watson, W. A. Majewski, J. Tennyson, S. Miller, S. K. Atreya, J. T. Clarke, J. H. Waite, and R. Wagener. Detection of H_3^+ on Jupiter. *Nature*, 340:539–541, August 1989.

V. R. Eshleman, G. L. Tyler, G. E. Wood, G. F. Lindal, J. D. Anderson, G. S. Levy, and T. A. Croft. Radio science with Voyager 1 at Jupiter - Preliminary profiles of the atmosphere and ionosphere. *Science*, 204:976–978, June 1979a.

V. R. Eshleman, G. L. Tyler, G. E. Wood, G. F. Lindal, J. D. Anderson, G. S. Levy, and T. A. Croft. Radio science with Voyager at Jupiter - Initial Voyager 2 results and a Voyager 1 measure of the Io torus. *Science*, 206:959–962, November 1979b.

M. C. Festou and S. K. Atreya. Voyager ultraviolet stellar occultation measurements of the composition and thermal profiles of the Saturnian upper atmosphere. *Geophys. Res. Lett.*, 9: 1147–1150, October 1982.

G. Fjeldbo, A. Kliore, B. Seidel, D. Sweetnam, and D. Cain. The Pioneer 10 radio occultation measurements of the ionosphere of Jupiter. *Astronomy & Astrophysics*, 39:91–96, February 1975.

R. G. French and P. J. Gierasch. Waves in the jovian upper atmosphere. *Journal of Atmospheric Sciences*, 31:1707–1712, 1974.

T. J. Fuller-Rowell. *A three-dimensional, time-dependent global model of the thermosphere.* PhD thesis, UCL, 1981.

T. J. Fuller-Rowell, D. Rees, S. Quegan, R. J. Moffett, M. V. Codrescu, and G. H. Millward. A coupled thermosphere-ionosphere model (ctim). In *STEP Handbook of Ionospheric Models*, pages 217–238. SCOSTEP, 1996.

J. Gérard, D. Grodent, J. Gustin, A. Saglam, J. T. Clarke, and J. T. Trauger. Characteristics of Saturn's FUV aurora observed with the Space Telescope Imaging Spectrograph. *J. Geophys Res.*, 109(18):9207, September 2004.

N. M. Gavrilov and V. A. Yudin. Model for coefficients of turbulence and effective Prandtl number produced by breaking gravity waves in the upper atmosphere. *J. Geophys Res.*, 97 (16):7619–7624, May 1992.

J. Geiss and A. Bürgi. Diffusion and thermal diffusion in partially ionized gases in the atmospheres of the sun and planets. *Astronomy & Astrophysics*, 159:1–2, April 1986.

G. Giampieri and M. K. Dougherty. Rotation rate of Saturn's interior from magnetic field observations. *Geophys. Res. Lett.*, 31:16701–+, August 2004.

G. R. Gladstone, M. Allen, and Y. L. Yung. Hydrocarbon Photochemistry in the Upper Atmosphere of Jupiter. *Icarus*, 119:1–52, January 1996.

D. Grodent, J. T. Clarke, J. Kim, J. H. Waite, and S. W. H. Cowley. Jupiter's main auroral oval observed with HST-STIS. *J. Geophys Res.*, 108(11):2–1, November 2003.

D. Grodent, J.-C. Gérard, S. W. H. Cowley, E. J. Bunce, and J. T. Clarke. Variable morphology of Saturn's southern ultraviolet aurora. *J. Geophys Res.*, 110(A9):7215, July 2005.

D. Grodent, J. H. Waite, and J. Gérard. A self-consistent model of the Jovian auroral thermal structure. *J. Geophys Res.*, pages 12933–12952, July 2001.

S. H. Gross and S. I. Rasool. The Upper Atmosphere of Jupiter. *Icarus*, 3:311, November 1964.

J. Gustin, P. D. Feldman, J.-C. Gérard, D. Grodent, A. Vidal-Madjar, L. Ben Jaffel, J.-M. Desert, H. W. Moos, D. J. Sahnow, H. A. Weaver, B. C. Wolven, J. M. Ajello, J. H. Waite, E. Roueff, and H. Abgrall. Jovian auroral spectroscopy with FUSE: analysis of self-absorption and implications for electron precipitation. *Icarus*, 171:336–355, October 2004.

J. Gustin, J.-C. Gerard, P. D. Feldman, W. R. Pryor, and J. Ajello. Ultraviolet Spectroscopy of Saturn: Determination of Auroral characteristics with FUSE, STIS and UVIS Spectra. *AAS/Division for Planetary Sciences Meeting Abstracts*, 37, August 2005.

J. D. Haigh. The Impact of Solar Variability on Climate. *Science*, 272:981–984, May 1996.

L. N. Hand and J. D. Finch. *Analytical mechanics*. Cambridge University Press, 1998.

M. G. Heaps. The roles of particle precipitation and Joule heating in the energy balance of the Jovian thermosphere. *Icarus*, 29:273–281, October 1976.

M. P. Hickey, R. L. Walterscheid, and G. Schubert. Gravity Wave Heating and Cooling in Jupiter's Thermosphere. *Icarus*, 148:266–281, November 2000.

T. W. Hill. Inertial limit on corotation. *J. Geophys Res.*, 84(13):6554–6558, November 1979.

T. W. Hill. Corotation lag in Jupiter's magnetosphere - Comparison of observation and theory. *Science*, 207:301–302, January 1980.

T. W. Hill. The Jovian auroral oval. *J. Geophys Res.*, pages 8101–8108, May 2001.

D. P. Hinson, F. M. Flasar, A. J. Kliore, P. J. Schinder, J. D. Twicken, and R. G. Herrera. Jupiter's ionosphere: Results from the first Galileo radio occultation experiment. *Geophys. Res. Lett.*, 24:2107–2110, September 1997.

D. P. Hinson, J. D. Twicken, and E. T. Karayel. Jupiter's ionosphere: New results from Voyager 2 radio occultation measurements. *J. Geophys Res.*, 103(12):9505–9520, May 1998.

T. S. Huang and T. W. Hill. Corotation lag of the Jovian atmosphere, ionosphere, and magnetosphere. *J. Geophys Res.*, 94:3761–3765, April 1989.

W. Hubbard, R. E. Nather, D. S. Evans, R. G. Tull, D. C. Wells, G. W. van Citters, B. Warner, and P. vanden Bout. The Occultation of Beta Scorpii by Jupiter and Io. I. Jupiter. *Astronomical Journal*, 77:41–59, February 1972.

W. B. Hubbard, C. C. Porco, D. M. Hunten, G. H. Rieke, M. J. Rieke, D. W. McCarthy, V. Haemmerle, J. Haller, B. McLeod, L. A. Lebofsky, R. Marcialis, J. B. Holberg, R. Landau, L. Carrasco, J. Elias, M. W. Buie, E. W. Dunham, S. E. Persson, T. Boroson, S. West, R. G. French, J. Harrington, J. L. Elliot, W. J. Forrest, J. L. Pipher, R. J. Stover, A. Brahic, and I. Grenier. Structure of Saturn's Mesosphere from the 28 SGR Occultations. *Icarus*, 130: 404–425, December 1997.

D. L. Huestis. $H^+ + H_2$ Ion-Molecule Reactions in the Ionospheres of the Outer Planets. *AAS/Division for Planetary Sciences Meeting Abstracts*, 37, August 2005.

D. M. Hunten. Energetics of Thermospheric Eddy Transport. *J. Geophys. Res*, 79:2533–2534, June 1974.

D. M. Hunten and A. J. Dessler. Soft electrons as a possible heat source for Jupiter's thermosphere. *Planetary & Space Science*, 25:817–821, September 1977.

J. Isbell, A. J. Dessler, and J. H. Waite. Magnetospheric energization by interaction between planetary spin and the solar wind. *J. Geophys Res.*, 89(18):10716–10722, December 1984.

K. K. Khurana. Influence of solar wind on Jupiter's magnetosphere deduced from currents in the equatorial plane. *J. Geophys Res.*, 106:25999–26016, November 2001.

K. K. Khurana and M. G. Kivelson. Inference of the angular velocity of plasma in the Jovian magnetosphere from the sweepback of magnetic field. *J. Geophys Res.*, 98:67–79, January 1993.

Y. H. Kim and J. L. Fox. The chemistry of hydrocarbon ions in the Jovian ionosphere. *Icarus*, 112:310–325, December 1994.

M. G. Kivelson and C. T. Russell. *Introduction to Space Physics.* Introduction to Space Physics, Edited by Margaret G. Kivelson and Christopher T. Russell, ISBN 0521451043. Cambridge, UK: Cambridge University Press, April 1995., April 1995.

A. J. Kliore, I. R. Patel, G. F. Lindal, D. N. Sweetnam, H. B. Hotz, J. H. Waite, and T. McDonough. Structure of the ionosphere and atmosphere of Saturn from Pioneer 11 Saturn radio occultation. *J. Geophys Res.*, 85(14):5857–5870, November 1980.

H. A. Lam, N. Achilleos, S. Miller, J. Tennyson, L. M. Trafton, T. R. Geballe, and G. E. Ballester. A Baseline Spectroscopic Study of the Infrared Auroras of Jupiter. *Icarus*, 127: 379–393, June 1997.

D. R. Lide. *CRC Handbook of chemistry and physics.* ed., by David R. Lide. Boca Raton: CRC Press, 1997.

G. F. Lindal, D. N. Sweetnam, and V. R. Eshleman. The atmosphere of Saturn - an analysis of the Voyager radio occultation measurements. *Astronomical Journal*, 90:1136–1146, June 1985.

I. C. F. Müller-Wodarg, R. V. Yelle, M. J. Mendillo, L. A. Young, and A. D. Aylward. The thermosphere of Titan simulated by a global three-dimensional time-dependent model. *J. Geophys Res.*, 105(A9):20833–20856, September 2000.

T. Majeed and J. C. McConnell. Voyager electron density measurements on Saturn: Analysis with a time dependent ionospheric model. *J. Geophys Res.*, 101(10):7589–7598, 1996.

T. Majeed, J. H. Waite, S. W. Bougher, R. V. Yelle, G. R. Gladstone, J. C. McConnell, and A. Bhardwaj. The ionospheres-thermospheres of the giant planets. *Advances in Space Research*, 33:197–211, 2004.

T. Majeed, R. V. Yelle, and J. C. McConnell. Vibrationally excited H2 in the outer planets thermosphere - Fluorescence in the Lyman and Werner bands. *Planetary & Space Science*, 39:1591–1606, November 1991.

K. I. Matcheva and D. F. Strobel. Heating of Jupiter's Thermosphere by Dissipation of Gravity Waves Due to Molecular Viscosity and Heat Conduction. *Icarus*, 140:328–340, August 1999.

H. Melin. *Comparative Aeronomy of the Upper Atmospheres of the Giant Planets.* PhD thesis, UCL, 2006.

H. Melin, S. Miller, T. Stallard, and D. Grodent. Non-LTE effects on H_3^+ emission in the jovian upper atmosphere. *Icarus*, 178:97–103, November 2005.

S. E. Milan, E. J. Bunce, S. W. H. Cowley, and C. M. Jackman. Implications of rapid planetary rotation for the Dungey magnetotail of Saturn. *J. Geophys Res.*, 110(A9):3209, March 2005.

S. Miller, N. Achilleos, G. E. Ballester, T. R. Geballe, R. D. Joseph, R. Prange, D. Rego, T. Stallard, J. Tennyson, L. M. Trafton, and J. H. Waite. The role of H_3^+ in planetary atmospheres. *Royal Society of London Philosophical Transactions Series A*, 358:2485–2502, September 2000.

S. Miller, N. Achilleos, G. E. Ballester, H. A. Lam, J. Tennyson, T. R. Geballe, and L. M. Trafton. Mid-to-Low Latitude H_3^+ Emission from Jupiter. *Icarus*, 130:57–67, November 1997.

G. Millward, S. Miller, T. Stallard, N. Achilleos, and A. D. Aylward. On the dynamics of the jovian ionosphere and thermosphere IV: Ion-neutral Coupling. *Icarus*, 173:200–211, January 2005.

G. Millward, S. Miller, T. Stallard, A. D. Aylward, and N. Achilleos. On the Dynamics of the Jovian Ionosphere and Thermosphere III: The Modelling of Auroral Conductivity. *Icarus*, 160:95–107, November 2002.

G. H. Millward, I. C. F. Müller-Wodarg, A. D. Aylward, T. J. Fuller-Rowell, A. D. Richmond, and R. J. Moffett. An investigation into the influence of tidal forcing on F region equatorial vertical ion drift using a global ionosphere-thermosphere model with coupled electrodynamics. *J. Geophys Res.*, 106(A11):24733–24744, November 2001.

G. H. Millward, R. J. Moffett, S. Quegan, and T. J. Fuller-Rowell. A coupled thermosphere-ionosphere-plasmasphere model (ctip). In *STEP Handbook of Ionospheric Models*, pages 239–279. SCOSTEP, 1996.

T. Moffat. *Developing and Validating the UCL Mars Thermosphere/Ionosphere Global Circulation Model.* PhD thesis, University College, London, UK, 2005.

L. E. Moore, M. Mendillo, I. C. F. Müller-Wodarg, and D. L. Murr. Modeling of global variations and ring shadowing in Saturn's ionosphere. *Icarus*, 172:503–520, December 2004.

J. I. Moses, B. Bézard, E. Lellouch, G. R. Gladstone, H. Feuchtgruber, and M. Allen. Photochemistry of Saturn's Atmosphere. I. Hydrocarbon Chemistry and Comparisons with ISO Observations. *Icarus*, 143:244–298, February 2000.

J. I. Moses and S. F. Bass. The effects of external material on the chemistry and structure of Saturn's ionosphere. *J. Geophys Res.*, pages 7013–7052, March 2000.

I. C. F. Müller-Wodarg, M. Mendillo, R. V. Yelle, and A. D. Aylward. A global circulation model of Saturn's thermosphere. *Icarus*, 180:147–160, January 2006.

J. Nichols and S. Cowley. Magnetosphere-ionosphere coupling currents in Jupiter's middle magnetosphere: effect of precipitation-induced enhancement of the ionospheric Pedersen conductivity. *Ann. Geophys.*, 22:1799–1827, May 2004.

C. D. Parkinson, A. I. F. Stewart, A.-S. Wong, Y. L. Yung, and J. M. Ajello. Enhanced Transport in the Polar Mesosphere of Jupiter: Evidence from Cassini UVIS Helium 584 Å Airglow. *J. Geophys Res.*, 111, February 2006.

D. H. Pontius. Implications of variable mass loading in the Io torus: The Jovian flywheel. *J. Geophys Res.*, 100(9):19531–19540, October 1995.

D. H. Pontius. Radial mass transport and rotational dynamics. *J. Geophys Res.*, 102:7137–7150, April 1997.

S. S. Prasad. Possible new Jovian thermospheric models. *Astrophys. Journal*, 200:L171–L174, September 1975.

C. H. B. Priestley and W. C. Swinbank. Vertical transport of heat by turbulence in the atmosphere. *Proc. Roy. Soc. London, A*, 189:543–561, 1947.

J. A. Ratcliffe. *An introduction to the ionosphere and magnetosphere.* London: Cambridge University Press, 1972.

P. L. Read. Super-rotation and diffusion of axial angular momentum: II. A review of quasi-axisymmetric models of planetary atmospheres. *Quarterly Journal of the Royal Meteorological Society*, 112:253–272, January 1986.

J. D. Richardson. Thermal ions at Saturn - Plasma parameters and implications. *J. Geophys Res.*, 91(10):1381–1389, February 1986.

H. Rishbeth. The Ionosphere of Jupiter. *Australian Journal of Physics*, 12:466–468, December 1959.

T. Satoh and J. E. P. Connerney. Jupiter's H_3^+ Emissions Viewed in Corrected Jovimagnetic Coordinates. *Icarus*, 141:236–252, October 1999.

J. Saur, B. H. Mauk, A. Kaßner, and F. M. Neubauer. A model for the azimuthal plasma velocity in Saturn's magnetosphere. *J. Geophys Res.*, 109(18):5217, May 2004.

A. Seiff, D. B. Kirk, T. C. D. Knight, L. A. Young, F. S. Milos, E. Venkatapathy, J. D. Mihalov, R. C. Blanchard, R. E. Young, and G. Schubert. Thermal structure of Jupiter's upper atmosphere derived from the Galileo probe. *Science*, 276:102–104, 1997.

A. Seiff, D. B. Kirk, T. C. D. Knight, R. E. Young, J. D. Mihalov, L. A. Young, F. S. Milos, G. Schubert, R. C. Blanchard, and D. Atkinson. Thermal structure of Jupiter's atmosphere near the edge of a 5-μm hot spot in the north equatorial belt. *J. Geophys Res.*, 103(12): 22857–22890, September 1998.

M. Shimizu. The Upper Atmosphere of Jupiter. *Icarus*, 14:273, April 1971.

G. L. Siscoe and D. Summers. Centrifugally driven diffusion of Iogenic plasma. *J. Geophys Res.*, 86:8471–8479, September 1981.

C. G. A. Smith, S. Miller, and A. D. Aylward. Magnetospheric energy inputs into the upper atmospheres of the giant planets. *Ann. Geophys.*, 23:1943–1947, 2005.

G. R. Smith and D. M. Hunten. Study of planetary atmospheres by absorptive occultations. *Reviews of Geophysics*, 28:117–143, May 1990.

G. R. Smith, D. E. Shemansky, J. B. Holberg, A. L. Broadfoot, B. R. Sandel, and J. C. McConnell. Saturn's upper atmosphere from the Voyager 2 EUV solar and stellar occultations. *J. Geophys Res.*, 88:8667–8678, November 1983.

P. Song, T. I. Gombosi, and A. J. Ridley. Three-fluid Ohm's law. *J. Geophys Res.*, 106(15): 8149–8156, May 2001.

D. J. Southwood and M. G. Kivelson. A new perspective concerning the influence of the solar wind on the Jovian magnetosphere. *J. Geophys Res.*, 106:6123–6130, April 2001.

T. Stallard, S. Miller, G. E. Ballester, D. Rego, R. D. Joseph, and L. M. Trafton. The H^+_3 Latitudinal Profile of Saturn. *Astrophysical Journal*, 521:L149–L152, August 1999.

T. Stallard, S. Miller, G. Millward, and R. D. Joseph. On the Dynamics of the Jovian Ionosphere and Thermosphere. II. The Measurement of H_3^+ Vibrational Temperature, Column Density, and Total Emission. *Icarus*, 156:498–514, April 2002.

T. S. Stallard, S. Miller, S. W. H. Cowley, and E. J. Bunce. Jupiter's polar ionospheric flows: Measured intensity and velocity variations poleward of the main auroral oval. *Geophys. Res. Lett.*, 30:25–8, March 2003.

T. S. Stallard, S. Miller, L. M. Trafton, T. R. Geballe, and R. D. Joseph. Ion winds in Saturn's southern auroral/polar region. *Icarus*, 167:204–211, January 2004.

D. F. Strobel and S. K. Atreya. *Ionosphere*, pages 51–67. Physics of the Jovian Magnetosphere, 1983.

D. F. Strobel and G. R. Smith. On the temperature of the jovian thermosphere. *Journal of Atmospheric Science*, 30:718–725, 1973.

J. T. Trauger, R. E. Griffiths, J. J. Hester, J. G. Hoessel, J. A. Holtzman, J. E. Krist, J. R. Mould, R. Sahai, P. A. Scowen, K. R. Stapelfeldt, and A. M. Watson. Saturn's hydrogen aurora: Wide field and planetary camera 2 imaging from the Hubble Space Telescope. *J. Geophys Res.*, 103:20237–20244, September 1998.

V. M. Vasyliūnas and P. Song. Meaning of ionospheric Joule heating. *J. Geophys Res.*, 110(9): 2301, February 2005.

V. M. Vasyliunas. *Plasma distribution and flow*, pages 395–453. Physics of the Jovian Magnetosphere, 1983.

J. Veverka, L. H. Wasserman, J. Elliot, C. Sagan, and W. Liller. The occultation of beta SCO by Jupiter. I. The structure of the jovian upper atmosphere. *AJ*, 79:73–84, January 1974.

J. H. Waite, T. E. Cravens, J. Kozyra, A. F. Nagy, S. K. Atreya, and R. H. Chen. Electron precipitation and related aeronomy of the Jovian thermosphere and ionosphere. *J. Geophys Res.*, 88:6143–6163, August 1983.

A. D. C. Williams. *JIME - The Exoplanet Ionospheric Model.* PhD thesis, UCL, 2004.

J. Woch, N. Krupp, A. Lagg, B. Wilken, S. Livi, and D. J. Williams. Quasi-periodic modulations of the Jovian magnetotail. *Geophys. Res. Lett.*, 25:1253–1256, April 1998.

R. V. Yelle and S. Miller. Jupiter's Upper Atmosphere. In F. Bagenal, W. McKinnon, and T. Dowling, editors, *Jupiter: Planet, Satellites and Magnetosphere*, pages 185–218. Cambridge University Press, 2004.

L. A. Young, R. V. Yelle, R. Young, A. Seiff, and D. B. Kirk. Gravity Waves in Jupiter's Thermosphere. *Science*, 276:108–111, April 1997.